Development and Application of Chlorine Solid-State Nuclear Magnetic Resonance and Quantum Chemical Calculations to the Study of Organic and Inorganic Systems

Rebecca Chapman

Thesis submitted to the
Faculty of Graduate and Postdoctoral Studies
In partial fulfillment of the requirements
For the degree of Ph.D. in Chemistry

Ottawa-Carleton Chemistry Institute
Department of Chemistry
University of Ottawa

uOttawa

Table of Contents

List of Figures

List of Tables

List of Abbreviations and Symbols Used

ACQ	acquire or acquisition
α, β, γ	Euler angles
B_0	external magnetic field
B3LYP	Becke, three-parameter, Lee-Yang-Parr
C_Q	quadrupolar coupling constant
CP	cross-polarization
CS	chemical shift
CSA	chemical shift anisotropy
CT	central transition
cw	continuous wave
D	dipolar coupling constant
$\boldsymbol{\delta}$	chemical shift tensor
δ_{11}, δ_{22}, δ_{33}	principal components of the chemical shift tensor
δ_{iso}, δ	isotropic chemical shift
DFT	density functional theory
e	fundamental charge
EFG	electric field gradient
η_Q	asymmetry parameter
FID	free-induction decay
GIPAW	gauge including projector augmented wave
$\hat{H}$	Hamiltonian

h	Planck constant
$\hbar$	reduced Planck constant
HF	Hartree-Fock
I, **S**	nuclear spin operators
γ	magnetogyric ratio
I, S	nuclear spin angular momentum quantum numbers
κ	skew of the chemical shift or the magnetic shielding tensor
MAS	magic angle spinning
$\sigma_{11}, \sigma_{22}, \sigma_{33}$	principle components of the magnetic shielding tensor
MS, σ	magnetic shielding
MQMAS	multiple-quantum magic angle spinning
NA	natural abundance
Ω	span of the chemical shift or magnetic shielding tensor
PAS	principal axis system
ppm	parts per million
pXRD	powder X-ray diffraction
Q	electric quadrupole moment
QCPMG	quadrupolar Carr-Purcell-Meiboom-Gill
QI	quadrupolar interaction
REDOR	rotational echo double resonance
RESPDOR	rotary resonance echo saturation pulse double resonance
RHF	restricted Hartree-Fock
r	distance

rf	radio frequency
$\sigma_{11,}$ σ_{22}, σ_{33}	principal components of the magnetic shielding tensor
$\boldsymbol{\sigma}$	magnetic shielding tensor
σ_{iso}	isotropic magnetic shielding constant
SSNMR	solid state nuclear magnetic resonance
ST	satellite transitions
T	Tesla
T_1	longitudinal relaxation
T_2	transverse relaxation
T_2^*	apparent transverse relaxation
VOCS	variable offset cumulative spectrum
$\mathbf{V}$	electric field gradient tensor
V_{11}, V_{22}, V_{33}	principal components of the electric field gradient tensor
WURST	wideband uniform-rate smooth truncation
XRD	X-ray diffraction

Abstract

Chlorine solid-state nuclear magnetic resonance (SSNMR) is an ideal site specific probe of chloride-containing solids as SSNMR tensor properties are sensitive to the local chlorine environment. In this thesis, the development and use of chlorine SSNMR as a method to characterize a wide variety of chemical environments was explored. Ultrahigh field, and multi-field studies were essential to overcome the difficulties associated with the collection of chlorine SSNMR spectra.

Benchmark chemical shift (CS) and electric field gradient (EFG) tensor data were collected for organic chloride systems, including several amino acid hydrochlorides. These experiments demonstrated the sensitivity of chlorine SSNMR to slight changes in chemical environment. Quantum chemical calculations were used to complement experimental data, with the gauge-including projector augmented wave DFT (GIPAW-DFT) method shown to yield better agreement than B3LYP or RHF methods. The GIPAW-DFT method was found to slightly, but systematically, overestimate the chlorine quadrupolar coupling constant and the CS tensor span. Other organic chlorides examined by chlorine SSMR included a known ion receptor, *meso*-octamethylcalix[4]pyrrole. This compound was found to have a very small quadrupole interaction (QI), but significant chemical shift anisotropy (CSA). GIPAW-DFT calculations were also utilized and, in combination with the experimental results, used to identify the solvate structure of the material analyzed by NMR.

Chlorine SSNMR was further used to study different solvate structures and polymorphism. The technique was an effective means to distinguish different room temperature polymorphs of benzidine hydrochloride, despite the similarities of the chloride environments. In the case of magnesium chloride, chlorine SSNMR was sensitive to the level of hydration and

through the use of GIPAW-DFT calculations, the identity of an unknown hydrate was determined.

An analysis of several group thirteen chlorides demonstrated that chlorine SSNMR was also capable of characterizing the chlorine environment in cases where the QI is large, despite the resulting broad line widths. In these systems GIPAW-DFT calculations also yielded excellent agreement with experimental values.

Throughout this research, chlorine SSNMR has been shown to be a useful and effective means to study both organic and inorganic chlorides, with computational methods proving to be an important complement to experimental data.

Acknowledgments

Firstly, I would like to thank my supervisor David Bryce (that's Dave Br) for his guidance over the last five years. Dave was a great educator who was always ready to help with any issue (science or not) and his enthusiasm for research was contagious. I'm very lucky to have been a student in his group.

As the first graduate student in the Bryce lab, I feel privileged to have watched the lab grow over the years. I have had the benefit of working with many young undergraduate scientists over the years and would like to thank all of them, especially Greg, who was on team chlorine when I arrived, and my summer students Miranda, Melanie and Brittany. I would also like to thank the other graduate students who I've had the privilege of working with, all of whom made the Bryce lab a great place to work. And also a great place to pick up some français! Joey was a fabulous office-mate and an excellent host/attendee of scotch and/or Samiclaus parties (SPOILER ALERT, Samiclaus is not good). It was great working with Rob (Masters #2) and I wish him the best of luck in the future. The current MRN05 crew all made coming to work a lot more entertaining and deserve a special thank-you. Kevin "the Fresident" has become a full-on spectroscopist (and a good one too!), despite his past in organic chemistry. And it was certainly nice to have someone with synthetic experience around! I thank him (and Jaz!) for the all the delicious trips to F&S for breakfast. Jasmine is a welcome fellow female influence in the Bryce office and a great researcher whose presentation-making skills are second to none (I'm a little jealous). Fred (proud author of Fsolids) has a grasp of mathematics that is a little scary (and very impressive) and a passion for research that is uplifting. With you three around, I know I leave the lab in good hand. Lastly, I would like to thank Cory for being a great teacher, an excellent editor, always keeping me up to date on interesting articles, and for watching all of those

ridiculous online videos I enjoy (cat eating spaghetti, cats on a treadmill, BasilMarceaux.com, etc). Good luck in France Cory!

I need to thank Gillian Goward at McMaster University for being a great undergraduate supervisor, and for first introducing me to research and solid-state NMR. In her lab I was very fortunate to have worked with Lindsay Cahill, who was an excellent teacher and continues to be a great role model and friend.

I would also like to thank Glenn Facey, Andy Lo, Victor Terskikh, Shane Pawsey and Eric Ye for their technical support and guidance with my NMR experiments. Glenn was an excellent teacher, and was always willing and able to help with any NMR problem I had. At the 900 (a.k.a. The National Ultrahigh Field NMR Facility for Solids), Victor's knowledge was an invaluable resource and Shane/Eric's technical knowhow made my life a lot easier. I also need to thank Jennifer Hiscock and Philip Gale for providing the calix compound used in Chapter 4, Ilia Korbokov for carrying out the single crystal X-ray experiments in Chapter 3 and Sadok Letief for the TGA measurements in Chapter 4.

Graduate school isn't *all* about work and my experience was made much more enjoyable by my Marion colleagues. From the beginning James Hooper was a welcome visitor to the lab, always bringing great conversation and PEI friendliness! Cory, James and I had many evening conversations that made work a lot more enjoyable. The upstairs members of the Marion crew – Jess Priem and Ian Mallov - would always be up for wings when I needed it and were fantastic co-members of the CGSA (Cory too!). Although we'll all be finished soon (just waiting on Cory...), I'm sure there are many more years of hockey pools to come, and inevitably many more victories for James as well….

There are countless other people who have been wonder friends over the years and to whom I'm very grateful. I need to thank Elyse Bernard specifically for being a terrific flatmate, a great friend, and for loving French Kiss and Mulan as much as me. If I ever needed to talk/complain about anything Elyse was always there to listen.

I have pretty amazing parents. They gave me their love of learning and taught me the importance of hard work and dependability. Most importantly, they've taught me to have fun and not take myself or life too seriously. My Mom's strength in times of difficulty has been an inspiration and none of my successes would have been possible without her. I also thank Sandy and my extended family for their support.

On the subject of writing, I would like to thank the friendly staff at my local Bridgehead and Starbucks outlets for the sweet caffeine fixes, free wi-fi and comfy chairs. I also need to send shout outs to John Mayer, Ron Hawkins, James Iha, Leonard Cohen, Michael Franti (and Spearhead), Stars, the Weakerthans, and the friendly voices of CBC radio for helping me keep (most) of my sanity during the writing of this thesis.

Financial support from the University of Ottawa and NSERC is gratefully acknowledged.

Lastly, I would like thank my sweetie Dave Blair (that's Dave Bl) for always believing in me, making me laugh and downloading British panel shows for us to watch together. On top of that, for being my best friend. I cannot thank Dave enough for his encouragement, friendship and love.

I dedicate this thesis to my Dad who I'm sure would have legitimately found it fascinating.

Chapter 1

Introduction – Theory and Objectives

1.1 Introduction

Chlorine is a chemical element which occurs naturally throughout the environment. It is present in the earth's crust, sea water, and in the human body.[1] While elemental chlorine (Cl_2) is toxic to humans,[2] the chloride ion plays a part in a variety of inorganic and organic compounds in the liquid and solid states. For example, chlorine plays an important biological role in the body's chloride ion channels which help regulate a wide variety of properties and processes including pH, cell migration, solute transport, and many others.[3-6] Chloride also serves as an important ion in synthesis and finds itself a part of a variety of important inorganic catalysts, including the famous Grubbs' catalyst.[1] A site specific probe of the local environment about chloride ions in solids would thus be a useful tool to study a wide variety of solid chemicals and materials.

As there is a wide variety of chlorine containing compounds, there is a wide variety of tools available for their study. Among these, many spectroscopic techniques can only be used in solution or do not examine the chlorine environment explicitly. While this is useful in some cases, many of the natural occurrences and practical applications of chlorine occur in the solid state, and thus characterization of the solid chloride environment is desirable. X-ray diffraction is a powerful technique for the study of solids, but it has some limitations.[7-9] Single crystal X-ray is restricted to cases where crystals of sufficient size are available, while the information which can be extracted from powder X-ray diffraction is often limited unless more sophisticated Rietveld refinements are used.[10, 11] Moreover, in both cases only crystalline states can be

detected. Nuclear quadrupole resonance (NQR)[12] is another technique which can be useful for the study of solids, as it provides information about the electric field gradient (EFG) within a material, but is unable to provide much in the way of other information. An ideal method to study solids is solid-state nuclear magnetic resonance (SSNMR) spectroscopy, as it is an excellent probe of the local environment in many solid compounds and materials due to the technique's sensitivity to both the local electronic and structural environments. Unlike single crystal X-ray diffraction, SSNMR can be used to characterize powders (along with single crystals) and can also examine both crystalline and amorphous states. The method is also a non-destructive technique, in which the sample can be easily recovered. Therefore, application of chlorine SSNMR would be useful in gaining a better understanding of the local chlorine environments in a wide variety of compounds. Chlorine possesses many properties which render collection of its SSNMR signal difficult, which has prevented chlorine NMR studies in the past (*vide infra*). However, with the introduction of higher magnetic fields, improved hardware and new pulse sequences, a wide variety of materials are now amenable to chlorine SSNMR studies.

1.2 NMR Spectroscopy

Since its discovery in the 1930's and 1940's,[13-15] nuclear magnetic resonance (NMR) spectroscopy has developed significantly and has become an extremely important tool for structural, biophysical and imaging studies. There have been a total of 6 Nobel prizes (3 in physics, 2 in chemistry and 1 in medicine)[16-18] awarded for the development and advancement of NMR, and a NMR spectrometer (or many!) is now an essential part of any university chemistry department. Below is a brief description of the basic theory behind NMR. This will be followed by a more detailed description of the NMR theory as it relates to chlorine.

1.2.1 Background Theory

NMR is a spectroscopic technique which exploits the properties of a nucleus within an external magnetic field. All nuclei with a nuclear magnetic spin number (I) greater than zero possess spin angular momentum and their resulting dipole moment will interact with an external magnetic field. These nuclei are amenable for NMR experiments and are known as being 'NMR-active'. Almost all of the naturally occurring elements on the periodic table have at least one NMR-active isotope with a non-negligible natural abundance. When placed in an external magnetic field, the magnetic moments associated with NMR-active nuclei will precess about that field, resulting in an interaction which can be visualized as net magnetization, as shown in Figure 1.1.[19] This effect is known as the Zeeman Interaction. The number of possible eigenstates of a nucleus is equal to $2I+1$, and when oriented in a magnetic field each of these states will have different energies. For example, in the case of an isolated nucleus with $I = ½$, there are two unique energy states ($m = ½, -½$). The energy of these states is equal to:

$$E_m = -m\hbar\gamma B_0 \qquad [1.1]$$

where m is the nuclear spin quantum number, γ is the magnetogyric ratio and B_0 is the strength of the external magnetic field. The γ ratio is an experimentally determined property and is unique to each nucleus. The frequency of precession is given by:

$$\nu_L = \frac{\gamma B_0}{2\pi} \qquad [1.2]$$

This value is known as the Larmor Frequency (ν_L). For the magnetic field strengths available for NMR spectroscopy, this separation is always in the radio frequency region of the electromagnetic spectrum.[20] As the states have different energies in a magnetic field, for a macroscopic samples consisting of many spins, a population difference will result, with the lower energy states being more highly populated than those states which are higher in energy.

This difference is described by the Boltzmann distribution, which is shown in equation 1.3:

$$\frac{N_m}{N_n} = e^{-\frac{E_m - E_n}{KT}} \qquad [1.3]$$

In this equation, N_m and N_n refer to the population in the m and n states, respectively, while E_m and E_n are their corresponding energies. The other terms, k and T, refer to the Boltzmann constant and the temperature (in Kelvin), respectively. Increasing the magnetic field increases the energy gap between the states, resulting in a larger population difference and therefore increases the signal observed. Similarly, the population difference can also be increased by *lowering* the temperature of the sample.

It is impractical to detect magnetization along the magnetic field (defined as the z-axis), and therefore a radio frequency (rf) pulse is applied to rotate the net magnetization vector into the xy plane. This can be accomplished with an rf pulse at the Larmor frequency of a nucleus. The amount of rotation afforded by the pulse (i.e., the flip angle) is determined by its length and power; with an angle of 90° leading to saturation (i.e., maximum signal for detection by the receiver coil). After the pulse, the system will begin to return to equilibrium, precessing about the z-axis in a cone of constant angle at its resonance frequency. This process is shown using the vector model in Figure 1.1:

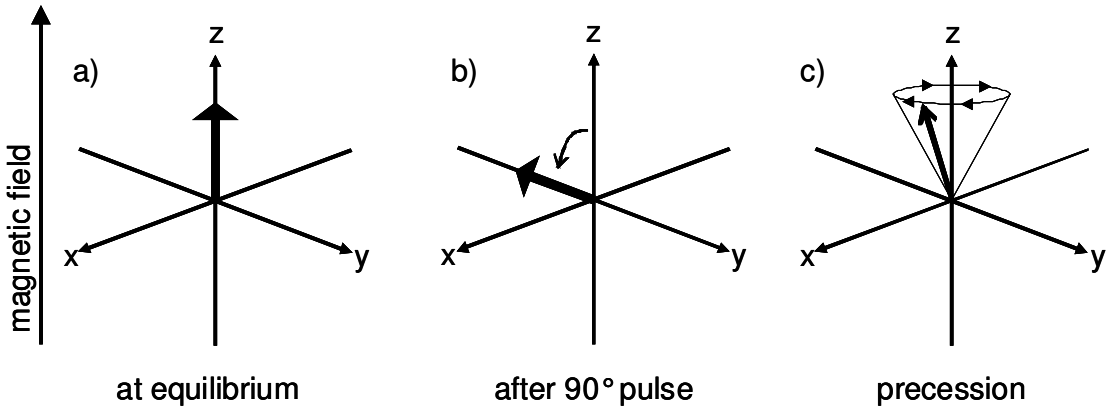

Figure 1.1. Vector model of a simple NMR experiment for an ensemble of isolated spins: a) net magnetization at equilibrium aligned along an external magnetic field, b) net magnetization after a 90º pulse along the x axis and c) precession about the magnetic field as it returns to equilibrium.

If there is more than one unique nuclear environments within a sample, these will precess at different rates (i.e., different frequencies). The receiver measures the free induction delay (FID) of the magnetization, which decays completely upon its return to equilibrium. The FID is then Fourier-transformed to give a spectrum in the frequency domain.

A more detailed description of the specific NMR properties of chlorine, along with the interactions specific to solids relevant to this project will be discussed below.

1.3 Chlorine SSNMR

1.3.1 NMR Properties

The two isotopes of chlorine, chlorine-35 and chlorine-37, are NMR-active quadrupolar nuclei (both $I = 3/2$) that have relatively high natural abundances. The NMR properties of the two isotopes of chlorine are shown in Table 1.1, along with those of the nucleus that is most commonly observed, ^{1}H.[21] Examination of this table reveals the primary challenges associated

with the collection of high quality chlorine NMR data: the moderately large quadrupole moment (Q) and the relatively low magnetogyric ratio. The Q results in broad lines in many cases while the low γ leads to a small resonance frequency and, subsequently, a small population difference and need for high field instruments. These difficulties will be discussed further below and in Chapter 2.

Table 1.1. NMR Properties of chlorine-35, chlorine-37 and hydrogen-1

	Natural Abundance / %	I	γ/ 10^7 rad T^{-1} s^{-1}	Ξ[a]/ MHz	Q[b] / *mb*	Receptivity Relative to ^{1}H
^{35}Cl	75.78	3/2	2.624	9.7979	–81.65(80)	0.0035
^{37}Cl	24.22	3/2	2.184	8.1557	–64.35(64)	0.0006
^{1}H	99.99	1/2	26.75	100	-	1

[a] Resonance frequency relative to ^{1}H at 100 MHz
[b] From P. Pyykkö, *Mol. Phys.* **2008,** *106*, 1965.

The equation for the Hamiltonian operator ($\hat{H}$) in the presence of an external magnetic field (B_0) is shown in Equation 1.4. For a non-paramagnetic nucleus within a solid sample, $\hat{H}$ contains terms arising from the interaction of the spin with the applied rf field ($\hat{H}_{rf}$) and the nuclear magnetic shielding ($\hat{H}_\sigma$) interaction acting as a perturbation to the Zeeman term ($\hat{H}_Z$). In the case of the quadrupolar chlorine nuclides, the Hamiltonian also contains a quadrupolar term ($\hat{H}_Q$).

$$\hat{H} = \hat{H}_Z + \hat{H}_{rf} + \hat{H}_\sigma + \hat{H}_Q \qquad [1.4]$$

Where the individual Hamiltonians are equal to:

$$\hat{H}_Z = -\gamma B_0 \hat{I}_Z \qquad [1.5]$$

$$\hat{H}_{rf} = -\gamma B_1 \hat{I}_X \qquad [1.6]$$

$$\hat{H}_\sigma = -\gamma \hat{\mathbf{I}} \cdot \sigma \cdot B_0 \qquad [1.7]$$

$$\hat{H}_Q = \frac{eQ}{2I(2I-1)\hbar}\hat{\mathbf{I}}\cdot\hat{\mathbf{V}}\cdot\hat{\mathbf{I}} \quad [1.8]$$

In equations 1.5 – 1.8, B_1 is the magnetic field associated with the rf pulse (which for this example is in the x-direction), $\hbar$ is the reduced Planck constant, $\boldsymbol{\sigma}$ is the magnetic shielding tensor, $\mathbf{V}$ is the EFG tensor, $\mathbf{I}$ is the nuclear spin vector, and the external magnetic field is B_0. Other terms including direct homonuclear and heteronuclear dipolar coupling, as well as indirect spin-spin coupling (J), are present in many cases, but these have a negligible impact on the chlorine $\hat{H}$ for the majority of chlorine compounds.[22] Thus, only the nuclear magnetic shielding (MS) and quadrupolar interactions will be described below.

1.3.2 Magnetic Shielding/Chemical Shift Interaction

When placed in an external magnetic field, the electrons surrounding a nucleus respond by creating an induced secondary field which interacts with the nucleus. The resulting interaction, known as magnetic shielding (MS), is orientation-dependent and can be represented by a second-rank tensor (MS tensor), shown in equation 1.9 (also shown in its principal axis system, PAS).[23]

$$\begin{pmatrix} \sigma_{XX} & \sigma_{XY} & \sigma_{XZ} \\ \sigma_{YX} & \sigma_{YY} & \sigma_{YZ} \\ \sigma_{ZX} & \sigma_{ZY} & \sigma_{ZZ} \end{pmatrix} \overset{PAS}{\longrightarrow} \begin{pmatrix} \sigma_{11} & 0 & 0 \\ 0 & \sigma_{22} & 0 \\ 0 & 0 & \sigma_{33} \end{pmatrix} \quad [1.9]$$

In liquid-state NMR, the MS tensor ($\boldsymbol{\sigma}$) is time-averaged to its isotropic value ($\sigma_{iso} = \frac{\sigma_{11}+\sigma_{22}+\sigma_{33}}{3}$) as a result of the rapid molecular tumbling which occurs in solution. This averaging does not occur in powdered solids and in the absence of magic-angle spinning (MAS), the shielding that arises from all molecular orientations will contribute to the SSNMR spectrum of a powdered sample. The breadth of the orientation-dependence is known as chemical shift anisotropy (CSA). While it is not generally possible to measure shielding constants directly in conventional NMR experiments, it is routine to measure the shielding difference between two

compounds, with one serving as a reference. This "chemical" shift (CS, δ) can be defined in terms of MS as:

$$\delta / \text{ppm} = \frac{\sigma_{ref} - \sigma}{1 - \sigma_{ref}} \times 10^6 \qquad [1.10]$$

where σ and σ_{ref} represent the MS of the sample and the reference, respectively. The CS may be more practically defined in terms of resonance frequencies in lieu of shielding constants, as shown below.

$$\delta / \text{ppm} = \frac{\nu - \nu_{ref}}{\nu_{ref}} \qquad [1.11]$$

In equation 1.11, ν and ν_{ref} represent the resonance frequency of the sample and the reference (in the same magnetic field), respectively.

Both the MS and CS are second-rank tensor quantities which, when diagonalized, have three principal components associated with their PAS, as shown in equation 1.9 for the MS tensor. Thus, equation 1.10 may be used to calculate each element of a CS tensor (δ_{ij}) from the corresponding MS tensor element (σ_{ij}) of the sample, if the isotropic MS value of the reference is also known. This is the case with chlorine, as the MS scale has been determined to high accuracy. This scale was determined through a combined experimental and theoretical study.[24] An isotropic MS constant (σ_{iso}) of 974(4) ppm was determined for a chloride ion in an infinitely dilute aqueous system.[24] The conversion between shielding and shift is therefore as follows (*cf.* eq. 1.10):

$$\delta = (974 - \sigma)/(1 - 974 \times 10^{-6}) \qquad [1.12]$$

and is an improvement over prior chlorine absolute shielding scales.[25,26] The principal components of the CS tensor are defined as $\delta_{11} \geq \delta_{22} \geq \delta_{33}$.

The convention for reporting CS tensor data is not uniform within the literature. Popular conventions include the Haeberlen-Mehring-Spiess convention[27-30] and the Herzfeld-Berger/Maryland convention.[29,31] While both conventions are still commonly used in the literature, only the Herzfeld-Berger/Maryland convention was used in this work and is therefore the only convention described below.

1.3.2.1 "Herzfeld-Berger"/"Maryland" Convention

The three principal components of the shielding tensor, σ_{11}, σ_{22} and σ_{33}, are always arranged as follows: $\sigma_{11} \leq \sigma_{22} \leq \sigma_{33}$. As mentioned above, the σ_{iso} is the average of the three principal components. The other parameters used to describe the MS tensor are the span (Ω), which describes the breadth of the pattern and the skew (κ), which describes the asymmetry. These parameters are defined below:

$$\Omega = \sigma_{33} - \sigma_{11} \qquad [1.13]$$

$$\kappa = \frac{3(\sigma_{iso} - \sigma_{22})}{\Omega} \qquad [1.14]$$

The span can take on any real number and, by definition, will be positive, while the skew ranges between -1 and +1. When discussing experimental results, the definitions are applied to the CS tensor, as shown below:

$$\delta_{iso} = \frac{\delta_{11} + \delta_{22} + \delta_{33}}{3} \qquad [1.15]$$

$$\Omega \approx \delta_{11} - \delta_{33} \qquad [1.16]$$

$$\kappa = \frac{3(\delta_{22} - \delta_{iso})}{\Omega} \qquad [1.17]$$

As long as 1-σ_{ref} is close to unity, equation [1.16] is valid, allowing for the direct comparison of CS and calculated MS data. This is practically always the case when discussing chlorine SSNMR data and is true for all data discussed in this document.

As mentioned, the data included in this thesis all follow the above convention. In cases where comparisons are made with experimental data written in a different convention, the appropriate conversions were done.

1.3.3 Nuclear Electric Quadrupolar Interaction

As the two isotopes of chlorine both are quadrupolar nuclei, the nuclear charge is distributed asymmetrically about the nucleus. The resulting Q couples with the EFG tensor at the nuclear centre. A negative Q value indicates an oblate spheroid nuclear charge, whereas a positive Q would indicate a prolate spheroid charge. The coupling between the Q of the nucleus and the surrounding EFG leads to a broadening of the resulting NMR spectrum, proportional to both the Q and the magnitude of the EFG tensor. The EFG tensor, shown in equation 1.18, is symmetric (i.e., the off-diagonal terms are the same above and below the diagonal of the matrix) and may be described by five independent parameters. In its PAS (also shown in equation 1.18), the three principal components of the tensor are labelled, V_{11}, V_{22}, and V_{33}, with the magnitudes arranged as shown: $|V_{33}| \geq |V_{22}| \geq |V_{11}|$.

$$\begin{pmatrix} V_{XX} & V_{XY} & V_{XZ} \\ V_{YX} & V_{YY} & V_{YZ} \\ V_{ZX} & V_{ZY} & V_{ZZ} \end{pmatrix} \overset{PAS}{\longrightarrow} \begin{pmatrix} V_{11} & 0 & 0 \\ 0 & V_{22} & 0 \\ 0 & 0 & V_{33} \end{pmatrix} \quad [1.18]$$

Three angles describe the orientation of the EFG PAS with respect to an external axis system. Since the EFG tensor is traceless, the principal components may be fully described using two independent parameters. These components are generally expressed in terms of the quadrupolar coupling constant (C_Q) and the asymmetry parameter (η_Q):

$$C_Q = \frac{eV_{33}Q}{h} \qquad [1.19]$$

$$\eta_Q = \frac{V_{11} - V_{22}}{V_{33}} \qquad [1.20]$$

where *e* is the elementary charge. The quadrupole moment is a constant and specific to a given ground-state nucleus (the values for chlorine are shown in Table 1.1).

In order to fully describe the CS and EFG tensors, the orientations of their PASs must be known. In practice, during the analysis of powdered samples one typically measures the relative orientation of the PASs of the CS and EFG tensors. This requires an additional three parameters, known as the Euler angles, α, β and γ. Under the Arfken convention,[32] these angles describe the counter-clockwise rotations of the CS tensor away from the stationary EFG reference tensor, assuming initial coincidence of the two PASs. Specifically, α describes the initial rotation about the original δ_{33} axis, β is the rotation about the new direction of δ_{22} and γ is the final rotation around the new direction of δ_{33}, as shown in Figure 1.2.

One of the primary challenges associated with chlorine-35/37 SSNMR stems from the moderately high *Q* values of both isotopes (see Table 1.1). In systems where the nucleus does not sit at a site of very high symmetry, e.g., octahedral or tetrahedral, the interaction between the *Q* of the nucleus and the EFG tensor is a significant perturbing interaction to the Zeeman Hamiltonian, which broadens the resulting NMR spectrum.

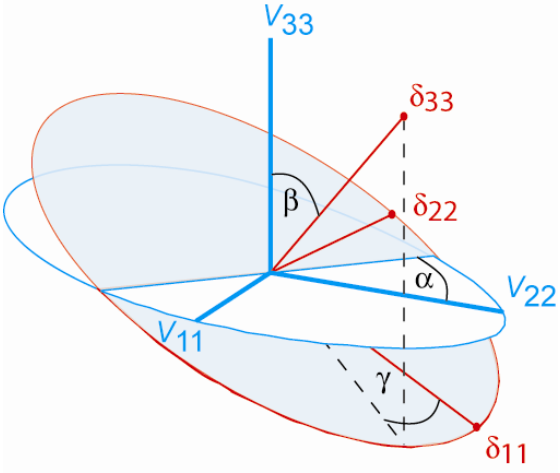

Figure 1.2. Depiction of the Euler angles α, β, γ used for relating the PAS of the EFG tensor (**V**) and the CS tensor (**δ**).[32] The angles may also be visualized as counterclockwise rotations of the δ tensor PAS away from the V PAS: α describes the initial rotation about the original δ_{33} axis, β is a rotation about the new direction of δ_{22} and γ is the final rotation around the new direction of δ_{33}.

As chlorine atoms do not sit at a site of high symmetry in most systems of interest, quadrupolar broadening is generally the dominant contribution to the observed line widths. Due to the moderately high *Q*, first-order perturbation theory generally fails to describe the SSNMR line shapes which are observed experimentally for chlorine-containing powdered samples. Second-order perturbation theory, however, often adequately describes the experimental SSNMR line shape (*vide infra*). Both isotopes of chlorine are half-integer quadrupoles (I =3/2) and therefore possess a central transition (CT, m = ½ ↔ −½) in addition to two satellite transitions (ST). Generally for chlorine, the quadrupolar interaction (QI) is sufficiently large to broaden the satellite transitions to such an extent that they cannot be observed, and experimentally only the CT can be detected; even the CT may be broadened to a significant extent, up to the order of

MHz in some cases.[33,34] The CT is not broadened by first order quadrupolar effects but is affected in the second order. This is shown in Figure 1.3, which is a representation of the energies of the spin states of chlorine (I = 3/2) due to the Zeeman interaction and the effects of the QI perturbation to the first and second order. In Figure 1.3, the CT is represented by the orange double-headed arrows while the black double-headed arrows represent the ST.

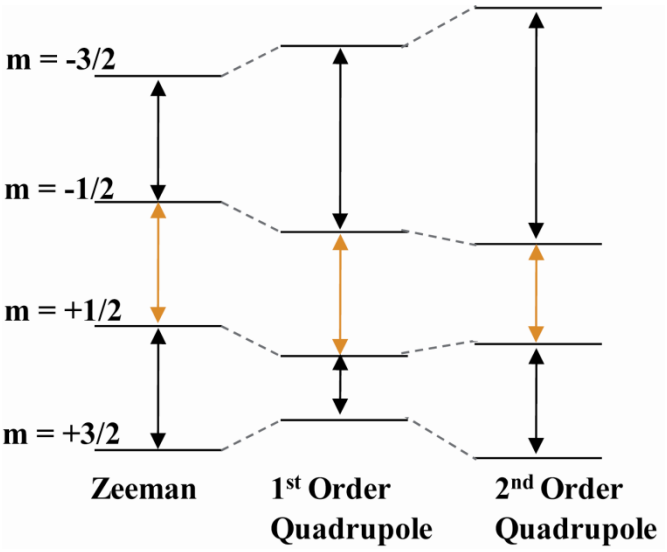

Figure 1.3. Energy level diagram for the transitions of an I= 3/2 nucleus, such as chlorine-35/37. The central transition is represented by the orange double-headed arrows while the black double-headed arrows represent the satellite transitions.

Figure 1.4 presents several simulations which demonstrate the typical second order quadrupolar CT lineshape under stationary and MAS conditions. These simulations are for an I = 3/2 nucleus and use a C_Q of 4.0 MHz, a δ_{iso} of 0 ppm, and no CSA. Changing the magnitude of C_Q would change only the breadth of the spectrum, not its shape.

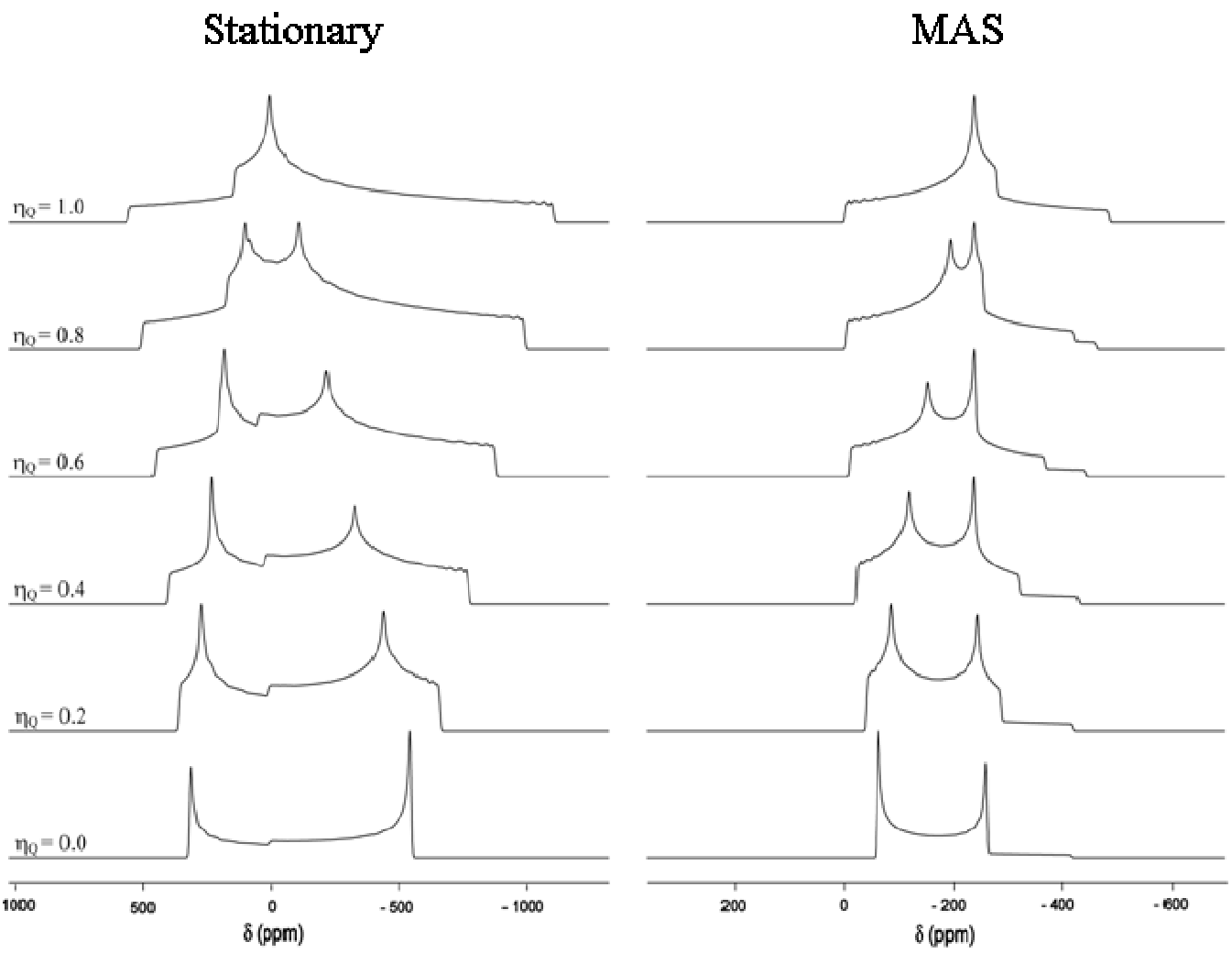

Figure 1.4. Second-order central transition lineshapes for different η_Q values under stationary and magic angle spinning conditions. All spectra are simulated using a C_Q of 4.0 MHz, a δ_{iso} of 0 ppm and no chemical shielding anisotropy. Note the different axes scales for the stationary and MAS spectra.

The breadth of the CT line shape ($\Delta\nu_{CT}$) of a stationary powdered sample depends on four parameters (C_Q, ν_0, I, and η_Q), as shown below:[35]

$$\Delta\nu_{CT} = \left[\frac{3C_Q}{2I(2I-1)}\right]^2 \frac{(\eta_Q{}^2 + 22\eta_Q + 25)(I(I+1) - 3/4)}{144\nu_0} \qquad [1.21]$$

where ν_0 is the Larmor frequency. The inverse proportionality between line width and the Larmor frequency demonstrates why higher magnetic fields are advantageous for the quadrupolar halogens: increasing B_0 increases ν_0, and therefore results in an overall decrease in the second-order quadrupolar broadening of the CT. It is also worth noting that the effects of CSA increase at higher fields, allowing for these effects to be more easily observed in cases where there is a significant QI. In addition, for a given EFG tensor, narrower CT powder patterns are obtained for higher half-integer spin nuclei (eq. 1.21), a further factor working against the chlorine nuclei, as they both are spin 3/2. With the increasing availability of high (and ultrahigh) magnetic fields (i.e. $\geq$ 11.7 T) in recent years, however, the difficulties associated with these nuclides have become surmountable and they are now quite accessible for SSNMR experiments.

For all of the results discussed in this thesis the high-field approximation is used. In this approximation the QI is modelled using only second order perturbation theory, and it is assumed that the Larmor frequency (ν_L, equation [1.2]) is much greater than the quadrupole frequency (ν_Q, equation [1.22]).

$$\nu_Q = \frac{3C_Q\sqrt{1+\frac{\eta_Q{}^2}{3}}}{2I(2I-1)} \qquad [1.22]$$

The validity of this approximation was recently tested through several simulations that highlighted the differences between the second-order and exact approaches.[34, 36] It was found

that the difference between the calculated exact and second-order CT resonance frequencies for a single crystal was negligible for practical purposes up until the point where ν_Q was $\nu_L/2$ for a spin-3/2 nucleus. The difference was even smaller in the case for the CT of a powdered sample. Thus, this approximation has been proven to be valid for all spectra presented in this document.

A chlorine solution-state NMR standard of 0.1 mol/dm^3 NaCl in D_2O has been recommended by IUPAC.[37] However, when using this standard the concentration must be carefully determined and noted as its CS varies with concentration.[26] The solvent (e.g., H_2O vs D_2O) is even more important, as significant isotope effects are known to exist.[38-40] The alternative reference of solid NaCl (-41.11 ppm w.r.t 0.1 mol/dm^3 NaCl in D_2O) has been suggested by Bryce *et al.* for $^{35/37}$Cl, as it produces a narrow line at relatively slow spinning speeds due to its cubic lattice structure. In addition, a solid state reference removes any ambiguity in terms of concentration or solvent.[40] Thus all spectra in this thesis are referenced to the solid reference at 0 ppm.

1.4 Chlorine-35/37 Experimental Data

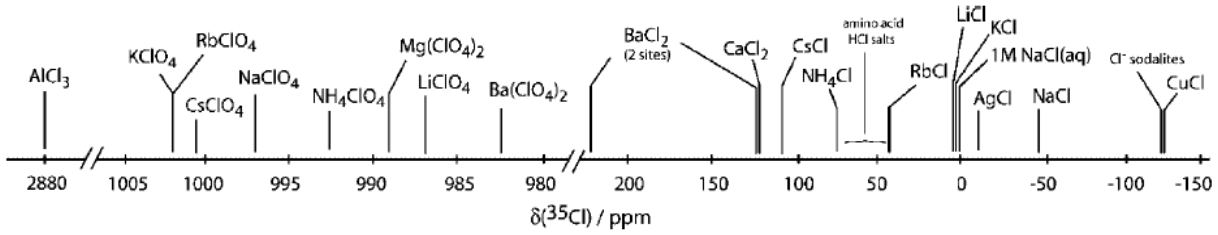

Figure 1.5. Representative solid-state chlorine isotropic chemical shifts with respect to 1 M NaCl(*aq*) published up until 2006. Reproduced from reference 41.

Presented in Figure 1.5 are the approximate solid-state CS ranges for all available $^{35/37}$Cl data prior to the beginning of this research. It is apparent that the majority of earlier studies have been performed on simple chlorides and perchlorates, due to the high symmetry about the

halogen nucleus in these compounds. There were also some limited cases where SSNMR had begun to be used to study selected organic systems, chlorine-containing glasses, and sodalite materials, in which non-zero EFGs lead to some quadrupolar broadening.[40] The chlorine CS range at this time was thought to span from -119.17 ppm for CuCl[41] to 2880 ppm for $AlCl_3$[42] (both w.r.t. 1M NaCl*(aq)*). Furthermore, there had only been a few studies in which chlorine CSA was extracted for selected organic chloride compounds.[40]

1.5 Objectives

Despite the difficulties associated with chlorine SSNMR, the potential wealth of information which can be extracted from spectra is significant. Unlike the case with solution state NMR, in which only the isotropic component of the CS tensor is measured, the full CS tensor can be determined using SSNMR. And while the quadrupolar nature of chlorine does make collection of spectra challenging, the presence of a significant QI provides *additional* information in the form of the EFG tensor parameters. Importantly, the mechanisms behind the EFG and CS tensors are different and thus both provide unique information about the electronic and chemical environment about chlorine. Thus the first goal of the work discussed in the following chapters was to demonstrate the utility of chlorine SSNMR for the study of a wide variety of organic and inorganic materials, and establish a large volume of benchmark chlorine EFG and CS tensor parameters. In addition, I hoped to test the *limits* of what types of materials can be successfully analyzed using chlorine SSNMR; for example determine if chlorine NMR could distinguish different, but similar, chlorine environments in cases where there is a very large QI and if chlorine NMR could distinguish polymorphism.

Quantum chemical calculations (which will be discussed in Chapter 2) can be combined with experiment to aid in the analysis of spectra *and* help find links between SSNMR parameters

and structure. The combination of experiment and theory also opens up many doors for structure refinement and the identification of unknown compounds. Thus, a further objective of this work was to use calculations for the above purposes in order to complement the experimental results. Part of this process would include the determination of the effectiveness of the Gauge-Including Projector Augmented Wave Density Functional Theory (GIPAW-DFT) method in calculating chlorine SSNMR parameters for both organic and inorganic systems.

1.6 References

1 C. E. Housecroft and A. G. Sharpe, *Inorganic Chemistry*, Prentice Hall, Harlow, England, 2008.

2 F. Cotton and G. Wilkinson, *Basic Inorganic Chemistry*, Wiley, New York, New York, 1976.

3 M. E. Loewen and G. W. Forsyth, *Physiol. Rev.,* **2005,** *85*, 1061.

4 R. Dutzler, E. B. Campbell, M. Cadene, B. T. Chait and R. MacKinnon, *Nature,* **2002,** *415*, 287.

5 R. Dutzler, E. B. Campbell and R. MacKinnon, *Science,* **2003,** *300*, 108.

6 F. M. Ashcroft, *Ion Channels and Disease*, Academic Press, San Diego, 2000.

7 P. Thibault and V. Elser, *Annu. Rev. Condens. Matter Phys.,* **2010,** *1*, 237.

8 M. C. Moron, *J. Mater. Chem.,* **2000,** *10*, 2617.

9 A. Guinier, *X-ray diffraction in crystals, imperfect crystals, and amorphous bodies*, Courier Dover Publications, New York, 1994.

10 H. M. Rietveld, *J. Appl. Crystallogr.,* **1969,** *2*, 65.

11 H. M. Rietveld, *Acta Cryst.,* **1967,** *22*, 151.

12 E. A. C. Lucken, *Nuclear Quadrupole Coupling Constants*, Academic Press, London, 1969.

13 a) I. I. Rabi, J. R. Zacharias, S. Millman and P. Kusch, *Phys. Rev.,* **1938,** *53*, 318. b) Y. Zavoisky, *J. Phys. USSR.,* **1945**, *9*, 221.

14 E. M. Purcell, H. C. Torrey and R. V. Pound, *Phys. Rev.,* **1946,** *69*, 37.

15 F. Bloch, *Phys. Rev.,* **1946,** *70*, 460.

16 Nobelprize.org, All Nobel Prizes in Physics, http://nobelprize.org/nobel_prizes/physics/laureates/, May 3, 2011.

17 Nobelprize.org, All Nobel Prizes in Chemistry, http://nobelprize.org/nobel_prizes/chemistry/laureates/, May 3, 2011.

18 Nobelprize.org, The Nobel Prize in Physiology or Medicine, http://nobelprize.org/nobel_prizes/medicine/laureates/, May 3, 2011.

19 M. H. Levitt, *Basics of Nuclear Magnetic Resonance*, Wiley, Chichester, 2001.

20 P.W. Atkins, *Physical Chemisty*, Oxford University Press, New York, 2006.

21 J. Mason, *Multinuclear NMR*, Plenum Press, New York, 1987.

22 P. M. Aguiar and S. Kroeker, *J. Non-Cryst. Solids,* **2007,** *353*, 1834.

23 M. J. Duer, *Solid-State NMR Spectroscopy*, Blackwell Publishing, Oxford, 2004.

24 H. Kampermann, A. D. Bain and R. S. Dumont, *J. Chem. Phys.,* **2002,** *116*, 2464.

25 C. Y. Lee and C. D. Cornwell, *Magnetic Resonance and Related Phenomena,* Groupement Ampere, Heidelberg, 1976.

26 W. Gauβ, S. Gunther, A. R. Haase, M. Kerber, D. Kessler, J. Kronenbitter, H. Kruger, O. Lutz, A. Nolle, P. Schrade, M. Schule and G. E. Siegloch, *Z.Naturforsch.A,* **1978,** *33*, 934.

27 M. Mehring, *Principals of High Resolution NMR in Solids*, Springer-Verlag, New York, 1983.

28 U. Haeberlen, *Advances in Magnetic Resonance, Supplement 1*, Academic Press, New York, 1976.

29 J. Mason, *Solid State Nucl. Magn. Reson.,* **1993,** *2*, 285.

30 H. W. Spiess and R. K. Sheline, **1971,** *54*, 1099.

31 J. Herzfeld and A. E. Berger, *J. Chem. Phys.,* **1980,** *73*, 6021.

32 G. B. Arfken, *Mathematical Methods for Physicists*, Academic Press, New York, 1985.

33 R. P. Chapman, C. M. Widdifield and D. L. Bryce, *Prog. Nucl. Magn. Reson. Spectrosc.,* **2009,** *55*, 215.

34 C. M. Widdifield, R. P. Chapman and D. L. Bryce, *Annu. Rep. Nucl. Magn. Reson. Spectrosc.,* **2009**, *66*, 195.

35 K. J. D. MacKenzie and M. E. Smith, *Multinuclear Solid-State NMR of Inorganic Materials*, Pergamon, Amsterdam, 2002.

36 A. D. Bain, *Mol. Phys.,* **2003,** *101*, 3163.

37 A. P. M. Kentgens and R. Verhagen, *Chem. Phys. Lett.,* **1999,** *300*, 435.

38 A. Loewnstein, M. Shporer, P. C. Lauterbur and J. E. Ramirez, *J. Chem. Soc., Chem. Commun.,* **1968,** 214.

39 J. Blaser, O. Lutz and W. Steinkilberg, *Phys. Lett. A,* **1970,** *32*, 403.

40 D. L. Bryce and G. D. Sward, *Magn. Reson. Chem.,* **2006,** *44*, 409.

41 S. Hayashi and K. Hayamizu, *J. Phys. Chem. Solids,* **1992,** *53*, 239.

42 M. Hattori, Y. Onoda, T. Erata, M. E. Smith, M. Hattori, H. Ohki and R. Ikeda, *Z. Naturforsch,* **1994,** *49a*, 291.

Chapter 2

Experimental and Computational Methods

2.1 Experimental NMR Methods for Powders

2.1.1 Tunable Parameters in NMR

The π/2 pulse (a.k.a. 90º pulse) is determined experimentally, and refers to the pulse length for which maximum signal can be achieved at a given power level, assuming a single scan and that the total available magnetization is initially directed along the applied field. Generally due to the low receptivity of chlorine, the π/2 pulse length is determined on a setup sample, often a cubic chloride such as NaCl or NH_4Cl, in which the chloride is purely ionic. When this is the case, the resulting value must be scaled by a factor equal to $I + ½$ to convert the "solution π/2" to the "solid π/2". In solutions, or solids in which the chlorine is in a cubic environment, the quadrupolar frequency is much smaller than the strength of the rf pulses and subsequently the pulses are non-selective. In cases where the quadrupolar frequency is non-zero, however, the pulses are selective to the central transition and these pulses are shorter than their non-selective counterparts (at the same power level). As both isotopes of chlorine are spin-3/2, the π/2 value determined on a cubic chloride must be scaled in half for use on a solid sample. The pulse length at a given power must be checked regularly as it will change with time.

A second parameter which is important in the collection of NMR spectra is the recycle delay. This delay allows the return of the magnetization to equilibrium after an rf pulse, is the cause of which is each nuclear spin interacting with the surrounding lattice. There are two main types of relaxation in NMR, spin-lattice and spin-spin, which are described by the time constants T_1 and T_2, respectively.[1,2] The T_1 time describes the longitudinal relaxation of magnetization,

and in solid samples it is always longer than T_2. It is T_1 which dictates the needed recycle delay. Unfortunately, T_1 values tend to be on the order of seconds for chlorine, which results in long experiment times. Differently, the T_2 time describes the transverse relaxation and, in theory, can be determined directly from the FID. In reality the effects of magnetic field inhomogeneity will increase the rate of spin-spin relaxation. Thus, the *observed* transverse relaxation is given another name, T_2*. As the Q of the two isotopes of chlorine generally result in relatively broad lineshapes, the T_2* values are generally very short, on the order of hundreds of microseconds. In most cases, the pulse delays chosen in this report were optimized on a single representative sample, and subsequently used for all experiments in a given chapter.

2.1.2 Magic-Angle Spinning

As mentioned, all of the SSNMR studies discussed in this document were performed on powdered samples. With powdered samples, MAS NMR experiments are a powerful method of study in cases when the broadening of the CT is small, allowing for the acquisition of a spectrum with resolution of spinning sidebands from the centreband. MAS removes the broadening associated with several anisotropic NMR interactions by exploiting their orientational dependence. Conveniently, the MS anisotropy, dipolar coupling and first order quadrupolar interactions are all proportional to $3\cos^2\theta-1$ (where θ is the angle of the rotor relative to the magnetic field). Therefore, spinning a sample at the root of the equation $3\cos^2\theta-1 = 0$ results in an averaging of the interactions to zero. This root, 54.74º, is the so-called 'magic angle'. The MAS rate (in Hz) must be greater (or equal) to the magnitude of the interactions if they are to be averaged to zero. If this is not the case, the spectrum will also contain a manifold of spinning sidebands separated from the isotropic signal by multiples of the MAS rate. The 2nd order quadrupolar interaction is not completely removed by spinning as it depends on second rank *and*

fourth rank rotation matrices; while the second rank terms are completely averaged by MAS, the fourth rank effects are only partially averaged. The resulting MAS spectrum allows for the extraction of C_Q, η_Q and δ_{iso}, as these are the only three parameters that dictate the line shape and position of the centreband. The effect of the QI is reduced under MAS, however, with the MAS spectrum generally having ~1/3 the breadth of the corresponding stationary spectrum.[3]

As the second-order broadening associated with the QI decreases with increasing magnetic field, the availability of high-field magnets has allowed for the acquisition of MAS spectra for materials with a greater range of C_Q magnitudes.[4-11] In addition, advancements in probe technology allowing for higher spinning rates open the door to the study of a variety of materials with larger quadrupolar–broadened NMR lineshapes. Currently, the highest magnetic field readily available and dedicated to SSNMR studies is 21.1 T, and a commercially available 1.0 mm rotor allows for the highest MAS spinning frequency of ~80 kHz. Limited by availability, however, the smallest rotor used in this research project was 3.2 mm (maximum MAS frequency ~ 20 kHz). A variety of two-dimensional MAS NMR experiments have been developed for solids, and some selected 2D experiments were attempted in the research discussed in this thesis. These will be introduced and discussed within the appropriate chapters.

2.1.3 Stationary Experiments

The simplest NMR pulse sequence consists of the application of a single rf pulse, followed by the collection of the resulting spectrum. Unfortunately, due to the non-ideal properties of chlorine and the resulting acoustic ringing (*vide infra*), this pulse sequence is often not effective for the collection of chlorine SSNMR spectra. Described below are the pulse sequences most commonly used for collection of the chlorine SSNMR spectra presented in this

thesis. Other pulse sequences that were used for only one project will be described in the appropriate chapter.

A common experimental technique used to improve the quality of the CT spectrum of quadrupolar nuclei is a simple solid echo (also known as the Solomon echo),[12-14] shown in Figure 2.1. Due to the large Q values of the nuclides of chlorine, the lines in the resulting spectra are often very broad and therefore have rapidly decaying free induction decays (FIDs). In the case of chlorine, this rapid FID is coupled with the presence of acoustic ringing in the coil, which can overpower the signal.

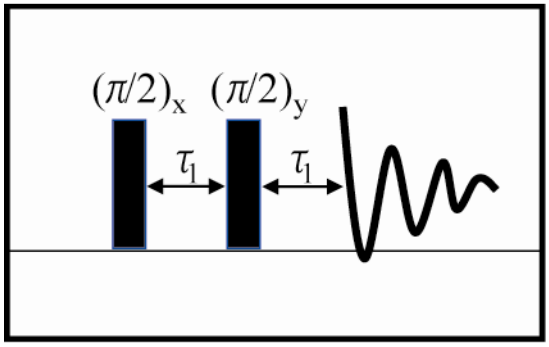

Figure 2.1. Schematic representation of the solid echo pulse sequence.

This problem is remedied by the use of a solid echo, which shifts the FID forward in the time domain. This pulse sequence consists of an initial π/2 pulse after which the spins are allowed to precess for a time, τ_1, before the second π/2 pulse. This differs from the Hahn-echo in which the second π/2 pulse sequence is replaced with a π pulse. The spectrum is then collected after a period of τ_1, which is enough time for the signal to refocus and for the ringing in the coil to dissipate. The solid echo can also be used to collect MAS NMR spectra provided the positions of the pulses are rotor synchronized with the spin frequency. Fourier-transformation of the FID at the top of the echo (i.e., after the signal is completely refocused) is necessary in order to obtain the proper NMR lineshape. This can be accomplished either during the acquisition, or later,

during the offline processing of the spectrum. During acquisition, the delay τ_1 can be tuned to ensure collection of the spectrum begins at the top of the echo (as shown in Figure 1.1); however, this can be time-consuming with a nucleus like chlorine where the signal-to-noise ratio is often low. Alternatively, shifting the FID to the top of the echo after acquisition can also be done by 'left-shifting' the FID prior to Fourier-transformation. This method eliminates all points in the FID which were collected before the top of the echo, essentially mimicking the spectrum which would be collected with a longer delay τ_1. Left-shifting was used when necessary for the studies described in this thesis.

The quadrupolar Carr-Purcell-Meiboom-Gill (QCPMG) pulse sequence, shown in Figure 2.2 is another pulse sequence used in this research to improve experimental sensitivity.[15] The QCPMG sequence consists of the collection of the FID after each pulse, using a train of refocusing π pulses after an initial $\pi/2$ pulse. Upon Fourier-transformation, the frequency-domain spectrum is a powder pattern split into "spikelets" which are separated by $1/\tau$, where τ is the delay separating the π pulses. The experiment can be carried out under stationary or MAS conditions and improves experimental sensitivity on two fronts: firstly, there are multiple signal acquisition periods per relaxation delay and secondly, the total signal intensity is concentrated into the spikelets. The improved sensitivity greatly reduces the acquisition time needed to collect a spectrum with an adequate signal-to–noise ratio, when compared to the Hahn/quadrupolar echo sequences. The disadvantage of the QCPMG sequence is that the resulting spectra tend to be more difficult to fit precisely and therefore using an echo is preferred, if possible.

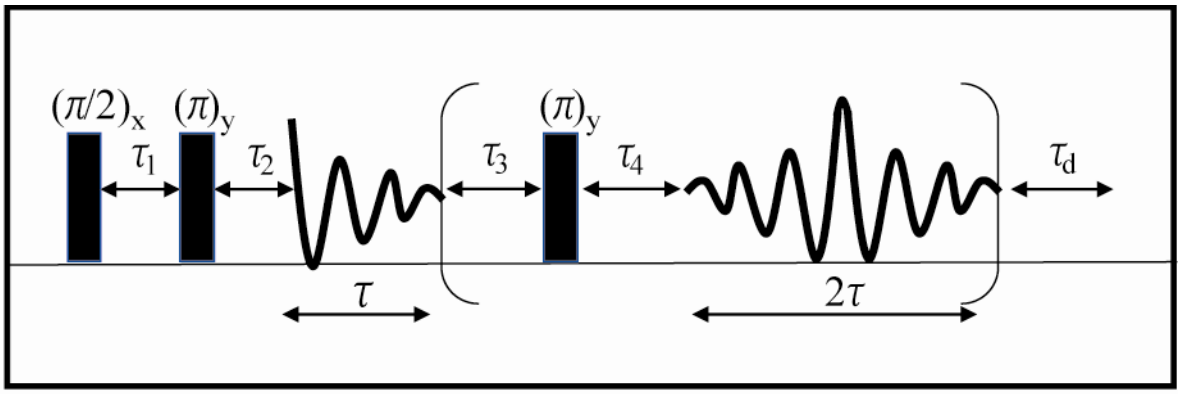

Figure 2.2. Schematic representation of the quadrupolar Carr-Purcell-Meiboom-Gill (QCPMG) pulse sequence.

In some instances, the broadening of the CT is so large that it is not possible to uniformly excite the entire CT. In these cases, the collection of a variable-offset cumulative spectrum (VOCS) is required to collect the full SSNMR lineshape.[16] The approach of these experiments is simple: the rf transmitter is systematically stepped across the entire breadth of the CT, with a 'subspectrum' being acquired at each transmitter settting. The series of subspectra are then overlapped (skyline processed) or summed (co-addition processed) to produce the entire CT spectrum. In cases where the QCPMG method is used, the rf frequency intervals must be chosen so that the spikelets from different experiments overlap constructively. Use of the QCPMG sequence is advantageous in order to achieve the needed signal-to-noise ratio for stepped frequency experiments involving chlorine, due to its low receptivity. An example is presented in Figure 2.3, where the QCPMG stepped-frequency approach has been applied to acquire the ^{35}Cl CT spectrum of indium trichloride tetrahydrate at 21.1 T. Each individual experiment is shown in a different colour and is described as a 'piece'; the importance of constructive overlap is shown in Figure 2.3 as each piece overlaps with several others. This method greatly expands the

range of chlorine containing compounds that can be studied with SSNMR, as it is a relatively 'simple' technique which allows for acquisition of spectra where the linewidths exceed the spectral window.

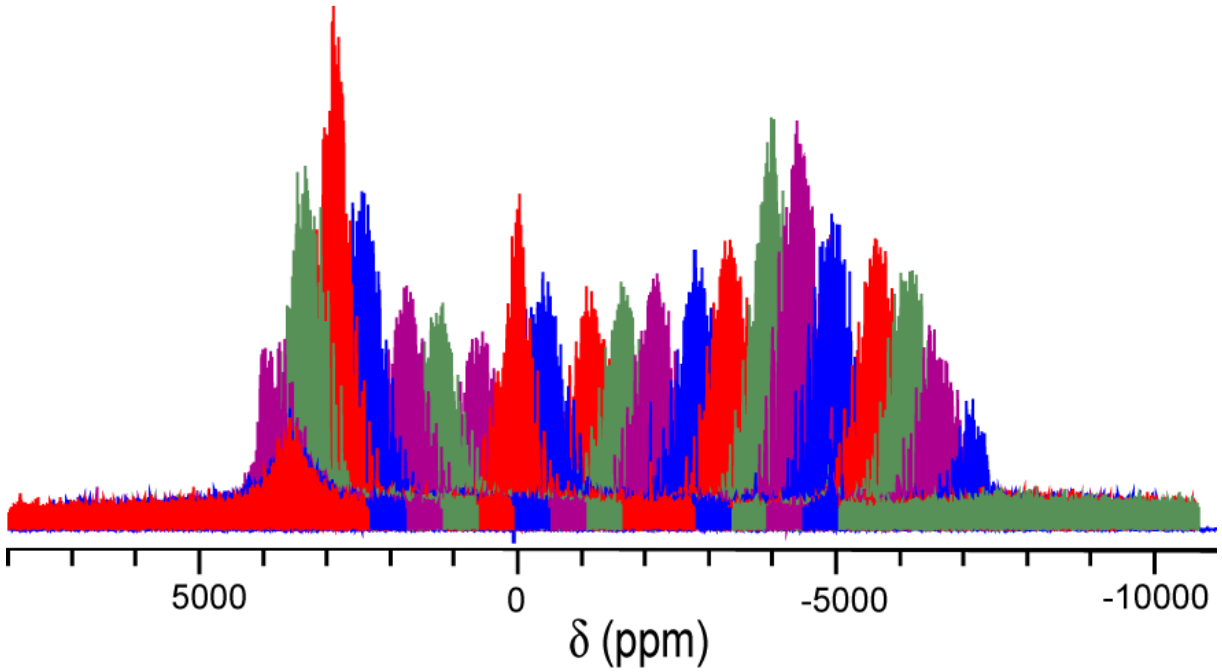

Figure 2.3. Variable-offset chlorine-35 CT NMR spectrum of $InCl_3 \cdot 4H_2O$. The 25 QCPMG subspectra have been overlaid to give the shape of the overall spectrum, which covers about 1 MHz at 21.1 T.

2.1.4 Extraction of SSNMR Parameters

As mentioned above, the centreband of the CT under fast MAS conditions depends only on δ_{iso}, C_Q, and η_Q. These parameters can typically be determined by line shape analysis (as implemented in the WSolids,[17, 18] SIMPSON[19] or DMFIT programs,[20] for example). In this work, the WSolids program was used exclusively to extract parameters from SSNMR spectra, although occasionally the SIMPSON program was used to confirm the determined values. Thus, where possible, the desired method to extract both the CS and QI parameters from a sample is to

first analyze the MAS spectrum to extract δ_{iso}, C_Q, and η_Q, and then perform a line shape analysis of a spectrum collected under stationary conditions to extract the remaining parameters: Ω, κ, α, β, γ. In cases where the QI is too great to obtain a MAS spectrum, the static spectrum must be fit with all 8 parameters as variables. In some cases, crystallographic site symmetry limits the value of certain parameters (η_Q, κ and the Euler angles), however there are no limitations when the site symmetry is C_1. As there is often more than one combination of the 8 parameters that can give the same spectrum, collection of the spectrum at multiple fields is preferred in order to confirm the accuracy of the determined parameters, as the same set of parameters must fit all the spectra acquired for a given material. Conveniently, in the case of chlorine there is a second "built-in" field, as there are two NMR-active isotopes with reasonable natural abundances. To a good approximation, the only parameter that changes when comparing the two isotopes of chlorine is the C_Q value, due to different Q values. In the case of chlorine, the chlorine-37 quadrupole coupling constant is 78.8% that of the chlorine-35 value.[21] In principle, one must be aware of possible isotope effects on the CS, but these are expected to be negligible,[22] particularly in the analysis of broad powder patterns.

2.1.5 Decoupling

As many chlorine-containing compounds have organic functional groups, chlorine-hydrogen interactions often leads to dipolar coupling between those two nuclei. Conveniently, heteronuclear dipolar coupling has the same orientational dependence as CSA and is thus removed by MAS at fast MAS spin frequencies. However, in cases where MAS is not possible or when the spin frequency is lower than the magnitude of the interaction, dipolar coupling will result in a reduction of signal and 'smoothing' out of the spectrum, making interpretation difficult. The effects of this coupling can be removed, however, through the use of hydrogen

decoupling, which implements a pulse, or pulses on the hydrogen channel during the acquisition of a chlorine experiment. The decoupling pulse(s) cause spin saturation and fast interconversion of the hydrogen spins; thus there are no long lived hydrogen spin states to couple with the chlorine nucleus being observed. While many different decoupling sequences are available, in the case of chlorine continuous wave (cw) decoupling is sufficient in most cases. The cw method consists of continuous radiation on the hydrogen channel between the X-channel pulse and acquisition.[23]

2.2 Computational Methods

Often, computational studies can serve as a useful complement to SSNMR experiments, providing additional information and aiding analysis.[24-28] In this thesis, quantum chemical calculations were used frequently in order to aid interpretation, gain additional information and help identify the compounds analyzed. As chlorine SSNMR is a relatively underexplored field, calculations were also carried out to test the accuracy of selected levels of theory for calculating chlorine SSNMR parameters in different types of systems. Two computational programs were used: the Gaussian03 software package[29] was used to carry out hybrid Becke, three-parameter, Lee-Yang-Parr (B3LYP) and Restricted Hartree Fock (RHF) calculations while the CASTEP[30, 31] program was used to carry out GIPAW-DFT calculations. The basic theory behind these calculation methods will be described below.

2.2.1 B3LYP/RHF

The Gaussian quantum chemical calculation software package was introduced by John Pople in 1970, and has since become ubiquitous in chemistry research. The Gaussian03 edition of the program[29] was used for all of the B3LYP/RHF calculations presented in this document. The program's name stems from the use of Gaussian basis sets for calculations, and is capable of

performing calculations using a wide variety of theories including molecular mechanics, semi-empirical, Hartree-Fock, DFT, and others. Gaussian basis sets are atom-based, and therefore no periodicity is included in the calculation (i.e., the calculation is done considering only the atoms explicitly listed in the input file). Thus, in the case of solids, a cluster model must be made for each calculation from the crystal structure of a given system. In this document, the model generally consisted of central chlorine and includes all moieties in a certain coordination sphere (~3 Å). The calculations are then carried out in the gas phase, with the cluster in isolation.

In 2006, two systematic studies of several amino acid hydrochlorides established an effective method for calculating chlorine SSNMR parameters using the Gaussian software package.[6,7] This method is shown in Table 2.1. In cases where a neutron structure was not available, it was found that hydrogen atom position optimization was essential to achieve good agreement with experimental values.[6] As the method described by Table 2.1 has been shown to be accurate for calculations of chlorine NMR tensor parameters, it was utilized for all cluster model calculations included in this thesis.

The *ab initio* RHF level of theory has been determined to be effective for EFG tensor parameters calculations, while the B3LYP DFT hybrid level of theory was found to be ideal for MS tensor parameter calculations.[32] In the RHF level of theory, an iterative cycle calculates the energy and Schrodinger equation of each electron individually, and then repeats the calculations using the improved orbitals determined for each electron.[32] The calculations continue until it is deemed "self-consistent" (i.e. a cycle does not change the energy of any orbitals beyond a user-specified level of tolerance). One of the main limitations of RHF is that it treats all of the electrons as averaged (i.e. not making any corrections for electron correlation). The "restricted" HF method is used in cases where all the electrons are paired (i.e. diamagnetic). Differently,

DFT methods calculate properties based on the electron density of the molecule and not the individual electron wavefunctions.[32] B3LYP is deemed a "hybrid' method as it combines both the HF and DFT approximations to calculate the exchange energy, along with a functional that includes electron correlation in an approximate way.[32] For the calculation of the parameters for both the EFG and MS tensors, correlation consistent basis sets are utilized. This family of basis sets was developed by Dunning and co-workers, and consists of shells of functions to a core HF atomic functional.[32] These basis sets follow a cc-pVXZ nomenclature, where cc stands for correlation consistent, p for polarization, V for valence, X for the number of shells into which the valence function is split while Z stands for zeta. The X factor can be increased to raise the level of the basis set.[32] In addition, diffuse and extra polarization functions can be added with the 'aug' term (eg. aug-cc-pVDZ), which can better model anions such as chloride.[32] In the method described in Table 2.1, the level of the basis set of chlorine is higher than those of the other atoms included in the calculations.

Table 2.1. Method used for calculating chlorine SSNMR parameters using the Gaussian03 software package

Tensor	Level of Theory	Basis Set on Chlorine Atoms	Basis Set on Other Atoms
Electric Field Gradient (EFG)	Restricted Hartree Fock (RHF)	cc-pVTZ	cc-pVDZ
Magnetic Shielding (MS)	Becke, three-parameter, Lee-Yang-Parr (B3LYP)	aug-cc-pVDZ	cc-pVDZ

2.2.2 GIPAW-DFT

As mentioned above, calculations carried out using Gaussian orbitals require the use of cluster models, which often do not accurately model the environment in solids. However, the GIPAW-DFT method, as implemented in the CASTEP program,[31,33,34] is ideal for solids as it utilizes planewaves and pseudopotentials. This allows for the description of the system as an infinite crystal lattice. Conveniently, using periodic boundary conditions allows for calculating on the assumption of an infinite lattice at the computational cost of simulating only the unit cell. While Projector Augmented Wave (PAW) methods have been available since the early nineties,[35] their application to the calculation of NMR parameters - through the GIPAW method - is more recent.[33] The method reintroduces the translational invariance into the PAW method as this is needed for NMR calculations as the NMR properties are independent of the gauge position. Although the technique is relatively new, in the past few years GIPAW-DFT calculations have been growing in popularity worldwide for the calculation of SSNMR parameters in a variety of solids.[35] At the commencement of this research, only two studies had examined the effectiveness of the GIPAW-DFT method for the calculation of chlorine NMR parameters, with only a few compounds studied, the majority of which were inorganic chlorides.[36,37] While GIPAW calculations are not limited to the DFT level of theory, in cases where periodic boundary conditions are employed DFT is used almost exclusively. This is because using other methods (for example, HF) require the evaluation of more demanding exchange integrals.

Unlike Gaussian basis sets, planewaves are not associated with an atomic centre as they are wave functions. In GIPAW-DFT calculations, planewaves are used in combination with pseudopotentials, with the planewaves modelling the valence electron density and the

pseudopotential modelling the density at the core.[33] This is shown visually in Figure 2.4. It is important to note that Figure 2.4 is only an illustration, and planewaves are in reality periodic in *three* dimensions. For a given calculation, a 'cut-off energy' and k-point grid are defined. Only planewaves with kinetic energies lower than the cut-off energy are used in the calculation, while the k-point grid describes the number of points sampled in the Brillouin zone, which is a primitive cell in reciprocal space.[33] The number of k-points needed for a calculation depends on the input crystal structure and varies greatly between compounds. Increasing the energy of the planewaves in GIPAW-DFT is analogous to increasing the level of the basis set in Gaussian, and a higher cut-off energy therefore results in a more accurate and computationally expensive calculation. To restate, the specific cut-off energy needed for an accurate calculation is dependent on the input crystal structure, and will be listed for each individual case in the appropriate chapters.

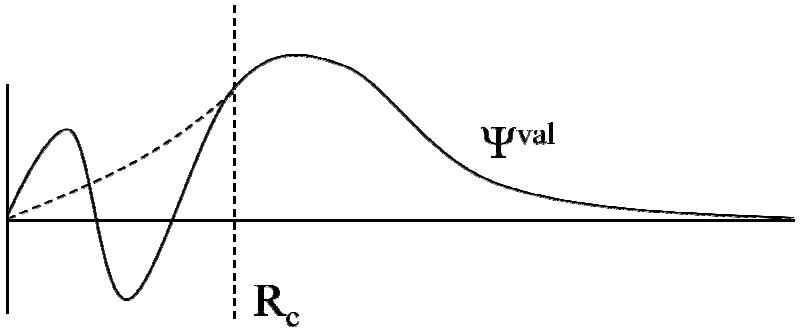

Figure 2.4. Schematic illustration of the pseudopotentials used in GIPAW-DFT method. R_c is the chosen core radius, above which planewaves are used to model the valence wavefunction (Ψ^{val}).

Input files for all of the GIPAW-DFT calculations discussed in this thesis were generated using Materials Studio 3.2 and were carried out using version 4.1 of CASTEP-NMR.[31, 33, 34] In order to calculate NMR parameters, on the fly generation (.otfg) pseudopotentials must be used. In the majority of cases, the necessary .otfg pseudopotentials were included in the Materials Studio 3.2 program although there were instances where the files were obtained directly from the maker of the program, Accelrys, as described in the appropriate chapter. Specific details on the chlorine .otf pseudopotential used for all calculations are included in Appendix 1.

2.3 References

1 M. J. Duer, *Solid-State NMR Spectroscopy*, Blackwell Publishing, Oxford, 2004.

2 M. H. Levitt, *Basics of Nuclear Magnetic Resonance*, Wiley, Chichester, 2001.

3 A. Samoson, E. Lippmaa and A. Pines, *Mol. Phys.,* **1988,** *65*, 1013.

4 K. J. Ooms, K. W. Feidel, V. V. Terskikh and R. E. Wasylishen, *Inorg. Chem.,* **2006,** , 8492.

5 D. L. Bryce, S. Adiga, E. K. Elliot and G. W. Gokel, *J. Phys. Chem. A,* **2006,** *110*, 13568.

6 D. L. Bryce and G. D. Sward, *J. Phys. Chem. B.,* **2006,** *110*, 26461.

7 D. L. Bryce, G. D. Sward and S. Adiga, *J. Am. Chem. Soc.,* **2006,** *128*, 2121.

8 I. L. Moudrakovski and J. A. Ripmeester, *J. Phys. Chem. B,* **2007,** *11*, 491.

9 I. C. M. Kwan, X. Mo and G. Wu, *J. Am. Chem. Soc.,* **2007,** , 2398.

10 P. M. Aguiar and S. Kroeker, *J. Non-Cryst. Solids,* **2007,** *353*, 1834.

11 A. Y. H. Lo, V. Sudarsan, S. Sivakumar, F. van Veggel and R. W. Schurko, *J. Am. Chem. Soc.,* **2007,** *129*, 4687.

12 I. Solomon, *Phys. Rev.,* **1958,** *110*, 61.

13 A. C. Kunwar, G. L. Turner and E. Oldfield, *J. Mag. Reson.,* **1986,** *69*, 124.

14 I. D. Weisman and L. H. Bennett, *Phys.Rev.,* **1969,** *181*, 1341.

15 F. H. Larsen, H. J. Jakobsen, P. D. Ellis and N. C. Nielsen, *J. Phys. Chem. A,* **1997,** *101*, 8597.

16 D. Massiot, I. Farnan, N. Gautier, D. Trumeau, A. Trokiner and J. P. Coutures, *Solid State Nucl. Magn. Reson.,* **1995,** *4*, 241.

17 K. Eichele and R. E. Wasylishen, WSolids Simulation Software, 2001, version 1.17.30.

18 D. W. Alderman, M. S. Solum and D. M. Grant, *J. Chem. Phys.,* **1986,** *84*, 3717.

19 M. Bak, J. T. Rasmussen and N. C. Nielsen, *J. Magn. Reson.,* **2000,** *147*, 296.

20 D. Massiot, F. Fayon, M. Capron, I. King, S. Le Calve, B. Alonso, J. -O. Durand, B. Bujoli, Z. Gan and G. Hoatson, *Magn. Reson. Chem.,* **2002,** *40*, 70.

21 P. Pyykkö, *Mol. Phys.,* **2008,** *106*, 1965.

22 P. E. Hansen, *Prog. Nucl. Magn. Reson. Spectrosc.,* **1988,** *20*, 207.

23 R. Freeman and E. Kupce, *NMR Biomed.,* **1997,** *10*, 372.

24 M. Kaupp, M. Bühl and V. G. Malkin, Eds., *Calculation of NMR and EPR Parameters.* Wiley-VCH, Weinheim, 2004.

25 C. M. Widdifield, R. P. Chapman and D. L. Bryce, *Annu. Rep. Nucl. Magn. Reson. Spectrosc.,* **2009**, *66*, 195.

26 R. P. Chapman, C. M. Widdifield and D. L. Bryce, *Prog. Nucl. Magn. Reson. Spectrosc.,* **2009,** *55*, 215.

27 D. L. Bryce and G. D. Sward, *Magn. Reson. Chem.,* **2006,** *44*, 409.

28 T. Charpentier, *Solid State Nucl. Magn. Reson.,* **2011,** *40*, 1.

29 M. J. Frisch, G. Trucks, H. B. Schlegel, G. E. Scuseria, M. A. Robb, J. R. Cheeseman, J. Montgomery J.A., T. Vreven, K. N. Kudin, J. C. Burant, J. M. Millam, S. S. Iyengar, J. Tomasi, V. Barone, B. Mennucci, M. Cossi, G. Scalmani, N. Rega, G. A. Petersson, H. Nakatsuji, M. Hada, M. Ehara, K. Toyota, R. Fukuda, J. Hasegawa, M. Ishida, T. Nakajima, Y. Honda, O. Kitao, H. Nakai, M. Klene, X. Li, J. E. Knox, H. P. Hratchian, J. B. Cross, V. Bakken, C. Adamno, J. Jaramillo, R. Gomperts, R. E. Stratmann, O. Yazyev, A. J. Austin, R. Cammi, C. Pomelli, J. W. Ochterski, P. Y. Ayala, K. Morokuma, G. A. Voth, P. Salvador, J. J. Dannenberg, V. G. Zakrzewski, S. Dapprich, A. D. Daniels, M. C. Strain, O. Farkas, D. K. Malick, A. D. Rabuck, K. Raghavachari, J. B. Foresman, J. V. Ortiz, Q. Cui, A. G. Baboul, S. Clifford, j. Cioslowski, B. B. Stefanov, G. Liu, A. Liashenko, P. Piskorz, I. Komaromi, R. L. Martin, D. J. Fox, T. Keith, M. A. Al-Laham, C. Y. Peng, A. Nanayakkara, M. Challacombe, P. M. W. Gill, B. Johnson, W. Chen, M. W. Wong, C. Gonzalez and J. A. Pople, *Revision C.02 Gaussian, Inc.*, Gaussian Inc.,Wallingford, CT, 2004.

30 M. D. Segall, P. J. D. Lindan, M. J. Probert, C. J. Pickard, P. J. Hasnip, S. J. Clark and M. C. Payne, *J. Phys. : Condens. Matter,* **2002,** *14*, 2717.

31 S. J. Clark, M. D. Segall, C. J. Pickard, P. J. Hasnip, M. I. J. Probert, K. Refson and M. C. Payne, *Z. Kristallogr.,* **2005,** *220*, 567.

32 E. G. Lewars, *Computational Chemistry: Introduction to the Theory and Applications of Molecular and Quantum Mechanics*, Springer, Dordrecht, NLD, 2011.

33 C. J. Pickard and F. Mauri, *Phys. Rev. B,* **2001,** *63*, 245101.

34 J. R. Yates, C. J. Pickard and F. Mauri, *Phys. Rev. B,* **2007,** *76*, 024401.

35 Accelrys, NMR CASTEP Scientific References, http://accelrys.com/products/materials-studio/publication-references/nmrcastep-references.html (accessed May 17, 2011).

36 D. L. Bryce and E. B. Bultz, *Chem. Eur. J.,* **2007,** *13*, 4786.

37 C. Gervais, R. Dupree, K. J. Pike, C. Bonhomme, M. Profeta, C. J. Pickard and F. Mauri, *J. Phys. Chem. A,* **2005,** *109*, 6960.

Chapter 3

Solid-State $^{35/37}$Cl NMR and Quantum Chemical Investigation of the Chlorine Quadrupolar and Chemical Shift Tensors in Amino Acid Hydrochlorides

3.1 Introduction and Objectives

3.1.1 Introduction

Inorganic elements play an important role in many essential biological processes.[1] As the study of the structural and binding environments of inorganic atoms within biochemical systems continues to progress, the need for improved models and methods of study grows. Chlorine is of significant biochemical relevance as chloride ion channels are carriers of electric current across cell membranes and are consequently essential for many biological processes.[2,3] Defects in, or absences of, these channels result in significant health problems, such as cystic fibrosis, Dent's disease, Bartter's syndrome, startle disease, and myotonia.[2] Study of the physiological function of chloride channel family continues to be a 'hot' topic for many researchers, as the exact nature of passive and active chlorine transport is still not fully understood.[4] Knowledge of the structure of these channels has increased in the last decade due in large part to the X-ray crystal structure, and subsequent studies, of the ClC ion channel.[5,6]

X-ray crystallography continues to provide much information on many biologically important systems, but this technique is limited to molecules for which high quality single crystals can be grown.[7] This is particularly limiting in the case of proteins, where crystallization is dependent on a wide variety of factors, many of which are beyond the control of researchers. These include the inherent dynamics, solubility, flexibility and possibility of post-translation modification belonging to a particular protein.[7] Even for the relatively small single-domain

prokaryotic proteins, it has been estimated that fewer than 25% will produce single crystals of high enough quality for X-ray analysis, using routine screening processes.[8,9] In addition, X-ray crystallography is also unable to probe the exact nature of the interactions between proteins and other biological molecules.[10,11] The application of NMR spectroscopy to the study of biological molecules such as proteins has proven fruitful in the determination of structure and dynamics in both the solution and solid states.[12-20] Most often, the technique is used to determine the structure of protein or nucleic acid backbones, but both solution NMR and SSNMR have also been used to directly probe the environment of inorganic metal cations in biologically relevant systems.[21-32] For example, ^{113}Cd SSNMR has been used by Ramamoorthy and co-workers to elucidate the metal cation binding environments of compounds which model metalloproteins,[32] and Lipton *et al.* have used ^{67}Zn SSNMR to characterize the zinc binding environment in zinc anhydrase.[22,23] The Bryce group has applied ^{23}Na and ^{39}K SSNMR to examine the nature of noncovalent cation-π interactions in complexes which model biologically relevant systems.[29,30] In many of these studies, quantum chemical calculations serve as an important complement to the experimental NMR results, providing additional information to aid in the interpretation of NMR data.[22,24,26-30,32,33] Provided that signal-to-noise issues can be overcome, chlorine SSNMR may be an ideal complement to X-ray diffraction in the study of small chloride ion channels, as NMR examines the local structural and electronic environment around the chloride within the channel. Chlorine SSNMR studies have previously been reported for several of organic hydrochloride salts, including earlier work from the Bryce group on a series of amino acid hydrochloride salts.[34-40] These studies demonstrated the utility of chlorine NMR in the characterization of chloride ion binding sites; however, study of additional model systems is still necessary in order to establish the benchmarks which will be necessary for the study of larger

systems or systems of unknown structure. We are furthermore generally interested in better understanding the fundamental relationships between the $^{35/37}$Cl EFG and CS tensors and the chloride hydrogen bonding environment in organic hydrochlorides. Variable temperature (VT) MAS experiments can provide additional information about the possibility for motion within a solid. In cases where there are dynamics within a lattice, for example rotations or exchange, there is often a temperature dependence to the NMR parameters, as an increase in temperature will increase this motion and therefore will modify the average electronic environment about a nucleus.

As mentioned above, and in chapter 1 and 2, quantum chemical calculations often serve as an important complementary technique to SSNMR and were used as such in this study. In earlier studies of similar systems, the optimal method for determination of chlorine NMR parameters was determined: B3LYP for structural optimization and calculation of the CS tensor and RHF for calculation of the EFG tensor.[37,38] As such, these methods were chosen for this study, to complement the experimental data and illustrate the sensitivity of the calculated parameters to the accuracy of the structures available. The self-consistent charge field perturbation (SC-CFP) model was also utilized to demonstrate the impact of surrounding ions in the crystal lattice on the chlorine SSNMR parameters.[41]

In addition, GIPAW-DFT calculations were done in order to test the robustness of the technique for calculating chlorine NMR parameters in small organic systems. While the method has been shown to be effective in a few cases for calculation of chlorine NMR parameters,[40,42] a systematic study involving a large data series is required to confirm the validity of the method in calculating chlorine NMR tensor parameters. With the completion of this study, there are

experimental data and X-ray (or neutron) structures available for fifteen amino acid hydrochlorides, making the series ideal for this endeavour.

3.1.2 Objectives

A chlorine SSNMR NMR study of several amino acid hydrochlorides was undertaken in order to further establish benchmark EFG and CS tensor data for organic hydrochlorides and correlate changes in NMR parameters to changes in the chlorine chemical environment. These data were also used, in combination with those from earlier amino acid hydrochloride NMR studies, to determine the effectiveness of GIPAW-DFT in calculating the chlorine SSNMR tensor parameters of organic hydrochlorides and compare the results to those of RHF/B3LYP methods.

3.2 Experimental

3.2.1 Sample Preparation

The six amino acids included in this study which have not previously characterized are pictured in Chart 3.1. L-Cysteine hydrochloride monohydrate (**1**) and arginine hydrochloride monohydrate (used in VT experiments) were purchased from Aldrich and used as received. L-Alanine hydrochloride (**2**), L-aspartic acid hydrochloride (**3**), L-histidine hydrochloride monohydrate (**4**), L-methionine hydrochloride (**5**) and L-threonine hydrochloride (**6**) were prepared by dissolving the appropriate amino acid (from Aldrich) in hot, dilute hydrochloric acid and filtering the resulting salt. Phase purity of the samples was confirmed by ^{13}C CP/MAS NMR spectra collected with a spinning rate of 4 kHz at 4.7 T. The pulse lengths used were typically 4μs with a contact time of 10 ms and a recycle delay of 1 s. Phase purity was further confirmed by powder X-ray diffraction (*vide infra*).

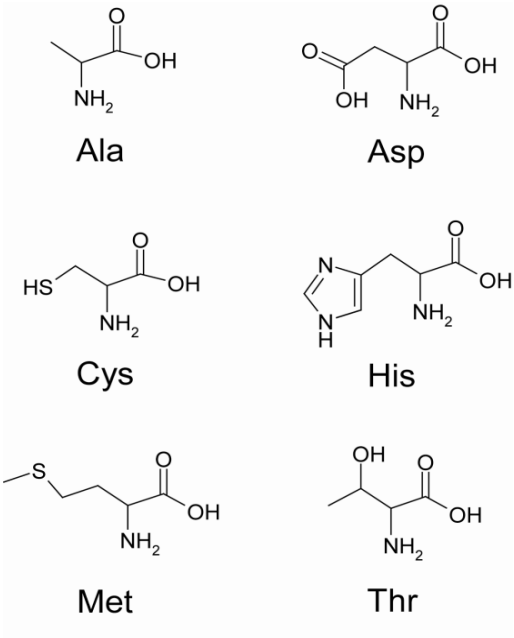

Chart 3.1. Structures of the primary amino acids whose hydrochloride salts were examined in this study.

Melting points were determined for all samples using a Barnstead/Electrothermal Mel-Temp melting point apparatus: 196-199˚C (L-alanine hydrochloride), 178-182˚C (L-aspartic acid hydrochloride), 90-93˚C (L-cysteine hydrochloride monohydrate), 237-241˚C (L-histidine hydrochloride monohydrate), 177-179˚C (L-methionine hydrochloride), 147-150˚C (L-threonine hydrochloride). The melting point for arginine hydrochloride monohydrate was previously found to be 128-130˚C.[38] All values are consistent with those reported for other amino acid hydrochlorides in previous studies in the Bryce research group.[38]

3.2.2 X-ray Diffraction

All six samples were analyzed by powder X-ray diffractometry to confirm their identities. Powder X-ray diffraction data were collected using a Philips PW3719 diffractometer and $Cu_{K\alpha 1}$ radiation (λ=1.54056 Å); operating conditions were 45 kV and 40 mA. A 10 mm slit was used at the X-ray source; the scattering slit had a fixed width of 0.2 mm, and a 1° receiving slit was

used. Data were collected in continuous mode over the range $2\theta = 5$ to 80° in steps of 0.02° at a rate of 1.2° per minute. In cases where a previously published X-ray structure was available, a theoretical X-ray powder diffraction pattern was produced using the Diamond 3.0 program.[43] In all cases, the predicted pattern and the experimental pattern were in agreement.

Single crystal samples of **1**, **3**, and **6** were grown by dissolving the appropriate salt in excess dilute hydrochloric acid and allowing for slow crystallization. Suitable crystals were selected and taken to the Single Crystal X-ray Diffraction Facility at the University of Ottawa where they were analyzed by Dr. Ilia Korobkov using the following procedure. The crystals were mounted on a thin glass fibre using paraffin oil, and cooled to the data collection temperature of 203 ºC for **1**, 200 ºC for **3** and 217 ºC for **6**. Data were collected on a Bruker AXS SMART 1K CCD diffractometer. For **1** and **6** data collection was performed with three batch runs at Φ= 0.00º (650 frames), at Φ = 120.00º (650 frames), and at Φ = 240.00º (650 frames). For **3,** data collection was performed with four batch runs at Φ = 0.00º (650 frames), at Φ = 90.00º (650 frames), at Φ = 180.00º (650 frames), and at Φ = 270.00º (650 frames). Initial unit cell parameters were determined from 60 data frames collected at different sections of the Ewald sphere. Semi-empirical absorption corrections based on equivalent reflections were applied.[44] The systematic absences and unit cell parameters were consistent with $P1$ for **3**, $P2_1$ for **6** and $P2_12_12_1$ for **1.** The structures were solved by direct methods, completed with difference Fourier syntheses, and refined with full-matrix least-squares procedures based on $F2$. All non-hydrogen atoms were refined with anisotropic displacement parameters. All hydrogen atoms were treated as idealized contributions. All scattering factors and anomalous dispersion factors are contained in the SHELXTL 6.12 program library.[45]

3.2.3 NMR Spectroscopy

3.2.3.1 Experiments Carried out at 11.7 T

Chlorine-35/37 SSNMR experiments were carried out on a 500 MHz (B_0 = 11.75 T) Bruker Avance spectrometer at the University of Ottawa. Two probes were used: a 4 mm Bruker HX probe, tuned to 49.00 MHz (^{35}Cl) or 40.79 MHz (^{37}Cl). Samples were ground into fine powders and packed into either 4 mm o.d. zirconia rotors or 10 mm glass tubes cut to appropriate length. Experimental setup and pulse calibrations were performed using solid NaCl or NH_4Cl. All $^{35/37}$Cl NMR spectra were referenced to the $^{35/37}$Cl centreband of solid NaCl at 0 ppm (NH_4Cl at 121.1 ppm) and collected at room temperature. The 'solid' $\pi/2$ chlorine-35 pulse was found by halving the non-selective $\pi/2$ pulse measured on solid NaCl or NH_4Cl, and was typically 2.3 μs for the 4 mm. Typical pulse lengths for ^{37}Cl were 2.4 μs for the 4 mm. Recycle delays used were 2 to 5 seconds and signals were averaged over a period of 8-20 hours. All spectra were collected under stationary conditions using the $\pi/2 - \tau - \pi/2 - \tau$ - ACQ quadrupolar echo sequence. Proton decoupling was applied during acquisition on the 4 mm probe only.

The VT MAS experiments on arginine hydrochloride monohydrate were performed at 11.7 T at 14 kHz using a 4 mm HX probe. Proton decoupling applied using the cw method. The temperature was varied in increments of 10 K between 278 and 338 K. In each case, pulse lengths of 1.7 μs and a delay of 4 seconds were used, with 512 transients being collected and averaged for each experiment. The temperature reported refers to the temperature of the air outside the rotor; no corrections are added for sample heating due to MAS.

3.2.3.2 Experiments Carried out at 21.1 T

Chlorine-35 NMR experiments were also performed on a 900 MHz (B_0 = 21.14 T) Bruker Avance II spectrometer at the National Ultrahigh-Field NMR Facility for Solids in Ottawa. A 3.2 mm Bruker DVT MAS HX probe (serial number 0001), tuned to 88.2 MHz (^{35}Cl) was used for all experiments. Experimental setup, pulse calibration and referencing were done using solid NaCl, the ^{35}Cl central-transition centreband of which was set to 0 ppm. Spectra of stationary samples were collected using the quadrupolar echo or QCPMG sequence.[46-49] The QCPMG experiment typically used a train of π pulses with a spacing of 200 μs following the initial $\pi/2$ pulse; this experiment was useful to rapidly assess the shape and breadth of the powder patterns. A single pulse was used for all MAS experiments. The 'solid' $\pi/2$ chlorine-35 pulse was found to be 2.0 μs and a recycle delay of two seconds was used for all acquisitions. All experiments were done at room temperature with proton decoupling and no corrections were made for sample heating under MAS.

3.2.4 Data Processing and Simulations

All NMR spectra were processed using TopSpin 1.3. The FIDs of those experiments acquired using the quadrupole-echo pulse sequences were left-shifted as necessary. NMR spectra were simulated using the WSolids software package,[50] which incorporates the space-tiling algorithm of Alderman *et al.*[51] MAS NMR spectra were also simulated with SIMPSON,[52] using the large zcw317810 crystallite file for powder averaging in the final presented simulations.[53] Interpretations of the spectra were done within the high-field approximation and all spectra were simulated assuming a single magnetically unique site, consistent with the diffraction-based structures. All stack plots presented were created using DMFit.[54]

3.2.5 Quantum Chemical Calculations

3.2.5.1 Calculations using the B3LYP/RHF Levels of Theory

All B3LYP and RHF quantum chemical calculations were carried out using the Gaussian 03 software package.[55] Calculations of the chlorine nuclear MS and EFG tensors were done based on models generated using atomic coordinates from the X-ray structures of Di Blasio *et al.* for L-alanine hydrochloride and L-methionine hydrochloride;[56,57] the atomic coordinates used for L-cysteine hydrochloride, L-aspartic acid hydrochloride and L-threonine hydrochloride were obtained from the X-ray structures collected in the present study. The atomic coordinates of the neutron diffraction structure by Fuess *et al.* were used for L-histidine hydrochloride monohydrate;[58] however, due to a typographical error in two of the coordinates, the z-coordinate for carbon 5 and the estimated position for hydrogen 9 were taken from the X-ray structure of Donohue and Caron.[59] Using the atomic coordinates, cell parameters and space group of the amino acid hydrochloride salts, a lattice extending several unit cells in each direction was created using the Diamond program.[43] From this lattice, a chloride ion and all moieties to which it was hydrogen bonded (i.e., amino acids and/or water) were selected and used as models for calculations. Prior to NMR tensor calculations, proton positions were optimized when needed using the B3LYP method and the 3-21G* basis set.

As described in the introduction, the optimal method for determining chlorine shielding and EFG tensors have been determined in earlier studies from the Bryce group.[37] These methods, RHF level of theory with the Dunning type cc-pVTZ basis set for the central chloride ion and the cc-pVDZ basis set for all other atoms for the EFG tensor and the hybrid B3LYP DFT method using a basis set of aug-cc-pVDZ for chlorine and cc-pVDZ for all other atoms for the MS tensor, were employed for the calculation of these materials. The chlorine EFG and

shielding tensors contained in the Gaussian output files were then analyzed using the EFGShield program (version 2.2).[60]

In addition, the SC-CFP model was employed for selected amino acid hydrochlorides. In these calculations, all chloride ions within 10.5 Å of the central chlorine were included as point charges, as described by Zhang and co-workers.[41] The magnitude of the point charges was determined by matching the charge on the central chlorine to the point charges through iterative single point energy calculations. The level of theory used for the determination of the magnitude of the point charges was B3LYP/cc-pVDZ and two to five cycles were needed. For initial optimization of proton positions, all chlorine ions were included as real ions (rather than point charges). The level of theory and basis sets used for the NMR tensor calculations using the SC-CFP model were the same as described above.

3.2.5.2 Calculations using the GIPAW-DFT Level of Theory

In addition to the amino acids examined experimentally in this study, in order to test the robustness of GIPAW-DFT level of theory for the calculation of chlorine NMR parameters, extensive calculations were also carried out on all the amino acid hydrochlorides which have been analyzed using SSNMR. All GIPAW-DFT quantum chemical calculations were carried out using the CASTEP program in the Accelyrs software package. The setup files were produced using Material Data Studio version 3.2.[61,62] The atomic coordinates, cell parameters and space group of the amino acid hydrochlorides were used as the input file. The cutoff energies and k-points used for each amino acid are listed in Appendix 2. In all cases, the number of k-points was determined by using the "ultra-fine" or "fine" setting on Material Data Studio, with the exception of arginine hydrochloride monohydrate (lower setting used due to convergence issues). The cutoff energy was 610 eV for all those amino acid hydrochlorides for which there was a

neutron structure and 450 eV for those that required proton optimization (those with X-ray diffraction structures). For those amino acid hydrochlorides mentioned above, the crystal structures used are those listed in the previous section. In the other cases, the input file was taken from the neutron diffraction study of Al-Karaghouli and Koetzle for L-phenylalanine hydrochloride,[63] Koetzle *et al.* for L-valine hydrochloride,[64] Frey *et al.* for L-tyrosine hydrochloride,[65] Sequeira *et al.* for L-glutamic acid,[66] Bugayong *et al.* for L-lysine hydrochloride dehydrate,[67] and Al-Karaghouli for glycine hydrochloride.[68] The X-ray diffraction study of Dow *et al.* was used arginine hydrochloride monohydrate,[69] Mitsui *et al.* for DL-proline hydrochloride,[70] and Takigawa *et al.* for L-tryptophan hydrochloride.[71] A computer program provided by Dr. John Griffin was used to fix all non-hydrogen atoms prior to optimization.[72]

The EFG and shielding tensors contained in the CASTEP output files were first analyzed using a modified version of the EFGShield program (version 2.2)[60] called EFGCastep, which gives a readout of 'dummy' Gaussian file which can then be analyzed with the EFGShield program.

3.3 Results and Discussion

3.3.1 X-ray Diffractometry

In order to analyze the relationship between the local environment of the chloride ion and the chlorine NMR spectra, and to complete a full quantum chemical study of all six amino acid hydrochloride salts, atomic coordinates and unit cell parameters from X-ray or neutron diffraction studies were required. Despite thorough literary searches, no structures have been found for aspartic acid hydrochloride or threonine hydrochloride. Therefore, single crystal X-ray analyses of these materials were completed. The cell parameters obtained for both salts are reported in Table 3.1. Threonine hydrochloride was found to crystallize in the monoclinic $P2_1$ space group while aspartic acid hydrochloride displayed triclinic $P1$ symmetry. Interestingly,

these particular salts crystallize in low-symmetry space groups when compared to the structures of the salts of other L-amino acids. The triclinic structure, indicating no symmetry, is confined to only aspartic acid hydrochloride while only four others in addition to threonine hydrochloride crystallize in the low symmetry $P2_1$ monoclinic group. The majority of the amino acid salts crystallize in the higher symmetry orthorhombic space group.

Table 3.1. Crystal cell parameters determined in this study for aspartic acid hydrochloride, cysteine hydrochloride monohydrate and threonine hydrochloride

Aspartic Acid Hydrochloride	Cysteine Hydrochloride Monohydrate[a]	Threonine Hydrochloride
P1 - Triclinic	$P2_12_12_1$ - Orthorhombic	$P2_1$ – Monoclinic
a = 5.612(2) Å α = 114.218(3)°	a = 5.4588(9) Å	a = 7.275(4) Å
b = 5.647(2) Å β = 97.874(4)°	b = 7.1570(11) Å	b = 5.263(3) Å β = 92.545(5)°
c = 6.169(2) Å γ = 95.710(4)°	c = 19.389(3) Å	c = 9.556(5) Å

[a]The cell parameters previously determined for cysteine hydrochloride monohydrate were 5.52 Å, 7.12 Å , and 19.41 Å, respectively.[73]

In addition to the two new crystal structures, an improved crystal structure for cysteine hydrochloride monohydrate was also obtained. The cell parameters are listed in Table 3.1. The motivation behind obtaining the improved structure was the large deviation between theoretical NMR results calculated using the published X-ray coordinates of Ayyar and those determined experimentally (*vide infra*). The improved precision of the X-ray structure presented here is demonstrated by the improved *R* value of 5.2 %, compared to 12.4 % for the 1968 structure.[73] Although the two structures are quite similar, having essentially identical cell parameters, the slight improvements in atomic coordinates have a significant impact on bond distances and subsequently on the accuracy of the calculated NMR parameters (*vide infra*). The cif files for all three hydrochloride salts are included in Appendix 2.

3.3.2 NMR Spectroscopy

3.3.2.1 NMR Parameters

The experimentally determined EFG and CS tensor data, obtained by spectral simulation of ^{35}Cl and ^{37}Cl NMR spectra of the amino acid hydrochloride salts, are listed in Table 3.2. When possible, a ^{35}Cl NMR spectrum of a MAS sample was initially acquired at 21.1 T and fitted to give $C_{Q,}$ η_Q, and δ_{iso}.

Table 3.2. Chlorine-35/37 EFG and CS tensor data for amino acid hydrochloride salts studied in the present work

Hydrochloride Salt[a]	$C_Q(^{35}Cl)$ / MHz[b]	η_Q	δ_{iso} / ppm[c]	Ω / ppm	κ	α, β, γ/°
Alanine	(-) 6.4(1)	0.75(6)	106(5)	60(30)	-0.3(5)	90(15), 0(15), 0(15)
Aspartic Acid	(-) 7.1(1)	0.42(5)	102(5)	75(30)	-0.9(1)	0(20), 30(20), 93(20)
Cysteine	(-) 3.92(1)	0.47(2)	104.2(5)	66(10)	0.12(12)	155(20), 0(10), 0(20)
Histidine	(-) 4.59(3)	0.46(2)	93(1)	< 150	[d]	[d]
Methionine	(+) 4.41(2)	0.35(3)	99(1)	100(20)	0.3(3)	93(20), 163(15), 7(20)
Threonine	(-) 5.4(1)	0.94(2)	99(10)	95(40)	-0.2(5)	95(15), 0(10), 0(15)

[a]Cysteine and histidine salts are monohydrates. [b]Chlorine-37 quadrupolar coupling constants were identical to $C_Q(^{35}Cl)$ x $Q(^{37}Cl)/Q(^{35}Cl) = C_Q(^{35}Cl)$ x 0.788. Negative or positive signs given in brackets are assigned based on quantum chemical calculations. [c]Isotropic chemical shifts are reported relative to solid NaCl at 0 ppm. [d]Not determined.

For each of the salts, simulations were performed simultaneously on a minimum of three spectra acquired under stationary conditions: ^{35}Cl NMR spectra at both 11.75 and 21.1 T, and a ^{37}Cl NMR spectrum at 11.75 T. Fitting multiple spectra with the same parameters is crucial to ensure the accuracy and precision of the resulting NMR tensor parameters. Chlorine-35 QCPMG NMR spectra acquired under static conditions at 21.1 T were also collected for each salt and are consistent with the corresponding powder pattern.

Examination of the data reveals the sensitivity of the EFG tensor to the local chloride ion environment, with values of $|C_Q(^{35}Cl)|$ ranging from 3.92 to 7.1 MHz and η_Q ranging from 0.35

to 0.94. As mentioned, the magnitude of C_Q is dependent on the largest component of the EFG tensor while η_Q is a measure of deviation of the tensor from axial symmetry. For all of the salts in this study, the magnitude of the ^{37}Cl quadrupolar coupling constant was, within experimental error, found to be equal to 78.8 % of the ^{35}Cl value, consistent with the ratio of the quadrupole moments, further confirming the accuracy and precision of the fits. Typically the magnitude of the chlorine-35 quadrupolar coupling constants measured from NMR spectra of chloride ions in organic and inorganic salts range from essentially zero to greater than 9.0 MHz, and the values observed in this study cover a substantial fraction of this total range. One of the salts in the current study, aspartic acid hydrochloride, exhibited a value for C_Q larger than has been previously observed for an organic hydrochloride salt.

The chlorine CS tensor also demonstrates sensitivity to the local chloride environment, with spans ranging from 60 to 100 ppm and skews ranging from -0.9 to 0.3 for the salts studied presently. These values are consistent with the range observed in previous studies of organic hydrochloride salts.[37-39]

For all six samples, the anisotropic broadening of the central transition in the ^{35}Cl NMR spectrum, resulting from the second-order quadrupolar interaction and CSA, was too large for the resolution of spinning sidebands from the centreband with MAS at 11.75 T, as the fastest spinning speed available was 15 kHz and the smallest spectral breadth was almost 60 kHz, for cysteine hydrochloride monohydrate. Even at the higher field of 21.1 T, the maximum spinning rate used, 22 kHz, was only sufficiently rapid for three of the salts studied: cysteine hydrochloride monohydrate, histidine hydrochloride monohydrate and methionine hydrochloride. The ^{35}Cl MAS NMR spectrum of cysteine hydrochloride monohydrate is shown in Figure 3.1 along with spectral simulations performed using WSolids and Simpson.

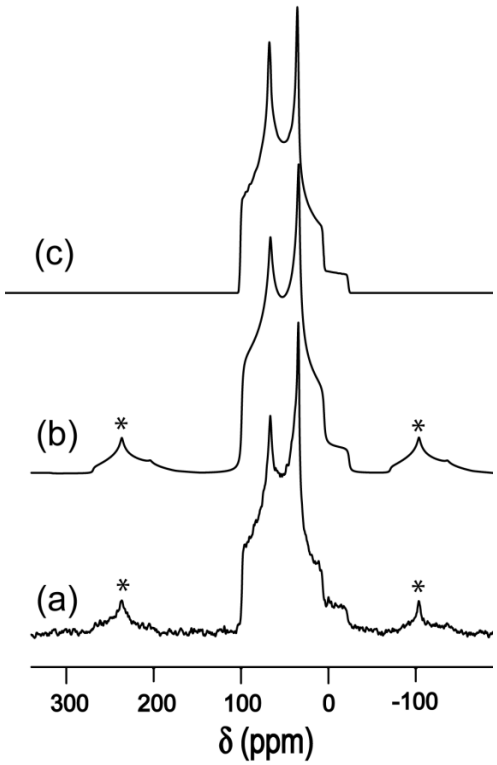

Figure 3.1. Solid-state chlorine-35 MAS NMR spectroscopy of cysteine hydrochloride monohydrate at 21.1 T with ν_{rot} = 15 kHz (a) Experimental. (b) Best fit simulation using Simpson. (c) Best-fit simulation using WSolids under the assumption of an infinite MAS rate. Spinning sidebands are indicated by asterisks.

As described, the spectrum of the cysteine salt had the smallest spectral breadth observed in this study and had the quadrupolar coupling constant of smallest magnitude, 3.92 ± 0.01 MHz. The accuracy of the determined NMR parameters presented in Table 3.2 is clearly shown by the good agreement between the simulated and experimental spectra, with the Simpson simulation providing additional confidence in the accuracy of the determined parameters by demonstrating agreement between experimental and simulated spinning sidebands in addition to the centreband.

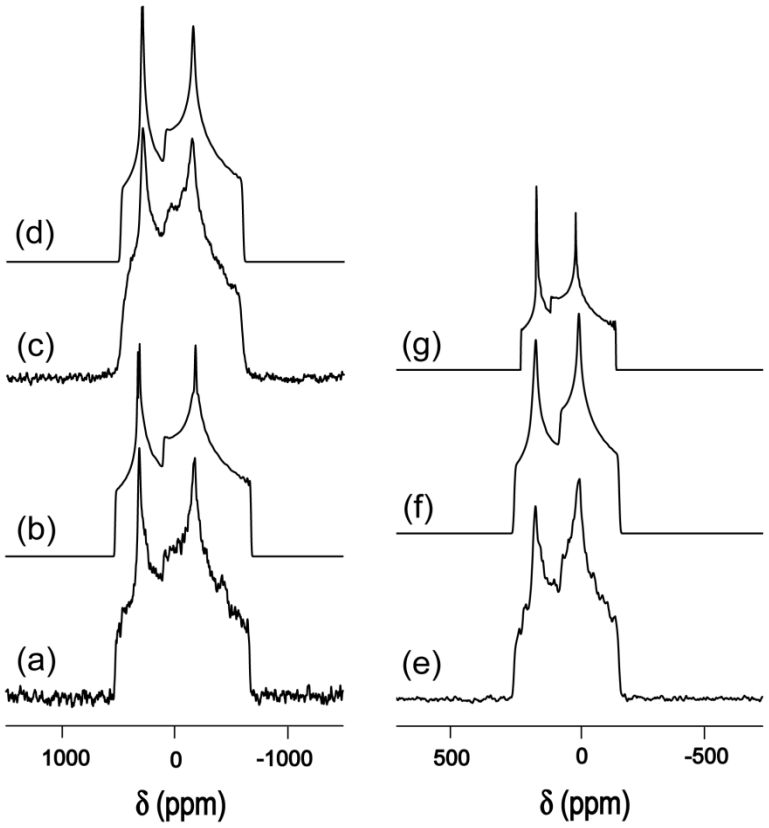

Figure 3.2. Solid-state chlorine NMR spectroscopy of cysteine hydrochloride monohydrate. Experimental spectra of stationary powdered samples: (a) ^{35}Cl at 11.75 T; (c) ^{37}Cl at 11.75 T; (e) ^{35}Cl at 21.1 T. Best-fit spectra simulated with WSolids using the EFG and CS parameters listed in Table 3 appear in (b), (d) and (f). (g) presents a simulation assuming no CSA.

As mentioned, spinning at the magic angle averages the three principal components of the CS tensor, and therefore simulations are simplified as only the isotropic shift, C_Q, and η_Q manifest themselves in the spectrum. Simulation of the spectra of stationary samples is therefore also greatly simplified as the magnitude of C_Q, the asymmetry parameter and isotropic shift are all accurately known from the MAS spectrum. The experimental and simulated $^{35/37}$Cl NMR spectra of the cysteine salt acquired under stationary conditions are shown in Figure 3.2.

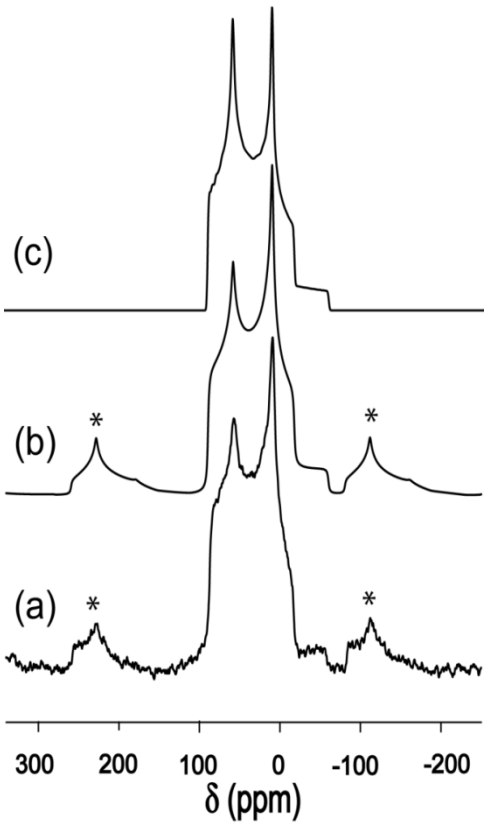

Figure 3.3. Solid-state chlorine MAS NMR spectroscopy of methionine hydrochloride at 21.1 T with ν_{rot} = 15 kHz. (a) ^{35}Cl at 21.1 T and best fit simulations using (b) Simpson and (c) WSolids under the assumption of an infinite MAS rate. Spinning sidebands are indicated by asterisks.

The small value of C_Q does not correspond to the lowest value for the CS span, consistent with the results of previous studies, although Ω is on the lower end at 66 ± 10 ppm. For all of the salts analyzed in this study, agreement between simulated and experimental spectra of stationary samples could not be achieved without the inclusion of CSA, demonstrating the importance of the chemical shift tensor interactions on the $^{35/37}$Cl lineshapes. The effects of the CS tensor on the spectral lineshapes were most apparent on the spectra of stationary powdered samples collected at 21.1 T as the effect of CSA, in hertz, is proportional to the magnetic field strength.

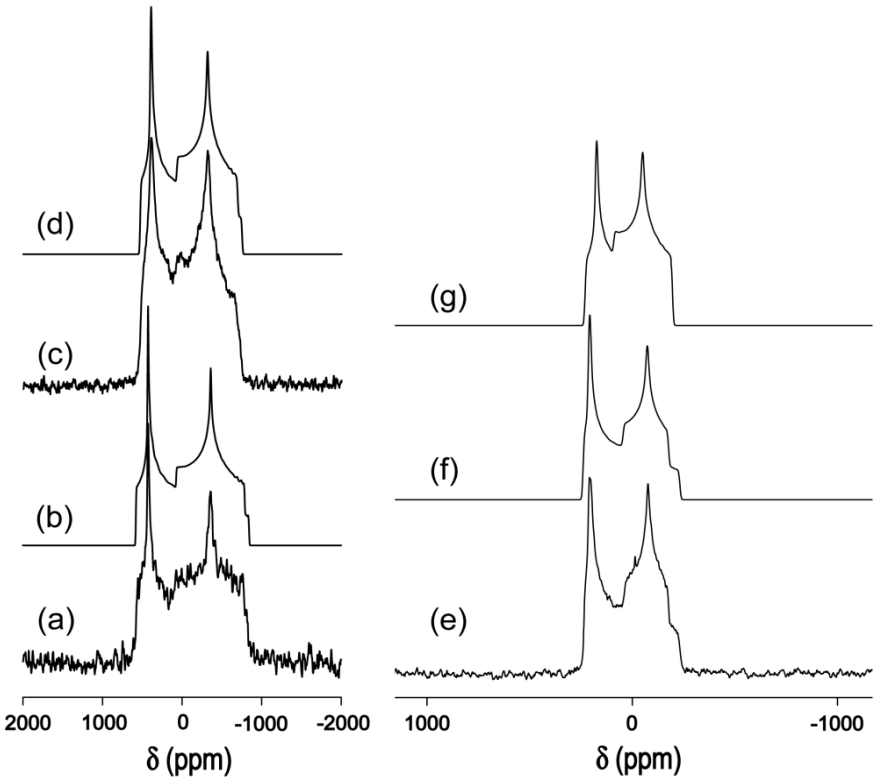

Figure 3.4. Solid-state chlorine NMR spectroscopy of methionine hydrochloride. Experimental spectra of stationary powdered samples: (a) ^{35}Cl at 11.75 T; (c) ^{37}Cl at 11.75 T; (e) ^{35}Cl at 21.1 T. Best-fit spectra simulated with WSolids are shown in (b), (d) and (f). (g) presents a simulation assuming no CSA. Trace NaCl(s) is visible in (e) at 0 ppm

The visibility of the CSA effect is also enhanced by the inverse relationship between field strength and the magnitude of the 2nd-order quadrupolar interaction, as shown by equation 15 in Chapter 1. Based on the simulation of its ^{35}Cl MAS NMR spectrum acquired at 21.1 T (Figure 3.3), methionine hydrochloride was found to have a chlorine-35 C_Q magnitude only slightly higher than that of the cysteine salt, at 4.41 ± 0.02 MHz.

Despite the similarities in the magnitude of the quadrupolar interaction for the methionine and cysteine salts, the former exhibits a larger chlorine CS span of 100 ± 20 ppm. The ^{35,37}Cl

NMR spectra acquired under stationary conditions, along with simulations, appear in Figure 3.4. The effect of the CS anisotropy is clearly manifested in the ^{35}Cl spectrum acquired under stationary conditions at 21.1 T, by the distinct shoulder on the low-frequency side of the spectrum. This spectral feature is visibly absent from the simulated spectrum assuming no CSA at 21.1 T included in Figure 3.4.

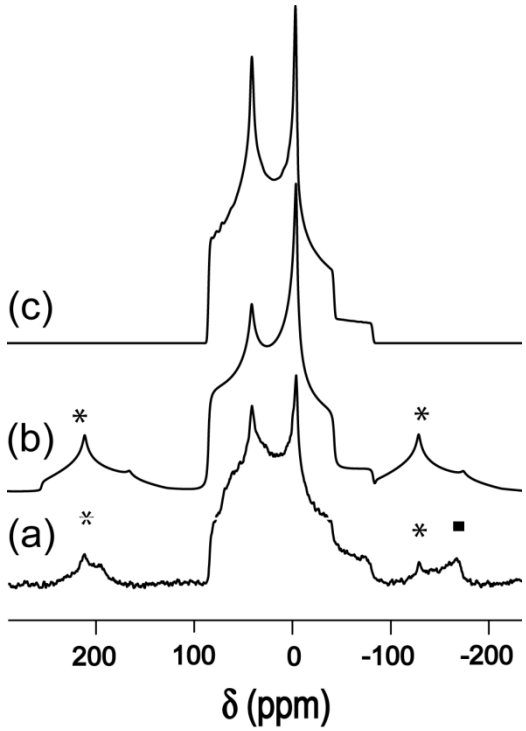

Figure 3.5. Solid-state chlorine MAS NMR spectroscopy of histidine hydrochloride monohydrate at 21.1 T with ν_{rot} = 15 kHz. (a) ^{35}Cl at 21.1 T and best fit simulations using (b) Simpson and (c) WSolids assuming an infinite MAS rate. Spinning sidebands are indicated by asterisks and an impurity in the sample is indicated by a square (this prohibited a precise measurement of the chlorine CS tensor in this sample).

The final salt for which a ^{35}Cl MAS spectrum could be obtained at 21.1 T was histidine hydrochloride monohydrate. The spectrum is shown in Figure 3.5, along with two simulations. The magnitude of C_Q (^{35}Cl) was found to be 4.59 ± 0.03 MHz with an η_Q of 0.46 ± 0.02.

Shown in Figure 3.6 are the ^{35}Cl NMR spectra and simulations for threonine hydrochloride collected at 11.75 and 21.1 T under static conditions. The magnitude of $C_Q(^{35}Cl)$ was found to be intermediate amongst those in this study at 5.4 ± 0.1 MHz. The asymmetry parameter of the ^{35}Cl EFG tensor of the threonine salt is 0.94 ± 0.02, which is the closest to unity for any of the salts in the current study. This indicates that the EFG tensor deviates greatly from axial symmetry. The CS span was found to be on the higher end at 95 ± 40 ppm and thus had a significant impact on the spectral lineshape, particularly at 21.1T, as demonstrated in Figure 3.6 by the simulation assuming CS isotropy.

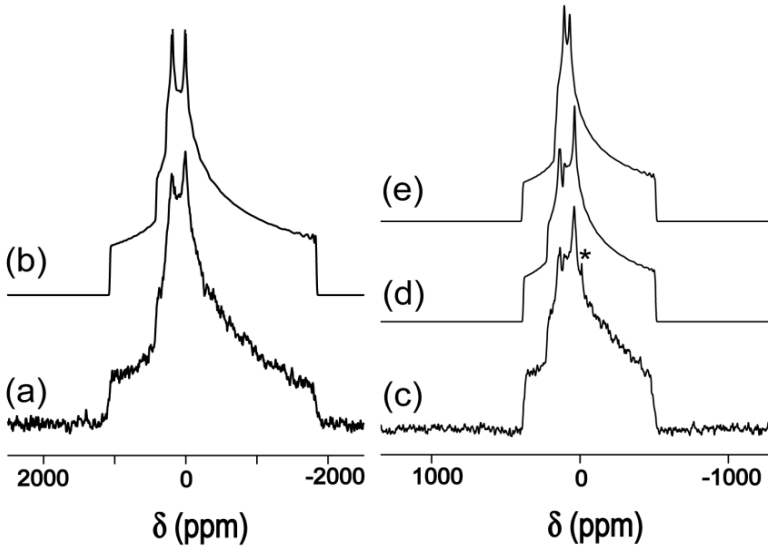

Figure 3.6. Solid-state chlorine NMR spectroscopy of threonine hydrochloride. Experimental spectra of stationary powdered samples: (a) ^{35}Cl at 11.75 T and (c) ^{35}Cl at 21.1 T. Best-fit spectra simulated using WSolids appear in (b) and (d). (e) presents a simulation assuming no CSA. The asterisk in (c) indicates trace NaCl(s).

The ^{35}Cl NMR spectra, and spectral simulations, of alanine hydrochloride collected at the two magnetic field strengths appear in Figure 3.7. The magnitude of C_Q was found to be 6.4 ± 0.1 MHz with an η_Q of 0.75 ± 0.06. Despite the large value of C_Q, the alanine salt was found to exhibit the smallest chlorine CS span of all the salts in this study at 60 ± 30 ppm. In addition, the

Euler angles relating the EFG and CS tensor PASs were found to be 90˚, 0˚, 0˚, indicating that the smallest principal component of the CS tensor, δ_{33}, is coincident with the V_{33} component of the EFG tensor. Interestingly, there are no symmetry elements in the crystal structure which require this to be the case.

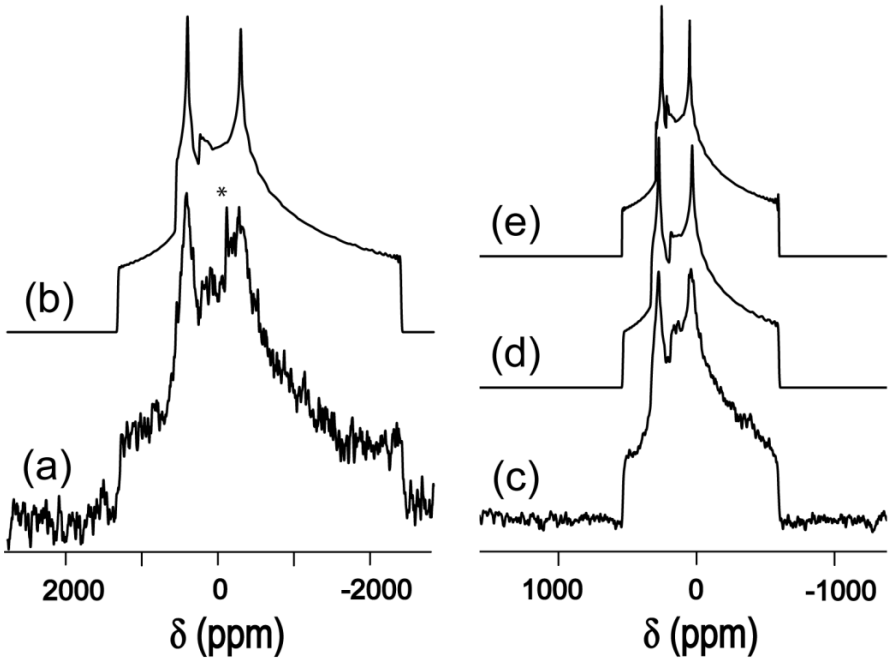

Figure 3.7. Solid-state chlorine NMR spectroscopy of alanine hydrochloride. Experimental spectra of stationary powdered samples: (a) ^{35}Cl at 11.75 T and (c) ^{35}Cl at 21.1 T. Best-fit spectra simulated using WSolids appear in (b) and (d). (e) presents a simulation assuming no CSA. The asterisk in (a) indicates trace NaCl.

Aspartic acid hydrochloride was found to have a C_Q of 7.1 ± 0.1 MHz, the largest observed to date for an amino acid hydrochloride, and an η_Q of 0.42 ± 0.05. The ^{35}Cl NMR spectra and accompanying simulations appear in Figure 3.8. The CS tensor span was determined to be intermediate amongst those found in this study at 75 ± 30 ppm. The isotropic CS of the

aspartic acid salt was found to be 102 ± 5 ppm, intermediate within the study as the chlorine isotropic shifts for the six salts were all within the small range of 93-106 ppm.

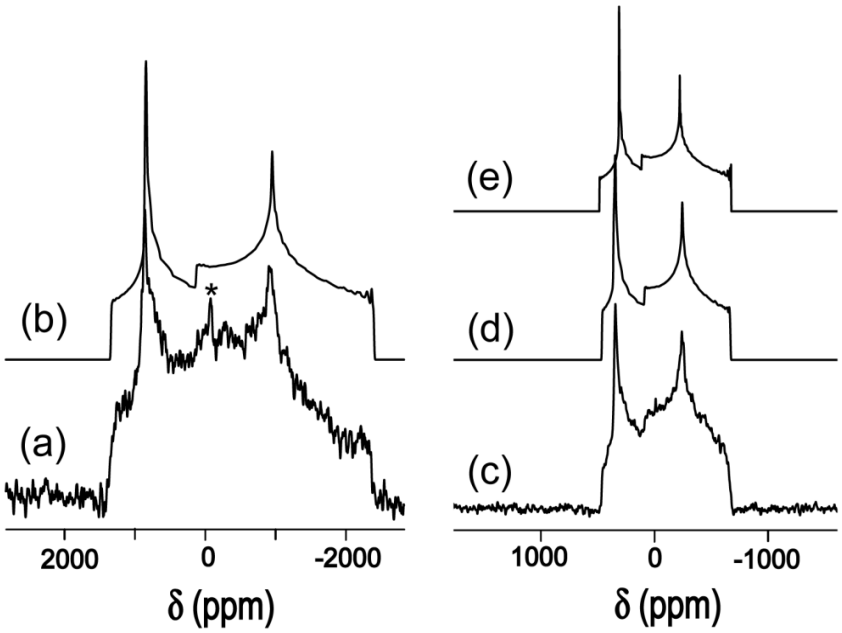

Figure 3.8. Solid-state chlorine NMR spectroscopy of aspartic acid hydrochloride. Experimental spectra of stationary powdered samples: (a) ^{35}Cl at 11.75 T and (c) ^{35}Cl at 21.1 T. Best-fit spectra simulated using WSolids appear in (b) and (d). (e) presents a simulation assuming no CSA. The asterisk indicates residual NaCl(s).

3.3.2.2 Interpretation of NMR Data

Using X-ray or neutron diffraction data, models of the local environment around the chloride ion in the amino acid salts were constructed in order to examine the effect of the chloride ion local environment on the ^{35,37}Cl NMR lineshapes; these models appear in Figure 3.9.

The models demonstrate that, although the chloride ion in all of the salts is participating in the same type of bonding, i.e., hydrogen-bonding primarily to –OH and -NH_3 groups (and –SH in the case of cysteine $HCl{\cdot}H_2O$), the environments are quite different. The number of hydrogen bonds ranges from three to six and the arrangement of the amino acids around the chloride ion varies significantly. The variation in the NMR parameters is thus not surprising given the differences in the local chlorine environment.

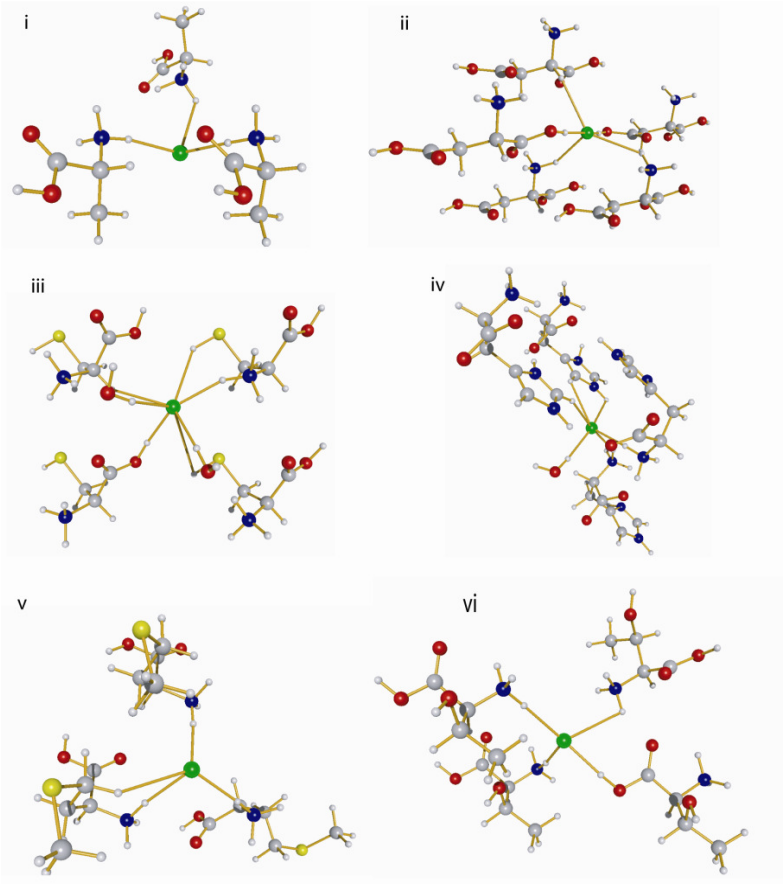

Figure 3.9. Coordination environment of the chloride ion (in green) in solid (i) alanine hydrochloride (ii) aspartic acid hydrochloride (iii) cysteine hydrochloride monohydrate (iv) histidine hydrochloride monohydrate (v) methionine hydrochloride and (vi) threonine hydrochloride. These are the models used for quantum chemical calculations of the chlorine NMR interaction tensors.

In previous studies on organic and amino acid hydrochloride salts, two correlations were noted: firstly the magnitude of C_Q seemed to be inversely proportional to the number of hydrogen bonds at the chlorine center and in addition, for amino acid hydrochloride salts, the magnitudes of C_Q and of the CS tensor span seemed to be indirectly related to the hydrophobicity of the amino acid.[37-39] Specifically, the salts of hydrophilic amino acids were found to have small magnitudes of C_Q and Ω, while hydrophobic amino acid salts had larger values for these two parameters. These two relationships are consistent with each other, as one would expect hydrophilic amino acids to have more hydrogen bonds in hydrochloride salts than their hydrophobic counterparts. Results from the current study also confirm that the mechanisms which control the EFG and CS tensors are quite distinct from one another, as demonstrated by the absence of correlation between the magnitudes of the CS tensor span and the quadrupolar coupling constant, as shown in Figure 3.10.

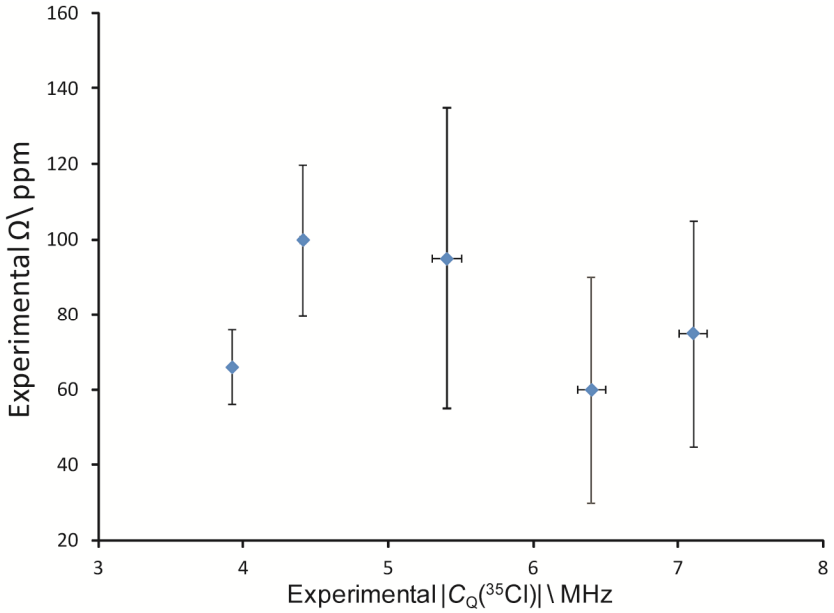

Figure 3.10. Comparison between the experimentally determined |C_Q(^{35}Cl)| and the experimentally determined chlorine CS tensor span for the five amino acid hydrochlorides fully characterized in section

The most obvious exception to both of these previously observed trends is the salt with the largest magnitude of C_Q, aspartic acid hydrochloride. Aspartic acid is a hydrophilic amino acid, and as demonstrated in Figure 3.9, its HCl salt has five hydrogen interactions to the central chlorine, which is greater than the number of hydrogen interactions for the alanine, methionine and threonine salts, all of which have smaller values of C_Q. As mentioned, however, there is no symmetry in the aspartic acid hydrochloride crystal structure, unlike all other amino acid salts. This absence of symmetry is also seen in the local environment around the chlorine ion, as all the hydrogen bonds appear to be on one face of the chloride ion, while the other side is more exposed. Upon inspection, the six amino acid hydrochlorides may be divided into two separate categories on the basis of the symmetry about the chloride ion: the cysteine, methionine and

histidine salts all have hydrogen bonds distributed more or less evenly about the central chloride while, like aspartic acid, the alanine and threonine salts have these bonds more heavily concentrated on one face of the ion. Previous studies have found that in ^{23}Na NMR of sodium complexes, as the symmetry of coordination about sodium deviates from perfectly symmetric (tetrahedral or octahedral), the quadrupole coupling constant increases in a consistent way: the greater the exposed area about the centre, the larger the value of C_Q.[74] For example, with deviation from octahedral symmetry, there is an increase in C_Q as the symmetry goes from octahedral, to trigonal bipyramidal to planar. The results of the current study are consistent with this model, as the three salts that have hydrogen bonds concentrated on one side of the chloride ion also have the three largest magnitudes of C_Q. In addition, the sodium studies also revealed that as symmetry deviated significantly from ideal, the quadrupole coupling constant *increased* as the number of ligands about the centre atom became larger. This relationship is consistent with the large C_Q observed for aspartic acid hydrochloride, indicating that when symmetry is very low about the chloride, an increase in hydrogen bonds may actually result in a larger quadrupole coupling constant, provided these additional hydrogen bonds maintain a relatively low-symmetry arrangement at Cl^-.

The ^{35}Cl isotropic chemical shifts observed in this study were between 93 and 106 ppm. These results are consistent with the results from previous studies; the majority of the chlorine isotropic chemical shifts for the seventeen amino acid hydrochlorides which have been characterized by chlorine SSNMR fall in the range of 90 to 110 ppm, with only serine hydrochloride and proline hydrochloride falling outside of this range. The chlorine-35 chemical shift range for amino acid hydrochlorides is depicted in Figure 3.11. The chemical shift of proline hydrochloride is the most anomalous, at 37 ppm, 53 ppm lower than the next smallest

shift. The origins of the low shift of the proline salt, or the large shift of the serine salt, are not clear.

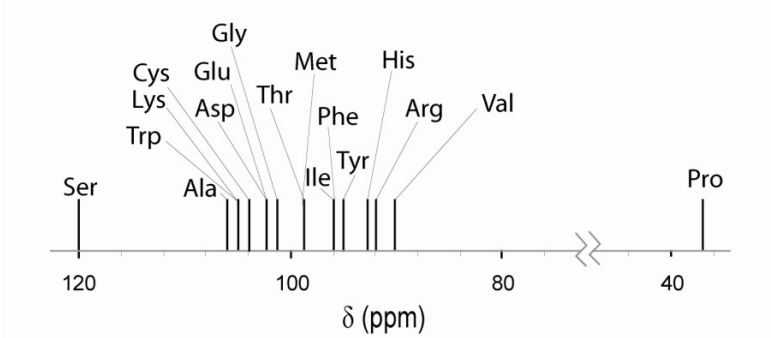

Figure 3.11. Solid-state ^{35}Cl isotropic chemical shifts for seventeen amino acid hydrochlorides for which these data are available. All shifts are shown with respect to solid NaCl at 0 ppm. Data are taken from this work and from references 37-39.

3.3.2.3 Variable Temperature NMR

To further study the nature of chlorine NMR parameters in amino acid hydrochlorides, VT-MAS NMR spectra were collected for arginine hydrochloride monohydrate between the temperatures of 278 and 338 K. As MAS spectra were collected, this set of experiments monitored the effect of temperature on only the EFG tensor parameters and the isotropic chlorine CS (see Chapter 2). Arginine hydrochloride monohydrate and MAS experiments were chosen for study due to the time constraints associated with collecting chlorine NMR spectra as the arginine salt has the smallest $C_Q(^{35}Cl)$ of all the amino acid hydrochlorides.

The chlorine-35 MAS NMR spectra of arginine hydrochloride collected at seven temperatures are shown in Figure 3.12. The asterisk in this figure indicates a large impurity peak which is likely the anhydrous arginine hydrochloride salt. Arginine hydrochloride monohydrate was included in an earlier study of amino acid hydrochlorides and in that study was found to have a

chlorine-35 C_Q of 2.035(20) MHz, an η_Q of 0.98(2), and a chlorine CS of 91.5(1.0) ppm w.r.t. solid sodium chloride.[38]

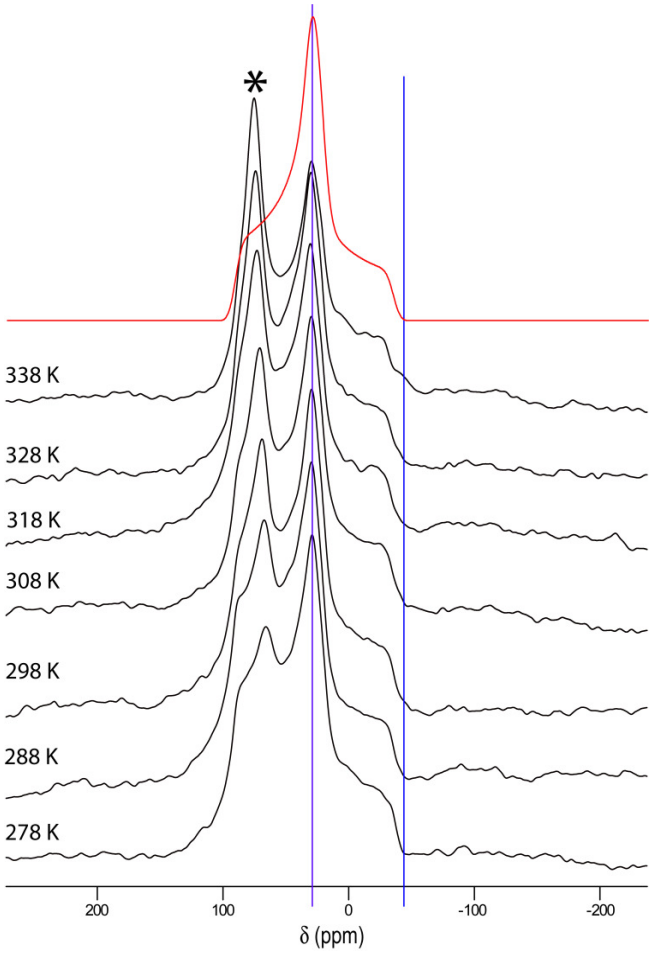

Figure 3.12. Solid-state chlorine NMR variable temperature spectroscopy of arginine hydrochloride monohydrate. Experimental spectra collected at ν_{rot} = 14 kHz. Temperatures appear on the left of each spectrum. The blue lines are present as a guide for the eye. The red spectrum is a simulation using the literature NMR parameters from reference 39.

These parameters, also listed in Table 3.4, were used as a starting point for simulations of the spectra at each temperature, and while there were slight differences at the different temperatures, these were negligible with the greatest temperature effect observed on the unknown impurity,

further indicating that the impurity is due to the presence of the anhydrous salt. The temperature independence of the chlorine NMR parameters indicates an absence of exchange and motion in the sample over this temperature range. While it cannot be assumed that this is true for all amino acid hydrochloride salts, the result is gratifying as it confirms that for *this* sample, the assumption that the chlorine SSNMR parameters are temperature independent is valid.

3.3.3 Quantum Chemical Calculations

3.3.3.1 BL3YP and RHF Calculations

The models based on the X-ray or neutron structures for the amino acid hydrochloride salts, shown in Figure 3.9, were employed in quantum chemical calculations of the NMR interaction tensors. The results of these calculations are presented in Table 3.3.

Table 3.3. B3LYP and RHF calculated chlorine-35 EFG and CS tensor data for amino acid hydrochloride salts studied experimentally in this study[a]

Hydrochloride Salt	C_Q / MHz	η_Q	δ_{iso}[b] / ppm	Ω / ppm	κ
Alanine	-5.90	0.23	67	83	0.20
Aspartic Acid	-8.33	0.19	86	111	-0.24
Cysteine	-3.48	0.43	28	72	-0.37
Cysteine[c]	-4.13	0.48	29	71	-0.52
Histidine	-4.83	0.66	103	195	-0.10
Methionine	5.00	0.15	69	90	-0.43
Threonine	-6.22	0.82	26	83	-0.45
Threonine[c]	-5.80	0.62	22	86	-0.50

[a]Quadrupolar and shielding parameters were calculated using the methods and basis sets described in the Experimental. [b] To convert from calculated shielding constants to chemical shifts, a shift of 45.37 ppm was used (for the conversion from solid to aqueous NaCl chemical shift scales) in addition to the absolute shielding conversion found in the introduction.
[c]Calculated using the SC-CFP method, as described in the Experimental.

The good agreement between the experimental data and those determined through quantum chemical calculations is demonstrated in Figures 3.13 and 3.14, which compare the experimental and best theoretical chlorine-35 quadrupolar coupling constants and CS tensor spans,

respectively. With the sole exception of the aspartic acid salt, the quadrupolar coupling constants were reproduced within 12 %. The aspartic acid hydrochloride calculation deviation was slightly higher, with an error of 17.2%.

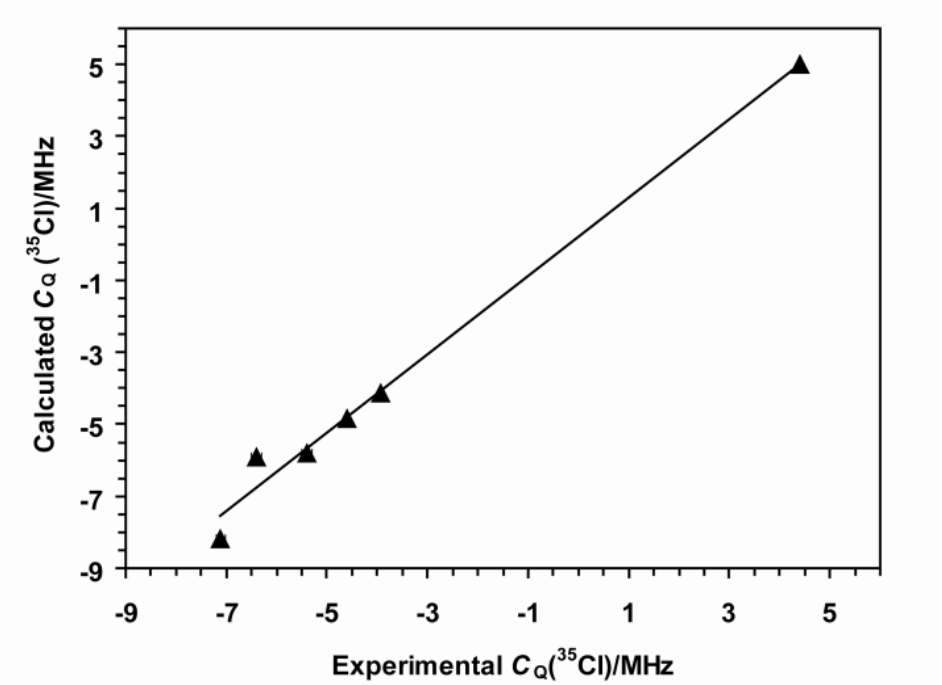

Figure 3.13. Comparison between the experimentally determined chlorine-35 quadrupolar coupling constants, on the x-axis and the B3LYP calculated values, on the y-axis. The calculated values plotted for the cysteine and threonine salts were determined using the SC-CFP model. The equation for the line of best fit is $y = 1.0892x + 0.2055$, with an R^2 value of 0.994.

Despite the error, it is of note that the calculation overestimates the coupling constant for the aspartic acid salt, demonstrating that its high value, compared to the other salts, is reproduced by theory. The EFG calculations also allow for designation of the sign of the quadrupole coupling constant, a classification that is not available from experiment.

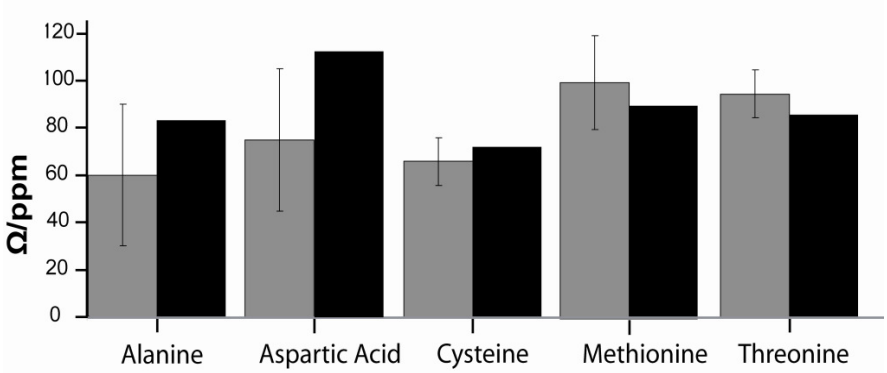

Figure 3.14. Comparison between the experimentally determined CS span (in gray) and the calculated values (in black). The calculated values plotted for the cysteine and threonine salts were determined using the SC-CFP model.

Good agreement between the calculated and experimental spans was also obtained, with the calculated values all either within, or very close to within, experimental error. As was found with previous studies, however, good agreement between experimental and calculated isotopic chemical shifts was not achieved, with the calculations underestimating this parameter in all cases except for histidine hydrochloride monohydrate. While perfect agreement between experiment and theory in all cases would be desirable, it is reassuring that, given the availability of a neutron diffraction structure, the EFG calculations for histidine hydrochloride monohydrate were most accurate. This result is in agreement with a previous study in which excellent correlation between experimental and calculated EFG tensor information was found for similar systems in which neutron diffraction structures were available.[37-39] However, some error is expected to be inherent in the calculations, as these were performed in the gas phase and not the solid state.

The importance of having accurate structures was also demonstrated by the improvement observed in the accuracy of the calculations of the quadrupolar and shielding parameters of

cysteine hydrochloride monohydrate upon using the newly re-determined X-ray structure to construct the model; for example, the error in the calculated quadrupolar coupling constant decreases from 52 % to 11 % upon switching from the published structure to that obtained in this study. This result highlights the utility of combining SSNMR and calculations to confirm structural characteristics.

3.3.3.2 Self-Consistent Charge Field Perturbation Model

In an attempt to improve on the calculated results for two amino acid hydrochloride salts which had large errors in C_Q relative to experiment (cysteine hydrochloride monohydrate and threonine hydrochloride), the SC-CFP method was also employed for the calculation of the NMR parameters. This method takes into account the effect of surrounding ionic charges in the crystal lattice in contrast to the previously discussed results which are for the isolated models shown in Figure 3.9. The resulting CS span and quadrupolar coupling constants are included in Table 3.3. While the SC-CFP method did slightly improve the accuracy of the span, the improvement was most significant for the magnitude of the quadrupolar coupling constant, reducing the error in the calculation of that parameter to only 5.2 % and 7.8 % for the cysteine and threonine salts, respectively. The chloride-chloride internuclear distance is less than 5.1 Å in these two systems; therefore, the large effect of one chloride ion on the EFG at another chlorine site is not surprising given the r^{-3} dependence of a charge element on the EFG at a point in space, where r is the distance between them.[75] If the systems are viewed as purely ionic, this result demonstrates that the EFG tensor at a chloride centre may be significantly affected by the surrounding chloride ions when these ions are relatively close to each other, and is not solely dependent on the local environment in the first coordination sphere, as is seen in some other systems.[76] The minimal improvement observed for the span is expected, given that the shielding tensor depends primarily

on molecular orbitals with large coefficients on the central chloride; these orbitals are most strongly influenced by atoms within the first coordination sphere of the chloride ion.

3.3.3.3 GIPAW-DFT Results

In addition to B3LYP/RHF calculations carried out using the Gaussian program, GIPAW-DFT calculations were performed. While the majority of the amino acid hydrochlorides that have been analyzed by chlorine SSNMR have had their structures determined through X-ray diffraction (true for the hydrochloride salts of alanine, arginine, aspartic acid, cysteine, histidine, methionine, proline, threonine and tryptophan), the existence of neutron structures for some of these salts (those of glutamic acid, glycine, lysine, phenylalanine, tyrosine and valine) allowed for more complete testing of the accuracy of the GIPAW-DFT method. Experimental knowledge of the hydrogen positions that is available from neutron diffraction structures means that the entire structure of those amino acid hydrochlorides is known more precisely, meaning any inaccuracy in the calculated NMR parameters compared to experiment is largely result of deficiencies in the method. This is not true in the case where only X-ray structures are available, as incorrect placement of the hydrogen atoms may be the primary cause of inaccuracies relative to experiment. Therefore, the amino acid hydrochloride series was ideal to determine how well GIPAW-DFT calculations match experimental chlorine SSNMR parameters in the case of organic chloride systems.

As the hydrogen positions are not known experimentally when calculating NMR parameters based on an X-ray structure (in any program), it is often standard to optimize the hydrogen positions prior to the NMR calculation, as was done for the B3LYP calculations in section 2.3.3.1. Thus, we also chose to use the amino acid hydrochlorides to test the effect of

optimizing the proton positions in GIPAW-DFT calculations in order to determine if the method would lead to a significant improvement in the accuracy of the calculated NMR parameters.

The calculated chlorine NMR parameters for the amino acid hydrochlorides for which there are X-ray structures appear in Table 3.4, while those that have a neutron structure appear in Table 3.5. In both of these tables, the experimental data from both the literature and this study are also included for easier comparisons. The data in Table 3.4, presents the results after the hydrogen positions were optimized, with the exception of arginine hydrochloride for which the hydrogen positions optimization did not converge. In all cases, visualization of the salt was done after the optimization calculations to ensure the position of the hydrogen atoms were reasonable and only changed slightly. As expected, hydrogen positions optimization improved the accuracy of the calculations in most cases, and while this is not true in all cases, all further comparisons to experimental data will be done with the values listed in Table 3.4. A Table presenting the calculated NMR parameters prior to hydrogen positions optimization appears in Appendix 2 and did not possess the same *qualitative* agreement observed in Table 3.4. The results confirm that, as with B3LYP calculations, it is recommended to optimize the hydrogen positions in all cases for which they are not known experimentally, provided it is computationally feasible.

Table 3.4. GIPAW-DFT calculated and experimental chlorine-35 EFG and chemical shift data for amino acid hydrochloride salts for which X-ray structures are available

Amino Acid Hydrochloride[a,b]	$\lvert C_Q(^{35}Cl)\rvert$ / MHz	η_Q	δ_{iso} / ppm[c,d]	Ω / ppm	κ	α, β, γ /°
Alanine – calculation[e]	8.45	0.775	146	75	0	16, 16, 86
Alanine – experimental	6.4(1)	0.75(6)	106(5)	60(3)	-0.3(5)	90(15), 0(15), 0(15)
Arginine – calculation	2.45	0.197	51	44	-0.2	65, 71, 54
Arginine – experimental	2.035(20)	0.98(2)	91.5(1.0)	57.5(3.0)	0.27(10)	85 (15), 77.5(12.0), 30(30)
Aspartic Acid – calculation[e]	10.31	0.396	149	91	-0.7	13, 18, 118
Aspartic Acid – experimental	7.1(1)	0.42(5)	102(5)	75(30)	-0.9(1)	0(20), 30(20), 93(20)
Cysteine – calculation[e]	4.0	0.505	155	86	0.1	8, 6, 155
Cysteine – experimental	3.92(1)	0.47(2)	104.2(5)	66(10)	0.12(12)	155(20), 0(10), 0(20)
Histidine – calculation[e]	2.72	0.716	112	99	-0.5	158, 74, 173
Histidine – experimental	4.59(3)	0.46(2)	93(1)	< 150	[f]	
Methionine – calculation[e]	6.2	0.375	138	137	0.2	75, 13, 18
Methionine – experimental	4.41(2)	0.35(3)	99(1)	100(20)	0.3(3)	93(20), 163(15), 7(20)
Proline – calculation[e]	9.23	0.906	110	105	0.4	90, 88, 51
Proline – experimental	4.50(5)	0.63(5)	37(5)	63(5)	-0.54(8)	48(15), 69(15), 9(15)
Threonine – calculation[e]	12.21	0.849	149	133	0.2	110, 4, 18
Threonine – experimental	5.4(1)	0.94(2)	99(10)	95(40)	-0.2(5)	95 (15), 0(10), 0(15)
Tryptophan – calculation[e]	11.62	0.816	151	127	0.5	56, 7, 38
Tryptophan – experimental	5.05(4)	0.86(3)	105(1)	72(5)	0.1(1)	90(15), 20(15), 2(20)

[a]Arginine, cysteine and histidine hydrochloride salts are monohydrates. [b]All amino acids are of the L-variety. [c]To convert from calculated shielding constants to chemical shifts, a shift of 45.37 ppm was used (for the conversion from solid to aqueous NaCl chemical shift scales) in addition to the absolute shielding conversion found in Chapter 1. [d]Experimental values are all w.r.t. solid

NaCl. [e]NMR calculation performed after the hydrogen positions were optimized using the method described in the Experimental (section 3.2.5.1). [f]Not determined.

Table 3.5. GIPAW-DFT calculated and experimental chlorine-35 EFG and chemical shift data for amino acid hydrochloride salts for which neutron structures are available

Amino Acid Hydrochloride[a,b]	$C_Q(^{35}Cl)$ / MHz	η_Q	δ_{iso} / ppm[c,d]	Ω / ppm	κ	α, β, γ /°
Glutamic Acid – calculation	4.3	0.30	142	84	0.3	21, 79, 17
Glutamic Acid – experimental	3.61(1)	0.65(2)	102(1)	66(15)	0.0(3)	6(20), 77(20), 6(20)
Glycine – calculation	8.14	0.80	133	110	0.3	123, 6, 142
Glycine – experimental	6.42(5)	0.61(3)	101(5)	100(20)	0.3(3)	95(20), 0(20), 0(20)
Lysine – calculation	4.41	0.77	107	54	-0.2	70, 79, 8
Lysine – experimental	2.49 (1)	0.42 (2)	105(5)	26(10)	-0.4(4)	0(20), 52(20), 0(20)
Phenylalanine – calculation	7.71	0.55	129	147	0.1	95, 12, 176
Phenylalanine – experimental	6.08(5)	0.52 (3)	96(5)	129(20)	0.26(25)	91(20), 13(20), 10(20)
Tyrosine – calculation	3.27	0.35	142	129	-0.5	13, 39, 54
Tyrosine – experimental	2.23(2)	0.72(3)	94.7(5)	< 150	[e]	
Valine – calculation	7.96	0.55	128	149	0.1	83, 7, 14
Valine – experimental	5.89(5)	0.51(5)	90(10)	125(40)	0.35(50)	65(20), 0(20), 0(20)

[a] Lysine hydrochloride salt is a dihydrate. [b]All amino acids are of the L-variety. [c]To convert from calculated shielding constants to chemical shifts, a shift of 45.37 ppm was used (for the conversion from solid to aqueous NaCl chemical shift scales) in addition to the absolute shielding conversion found in Chapter 1. [d]Experimental values are all w.r.t. solid NaCl. [e]Not determined.

A comparison of the experimental and calculated chlorine-35 C_Q magnitudes listed in Table 3.4 and Table 3.5 clearly demonstrates that, even in cases where the full structure of the salt is known experimentally, the quadrupolar coupling constant is significantly overestimated by GIPAW-DFT calculations. Figure 3.15 is a graph of the experimental versus calculated chlorine-35 $|C_Q|$ for all of the salts.

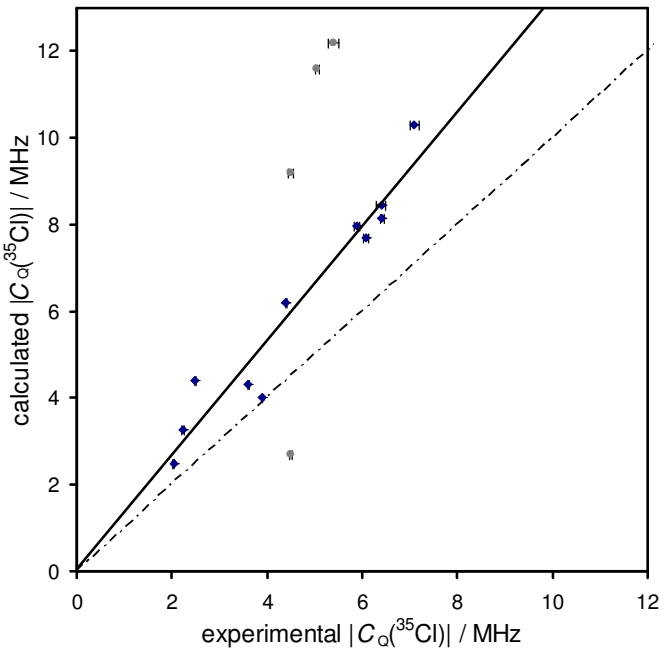

Figure 3.15. Comparison between the experimentally determined chlorine-35 quadrupolar coupling constant, on the x-axis and the GIPAW-DFT calculated values, on the y-axis for the amino acid hydrochlorides. The grey circles present the data for the salts of proline, threonine, histidine and tryptophan. The blue diamonds represent the remaining 11 amino acid salts. The equation for the line of best fit for the blue diamonds is $y = 1.3203x + 0.045$, with an R^2 value of 0.9356. The dotted line represents the equation $y = x$. Experimental data not included in this chapter are from references 37-39.

Eleven of the amino acid hydrochloride salts (blue diamonds) demonstrate a fairly linear relationship between experimental and calculated $|C_Q(^{35}Cl)|$, but also overestimation by calculation. Error in the calculation is demonstrated by the line of best fit shown on Figure 3.14: the slope of the line is 1.3203 (perfect agreement would give a slope of 1), the y-intercept is + 0.9356 MHz (indicating an overestimation of, on average, this amount) and the R^2 is 0.9356 (demonstrating the linear nature of the data). Three of the remaining amino acid salts (those of proline, threonine and tryptophan) are also plotted on Figure 3.15 as grey circles. The calculated chlorine-35 coupling constant for these points are highly overestimated compared to theory. And while these three amino acid hydrochlorides do not appear on the line corresponding to the majority of the data, they do form their own linear series. It is not known why these three amino acid hydrochlorides form their own trend, but it is significant to note that as their calculated coupling constants are *more* overestimated, it is clear that GIPAW-DFT calculations consistently overestimate this parameter. The overestimation of the parameter is consistent with the results obtained for calculations using the RHF level of theory, as shown in Figure 3.13 and in earlier studies.[37,38] Histidine hydrochloride monohydrate was an outlier for the graph displayed in Figure 3.15 and, in the only salt for which C_Q was underestimated. The poor agreement for this one single salt is puzzling and may indicate that there are additional issues with the published crystal structures, in addition to the obvious typos (*vide supra*). Attempts were made to grow a single crystal of sufficient quality to collect a new crystal structure, but these were unsuccessful.

In the case of the asymmetry parameter, the results were not as consistent. While η was calculated very accurately, to within 0.1, in most cases, there were instances where the calculated values were very different from the experimental value. And unlike the case observed for the quadrupolar coupling constant, η_Q was both overestimated and underestimated by calculation.

The agreement observed was, in general, better than observed for the calculations using RHF level of theory.

The trend observed for the CS tensor parameters was similar to that observed for those of the EFG tensor. Comparison of the calculated and experimental spans in Table 3.4 and Table 3.5 again reveals consistent overestimation by calculation. Figure 3.16 demonstrates this relationship graphically for 12 data points, with the exclusion of only one outlier (the salt of arginine – there is no experimental span data available for the salts of histidine or tyrosine). The line of best fit has a slope of 0.9158, a y-intercept of 33.603 ppm and an R^2 value of 0.7675. More telling, however, are the data presented in Figure 3.17, which uses only the data points for those amino acid salts for which there is a *neutron* crystal structure and experimental data.

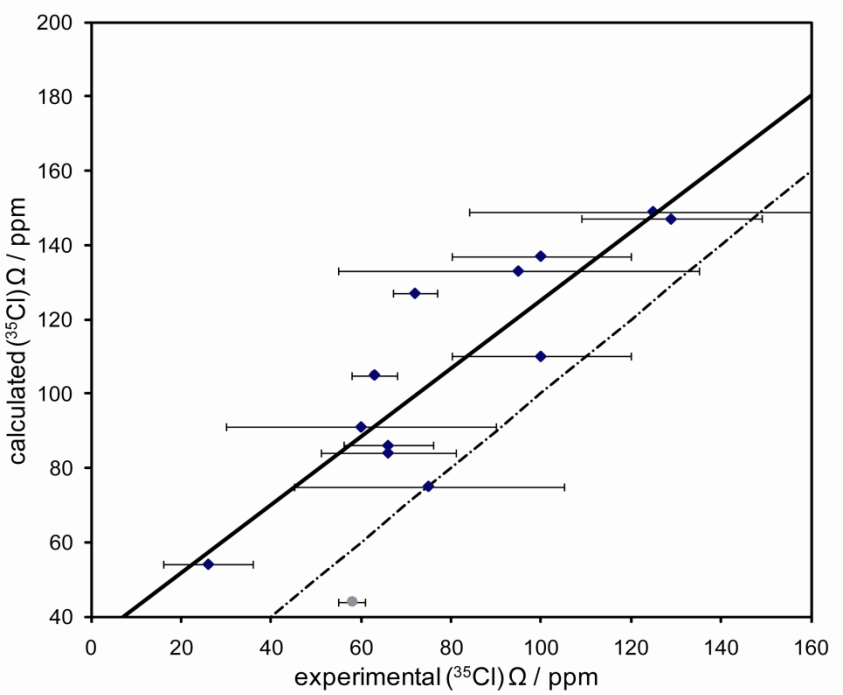

Figure 3.16. Comparison between the experimentally determined chlorine-35 CS tensor span, on the x-axis and the GIPAW-DFT calculated values, on the y-axis for all of the amino acid hydrochlorides for which experimental data is available. The equation for the line of best fit (blue diamonds) is $y = 0.9158x + 33.603$, with an R^2 value of 0.7675. The grey circle is an outlier (arginine hydrochloride monohydrate) and is not included in the line of best fit. The dotted line represents the equation $y = x$. Experimental data not included in this chapter are from references 37-39.

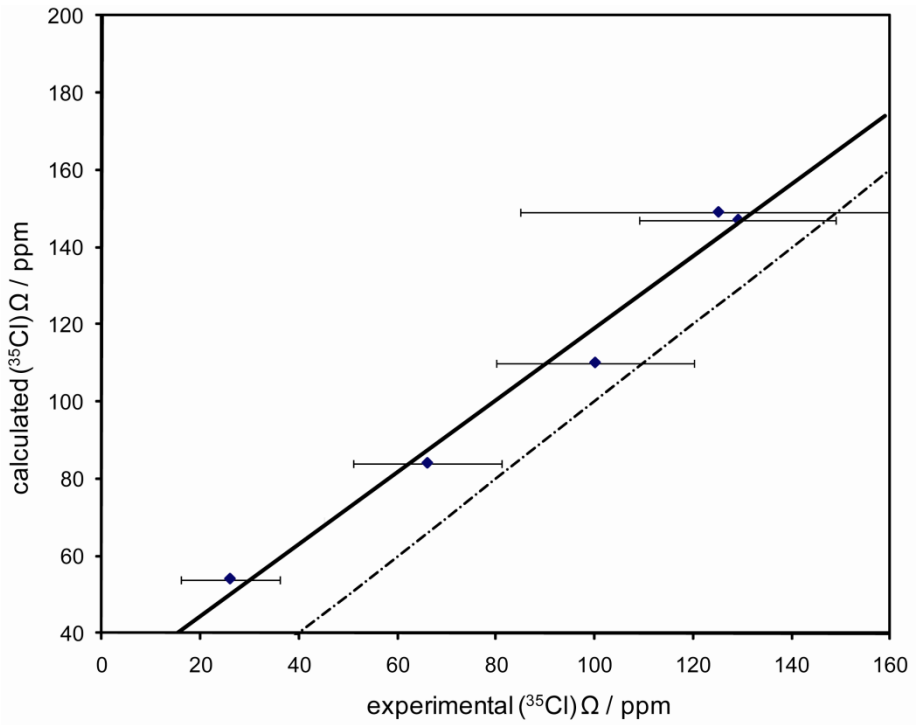

Figure 3.17. Comparison between the experimentally determined chlorine-35 CS tensor span, on the x-axis and the GIPAW-DFT calculated values, on the y-axis for the amino acid hydrochlorides for which there are neutron diffraction structures. The equation for the line of best fit is $y = 0.933x + 25.578$, with an R^2 value of 0.9771. The dotted line represents the equation $y = x$. Experimental data not included in this chapter are from reference 39.

In these structures, all atomic positions are known experimentally, meaning incorrect placement of the hydrogen atoms is not likely a significant cause for errors in the calculation. In Figure 3.17 the line of best fit has a slope of 0.933, a y-intercept of 25.578 ppm and a very high R^2 value of 0.9771. These results differ from those obtained in this and in earlier studies, using the B3LYP hybrid functional, in which the *trends* in CS tensor span were not reproduced, with the experimental values of the span being either overestimated or underestimated by calculation.[37,38] These results indicate, that even in ideal conditions, the CS tensor span is overestimated by

GIPAW-DFT methods. This overestimation is significant, usually outside the error bounds of the experimental value. It is pleasing, however, that as the overestimation in the calculated span value is consistent, the trends in span observed experimentally are reproduced well by the GIPAW-DFT calculations – a result that was not observed in the case of the gas-phase B3LYP calculations. Similar to the CS tensor span, the calculated isotropic chlorine chemical shifts were significantly overestimated, by 30-50%, in almost all cases. This demonstrates that all three components of the CS tensor are generally overestimated by calculation, not just the range which they cover. Unfortunately, the same *qualitative* agreement between the experimental and calculated values as was observed with the $|C_Q(^{35}Cl)|$ and CS tensor span was not observed for this parameter.

3.4 Conclusions

Chlorine-35/37 SSNMR spectroscopy has been used to study the local environment of chlorine in six L-amino acid hydrochloride salts. The study has aided in the understanding of the relationship between chlorine binding environments and ^{35,37}Cl NMR properties in organic salts. The $^{35/37}$Cl EFG and CS tensors, including their relative orientations, were determined and these demonstrated high sensitivity to slight differences in the local environment at chlorine. The accuracy of the determined parameters was ensured by the collection of data at two magnetic fields, with experiments at 21.1 T allowing for selected MAS experiments and visible manifestation of chlorine CSA in experiments run under static conditions. Chlorine-35 quadrupolar coupling constants ranged from -7.1 to 4.41 MHz with the value observed for aspartic acid hydrochloride, -7.1 MHz, being the largest value, in magnitude, observed to date for an organic hydrochloride salt. In addition to the general trend of correlation between the the hydrophobicity of the amino acid and magnitude of the C_Q and span observed in previous

studies, symmetry about the chloride ion was demonstrated to be extremely important in determining the magnitude of C_Q, explaining the large value observed for the aspartic acid salt.

Quantum chemical calculations using B3LYP/RHF theory were found to be in good agreement with the experimental values, particularly when accurate crystal structures are available. The importance of the quality of the structure was demonstrated in the case of cysteine hydrochloride monohydrate; the calculated parameters improved significantly upon the use of the more accurate crystal structure acquired in this study. Use of the SC-CFP method for calculating the NMR parameters was also found to significantly improve the accuracy of the quadrupolar coupling constants, demonstrating that the negative charges associated with neighbouring chloride ions in the structure can have a significant effect on the electric field gradient about the central nucleus, especially when the chloride-chloride internuclear distance is small.

Calculations were also carried out using the GIPAW-DFT method on the entire series of amino acid hydrochlorides for which there is experimental data. The results clearly demonstrated that, even in cases where the entire structures are known, both the chlorine quadrupolar coupling constant and chemical shift tensor span are consistently overestimated but are quantitatively correct. In addition the chlorine-35 chemical shift is also significantly overestimated but, with this parameter, the experimental trends are not reproduced. The advantages of the GIPAW-DFT method, however, are greater than those of the B3LYP/RHF level of theory, therefore it can be stated that the former method is better for calculating chlorine SSNMR parameters in organic chlorides.

This study, in combination with previous amino acid hydrochloride studies, has contributed some of the necessary groundwork to now apply chlorine-35/37 SSNMR in the

examination of the local environment of chlorine in larger systems and in systems of unknown structure. In addition, the success of the study demonstrates the feasibility of chlorine SSNMR for investigations of organic hydrochlorides and the strengths and limitations of both B3LYP and GIPAW-DFT calculations. Both the experimental and computational data included in this chapter will aid with the interpretation of data in future chlorine SSNMR studies of organic-chloride systems.

3.5 References

1 R. H. Holm and E. I. Solomon, *Chem. Rev.,* **1996**, *96*, 2237.

2 W. B. Guggino. In *Chloride Channels: Current Topics Membranes,* A. Kleinzeller, D. M. Fambrough, Eds., Academic Press, San Diego, 1994; Vol. 42.

3 F. M. Ashcroft, *Ion Channels and Disease*, Academic Press, San Diego, 2000.

4 A. J. Smith and B. Schwappach, *Science,* **2010**, *328*, 1364.

5 R. Dutzler, E. B. Campbell, M. Cadene, B. T. Chait and R. MacKinnon, *Nature,* **2002**, *415*, 287.

6 R. Dutzler, E. B. Campbell and R. MacKinnon, *Science,* **2003**, *300*, 108.

7 Z. S. Derewenda, *Acta Crystallogr., Sect. D: Biol. Crystallogr.,* **2010**, *66*, 604.

8 J. M. Canaves, R. Page, I. A. Wilson and R. C. Stevens, *J. Mol. Biol.,* **2004**, *344*, 977.

9 W. N. I. Price, C. Yang, S. K. Handelman, H. Neely, P. Manor, R. Karlin, R. Nair, J. Liu, M. Baran, J. Everett, S. N. Tong, F. Forourhar, S. S. Swaminathan, T. Acton, R. Xiao, J. R. Luft, A.

Lauricella, G. T. DeTitta, B. Rost, G. T. Montelione and J. F. Hunt, *Nature Biotechnol.,* **2009**, *27*, 51.

10 I. L. Alberts, K. Nadassy and S. J. Wodak, *Protein Sci.,* **1998**, *7*, 1700.

11 A. C. Rosenzweig, D. L. Huffman, M. Y. Hou, A. K. Wernimont, R. A. Pufahl and T. V. O'Halloran, *Structure,* **1999**, *7*, 605.

12 A. Bax, *Protein Sci.,* **2003**, *12*, 1.

13 D. Marulanda, M. L. Tasayco, A. McDermott, M. Cataldi, V. Arriaran and T. Polenova, *J. Am. Chem. Soc.,* **2004**, *126*, 16608.

14 A. E. McDermott, *Curr. Opin. Struct. Biol.,* **2004**, *14*, 554.

15 P. C. A. van der Wel, J. R. Lewandowski and R. G. Griffin, *J. Am. Chem. Soc.,* **2007**, *129*, 5117.

16 R. H. Havlin, F. J. Blanco and R. Tycko, *Biochemistry,* **2007**, *46*, 3586.

17 L. Chen, R. A. Olsen, D. W. Elliott, J. M. Boettcher, D. H. Zhou, C. M. Rienstra and L. J. Mueller, *J. Am. Chem. Soc.,* **2006**, *128*, 9992.

18 I. Marcotte, J. D. van Beek and B. H. Meier, *Macromolecules,* **2007**, *40*, 1995.

19 H. J. Kim, S. C. Howell, W. D. Van Horn, Y. H. Jeon and C. R. Sanders, *Prog. Nucl. Magn. Reson. Spectrosc.,* **2009**, *55*, 335.

20 A. A. Arnold and I. Marcotte, *Concepts Magn. Reson. A,* **2009**, *24A*, 24.

21 J. M. Aramini and H. J. Vogel, *Biochem. Cell Biol.,* **1998**, *76*, 210.

22 A. S. Lipton, C. Bergquist, G. Parkin and P. D. Ellis, *J. Am. Chem. Soc.,* **2003**, *125*, 3768.

23 A. S. Lipton, R. W. Heck and P. D. Ellis, *J. Am. Chem. Soc.,* **2004**, *126*, 4735.

24 A. S. Lipton, T. A. Wright, M. K. Bowman, D. L. Reger and P. D. Ellis, *J. Am. Chem. Soc.,* **2002**, *124*, 5850.

25 A. S. Lipton, G. W. Buchko, J. A. Sears, M. A. Kennedy and P. D. Ellis, *J. Am. Chem. Soc.,* **2001**, *123*, 992.

26 W. Huang, L. Todaro, G. P. A. Yap, R. Beer, L. C. Francesconi and T. Polenova, *J. Am. Chem. Soc.,* **2004**, *126*, 11564.

27 N. Pooransingh, E. Pomerantseva, M. Ebelm, S. Janzen, D. Rehder and T. Polenova, *Inorg. Chem.,* **2003**, *42*, 1256.

28 N. Pooransingh-Margolis, R. Renirie, Z. Hasan, R. Wever, S. J. Vega and T. Polenova, *J. Am. Chem. Soc.,* **2006**, *128*, 5190.

29 D. L. Bryce, S. Adiga, E. K. Elliot and G. W. Gokel, *J. Phys. Chem. A,* **2006**, *110*, 13568.

30 P. K. Lee, R. P. Chapman, L. Zhang, J. Hu, L. J. Barbour, E. K. Elliot, G. W. Gokel and D. L. Bryce, *J. Phys. Chem. A,* **2007**, *111*, 12859.

31 G. Wu, A. Wong, Z. Gan and J. T. Davis, *J. Am. Chem. Soc.,* **2003**, *125*, 7182.

32 S. S. Kidambi, D. -K. Lee and A. Ramamoorthy, *Inorg. Chem.,* **2003**, *42*, 3142.

33 M. Kaupp, M. Bühl and V. G. Malkin, Eds., *Calculation of NMR and EPR Parameters.* Wiley-VCH, Weinheim, 2004.

34 D. L. Bryce and G. D. Sward, *Magn. Reson. Chem.,* **2006**, *44*, 409.

35 R. P. Chapman, C. M. Widdifield and D. L. Bryce, *Prog. Nucl. Magn. Reson. Spectrosc.,* **2009**, *55*, 215.

36 C. M. Widdifield, R. P. Chapman and D. L. Bryce, *Annu. Rep. Nucl. Magn. Reson. Spectrosc.,* **2009**, *66*, 195.

37 D. L. Bryce and G. D. Sward, *J. Phys. Chem. B.,* **2006**, *110*, 26461.

38 D. L. Bryce, G. D. Sward and S. Adiga, *J. Am. Chem. Soc.,* **2006**, *128*, 2121.

39 D. L. Bryce, M. Gee and R. E. Wasylishen, *J. Phys. Chem. A,* **2001**, *105*, 10413.

40 C. Gervais, R. Dupree, K. J. Pike, C. Bonhomme, M. Profeta, C. J. Pickard and F. Mauri, *J. Phys. Chem. A,* **2005**, *109*, 6960.

41 Y. Zhang, S. Mukherjee and E. Oldfield, *J. Am. Chem. Soc.,* **2005**, *127*, 2370.

42 D. L. Bryce and E. B. Bultz, *Chem. Eur. J.,* **2007**, *13*, 4786.

43 K. Bradenburg, *Diamond,* version 3.0e, Crystal Impact GbR, Bonn, Germany, 1997–2005.

44 R. Blessing, *Acta Crystallogr., Sect. A: Cryst. Phys., Diffr., Theor. Gen. Crystallogr.,* **1995**, *51*, 33.

45 G. M. Sheldrick, SHELXTL; Bruker AXS: Madison, Wisconsin, USA, 2001.

46 H. Y. Carr and E. M. Purcell, *Phys. Rev.,* **1954**, *94*, 630.

47 S. Meiboom and D. Gill, *Rev. Sci. Instrum.,* **1958**, *29*, 688.

48 J. T. Cheng and P. D. Ellis, *J. Phys. Chem.,* **1989**, *93*, 2549.

49 F. H. Larsen, H. J. Jakobsen, P. D. Ellis and N. C. Nielsen, *J. Phys. Chem. A,* **1997**, *101*, 8597.

50 K. Eichele and R. E. Wasylishen, WSolids Simulation Software, 2001, version 1.17.30.

51 D. W. Alderman, M. S. Solum and D. M. Grant, *J. Chem. Phys.,* **1986**, *84*, 3717.

52 M. Bak, J. T. Rasmussen and N. C. Nielsen, *J. Magn. Reson.,* **2000**, *147*, 296.

53 Downloaded from http://bionmr.chem.au.dk/download/simpson/crystal_files/ (accessed November 2007).

54 D. Massiot, F. Fayon, M. Capron, I. King, S. Le Calve, B. Alonso, J. -. Durand, B. Bujoli, Z. Gan and G. Hoatson, *Magn. Reson. Chem.,* **2002**, *40*, 70.

55 M. J. Frisch, G. Trucks, H. B. Schlegel, G. E. Scuseria, M. A. Robb, J. R. Cheeseman, J. Montgomery J.A., T. Vreven, K. N. Kudin, J. C. Burant, J. M. Millam, S. S. Iyengar, J. Tomasi, V. Barone, B. Mennucci, M. Cossi, G. Scalmani, N. Rega, G. A. Petersson, H. Nakatsuji, M. Hada, M. Ehara, K. Toyota, R. Fukuda, J. Hasegawa, M. Ishida, T. Nakajima, Y. Honda, O. Kitao, H. Nakai, M. Klene, X. Li, J. E. Knox, H. P. Hratchian, J. B. Cross, V. Bakken, C.

Adamno, J. Jaramillo, R. Gomperts, R. E. Stratmann, O. Yazyev, A. J. Austin, R. Cammi, C. Pomelli, J. W. Ochterski, P. Y. Ayala, K. Morokuma, G. A. Voth, P. Salvador, J. J. Dannenberg, V. G. Zakrzewski, S. Dapprich, A. D. Daniels, M. C. Strain, O. Farkas, D. K. Malick, A. D. Rabuck, K. Raghavachari, J. B. Foresman, J. V. Ortiz, Q. Cui, A. G. Baboul, S. Clifford, j. Cioslowski, B. B. Stefanov, G. Liu, A. Liashenko, P. Piskorz, I. Komaromi, R. L. Martin, D. J. Fox, T. Keith, M. A. Al-Laham, C. Y. Peng, A. Nanayakkara, M. Challacombe, P. M. W. Gill, B. Johnson, W. Chen, M. W. Wong, C. Gonzalez and J. A. Pople, *Revision C.02 Gaussian, Inc.*, Gaussian Inc.,Wallingford, CT, 2004.

56 B. Di Blasio, V. Pavone and C. Pedone, *Cryst. Struct. Commun.,* **1977**, *6*, 745.

57 B. Di Blasio, V. Pavone and C. Pedone, *Cryst. Struct. Commun.,* **1977**, *6*, 845.

58 H. Fuess, D. Hohlwein and S. A. Mason, *Acta Crystallogr., Sect. B: Struct. Sci.,* **1977**, *33*, 654.

59 J. Donohue and A. Caron, *Acta Crystallogr.,* **1964**, *17*, 1178.

60 S. Adiga, D. Aebi and D. L. Bryce, *Can. J. Chem.,* **2007**, *85*, 496.

61 M. D. Segall, P. J. D. Lindan, M. J. Probert, C. J. Pickard, P. J. Hasnip, S. J. Clark and M. C. Payne, *J. Phys.: Condens. Matter,* **2002**, *14*, 2717.

62 S. J. Clark, M. D. Segall, C. J. Pickard, P. J. Hasnip, M. I. J. Probert, K. Refson and M. C. Payne, *Z. Kristallogr.,* **2005**, *220*, 567.

63 A. R. Al-Karaghouli and T. F. Koetzle, *Acta Crystallogr., Sect. B: Struct. Sci.,* **1975**, *31*, 2461.

64 T. F. Koetzle, L. Golic, M. S. Lehmann, J. J. Verbist and W. C. Hamilton, *J. Chem. Phys.,* **1974**, *60*, 4690.

65 M. N. Frey, T. F. Koetzle, M. S. Lehmann and W. C. Hamilton, *J. Chem. Phys.,* **1973**, *58*, 2547.

66 A. Sequeira, H. Rajagopal and R. Chidambaram, *Acta Crystallogr., Sect. B: Struct. Sci.,* **1972**, *28*, 2514.

67 R. R. Bugayong, A. Sequeira and R. Chidambaram, *Acta Crystallogr., Sect. B: Struct. Sci.,* **1972**, *28*, 3214.

68 A. R. Al-Karaghouli, F. E. Cole, M. S. Lehmann, C. F. Miskell, J. J. Verbist and T. F. Koetzle, *J. Chem. Phys.,* **1975**, *63*, 1360.

69 J. Dow, L. H. Jensen, S. K. Mazumdar, R. Srinivasan and G. N. Ramachandran, *Acta Crystallogr., Sect. B: Struct. Sci.,* **1970**, *26*, 1662.

70 Y. Mitsui, M. Tsuboi and Y. Iitaka, *Acta Crystallogr., Sect. B: Struct. Sci.,* **1969**, *25*, 2182.

71 T. Takigawa, T. Ashida, Y. Sasada and M. Kakudo, *Bull. Chem. Soc. Jpn.,* **1966**, *39*, 2369.

72 J. Griffin, **Private Communication**, 2009.

73 R. R. Ayyar, *Z. Kristallogr.,* **1968**, *126*, 227.

74 H. Koller, G. Engelhardt, A. P. M. Kentgens and J. Sauer, *J. Phys. Chem.,* **1994**, *98*, 1544.

75 T. H. Walter and E. Oldfield, *J. Phys. Chem.,* **1989**, *93*, 6744.

76 H. Koller, E. L. Meijer and R. A. van Santen, *Solid State Nucl. Magn. Reson.,* **1997**, *9*, 165.

Chapter 4

Solid-State $^{35/37}$Cl NMR and GIPAW-DFT Study of a Chloride Ion Receptor

4.1 Introduction and Objectives

4.1.1 Introduction

Calix[*n*]arene rings are metacyclophanes made up of aromatic units bridged with methylene links. These units have a hydrophobic wide rim and a hydrophilic narrow rim which encompass a cavity, making them ideal for encapsulating smaller guest molecules.[1,2] The rings can be functionalized to tune a variety of physical properties, such as their hydrophobicity, solubility, reactivity, etc. For example, conversion of calixarenes to esters greatly increases their solubility in organic solvents while sulfonation increases water solubility.[2] Calix[*n*]arene rings are known for their high melting points, generally around or over 250 ºC, which was one of the initial features that drew interest to this family of compounds.[2] Given their tunability and thermal stability, calix[*n*]arene rings have been used for a wide range of applications including field effect transistors, biomimetic catalysts, non-linear optic materials, potential drug carriers, and ion separators.[1-3] Calix[4]arenes are the most prevalent member of the calixarene family, with a great number of different functionalized rings having been produced. In the anion complexation arena compounds containing pyrrole have been shown to be effective anion receptors.[4,5] Simple and easy-to-make macrocyclic polypyrroles such as *meso*-octamethylcalix[4]pyrrole, a known anion receptor and shown in scheme 1, have been known since 1886,[6] but their anion complexation properties, only reported in 1996, together with salt binding properties, continue to be explored.[7-14]

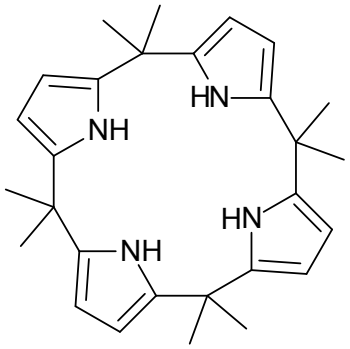

Scheme 4.1. Structure of meso-octamethylcalix[4]pyrrole

This compound can be regarded as a pyrrolic analogue of a calixarene and has been found to adopt a cone conformation when complexed with a halide ion (including Cl^-) in the solid state.[8-11,14] The presence of an 'NMR signature' for cases where a halide is encapsulated within an anion receptor would be useful for identification of this interaction.

As discussed in Chapter 1, the majority of chlorine SSNMR spectra of noncubic materials are dominated by the QI, due to the moderately high *Q* values of both isotopes of chlorine. Even in cases where the CSA can be easily observed, the spectrum obtained usually displays a typical second order quadrupolar lineshape, as was the case for all of the compounds studied in Chapter 3 in which the $|C_Q(^{35}Cl)|$ values ranged from 3.92-7.1 MHz. As the effects of CSA *increase* with the magnetic field while those of the QI decrease, the availability of high fields suggests that it is possible to obtain chlorine SSNMR spectra which display a CSA dominated lineshape. Presented in this chapter is a $^{35/37}Cl$ SSNMR and computational study of the chloride ion receptor, 1-butyl-3-methylimidazolium chloride complex of *meso*-octamethylcalix[4]pyrrole (**1**).

4.1.2 Objectives

A chlorine SSNMR study on **1** was undertaken in order to characterize the chemical environment of a chloride ion encapsulated in an anion receptor, and determine if/how it differed from other organic chlorides; in addition complementary GIPAW-DFT calculations were used to determine the *exact* solvate composition of the compound analyzed.

4.2.1 Sample Preparation

The 1-butyl-3-methylimidazolium chloride complex of *meso*-octamethylcalix[4]pyrrole (**1**) was prepared by Jennifer Hiscock from the research group of Prof. Philip Gale at the University of South Hampton, using the procedure described in reference 7. The structure consists of a chloride ion bound to a *meso*-octamethylcalix[4]pyrrole ring and a 1-butyl-3-methylimidazolium group. The crystal structure collected also includes one dichloromethane and two water solvent molecules. Phase purity of the sample was confirmed by ^{13}C CP/MAS NMR collected with a spinning frequency of 8 kHz at 9.4 T. This spectrum is shown below in Figure 4.1.

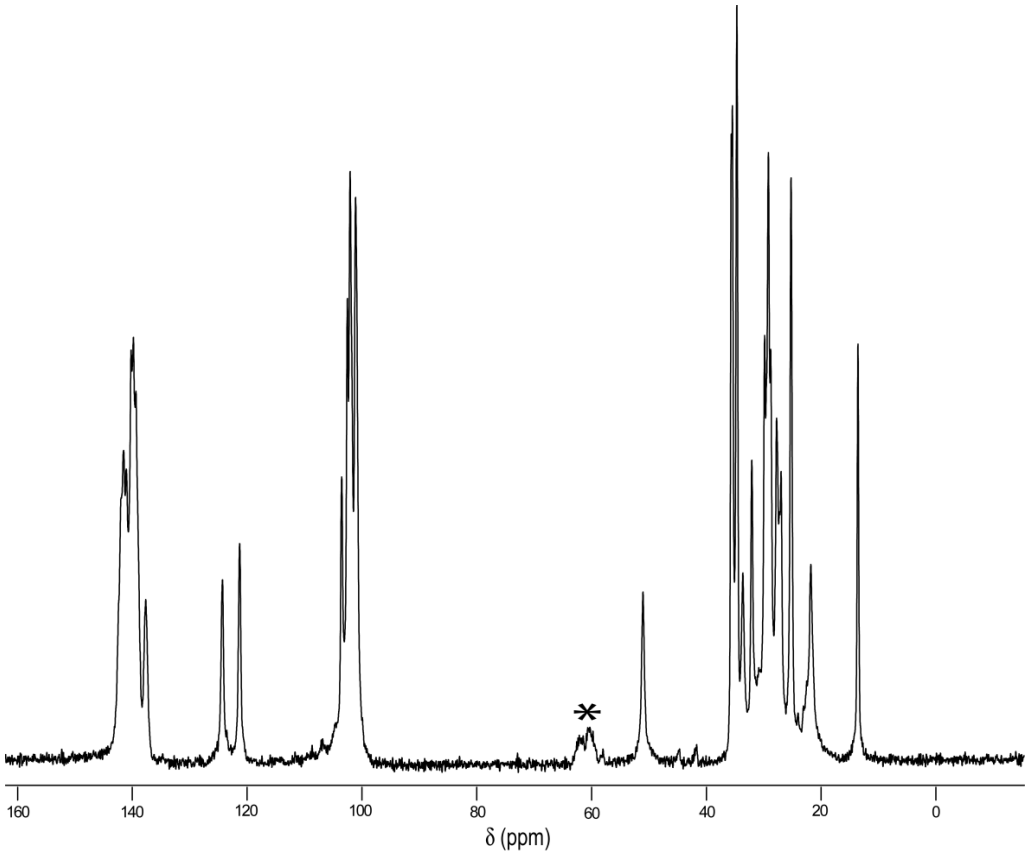

Figure 4.1. Experimental solid-state ^{13}C cross polarization magic-angle spinning spectrum of **1** at 9.4 T. The asterisk indicates a spinning sideband.

The sample was also analyzed using thermogravimetric analysis (TGA) using a TA instruments 2960 SDT V3.0F unit in the temperature range of 25-593 ºC, the outcome of which will be addressed in the Results and Discussion section. The TGA was collected by Dr. Sadok Letaief at the Thermal Analysis Facility at the University of Ottawa.

4.2.2 NMR Spectroscopy

4.2.2.1 Experiments Carried out at 9.4 T

Chlorine-35/37 SSNMR experiments were carried out on a 400 MHz (B_0 = 9.4 T) Bruker Avance III spectrometer at the University of Ottawa. A 4 mm Bruker HX MAS probe, tuned to 39.2 MHz (^{35}Cl) or 32.6 MHz (^{37}Cl) was used. Samples were ground into fine powders and packed into 4 mm o.d. zirconia rotors. Experimental setup and pulse calibrations were performed using solid NaCl or NH_4Cl, and all $^{35/37}$Cl NMR spectra were referenced to the $^{35/37}$Cl MAS centreband of solid NaCl at 0 ppm. The 'solid' $\pi/2$ chlorine pulse was found by halving the non-selective $\pi/2$ pulse measured using solid NaCl or NH_4Cl, and was typically 2.3 μs and 2.4 μs for ^{35}Cl and ^{37}Cl, respectively. Recycle delays were 2 s. All spectra collected under stationary conditions used the $\pi/2 - \tau - \pi/2 - \tau$ - ACQ echo sequence[15-17], while MAS experiments used only a single pulse. Proton decoupling was applied during all experiments. To offset the effects of sample heating due to fast spinning during MAS experiments, sample cooling to ~283 K was achieved using liquid nitrogen boil-off.

4.2.2.2 Experiments Carried out at 21.1 T

Chlorine-35/37 SSNMR experiments were also performed on a 900 MHz (B_0 = 21.1 T) Bruker Avance II spectrometer at the National Ultrahigh-Field NMR Facility for Solids in Ottawa. A 4 mm Bruker DVT MAS HX probe tuned to 88.2 MHz (^{35}Cl) or 73.4 MHz (^{37}Cl) was used for all experiments. Experimental setup, pulse calibration and referencing were done using solid NaCl, as above. The pulse sequences used were identical to those used at 9.4 T, again with proton decoupling. The 'solid' $\pi/2$ ^{35}Cl pulse was found to be 3.4 μs and a recycle delay of 2 s was used for all acquisitions. The same parameters were used for ^{37}Cl. All experiments, both static and MAS, were conducted with cooling to ~ 283 K.

4.2.4 Data Processing and Simulations

All data processing and simulations were done with the same method as described in Chapter 3. Simulations for **1** assumed a single chlorine site, consistent with the crystal structure.

4.2.5 Calculations using the GIPAW-DFT Level of Theory

The same method as described in Chapter 3 was used to prepare and analyze the GIPAW-DFT calculations discussed in this Chapter. The planewave energy cutoffs and number of k-points used are included in Appendix 3. For the models based on the available crystal structure of **1**, the highest energy cutoff which allowed for the calculations to complete was used as the large cell volume of both anion receptors limited this value. Calculations of the chlorine MS and EFG tensors used the atomic coordinates and unit cell parameters from the X-ray structure found in reference 7 for **1.**

4.3 Results and Discussion

4.3.1 Experimental Results

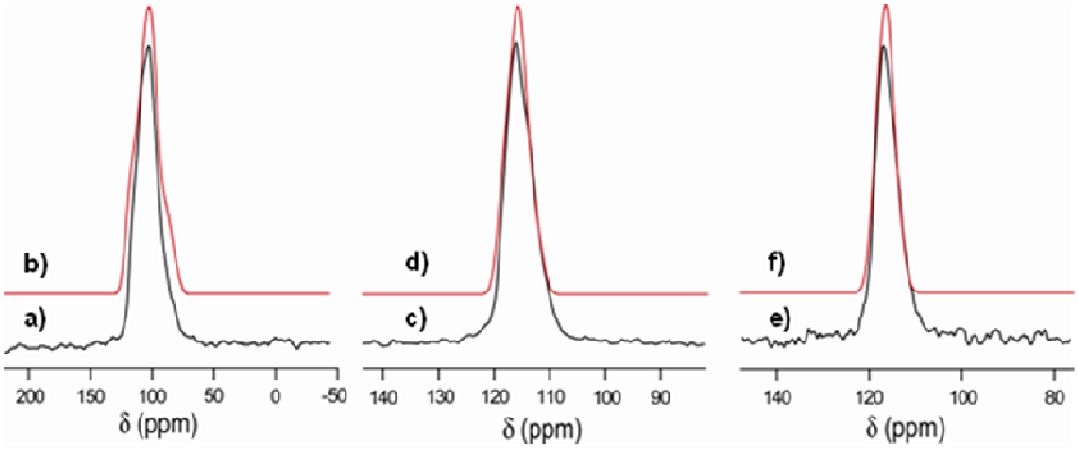

Figure 4.2. Experimental (a, c, e) and simulated (b, d, f) solid-state ^{35}Cl (left and middle) and ^{37}Cl (right) magic-angle spinning NMR spectra of **1** at 9.4 T (left) and 21.1 T (middle and right).

The three MAS NMR spectra collected, and the corresponding spectral simulations are presented in Figure 4.2. The EFG tensor parameters and isotropic chemical shift were first extracted from the MAS NMR spectra, as CSA is averaged out by the fast rotation of the sample. The EFG and CS tensor parameters for **1** are shown in Table 4.1.

Table 4.1. Chlorine EFG and CS tensor parameters for **1**

Compound	$C_Q(^{35}Cl)$ / MHz[a]	η_Q	δ_{iso} / ppm[b]	Ω / ppm	κ	α, β, γ/°
1	1.0(1)	0.7(1)	120(10)	50(5)	0.4(4)	15(30), 27(20), 60(15)

[a]Chlorine-37 quadrupolar coupling constant was identical to $C_Q(^{35}Cl)$ x $Q(^{37}Cl)/Q(^{35}Cl)$ = $C_Q(^{35}Cl)$ x 0.788. [b]Chlorine-35 chemical shift with respect to solid sodium chloride.

It is evident from the spectra that the chlorine QI in **1** is very small, as the MAS NMR line shapes are relatively featureless. The linewidth at half height is ~ 500 Hz for the chlorine-35 spectra collected at 21.1 T. The collection of the spectra at two fields and for two isotopes (^{35}Cl at 9.4 T and 21.1 T, and ^{37}Cl at 21.1 T) was useful to ensure the accuracy of the fits as the same parameters were used to fit all three spectra (with the value of $C_Q(^{35}Cl)$ scaled by $Q(^{37}Cl)/Q(^{35}Cl)$ = 0.788 to give the value of $C_Q(^{37}Cl)$). The ^{35}Cl quadrupolar coupling constant of 1.0 MHz is small in magnitude compared to most other organic chloride systems which have been studied to date with chlorine SSNMR.[18,19] This small $|C_Q(^{35}Cl)|$ is consistent with lower end of those observed in the study of Honda on a series of *n*-alkylammonium chlorides, *n*-$C_xH_{(2x+1)}NH_3Cl$ (both deuterated and non-deuterated samples), in which the coupling constants observed were all between 1.0 and 1.5 MHz.[20] In *n*-$C_xH_{(2x+1)}NH_3Cl$, the chlorine lies on a high symmetry (C_4) axis which is not the case with **1**. In the case of the amino acid hydrochlorides, another comparable series of organic chlorides, the magnitude of $C_Q(^{35}Cl)$ ranges from 2.035 MHz in DL-arginine

hydrochloride monohydrate to 7.1 MHz in L-aspartic acid hydrochloride, demonstrating that the chloride ion in **1** sits at a site with a significantly smaller EFG compared to those systems.[19,21-23] This observation is consistent with the structure of the *meso*-octamethylcalix[4] pyrrole ring and the placement of the chloride ion within it. The chloride rests slightly above and close to the center of the *meso*-octamethylcalix[4] pyrrole ring (in a cone confirmation), near equidistant from the four amide groups on the arene ring that lie below. In addition, if we consider that the calix ring is lying directly "below" the chloride ion, then the 1-butyl-3-methyl imidazolium moiety lies directly above the chloride ion. Thus, the chloride ion interacts with hydrogens on all sides (six in total), which is more than most of the amino acid hydrochlorides.[24] The quadrupolar asymmetry parameter (η_Q) determined from the fits has a value of 0.7, showing that the EFG tensor is non axial. The accuracy of the parameters extracted from the fits was also confirmed with a nutation analysis,[25,26] which gave results that were consistent with the reported parameters and are below in Figure 4.3.

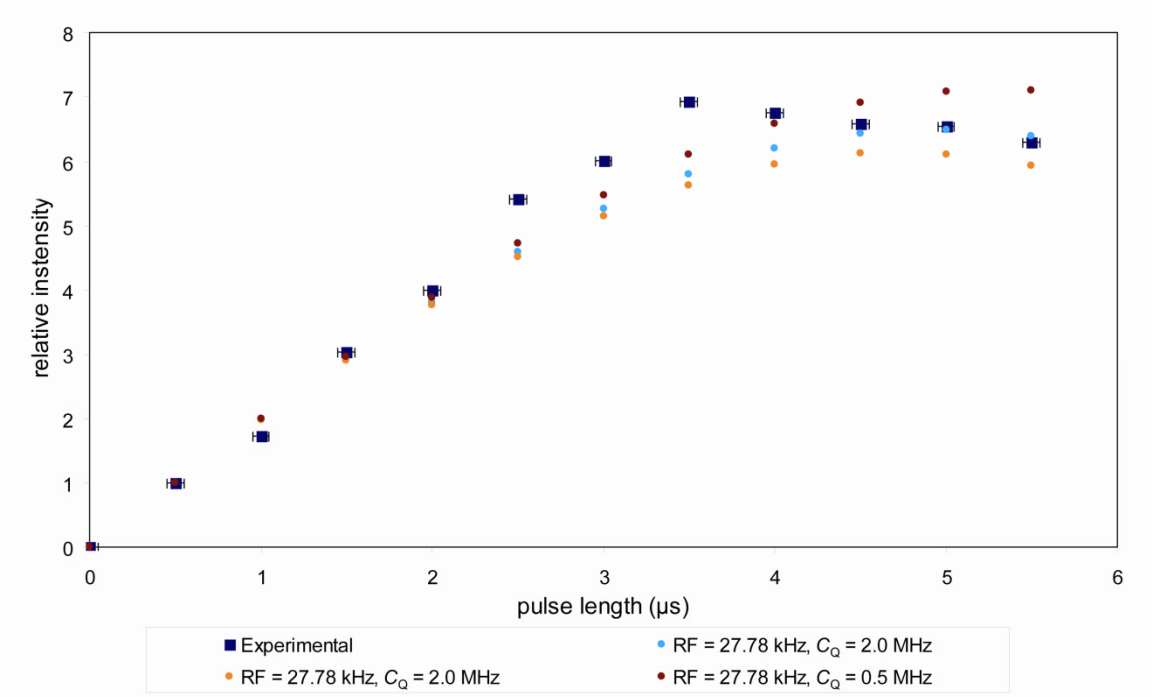

Figure 4.3. Experimental (blue squares) and computed intensities (all others) of the central transition of **1** as a function of pulse length. RF strength was determined on a sample of dilute aqueous NaCl. Calculated intensities use an η_Q value fixed at 0.7.

Shown in Figure 4.4 a-f, and g-l, are experimental and simulated ^{35}Cl NMR spectra of **1** collected at 9.4 T and 21.1 T under stationary conditions. Figure 4.4 m-n presents the ^{37}Cl experimental and simulated spectra at 21.1 T. As the EFG tensor parameters were known from the MAS experiments, these static spectra were fit to extract the CS tensor parameters (Table 4.1). The collection of spectra of both isotopes at two fields was essential to ensure the accuracy the extracted parameters. In addition, the small magnitude of $C_Q(^{35}Cl)$ resulted in the simulations being highly sensitive to slight changes in the magnitudes of the CS tensor parameters, giving further confidence in the values listed. Although small, the measured CS tensor span, 50 ppm, is within the range observed for the amino acid hydrochlorides, 26 to 129

ppm.[21-23] In addition, the chlorine chemical shift, 120 ppm, is at the high end limit of those observed for the amino acid hydrochlorides (37 – 120 ppm).[21-23] The shift is *within* the range observed for the alkaline earth chloride hydrates, but lower than the range observed for noncubic metal chlorides (eg. $AlCl_3$).[18, 19] The results demonstrate clearly that the EFG and CS tensors reflect different aspects of the chloride ion environment; while the EFG about chlorine in **1** is relatively small compared to other organic hydrochloride systems, the CS tensor components and CS tensor span are not. This result suggests that a large chlorine chemical shift may be indicative of binding with an anion receptor, such as a calix ring.

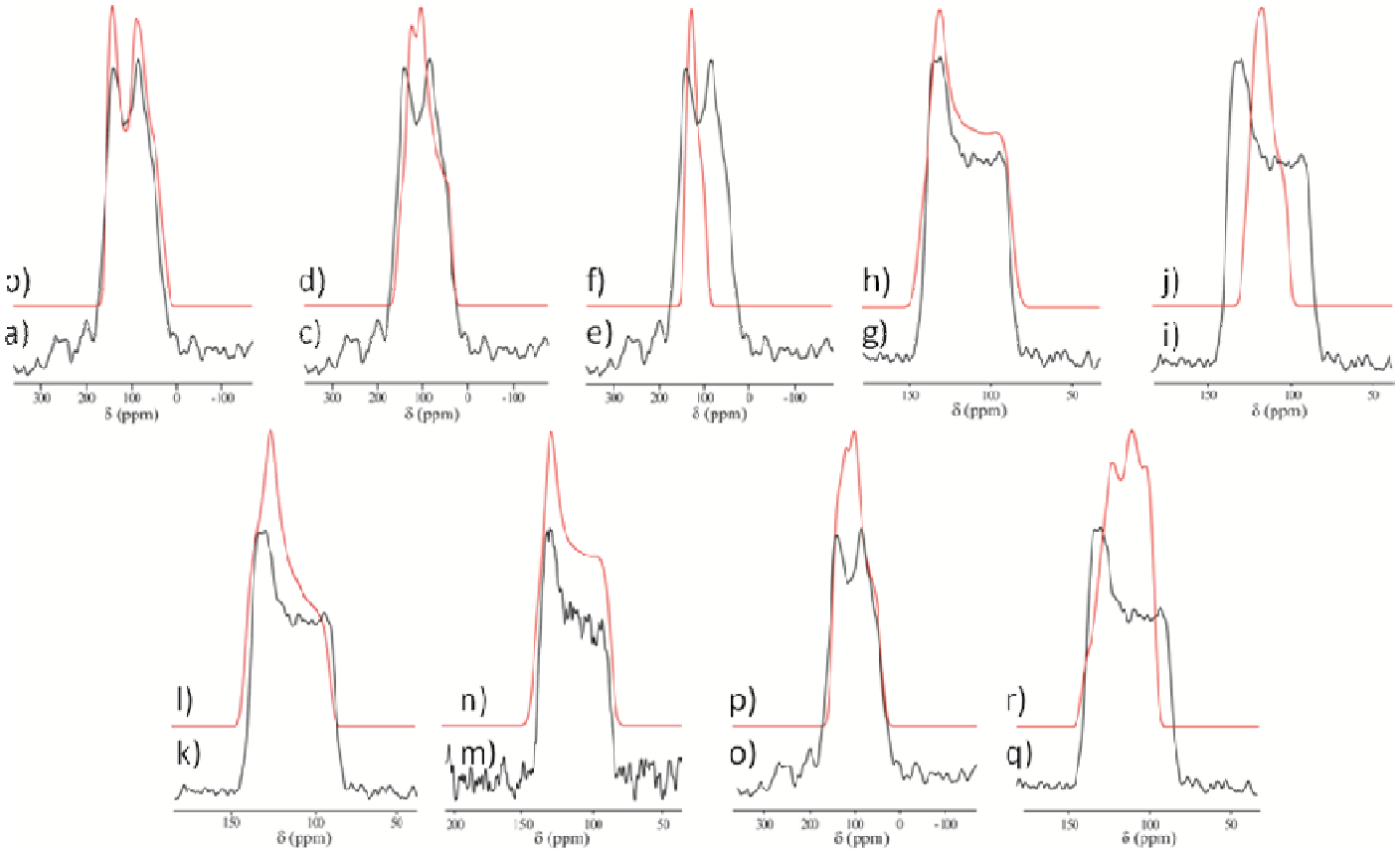

Figure 4.4. Experimental (a, c, e) and simulated (b, d, f) solid-state chlorine-35 NMR spectra of a static sample of **1** at 9.4 T. The best-fit simulation is shown in b. The simulation assuming no CSA is shown in d. The simulation assuming no QI is shown in f. Experimental (g, i, k) and simulated (h, j, l) solid-state chlorine-35 NMR spectra of a stationary sample of **1** at 21.1 T. The best-fit simulation is shown in h. The simulation assuming no CSA is shown in j. The simulation assuming no QI is shown in l. Experimental (m) and simulated (n) solid-state ^{37}Cl NMR spectra of a stationary sample of **1** at 21.1 T. The best-fit simulation is shown in n. Experimental (o, q) and simulated (p, r) solid-state chlorine-35 NMR spectra of **1** at 9.4 T (o, p) and 21.1 T (q, r). These simulations assume a β angle of 90º.

The experimental spectrum collected at 9.4 T under static conditions (Figure 4.4a), has a line shape which approximately resembles that due solely to a second-order quadrupolar interaction demonstrating that, at this field, the QI does dominate the spectrum despite the small magnitude of that interaction (shown by simulations in Figure 4.4d and 4.4f). However, the effects of CSA are clearly observable as shown by the simulated spectrum in Figure 4.4d, which assumes no CSA and is clearly not an ideal fit to the experimental spectrum. The QI is not the dominant interaction at 21.1 T (Figure 4.4 g-l), as both the experimental and best-fit simulation spectra have lineshapes that resemble the lineshape observed for static spin-1/2 powdered samples, in which CSA dictates the lineshape. This is demonstrated in Figures 4.4j and 4.4l, in which the simulation assuming no QI (l) is quite similar to the experimental lineshape, while that which assumes no CSA (j) is a very poor fit. This type of CSA-dominated NMR spectrum is not typical for chlorine, due to its moderately high Q value, and is a clear demonstration of the power of high field instruments to enhance the effects of CSA while reducing the effects of the QI.

4.2.2 Calculated Results

As an X-ray crystal structure is available for **1**,[7] along with high quality SSNMR data, complementary GIPAW-DFT calculations were carried out. In addition, in order to assess the effects of slight changes to the chlorine environment on the NMR interaction tensors, five different models were used for calculations in which parts of the structure were removed to observe the effect that this would have. These models are shown in Figure 4.5.

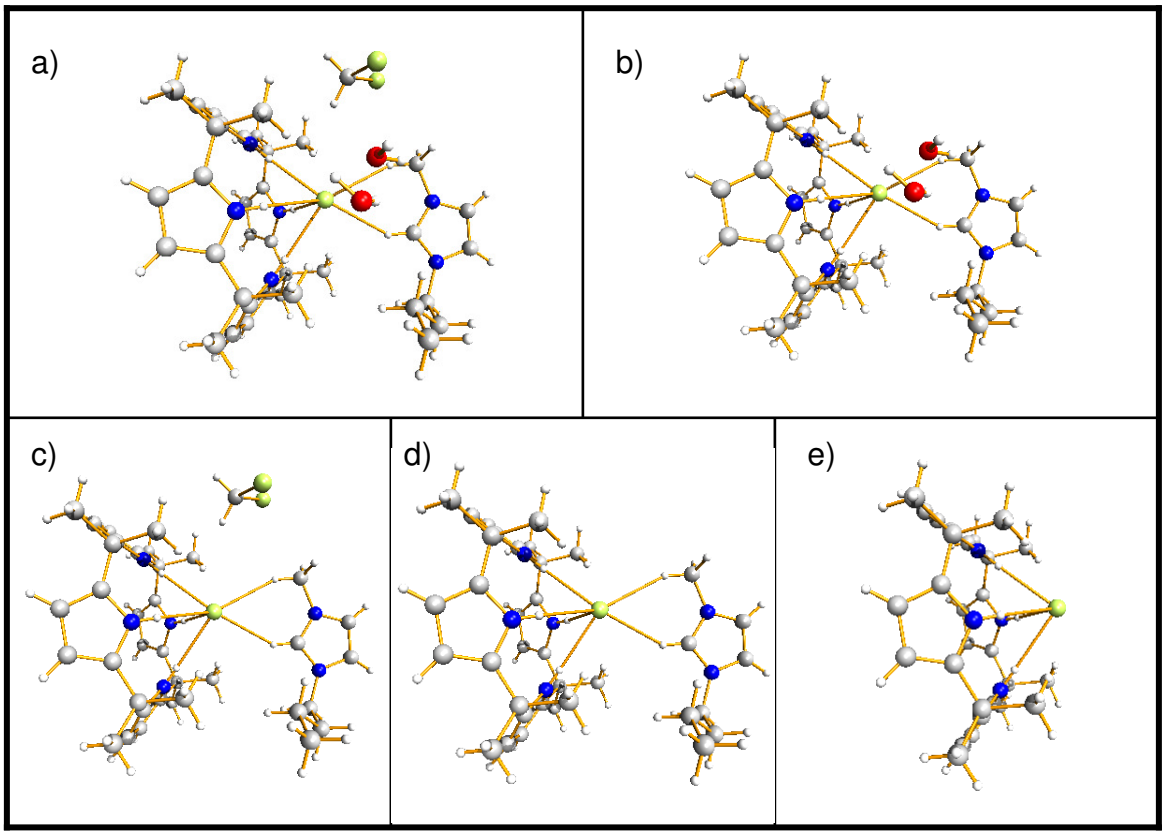

Figure 4.5. Models, based on the crystal structure of **1,** used for GIPAW-DFT calculations of chlorine EFG and MS tensor parameters. Model a): **1**·CH_2Cl_2·$2H_2O$ Model b): **1**·$2H_2O$ Model c): **1**·CH_2Cl_2. Model d): **1** Model e): *meso*-octamethylcalix[4]pyrrole chloride only.

All models employ the full X-ray crystal structure as a starting point: model a) consists of the full structure; in model b) the dichloromethane solvate is removed; model c) has only dichloromethane solvent and no waters of hydration; model d) has no solvent molecules and model e) has only the *meso*-octamethylcalix[4] pyrrole ring and the chloride ion. The results of the GIPAW-DFT calculations are shown in Table 4.2.

Table 4.2. GIPAW-DFT calculated chlorine EFG and MS tensor parameters for various *meso*-octamethylcalix[4] pyrrole 1-butyl-3-methyl imidazolium chloride models

Model[a]	$\lvert C_Q(^{35}Cl)\rvert$ / MHz	η_Q	δ_{iso} / ppm[b]	Ω / ppm	κ	α, β, γ/°
a	0.63	0.65	97.5	51	0.7	108, 64, 70
b	1.41	0.30	98.4	51	0.7	131, 85, 24
c*	1.00	0.91	186	65	0.8	57, 66, 100
d*	1.35	0.60	188	69	0.7	73, 25, 65
e*	1.21	0.57	336	346	0.2	136, 35, 46

[a]Models shown in Figure 5. [b]To convert from calculated shielding constants to chemical shifts, a shift of 45.37 ppm was used (for the conversion from solid to aqueous NaCl chemical shift scales) in addition to the absolute shielding conversion found in Chapter 1.[27] *NMR calculation performed after the optimization of proton positions

Inspection of the results in Table 4.2 reveals some interesting differences between the calculated NMR parameters for the five models. For example, the presence of the dichloromethane solvent molecule (model a) and c)) results in lower values of $\lvert C_Q(^{35}Cl)\rvert$ while the presence of water solvent molecules (models a) and b)) results in a much lower chlorine chemical shift, relative to those other models with it. The span only changes notably when the water solvent is removed from the model structure (models c) and d)). The results of the calculations on model e), are quite interesting and further demonstrate an observation made on the basis of the experimental spectrum. Removal of the 1-butyl-3-methyl imidazolium group from **1** (in addition to the solvent molecules) results in a structure with only the chloride ion lying slightly above, and roughly in the center of the *meso*-octamethylcalix[4]pyrrole ring. This results in an absence of chlorine-hydrogen bonds above the chloride ion, opposite the calix ring. One may expect this structure to result in both a large value for the $\lvert C_Q(^{35}Cl)\rvert$ and the CS tensor span, but this is not what the calculations predict. While both the CS tensor span and chlorine chemical shift jump significantly to 346 ppm and 336 ppm, respectively, which are values much greater than

those observed in typical organic chloride systems, the value of $|C_Q(^{35}Cl)|$ does not rise significantly. In fact, the calculated value of 1.21 MHz is still lower than *all* the chlorine-35 quadrupolar coupling constants observed for the amino acid hydrochloride salts and the calculated value for both models b) and d). These results are consistent with the experimental observation that while the calix environment results in a fairly symmetrical EFG about the chlorine nucleus, the span of the CS tensor remains significant. The large Ω value and chemical shift value calculated for model e) demonstrate that the calix ring environment alone results in a significant amount of anisotropy of the CS tensor. This result suggests that other chloride containing calix[*n*]arene systems may also display measureable CSA, and relatively high chlorine chemical shift, even while the QI may be small.

Comparison of the experimental NMR parameters from Table 4.1, with those from model a) reveals a significant discrepancy. Specifically, the GIPAW-DFT calculations predicted a β value close to 90º, which indicates non coincidence of the largest components of EFG and CS tensors. This result was *not* observed experimentally, as coincidence would result in a very different lineshape, as shown by Figure 4.4 o-r, which shows the poor agreement of the fits when a β angle of 90º is used. Only model d) has a GIPAW-DFT calculated β value that is consistent with the experimental value, and the lineshape observed. This observation suggests that the solvent molecules were not part of the structure as a result of the grinding of the sample prior to NMR experiments. This is not surprising as the water and dichloromethane solvent molecules are simply solvates which were included in the structure during crystallization. Further confirmation was provided by a TGA analysis, shown in Figure 4.6 which showed, definitively, that

there were no solvent molecules in the sample of **1** that was analyzed with SSNMR as only a single mass loss temperature of ~ 265 ºC was observed. This value is consistent with the melting point of a calix[4]arene system, indicating that that the calix ring is intact. If water or dichloromethane were part of the structure, they would evaporate near their respective boiling points of 100 ºC and 40 ºC, resulting in multiple mass loss points in the TGA curve.

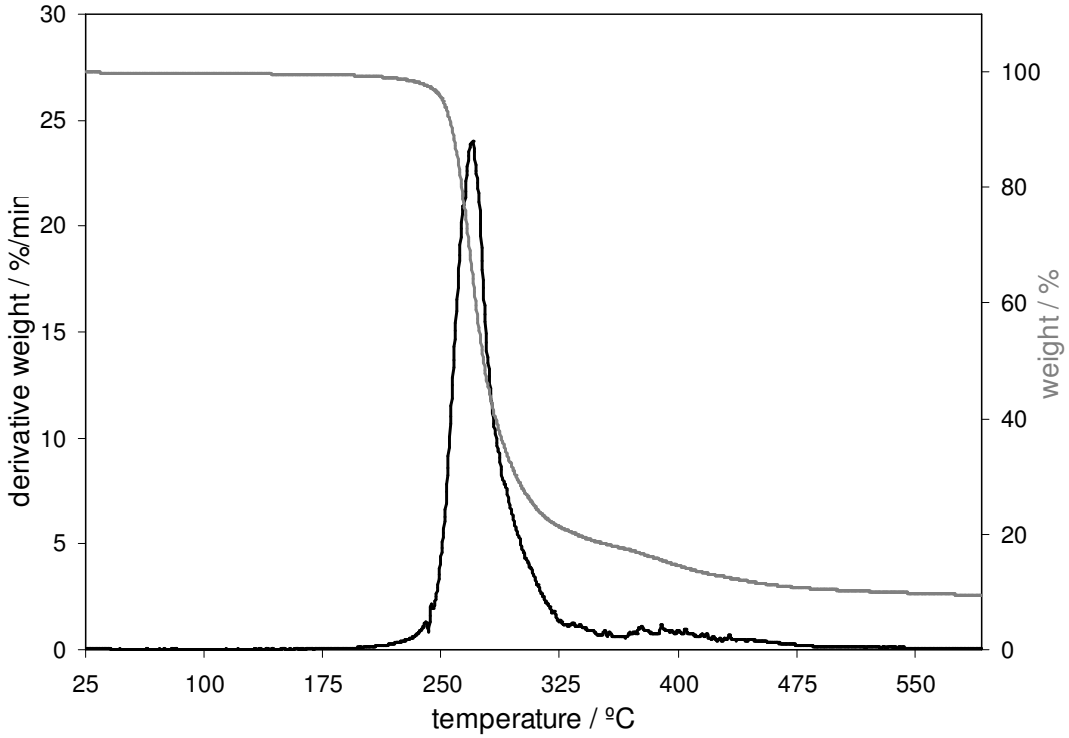

Figure 4.6. TGA (and derivative curve) of **1.**

In order to confirm the sample maintained similar packing (and therefore unit cell parameters) upon loss of solvent molecules, a powder X-ray diffraction pattern was collected. This pattern, along with a theoretical X-ray powder diffraction pattern produced using the Diamond 3.0 program,[28] is shown in Figure 4.7. The resulting pattern did not display all of the reflections of the parent compound, but was consistent with the

cell parameters of the parent compound (**1**·CH_2Cl_2·$2H_2O$) demonstrating the structure likely does not change significantly.

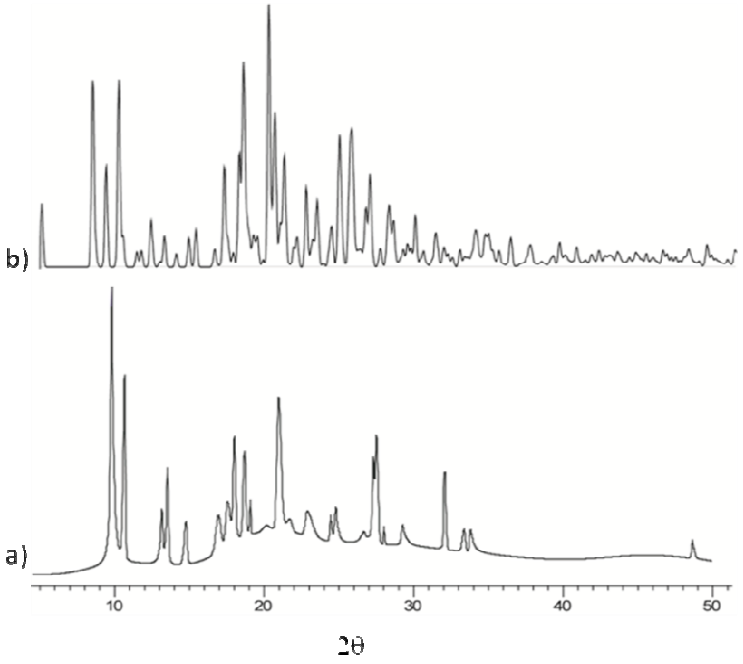

Figure 4.7. Experimental (a) powder X-ray diffraction pattern of (**1**) and calculated (b) pattern based on the crystal structure of (**1**·CH_2Cl_2·$2H_2O$). The pattern in a) is consistent with the cell parameters of **1**·CH_2Cl_2·$2H_2O$**.**

Comparison of the SSNMR tensor parameters calculated for model d) to the experimental values listed in Table 4.1 shows relatively good agreement but does reveal an overestimation of the value of $|C_Q(^{35}Cl)|$, CS tensor span and chlorine chemical shift. This result is not surprising, given the observations noted in Chapter 3, specifically Section 3.3.3.3.

In order to further confirm that model d) is a correct model of the chlorine environment in **1**, a direct comparison was made between the results obtained for that model and those observed for the amino acid hydrochlorides in Chapter 3. In terms of the $|C_Q(^{35}Cl)|$, the GIPAW-DFT results observed for **1,** where the calculated value of $|C_Q(^{35}Cl)|$ for model d) was 1.35 MHz, a 35 % overestimation of the experimental value (1.0 MHz), are totally consistent with the observations in Chapter 3. In fact, as shown in Figure 4.8, inclusion of the data point for **1** (1.0 MHz, 1.35 MHz) on Figure 3.14 from Chapter 3 shows that the agreement between experiment and theory for **1** is completely analogous to the agreement obtained for most of the amino acid hydrochlorides. These results further confirm that model d) is representative of the compound analyzed experimentally, as the predicted $|C_Q(^{35}Cl)|$ for the hydrated and solvated model a) is actually *underestimated*, and therefore inconsistent with the correlations established between experimental and computed $|C_Q(^{35}Cl)|$ values.

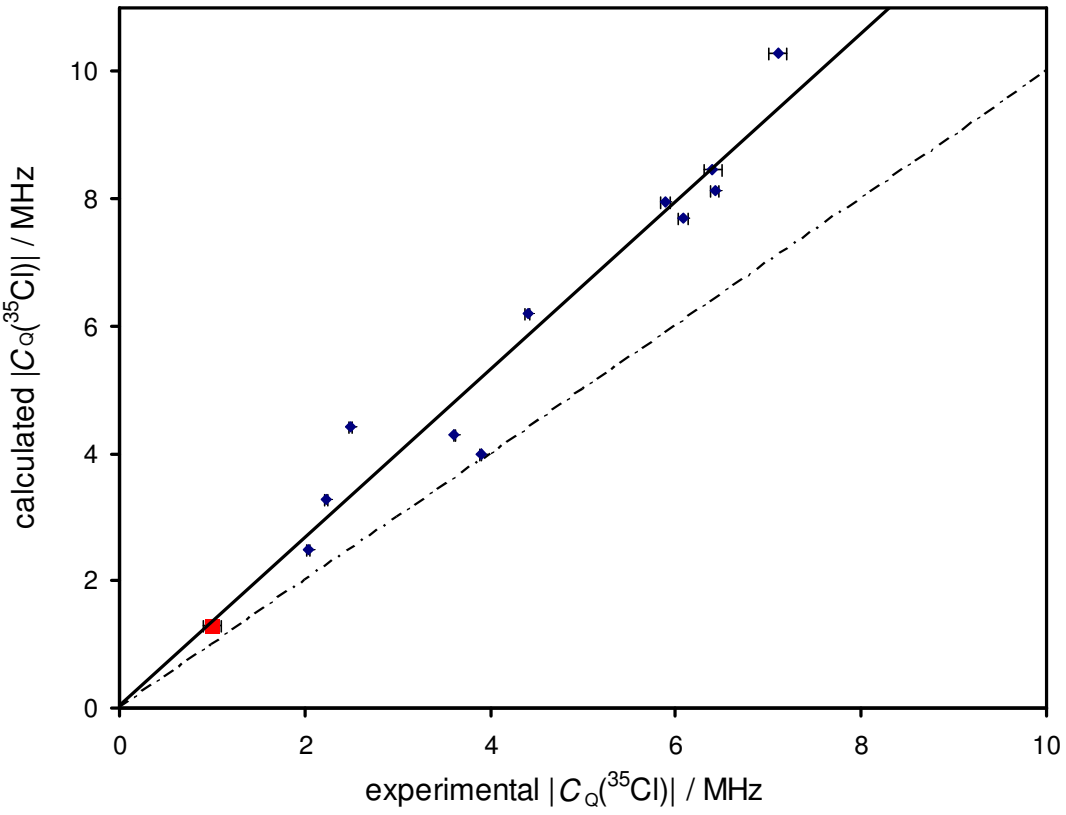

Figure 4.8. Comparison between the experimentally determined chlorine-35 quadrupolar coupling constant, on the *x*-axis and the GIPAW-DFT calculated values, on the *y*-axis, for the amino acid hydrochlorides, with the exception of four outliers (blue diamonds), as shown in Chapter 3. Included on the curve is the data point for **1** (red square). The dotted line represents the equation $y = x$. See Figure 3.14 in Chapter 3 for additional details and references.

Similarly, the GIPAW-DFT results for the Ω observed for **1** are in agreement with the trends observed in Chapter 3. Specifically, examination of the results for model d) shows that the experimental value of 50 ppm was overestimated by 34 % and predicted to

be 69 ppm. Similar to the chlorine quadrupolar coupling constant, the data point for **1** using the calculation for model d) (50 ppm, 69 ppm) fits the line of best fit for both Figure 3.15 and 3.16 from Chapter 3, demonstrating the agreement with those calculations, shown in Figure 4.9 and 4.10.

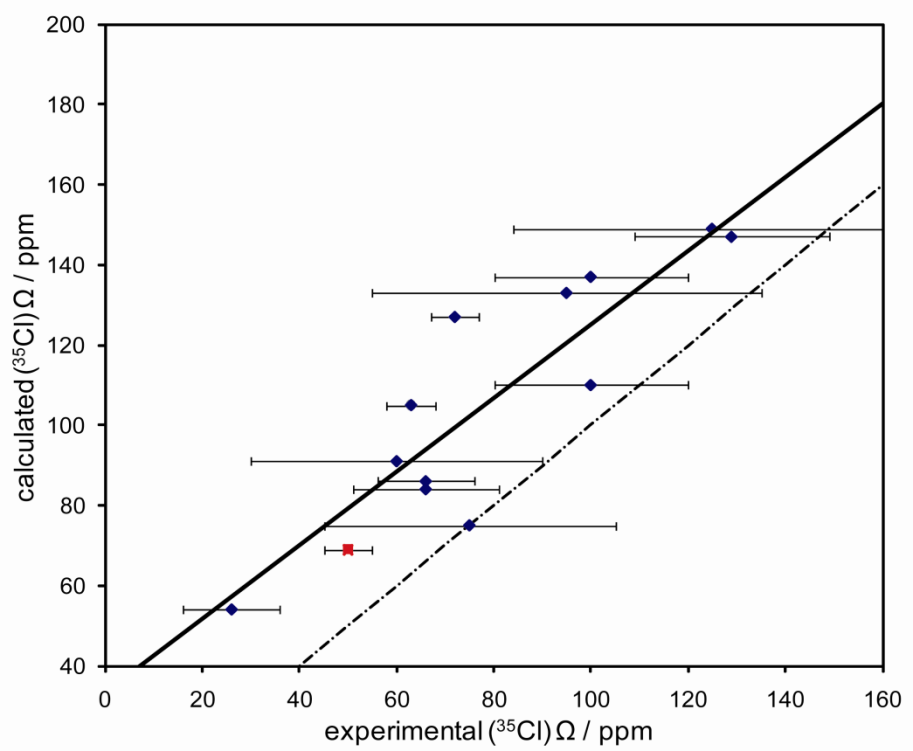

Figure 4.9. Comparison between the experimentally determined chlorine CS tensor span, on the *x*-axis and the GIPAW-DFT calculated values, on the *y*-axis for all of the amino acid hydrochlorides for which experimental data are available (blue diamonds, with the exception of one outlier (not shown). The dotted line represents the equation $y = x$. Included on the curve is the data point for **1** (red square). See Figure 3.15 in Chapter 3 for additional details and references.

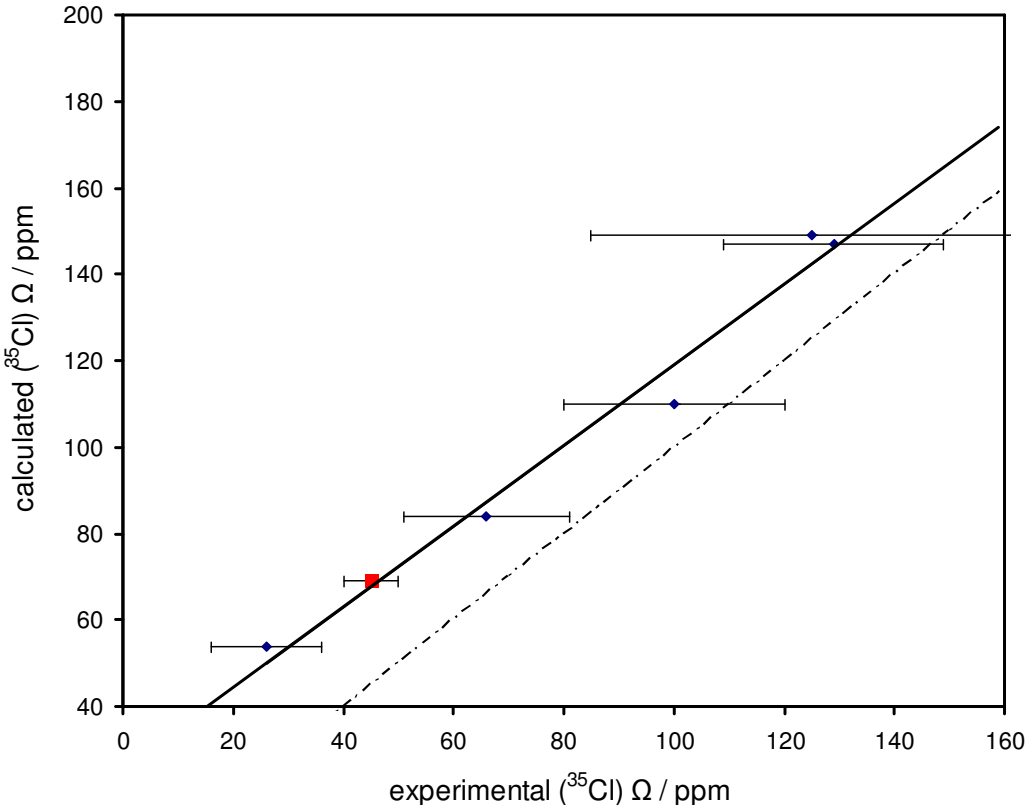

Figure 4.10. Comparison between the experimentally determined chlorine CS tensor span, on the x-axis and the GIPAW-DFT calculated values, on the *y*-axis for the amino acid hydrochlorides for which there are neutron diffraction structures (blue diamonds). Included on the curve is the data point for **1** (red square). The dotted line represents the equation $y = x$. See Figure 3.16 in Chapter 3 for additional details and references.

In the case of the chlorine chemical shift, in Chapter 3 it was noted that this parameter also tends to be overestimated by the GIPAW-DFT method. Although the calculated value of $\delta_{iso}(^{35}Cl)$ for **1**, 188 ppm, was slightly more overestimated compared to the amino acid hydrochloride results, its calculated value is also consistent with the

results for model d) as the computation using model a) results in an underestimation of the experimental chlorine chemical shift.

The GIPAW-DFT calculations of the chlorine SSNMR parameters of compound **1** are thus consistent with those carried out in Chapter 3, providing support that model d) best represents the material studied. The results also further demonstrate that with GIPAW-DFT calculations there is a consistent overestimation of the chlorine quadrupolar coupling constant, CS tensor span and chlorine chemical shift compared to experiment for organic hydrochlorides.

4.4 Conclusions

Chlorine SSNMR was used to characterize the chloride ion receptor **1** at two magnetic field strengths. The EFG and CS tensor parameters, along with their relative orientations, were extracted from simulations of the spectra collected. Interestingly, low field spectra were clearly QI dominated, while high field spectra were CSA dominated. The small $|C_Q(^{35}Cl)|$ observed, 1.0 MHz, demonstrated that the EFG about the chloride was small due to a relatively symmetric environment. The chemical shift of 120 ppm (w.r.t. solid sodium chloride), is higher than typically observed for other organic chlorides. Inclusion of CSA, and non-zero Euler angles were required in order to achieve quality fits to the experimental spectra. The CS tensor span was observed to be 50 ppm, which is within the range measured for other organic chlorides.

In addition, GIPAW-DFT calculations were carried out on a series of models based on the structure of **1,** and the results compared to those the experimental parameters extracted. As has been previously discovered, the GIPAW-DFT calculations systematically overestimate both $|C_Q(^{35}Cl)|$ and the Ω, value, and significantly

overestimate the chlorine chemical shift, under the assumption of the loss of dichloromethane and water solvent molecules. The loss of solvent was further confirmed with powder X-ray diffraction and TGA analysis. The calculations also suggest that the NMR parameters of chloride ion receptors will be highly sensitive to slight changes in structure, such as the loss of solvent or water molecules.

4.5 References

1 W. Sliwa and C. Kozlowski, *Calixarenes and Resorcinarenes: Synthesis, Properties and Applications*, Wiley-VCH Verlag GmbH& Co. KGaA, Weinheim, Germany, 2009.

2 C. D. Gutsche, *Calixarenes: An Introduction*, RSC Publishing, Cambridge, UK, 2008.

3 H. M. Dibama, I. Clarot, S. Fontanay, A. B. Salem, M. Mourer, C. Finance, R. E. Duval and J. -B. Regnouf-de-Dains, *Bioorg. Med. Chem. Lett.,* **2009**, *19*, 2679.

4 I. E. Vega, P. A. Gale, M. E. Light and S. J. Loeb, *Chem. Commun.,* **2005**, 4913.

5 L. S. Evans, P. A. Gale, M. E. Light and R. Quesada, *New J. Chem.,* **2006**, *30*, 1019.

6 A. Baeyer, *Ber. Dtsch. Chem. Ges.,* **1886**, *19*, 2184.

7 R. Custelcean, L. H. Delmau, B. A. Moyer, J. L. Sessler, W. -S. Cho, D. Gross, G. W. Bates, S. J. Brooks, M. E. Light and P. A. Gale, *Angew. Chem., Int. Ed.,* **2005**, *44*, 2537.

8 P. A. Gale, J. L. Sessler, V. Kral and V. Lynch, *J. Am. Chem. Soc.,* **1996**, *118*, 5140.

9 J. L. Sessler, A. Andrievsky, P. A. Gale and V. Lynch, *Angew. Chem., Int. Ed. Engl.,* **1996**, *35*, 2782.

10 S. Camiolo, S. J. Coles, P. A. Gale, M. B. Hursthouse and J. L. Sessler, *Acta Crystallogr., Sect. E: Struct. Rep.,* **2001**, *57*, o816.

11 C. J. Woods, S. Camiolo, M. E. Light, S. J. Coles, M. B. Hursthouse, M. A. King, P. A. Gale and J. W. Essex, *J. Am. Chem. Soc.,* **2002**, *124*, 8644.

12 J. L. Sessler, D. E. Gross, W. -S. Cho, V. M. Lynch, F. P. Schmidtchen, G. W. Bates, M. E. Light and P. A. Gale, *J. Am. Chem. Soc.,* **2006**, *128*, 12281.

13 G. W. Bates, P. A. Gale and M. E. Light, *Supramol. Chem.,* **2008**, *20*, 23.

14 D. E. Gross, F. P. Schmidtchen, W. Antonius, P. A. Gale, V. M. Lynch and J. L. Sessler, *Chem. Eur. J.,* **2008**, *14*, 7822.

15 I. Solomon, *Phys. Rev.,* **1958**, *110*, 61.

16 I. D. Weisman and L. H. Bennett, *Phys. Rev.,* **1969,** *181*, 1341.

17 A. C. Kunwar, G. L. Turner and E. Oldfield, *J. Mag. Reson.,* **1986**, *69*, 124.

18 C. M. Widdifield, R. P. Chapman and D. L. Bryce, *Annu. Rep. Nucl. Magn. Reson. Spectrosc.,* **2009**, *66*, 195.

19 R. P. Chapman, C. M. Widdifield and D. L. Bryce, *Prog. Nucl. Magn. Reson. Spectrosc.,* **2009**, *55*, 215.

20 H. Honda, *Z. Naturforsch,* **2003**, *58a*, 623.

21 D. L. Bryce, G. D. Sward and S. Adiga, *J. Am. Chem. Soc.,* **2006**, *128*, 2121.

22 D. L. Bryce and G. D. Sward, *J. Phys. Chem. B.,* **2006**, *110*, 26461.

23 R. P. Chapman and D. L. Bryce, *Phys. Chem. Chem. Phys.,* **2007**, *9*, 6219.

24 A. R. Al-Karaghouli and T. F. Koetzle, *Acta Crystallogr., Sect. B: Struct. Sci.,* **1975**, *31*, 2461.

25 A. Samoson and E. Lippmaa, *Phys. Rev. B,* **1983**, *28*, 6567.

26 P. P. Man, Introduction to the nutation NMR of quadrupole spins, http://www.pascal-man.com/presentation/nutation.shtml, (accessed 2009).

27 M. Gee, R. E. Wasylishen and A. Laaksonen, *J. Phys. Chem. A,* **1999**, *103*, 10805.

28 K. Bradenburg, *Diamond,* version 3.0e, Crystal Impact GbR, Bonn, Germany, 1997–2005.

Chapter 5

Examination of Polymorphism and Solvates using Solid-State $^{35/37}$Cl NMR and GIPAW-DFT Calculations

5.1 Introduction and Objectives

5.1.1 Introduction

Polymorphic compounds are those which can exist in more than one crystalline form.[1] For example, 80 % of pharmaceuticals are known to form more than one polymorph, with the different polymorphs often having different physiological effects.[2] Polymorphism is not limited to organic compounds; for example, many metals exist in multiple polymorphic forms.[3] In fact, in the opinion of microscopy expert Walter McCrone, "It is at least this author's opinion that every compound has different polymorphic forms and that, in general, the number of forms known for each compound is proportional to the time and money spent in research on that compound."[4] Variation in the synthetic conditions, such as concentration, temperature or pressure, can lead to the formation of different polymorphs, but different polymorphs may also form under the same conditions. Knowledge and identification of the polymorphs associated with a compound is important given the potential for different properties. Thus, non-destructive spectroscopic methods which can distinguish between different polymorphs are needed.

In addition to polymorphism, there can be an interaction between solvent molecules and a compound, resulting in a crystal type different from the parent compound. These compounds are known as solvates and generally involve electrostatic or van der Waals forces or, in some cases, the formation of hydrogen bonds.[3] Hydration

is a common form of solvation, as water is present in the atmosphere and it interacts with a wide variety of inorganic and organic compounds. The term *pseudopolymorphism* is sometimes used to describe solvates, but there is debate as to the necessity, relevance and clarity of the term.[1] As the label is not universally accepted, it will not be used in this chapter to describe solvates. In this chapter, both polymorphs and solvates will be examined with chlorine SSNMR. The former will be examined for two room temperature polymorphs of benzidine hydrochloride and the latter will be examined for a series of solvates of magnesium chloride.

During the course of this thesis work, chlorine SSNMR has been shown to be useful in distinguishing different polymorphs and hydrates of the same parent compounds. While this work was being completed, Hamaed *et al.* demonstrated in a larger study of pharmaceuticals, that three polymorphs of bupivacaine hydrochloride monochloride and two polymorphs of lidocaine hydrochloride monohydrate could be distinguished with chlorine SSNMR.[5] In addition, it was shown by Bultz and Bryce in 2007 that chlorine-NMR could distinguish anhydrous $SrCl_2$ from two of its hydrates.[6] In both studies, slight changes in the environment about chlorine in these compounds lead to noticeably different chlorine SSNMR tensor parameters.

Benzidine dihydrochloride is a simple compound which can be considered as representative of the family of planar compounds consisting of two aromatic rings linked by a single carbon-carbon bond, as shown in Figure 5.1. Multiple conformers of these materials are possible due to the possibility for rotation about the central C-C bond. The known crystal structure of benzidine dihydrochloride[7] was re-examined by Dobrzycki *et*

al. in 2006[8] and found to be incorrect, with the previous authors mistaking two distinct polymorphs for one and reporting unit cell parameters intermediate between the two forms, both of which are shown in Figure 5.1. Both polymorphs were found to crystallize at room temperature, although one does form in significant excess of the other. The dominant crystals have a triclinic structure with the remaining material crystallizing in an orthorhombic structure.[8] While the latter form definitively only has one unique chlorine site, two possible crystal structures for the triclinic form were proposed by the authors. The first takes into account only strong reflections and consists of planar benzidine cations and has a single chlorine site. The second structure, which includes weaker reflections, is non-planar and has two unique chlorine environments.

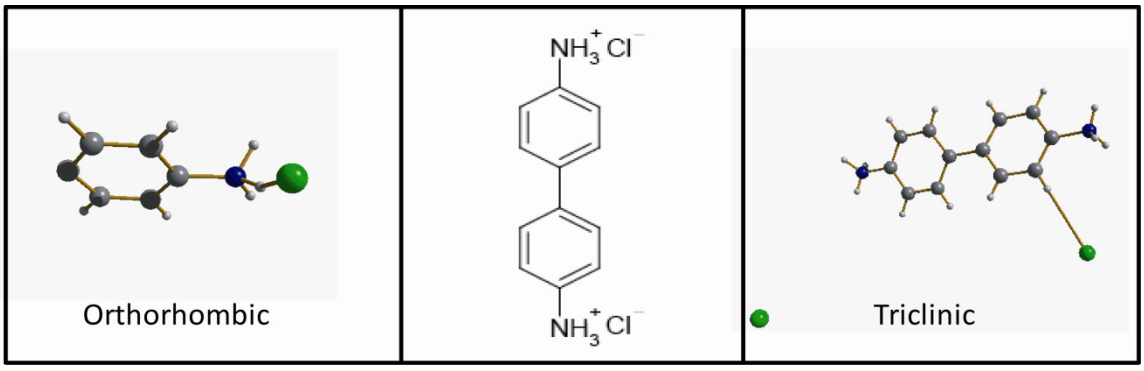

Figure 5.1. Structure of benzidine hydrochloride (center) and single repeating unit of the crystal structure of two forms of benzidine hydrochloride (left and right). The crystal structure images have the following colour scheme: chlorine atoms are in green, nitrogen atoms are in blue, carbons atoms are in grey and hydrogen atoms are in white.

Magnesium chloride is an alkaline earth metal which is known to be very hygroscopic. The most common hydrated form is the hexahydrate ($MgCl_2 \cdot 6H_2O$) which is a marine evaporate found naturally and is also known as bischofite, in honour of Karl

Gustav Bischof who discovered it in 1876.[9] The hexahydrate is also known to be hygroscopic. There are applications for both $MgCl_2$ and bischofite: the anhydrous form is produced, and reacted, in the process by which magnesium is extracted from seawater while bischofite has found uses in many applications including in construction materials, in oil extraction and in compresses which treat joint diseases.[3,9,10] Dehydration of bischofite is known to produce a variety of hydrates, some of which are solid at room temperature. The X-ray crystal structure of anhydrous magnesium chloride and several of the hydrates are known, while a neutron crystal structure exists for the hexahydrate.[9,11]

Ammonia is another solvent which will interact with anhydrous magnesium chlorine to form a solvate, $MgCl_2 \cdot (6NH_3)$. This material has been proposed as a potential hydrogen storage material as it can store 9.1 % hydrogen in the form of NH_3 as all of the ammonia is known to desorb at temperatures between 300 K and 650 K.[12-14] At 650 K, all of the ammonia is removed and the material returns to the structure of the anhydrous magnesium chloride, but can be re-aminated to once again produce the hexammine.[13]

5.1.2 Objectives

A chlorine SSNMR and GIPAW-DFT study of the two room temperature polymorphs of benzidine hydrochloride and a series of solvates of magnesium chloride was undertaken in order to demonstrate the ability of chlorine SSNMR to effectively distinguish between different materials of identical, or similar, chemical composition. In addition, determination of the chlorine SSNMR parameters for the hydrates of magnesium chloride provided an opportunity to confirm trends previously observed for hydrates in terms of chlorine chemical shift and $|C_Q(^{35}Cl)|$.

5.2 Experimental and Computational Details

5.2.1 Sample Preparation

Benzidine dihydrochloride (Bn2HCl) was purchased from Aldrich. Recrystallization to produce the two polymorphs was done from concentrated hydrochloric acid. All of the recrystallizations lead to the formation of powder, not crystals.

Anhydrous magnesium chloride was purchased from Aldrich as beads in a vial. Initially the sample was stored in a dessicator, which lead to hydration of the sample. A second vial was then purchased and opened then stored in an argon dry box.

Magnesium chloride hexammine was prepared following the procedure described by Christensen *et al.*[12] Anhydrous magnesium chloride beads were ground into a fine powder and then placed in an evacuated round bottom flask. The flask was then exposed to 1 bar of ammonia gas at 300 K overnight.[12] The identity of the product was confirmed by powder X-ray diffraction (pXRD).

5.2.2 Powder X-ray Diffraction

The identities of the Bn2HCl polymorph(s) present in a given sample were determined first by pXRD prior to NMR experiments. The identity of the $MgCl_2 \cdot (6NH_3)$ was also identified with pXRD prior to NMR experiments. The pXRD data were collected using a Philips PW3719 diffractometer and $Cu_{K\alpha 1}$ radiation (λ=1.54056 Å); operating conditions were 45 kV and 40 mA. A 10 mm slit was used at the X-ray source; the scattering slit had a fixed width of 0.2 mm, and a 1° receiving slit was used. Data

were collected in continuous mode over the range $2\theta = 5$ to 80° in steps of 0.02° at a rate of 1.2° per minute. In the case of the polymorphs of benzidine hydrochloride, the published X-ray structure[8] was used to produce a theoretical pXRD pattern using the Diamond 3.0 program.[15] For both polymorphs, the predicted pattern and the experimental pattern were in agreement. In the case of $MgCl_2 \cdot (6NH_3)$ the pXRD obtained was compared to a pattern from literature.[12]

5.2.3 NMR Experiments

5.2.3.1 Experiments Carried out at 9.4 T

Chlorine-35 SSNMR experiments were carried out on a 400 MHz (B_0 = 9.4 T) Bruker Avance III spectrometer at the University of Ottawa. A 4 mm Bruker HX probe tuned to 39.2 MHz was used for all experiments. Samples were ground into fine powders and packed into 4 mm o.d. zirconia rotors. Experimental setup and pulse calibrations were performed using solid NH_4Cl, the centreband of which was set to 121.1 ppm (NaCl(s) at 0 ppm). The 'solid' $\pi/2$ chlorine-35 pulse was 4 μs. Recycle delays used were 4 seconds and signals were averaged for one day. Spectra were collected under stationary conditions using the $\pi/2 - \tau - \pi/2 - \tau$ - ACQ quadrupolar echo sequence.[16-18] Proton decoupling using the cw method was applied during acquisition.

5.2.3.2 Experiments Carried out at 11.7 T

Chlorine-35/37 SSNMR experiments were carried out on a 500 MHz (B_0 = 11.7 T) Bruker Avance spectrometer at the University of Ottawa. A 4 mm Bruker HX probe tuned to 49.0 MHz (^{35}Cl) or 40.79 MHz (^{37}Cl) was used for all experiments. Experimental setup and pulse calibrations were done using the same method as on the 9.4 T instrument. The $\pi/2$ pulse ranged from 1.35 μs at a power level of -2.4 dB to 4.00 μs at

a power of 4 dB for chlorine-35. A pulse of 2.65 μs was used for chlorine-37 at -2.4 dB. Recycle delays used were 4 seconds. Signals were averaged between 12-24 hours for anhydrous magnesium chloride and benzidine hydrochloride and < 1 hour for magnesium chloride hexammine. The pulse sequence used was identical to that on the 9.4 T instrument. Proton decoupling was used on the majority of the compounds. The spectra presented for anhydrous magnesium chloride were collected without proton decoupling.

5.2.3.3 Experiments Carried out at 21.1 T

Chlorine-35/37 SSNMR experiments were carried out on a 900 MHz (B_0 = 21.1 T) Bruker Avance II spectrometer at National Ultrahigh-Field NMR Facility for Solids in Ottawa. Experiments were carried out on a 4 mm or 3.2 mm Bruker HX probe tuned to 88.2 MHz (^{35}Cl) or 73.4 MHz (^{37}Cl). Experimental setup and pulse calibrations were done using solid NaCl (centreband set to 0 ppm). The 'solid' π/2 pulse was typically 3.0 – 4.5 μs and 4.1 μs for chlorine-35 and chlorine-37, respectively. Recycle delays used were 2 - 5 seconds for both nuclides and signals were averaged over a period of 4 - 12 hours, with the exception of the experiments on magnesium chloride hexammine, which were collected in under 1 hour. The pulse sequence and decoupling used was identical to that on the 11.7 T instrument.

5.2.4 Data Processing and Simulations

All NMR data was processed in the same manner as in Chapter 3.

5.2.5 Quantum Chemical Calculations

The same method as described in Chapter 3 was used to prepare and analyze the GIPAW-DFT calculations of the polymorphs of benzidine hydrochloride, magnesium

chloride and the hydrates of magnesium chloride. The cut-off energies and k-points used for calculation are listed in Appendix 4. The cell parameters and atomic coordinates used were that of Dobrzycki *et al.*[8] for benzidine hydrochloride, Partin and O'Keefe[19] for anhydrous magnesium chloride, Agron and Busing[11] for magnesium chloride hexahydrate, and Sugimoto *et al.*[9] for the monohydrate, dihydrate, and tetrahydrate solvates of magnesium chloride. In cases where a neutron structure was not available and there were hydrogens in the structure, optimization of the proton positions was done as described in Chapter 3. While GIPAW-DFT calculations have already been reported by Bryce and Bultz[6] for magnesium chloride hexahydrate, they were repeated here. In the case of magnesium chloride hexammine, GIPAW-DFT calculations were not possible (*vide infra*) and therefore B3LYP/RHF calculations were done using the method described in Chapter 2 and 3. The material crystallizes in the crystal structure of K_2PtCl_6 (*Fm3m*) with ¾ occupancy of hydrogens in the 96j position.[20] The cell parameter from the structure of Hwang *et al.*[20] was used to construct the cluster model used, which was arbitrarily chosen as one central chlorine, four magnesiums and 24 ammonias.

5.3 Results and Discussion

5.3.1 Benzidine Hydrochloride Polymorphs

5.3.1.1 Powder X-ray Diffraction

Prior to NMR experiments, pXRD experiments were done in order to identify the polymorph(s) present, as described in Section 5.2.2. The first pXRD pattern collected demonstrated that the dominant triclinic polymorph, Bn2HCl **A**, was the major form present in the bulk material from Aldrich. Several recrystallization attempts were done with **polymorph A** the major product on every occasion except one. An example of an

experimental and simulated pXRD pattern of Bn2HCl **A** is shown in Figure 5.2. Also included in Figure 5.2 is the resulting experimental and simulated, diffraction pattern for the one instance where the less dominant form, Bn2HCl **B**, was the major product (although some polymorph **A** is present). In both cases, excellent agreement is observed between the experimental diffraction pattern and the pattern calculated based on the respective crystal structures.

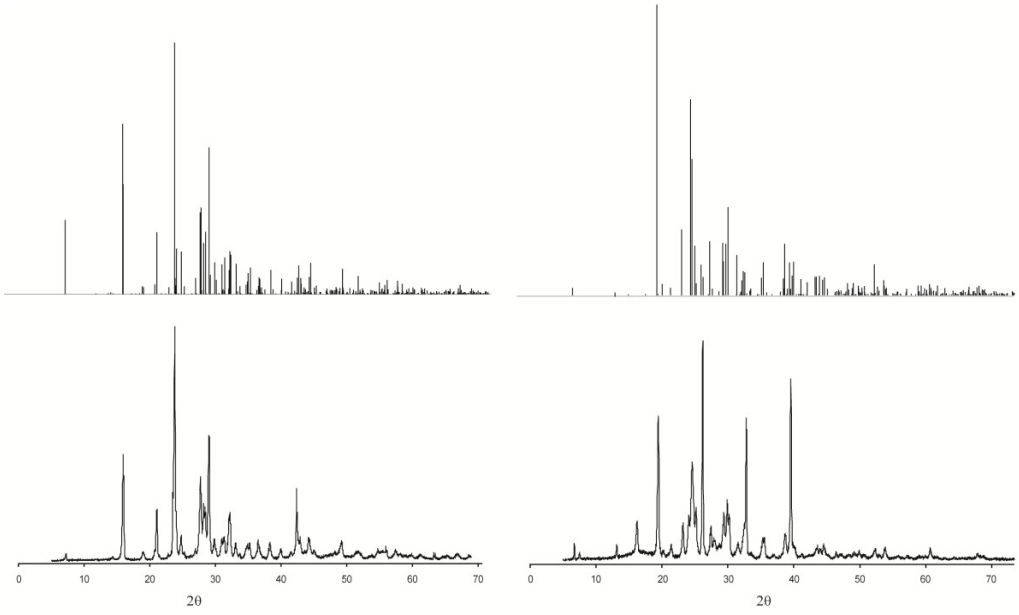

Figure 5.2. Powder X-ray diffraction patterns of the two polymorphs of benzidine hydrochloride. The patterns for form **A** appear on the left while those of form **B** are on the right. The patterns on the bottom are experimental and the corresponding calculated pattern appears above.

5.3.1.2 NMR Results

The experimental and simulated chlorine SSNMR spectra of the two polymorphs of Bn2HCl are shown in Figure 5.3, 5.4 and 5.5, while the chlorine SSNMR parameters extracted from the simulation of these spectra are listed in Table 5.1.

Table 5.1. Chlorine-35/37 EFG and CS tensor parameters for the two polymorphs of benzidine hydrochloride

Polymorph		$C_Q(^{35}Cl)$ / MHz	η_Q	δ_{iso} / ppm	Ω / ppm	κ	α, β, γ/°
triclinic	site 1	4.56(10)	0.47(6)	141.5(5.0)	145(30)	0.2(5)	80(15), 90(15), 0(15)
(**A**)	site 2	4.47(10)	0.67(5)	136.5(5.0)	145(30)	0.0(1)	80(20), 90(20), 0(20)
orthorhombic (**B**)		5.8(1)	0.02(5)	120(5)	< 100		[a]

[a]Not determined

While the pXRD patterns did serve to identify the polymorph present, this was also clear from the chlorine SSNMR spectra, as Bn2HCl **A** has two magnetically unique chlorine site while Bn2HCl **B** only has one site leading to very different chlorine SSNMR spectra. Immediately, this demonstrates that the crystal structure which uses only the strong reflections is wrong, as the triclinic form *must* have two chlorine sites. The absence of CS tensor data associated with Bn2HCl **B** result from the large impurity present in the spectra collected at 21.1 T.

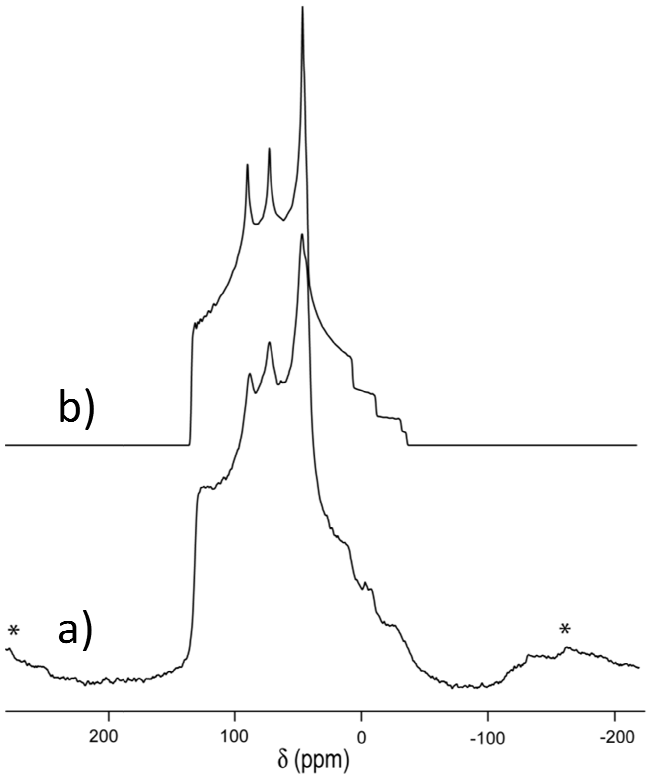

Figure 5.3. Solid-state chlorine-35 MAS NMR spectra of benzidine hydrochloride polymorph **A** at 21.1 T with ν_{rot} = 18 kHz (a) Experimental. (b) Best-fit simulation using WSolids under the assumption of an infinite MAS rate. Spinning sidebands are indicated by asterisks.

The two chlorine sites in polymorph **A** are quite similar, leading to a complicated, and difficult to interpret, second-order quadrupolar lineshape for the spectrum collected under stationary conditions, shown in Figure 5.4. Conveniently, an MAS spectrum could be collected at 21.1 T, shown in Figure 5.3 along with simulations, allowing for the accurate determination of the $|C_Q(^{35}Cl)|$, η_Q and δ_{iso} of the two sites. As expected, all three parameters were quite similar for the two sites with values of 4.56 MHz, 0.47 and 141.5 ppm for site 1 and 4.47 MHz, 0.67 and 136.5 ppm for site 1 and 2, respectively. The $|C_Q(^{35}Cl)|$ values are within the range observed for other organic hydrochlorides while the chemical shifts are quite high, on the order of the ion receptors.[21,22] The spectra collected under stationary conditions at 21.1 T and 11.7 T were then simulated to extract the CS tensor parameters and Euler angles. The additional peak marked by an asterisk in Figure 5.4 is a quadrature artifact resulting from a mismatch of the phase sensitive detectors. This was determined by noting that the peak is the result of a single data point and appears in the exact center of the spectrum. Both sites were found to have identical, and large, CS tensor spans of 145 ppm. The large effect that this CSA has on the spectrum is demonstrated by the poor agreement between the experimental spectra in Figure 5.4 and the simulation which assumes no CSA (simulations c) and f)).

As only one recrystallization led to the formation of Bn2HCl **B** there was only a small amount of sample available for NMR experiments. The pXRD and 11.7 T experiments were carried out shortly after recrystallization and both appear to be relatively free of impurities. Unfortunately the experiments at 21.1 T were done several months later, during which time the sample of Bn2HCl **B** decomposed significantly. This decomposition is demonstrated by the large amorphous hump in the center of the

chlorine-35 spectrum collected at 21.1 T. In addition, a colour change, from white to light grey, was noted. A carbon-13 NMR spectrum also confirmed the presence of an impurity in addition to the bulk Bn2HCl material with several unknown peaks appearing in the sp^3 carbon region, along with the expected carbon peaks. These peaks did not appear in the carbon-13 spectrum for polymorph **A**.

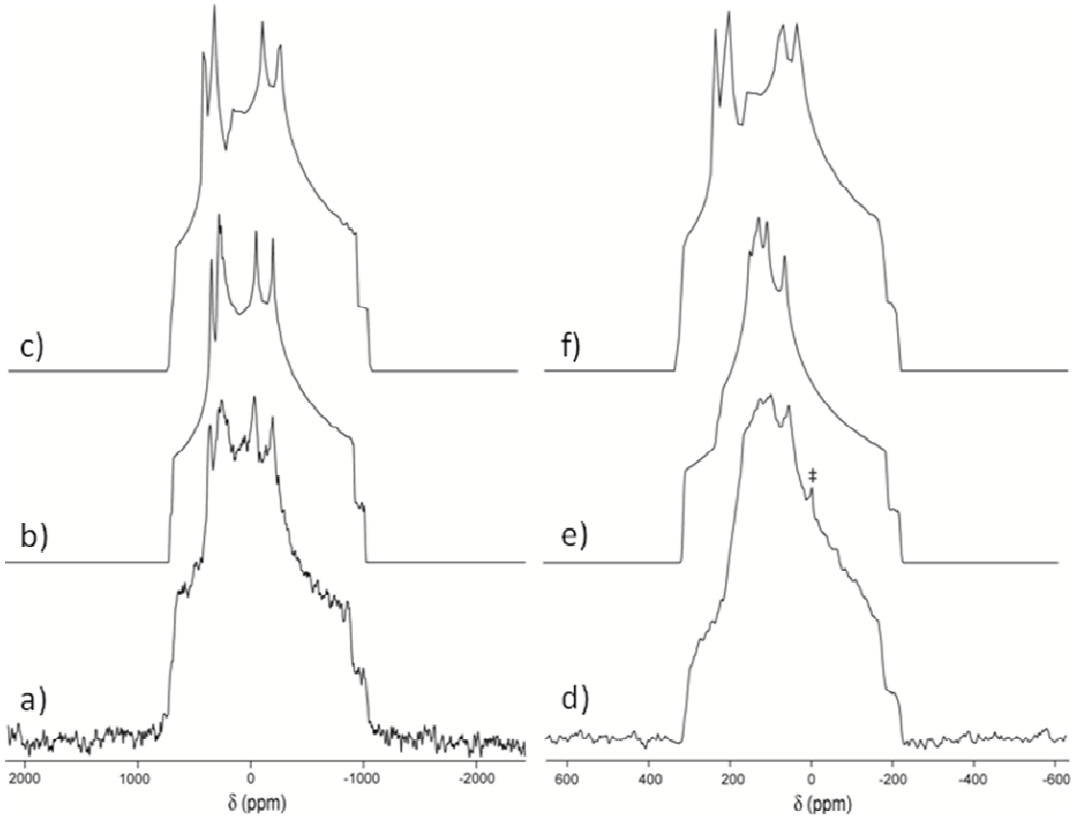

Figure 5.4. Solid-state chlorine NMR spectroscopy of benzidine hydrochloride polymorph **A**. Experimental spectra of stationary powdered samples: (a) ^{35}Cl at 11.75 T; (e) ^{35}Cl at 21.1 T. Best-fit spectra simulated with WSolids appear in b) and (e). (c) and (f) presents a simulation assuming no CSA. The double dagger in spectrum d) is a quadruature artifact.

The chlorine SSNMR parameters extracted from the fits of the experimental spectra in Figure 5.5, listed in Table 5.1, are significantly different from the values obtained for Bn2HCl **A**. Notably, the quadrupolar interaction is larger with a $|C_Q(^{35}Cl)|$ of 5.8 MHz while the CS tensor interaction must be smaller in magnitude with a $\Omega < 100$ ppm, with the simulation in Figure 5.5 assuming a value of 85 ppm. The δ_{iso} is also significantly lower at 120 ppm. And, unlike Bn2HCl **A**, the spectra of Bn2HCl **B** clearly display that the EFG tensor has near axial symmetry (found to be 0.02).

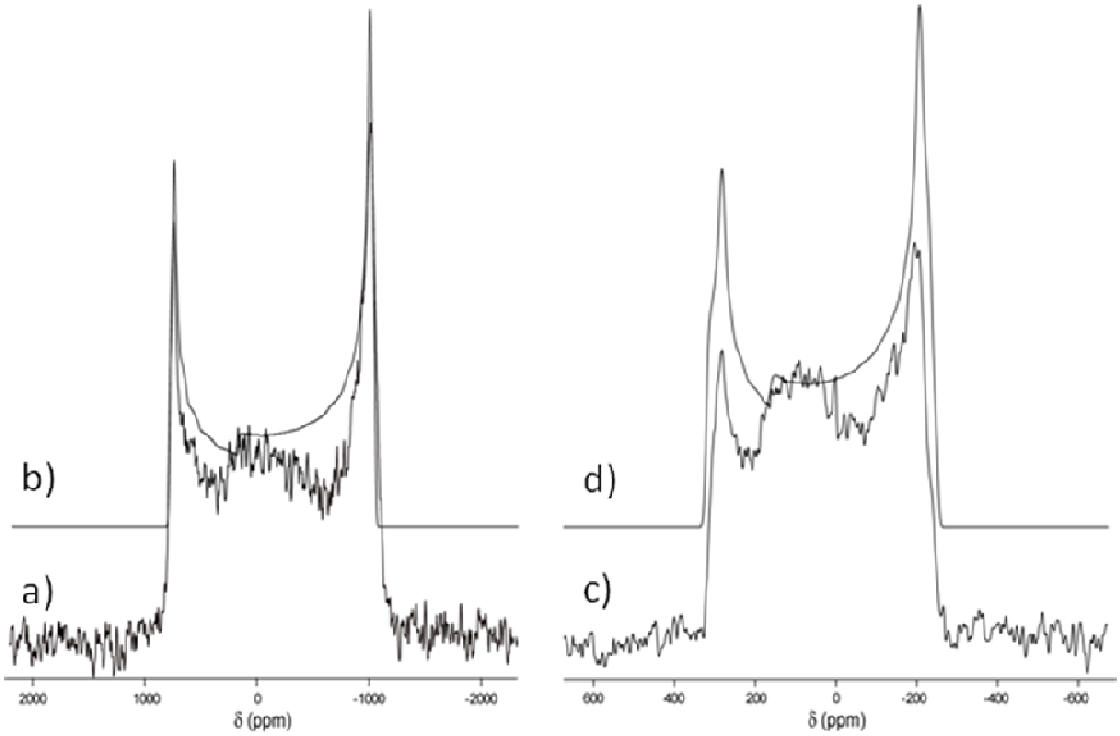

Figure 5.5. Solid-state chlorine NMR spectroscopy of benzidine hydrochloride polymorph **B**. Experimental spectra of stationary powdered samples: (a) ^{35}Cl at 11.75 T; (e) ^{35}Cl at 21.1 T. Best-fit spectra simulated with WSolids appear in b) and (d).

One of the primary differences between the two polymorphs is their crystal symmetry. While the more dominant **A** polymorph packs in a low symmetry triclinic space group, the **B** form packs in the relatively high orthorhombic symmetry. There is no symmetry associated with the chlorine site in either form. It is interesting to note that although the **B** form crystallizes with much higher symmetry, it has a larger QI, as demonstrated by the larger $|C_Q(^{35}Cl)|$. The magnitude of the CSA, however, is much smaller in **B** compared to **A**. This result further demonstrates the independence of the EFG and CS tensors and shows the need to examine the local environment about chlorine as opposed to that of the entire molecule.

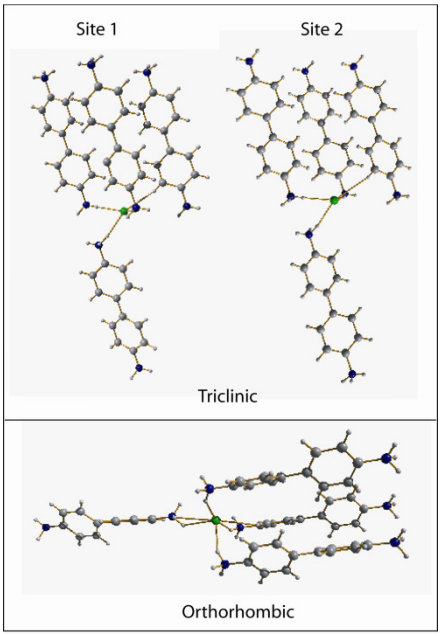

Figure 5.6. Local chlorine environment in the two polymorphs of benzidine hydrochloride. The crystal structure images have the following colour scheme: chlorine atoms are in green, nitrogen atoms are in blue, carbons atoms are in grey and hydrogen atoms are in white.

The local chlorine environments in both polymorphs are quite similar, as shown by the packing diagrams in Figure 5.6.[8] Both chlorine sites in polymorph **A** have an interaction (i.e., are within 3 Å) with four hydrogen atoms: three in H-N groups, and one H-C group. Each group is part of its own benzidine unit, meaning in the first coordination sphere, there are four benzidine units. This is different in polymorph **B**, in which the chlorine interacts with 6 hydrogens: one H-C group and four H-N groups, interacting with two of the hydrogens in one of the NH_3 units. This result seems to contradict the trend that more hydrogen bonds lead to a larger QI, but it should be noted that in **B** there are also only four benzidine units in the first coordination sphere. A small shift in the hydrogen positions, very possible as their positions are not known exactly, could lead to fewer Cl-H interactions. The two phenyl rings are closer to planarity in polymorph **A**, which may result in the large amount of CSA observed, as the benzidine in that polymorph would have a more extended π^* network available to interact with the chlorine nucleus.[8] It is also interesting to note the high chlorine chemical shifts of *both* polymorphs relative to other organic chloride systems are similar to the results observed in Chapter 4 for chloride ion receptors, systems in which there is also extended π^* systems interacting with the chloride ion.[23,24]

While chlorine SSNMR has been shown to be useful for the identification of polymorphs produced at different temperatures and synthetic conditions,[5] this is the first instance where this has been shown for polymorphs synthesized using *identical* reaction conditions. It is unfortunate that another pure sample of polymorph **B** could not be crystallized; however, the above results do clearly demonstrate the sensitivity of chlorine

SSNMR to very small changes in structure as well as definitely show that polymorph **A** does possess two unique chlorine positions.

5.3.1.3 GIPAW-DFT Calculations

As the two polymorphs of Bn2HCl are very similar, they proved a useful test of the robustness of GIPAW-DFT calculations. The hydrogen positions were optimized for both polymorphs, which required a low energy cutoff due to the size of the unit cell. The results of the calculations are shown in Table 5.2.

Table 5.2. GIPAW-DFT calculated chlorine-35 EFG and MS tensor parameters for the two polymorphs of benzidine hydrochloride

Polymorph		$C_Q(^{35}Cl)$ / MHz	η_Q	δ_{iso} / ppm[a]	Ω / ppm	κ
triclinic	site 1	6.72	0.57	196	131	0.3
(**A**)	site 2	6.57	0.71	194	126	0.7
orthorhombic (**B**)		8.3	0.15	162	124	-0.6

[a] To convert from calculated shielding constants to chemical shifts, a shift of 45.37 ppm was used (for the conversion from solid to aqueous NaCl chemical shift scales) in addition to the absolute shielding conversion found in Chapter 1.

As expected, from the earlier results, the magnitude of the chlorine-35 quadrupolar coupling constants were significantly overestimated, along with the chlorine chemical shift. The overestimation in $|C_Q(^{35}Cl)|$ is consistent with the results in Chapter 3, albeit slightly higher than the average, as shown by Figure 5.7 in which the data points for the two polymorphs of Bn2HCl are placed on Figure 3.14 from Chapter 3. Overestimation of the chlorine chemical shifts by the calculations were also observed for both polymorphs, as was the case for the other organic hydrochlorides discussed in Chapters 3 and 4. Unlike the results in previous chapters, however, the CS tensor span is actually *underestimated* for both sites in polymorph **A**, although it is within error. The Ω is still

overestimated for polymorph **B**. While agreement between experiment and theory is not as consistent as in Chapters 3 and 4, it is reassuring that the *trends* in $|C_Q(^{35}Cl)|$, **Ω** and δ_{iso} between the two polymorphs are reproduced by the calculations (i.e., Bn2HCl **A** has a smaller QI but larger CSA compared to polymorph **B**).

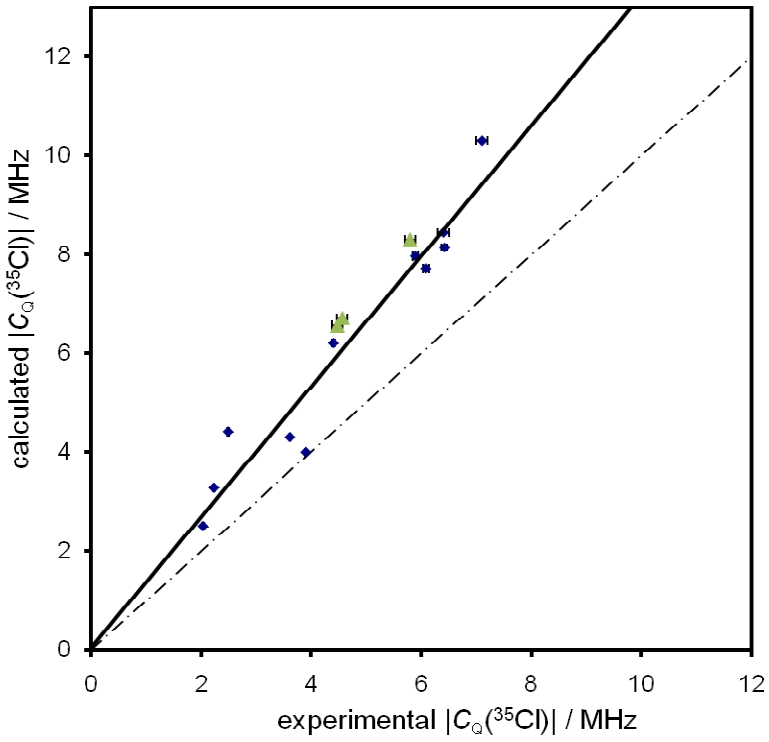

Figure 5.7. Comparison between the experimentally determined chlorine-35 quadrupolar coupling constant, on the *x*-axis and the GIPAW-DFT calculated values, on the *y*-axis, for the amino acid hydrochlorides, with the exception of four outliers (blue diamonds), as shown in Chapter 3. Included on the curve are the data points for the two polymorphs of benzidine hydrochloride (green triangles). See Figure 3.14 in Chapter 3 for additional details and references.

5.3.2 Magnesium Chloride Hydrates

Anhydrous magnesium chloride is a highly water-sensitive material, quickly absorbing water when left in the atmosphere. This is also true for bischofite (magnesium chloride hexahydrate), which looks like a 'wet' translucent powder and will, on grinding, develop a gel-like consistency. This is distinct from the anhydrous form, which is a white, fluffy powder. As mentioned above in Section 5.2.1, anhydrous magnesium chloride was received as beads, which were used directly for the NMR experiments (i.e., not ground). In the case of $MgCl_2 \cdot XH_2O$, once again the beads were put directly in an NMR rotor after having been exposed to air for some time. In both cases the beads looked identical, and did not resemble bischofite.

Table 5.3. Chlorine-35/37 EFG and CS tensor parameters for anhydrous magnesium chloride, the unknown magnesium chloride hydrate and magnesium chloride hexahydrate. The data for the hexahydrate come from reference 6.

	$\lvert C_Q(^{35}Cl)\rvert$ / MHz	η_Q	δ_{iso} / ppm	Ω / ppm	κ	α, β, γ/°
anhydrous magnesium chloride	4.61(10)	0.0	130(3)	10(5)	-1.0	0(10), 90(10), 0(10)
magnesium chloride hydrate[a]	3.75(5)	0.55(5)	56.5(1.0)	30(10)	-1.0(5)	45(10), 60(10), 45(10)
magnesium chloride hexahydrate[6]	3.02(5)	0.00	75(1)	< 75		[b]

[a]Unknown hydrate
[b]Not determined

5.3.2.1 NMR Results

Shown in Figure 5.8 and 5.9 are the experimental and simulated chlorine-35 spectra collected of anhydrous magnesium chloride collected at 11.7 T, and the chlorine-35/37 spectra collected at 21.1 T, all under stationary conditions. The chlorine SSNMR parameters extracted from simulation of these spectra are listed in Table 5.3. Examination of the shape of the experimental spectra immediately reveals near-axial asymmetry (η_Q = 0.01), consistent with a site of high symmetry, which is the case with the structure of $MgCl_2$ in which chlorine sits in a position with 3m symmetry.[19] The $|C_Q(^{35}Cl)|$ determined was 4.61 MHz and the QI dominates the spectra, all of which display typical second-order quadrupolar lineshapes. Despite this, however, CS tensor information could be reliably extracted and a CS tensor span of 10 ppm was determined. The spectrum collected at 21.1 T was essential to extract this value as can be seen by the inset in Figure 5.9, which zooms into a region in which a simulation neglecting CSA clearly does not match the experimental spectrum. In addition to a near zero asymmetry parameter, the symmetry of the chlorine site within $MgCl_2$ limits the possible skew and Euler angles, which aided the fitting procedure.

As mentioned, Bryce and Bultz included bischofite in their chlorine SSNMR study of some alkaline earth metals[6] and the parameters they extracted appear in Table 5.3. Comparison of the parameters for anhydrous $MgCl_2$ and $MgCl_2 \cdot 6H_2O$ show that they are significantly different, demonstrating the sensitivity of chlorine SSNMR to changes in hydration. These changes are not surprising as the local chlorine environment in $MgCl_2 \cdot 6H_2O$ is very different from its anhydrous counterpart (*vide infra*).

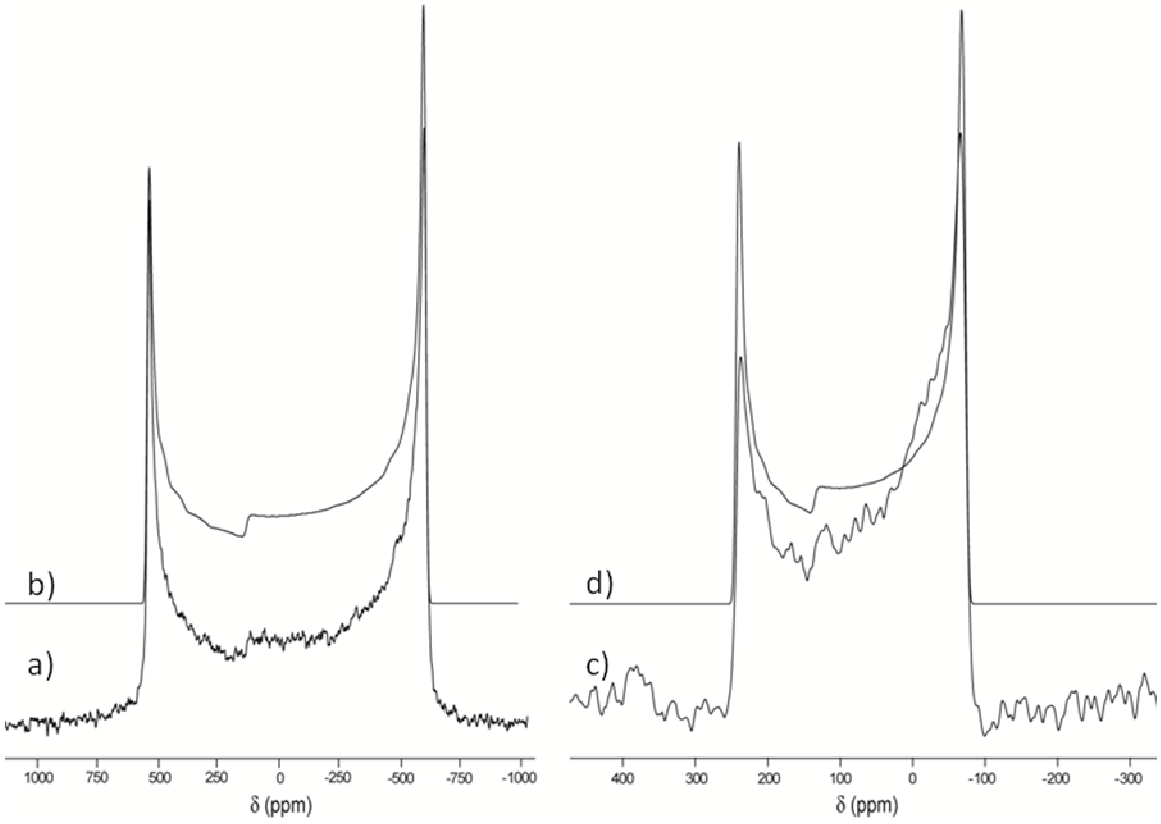

Figure 5.8. Solid-state chlorine NMR spectroscopy of anhydrous magnesium chloride. The Experimental spectra of stationary powdered samples: (a) ^{35}Cl at 11.75 T; (c) ^{37}Cl at 21.1 T. Best-fit spectra simulated with WSolids appear in 9b) and (d).

In the case of other alkaline earth chlorides, it has been noted that hydration almost always leads to a smaller chlorine quadrupolar coupling constant and also tends to lead to a lower chemical shift.[25] The results described above for magnesium chloride are consistent with this trend, as the anhydrous magnesium chloride has a $|C_Q(^{35}Cl)|$ and a chlorine chemical shift that is much greater than the hexahydrate.

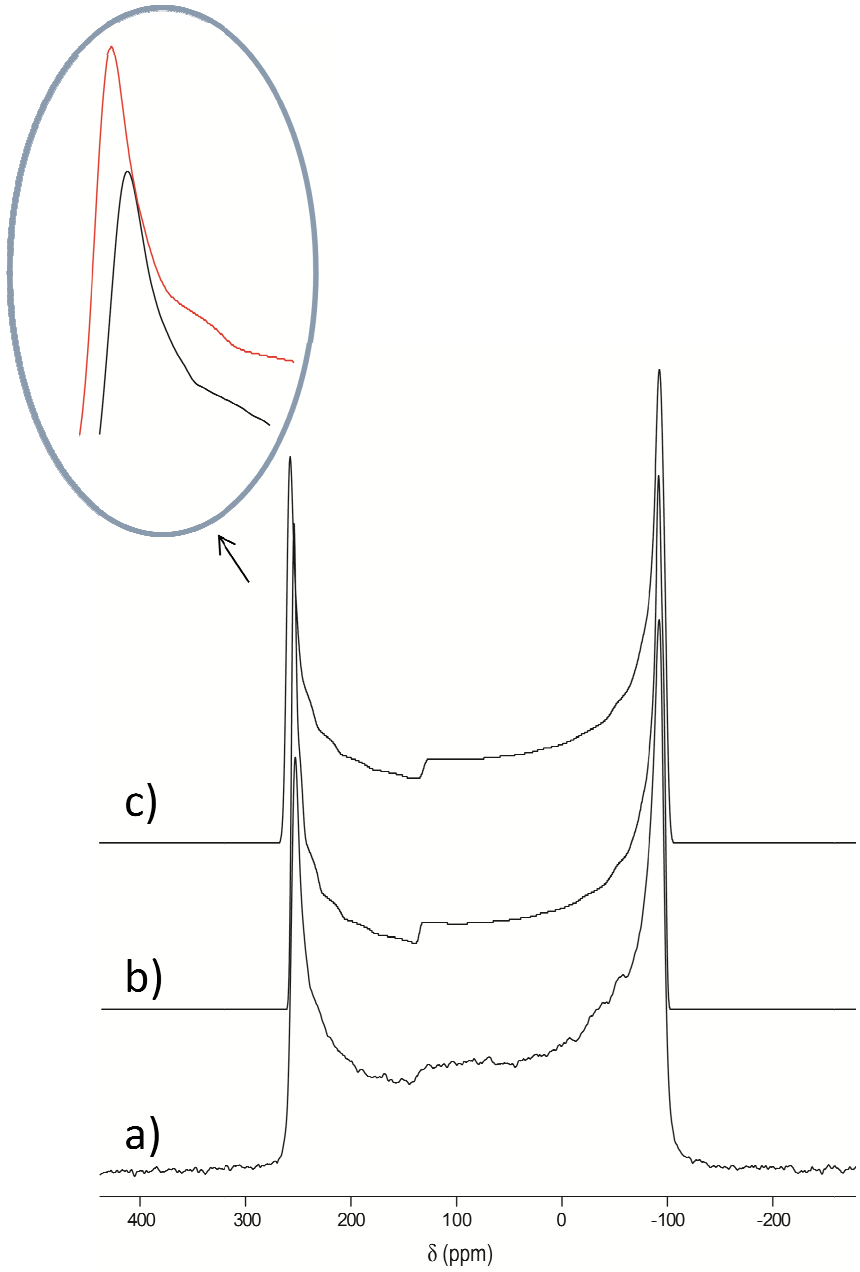

Figure 5.9. Solid-state chlorine-35 NMR spectroscopy of anhydrous magnesium chloride at 21.1 T. The experimental spectrum appers in (a), best-fit spectra simulated with WSolids appears in b) while c) presents a simulation assuming no CSA. The circle above the spectra zooms into the left horn of simulation c) and the experimental spectrum.

After the initial collection of the chlorine-35/37 SSNMR spectra of $MgCl_2$ beads at 11.7 T, the sample was left sealed with parafilm in a dessicator for several months. The sample was then repacked into rotor and recollected at 9.4 T. The resulting spectrum, shown in Figure 5.10, differed greatly from what was expected given the parameters expected from the 11.7 T spectrum. For example, the chlorine-35 experimental spectrum in Figure 5.10 definitely does not display axial symmetry. While this is clear evidence of decomposition of some sort, it was interesting that the spectrum still displayed a clear second order quadrupolar lineshape with a slight impurity, later identified as anhydrous $MgCl_2$. The same sample was kept packed and examined at 21.1 T. At that field, chlorine-35 spectra collected under stationary and MAS conditions were collected. The experimental and calculated chlorine-35 spectra collected at 9.4 and 21.1 T under stationary conditions are included in Figure 5.10. The MAS spectrum at 21.1 T is included in Appendix 4.

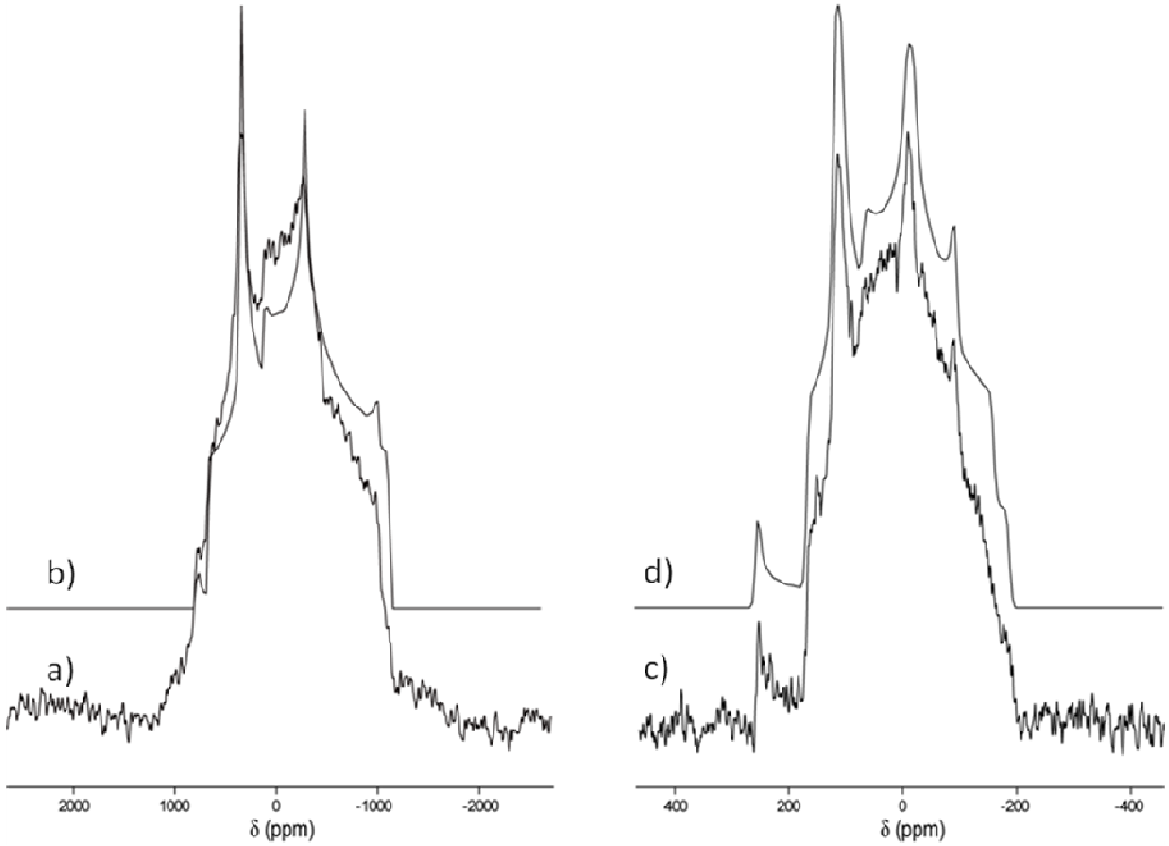

Figure 5.10. Solid-state chlorine NMR spectroscopy of the unidentified magnesium chloride hydrate. Experimental spectra of stationary powdered samples: (a) ^{35}Cl at 9.4 T; (c) ^{35}Cl at 21.1 T. Best-fit spectra simulated with WSolids appear in (b) and (d). Included in the simulations is a small amount of anhydrous magnesium chloride impurity.

While the presence of the anhydrous $MgCl_2$ made interpretation of the MAS spectrum difficult due to interference, approximate values for $|C_Q(^{35}Cl)|$, η_Q and δ_{iso} could be extracted and then refined using the spectra collected under stationary conditions. The anhydrous $MgCl_2$ 'impurity' is included in both the simulated fits shown in Figure 5.10. The parameters extracted from fitting the sample, labelled $MgCl_2 \cdot XH_2O$, spectra are shown in Table 5.3. It can be assumed that the spectrum is a hydrate as the sample was exposed to water in the air and it is known that

magnesium chloride readily forms several hydrates. All the parameters differ greatly from those of anhydrous magnesium chloride, which is not surprising given the differences in the spectra for the two compounds. Most notably, once again $MgCl_2 \cdot XH_2O$ does not display axial symmetry and has a smaller breadth then the anhydrous form. Importantly, the parameters also differed greatly from the most common hydrate, $MgCl_2 \cdot 6H_2O$. Clearly, the hydrated $MgCl_2$ beads were *not* the hexahydrate form, as the NMR parameters are significantly different and the powder making up the beads did not resemble that hydrate. There are several other hydrates of magnesium chloride which have been identified, mostly through the dehydration of the common bischofite, all of which have similar colour and morphology to anhydrous form.[9] These include the mono-, di- and tetrahydrates and these were all potential candidates for the identity of $MgCl_2 \cdot XH_2O$. There is also a dodeca- and octahydrate known, but these are not solid at room temperature and were therefore not considered.[26] Dehydration of bischofite also leads to other products, such as MgO and $MgOHCl \cdot nH_2O$ ($0 \leq n \leq 1$),[9] but as the anhydrous magnesium chloride beads were not exposed to any heat and had no visible change in appearance, the assumption was made that the change in structure could only be the result of absorption of water.

5.3.2.3 GIPAW-DFT Calculations

As GIPAW-DFT has been shown to be very effective in the calculation of chlorine SSNMR parameters (as demonstrated in Chapters 3 and 4) calculations were done in order to identify which hydrate was formed by the hydration of the anhydrous beads. This system provided an opportunity to demonstrate how experiment and theory could be combined to determine the identity of an unknown species. The results of calculations using the X-ray (or neutron) crystal structure of anhydrous, mono-, di-, tetra- and hexahydrate versions of magnesium chloride are shown in Table 5.4. The chlorine environments in these different

materials are displayed in Figure 5.11. The results obtained for the hexahydrate are generally in good agreement with those obtained by Bultz and Bryce,[6] with the differences observed attributed to the use of slightly different energy cutoffs.

Firstly, comparison between the GIPAW-DFT results for anhydrous magnesium chloride and magnesium chloride hexahydrate demonstrates excellent agreement between experiment and theory, with the expected overestimation in $|C_Q(^{35}Cl)|$, δ_{iso} and, in the case of the anhydrous $MgCl_2$, Ω. These results further demonstrate the *systematic* overestimation that seems to be inherent in GIPAW-DFT calculations of chlorine SSNMR parameters as, unlike the other compounds studied in this chapter, the positions of *all* the nuclei are known actually, as there is a neutron structure available for magnesium chloride hexahydrate.

Table 5.4. GIPAW-DFT calculated chlorine-35 EFG and CS tensor parameters for the anhydrous magnesium chloride and the mono-, di-, tetra- and hexahydrates of magnesium chloride

	$C_Q(^{35}Cl)$ / MHz	η_Q	δ_{iso} / ppm[a]	Ω / ppm	κ
anhydrous magnesium chloride	5.24	0.00	205	13	-0.92
magnesium chloride hydrate	site 1: 1.92 site 2: 7.29	0.20 0.12	181 136	17 49	-0.80 -0.45
magnesium chloride dihydrate	- 6.16	0.89	123	51	-0.17
magnesium chloride tetrahydrate	- 4.02	0.71	106	57	-0.66
magnesium chloride hexahydrate	- 3.91	0.01	97	23	0.0

[a]To convert from calculated shielding constants to chemical shifts, a shift of 45.37 ppm was used (for the conversion from solid to aqueous NaCl chemical shift scales) in addition to the absolute shielding conversion found in Chapter 1.

Examination of the results for the monohydrate reveals two chlorine sites with very different chlorine SSNMR parameters. This is not surprising as there are two unique chlorine sites in the crystal structure, as shown in Figure 5.11: one which only interacts only with magnesium (three interactions) and one which has an interaction with one magnesium and two hydrogens.[9] In this case, 'interaction' is arbitrarily defined as an interatomic distance of 3 Å or less, which is slightly longer than the sum of the van der Waals radii (1.75 Å and 1.09 Å for chlorine and hydrogen, respectively).[3] As the experimental spectra shown in Figure 5.10 only demonstrate one site in addition to the anhydrous magnesium chloride 'impurity', the monohydrate could be eliminated as the species. This leaves the dihydrate and the tetrahydrates as possible candidates. The chlorine environment in the dihydrate is similar to that of one of the sites in the monohydrate: interaction with two hydrogens and two magnesium, as shown in Figure 5.11. Differently, the single chlorine environment in the tetrahydrate interacts with four hydrogens and one magnesium ion.

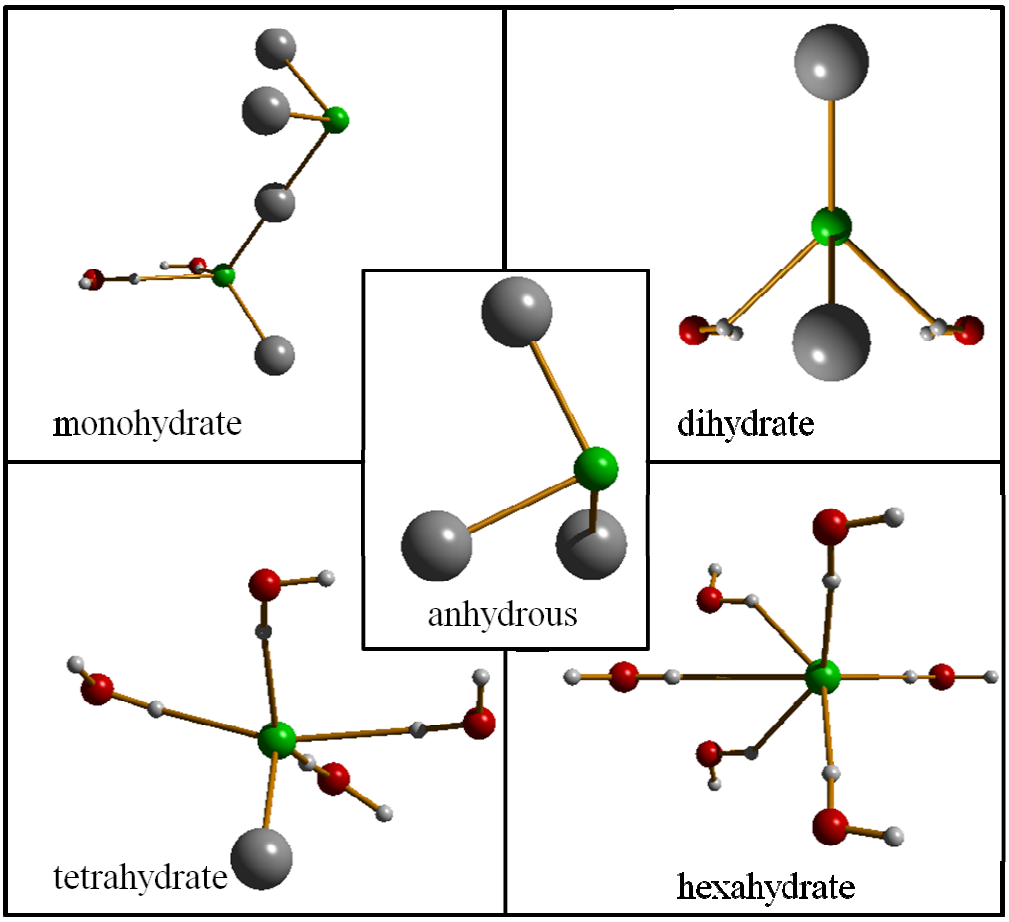

Figure 5.11. Models of the chlorine environment (within 3 Å) of the anhydrous, monohydrate, dihydrate, tetrahydrate and hexahydrate forms of magnesium chloride. Chlorine atoms are shown in green, magnesium atoms are grey, oxygen atoms are red and hydrogen atoms are white. The appropriate references for the crystal structures can be found in text.

As agreement between the experimental and calculated values has been most consistent for $|C_Q(^{35}Cl)|$, this was the parameter first examined to determine which hydrate was most likely the species in Figure 5.10. Notably, the calculated $|C_Q(^{35}Cl)|$ of the dihydrate is actually *larger* than that of the anhydrous compound while experimentally, the $|C_Q(^{35}Cl)|$ of $MgCl_2 \cdot XH_2O$ was significantly smaller than that of the anhydrous salt. Thus, the species is most likely

$MgCl_2 \cdot 4H_2O$, as the calculated value of $|C_Q(^{35}Cl)|$ for that hydrate is much smaller than that of the anhydrous form. Although the overestimation is not as great as has been observed for the organic hydrochlorides (as shown by Figure S4.2 in Appendix 4), it is consistent with the degree of overestimation observed for the anhydrous magnesium chloride, and magnesium chloride hexahydrate. Figure 5.12 demonstrates this agreement, presenting the computational and experimental $|C_Q(^{35}Cl)|$ graphically under the assumption that the unknown species is $MgCl_2 \cdot 4H_2O$. Comparison of the calculated Ω and $\delta_{iso}(^{35}Cl)$ values to the experimental value for $MgCl_2 \cdot XH_2O$ further validates the material is the tetrahydrate as the expected overestimation is observed. It should be noted, however, that the calculated value for the dihydrate would also conform to this expectation.

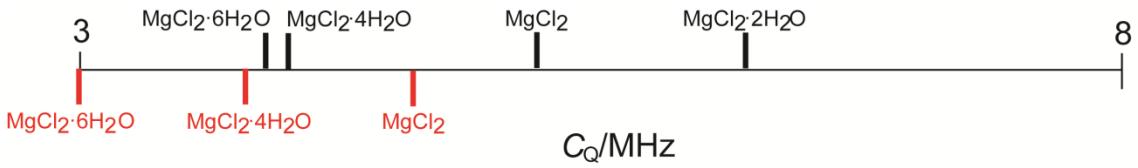

Figure 5.12. Scale of the magnitudes of the chlorine-35 quadrupolar coupling constants for magnesium chloride, magnesium chloride dihydrate, magnesium chloride tetrahydrate and magnesium chloride hexahydrate. Experimental values are in red and calculated values are in black. The experimental value for the hexahydrate is from reference 5.

The series of experimental data do conform to the earlier observations that the $|C_Q(^{35}Cl)|$ of a material decreases upon hydration.[6,25] In addition, experimentally an increase in the number of hydrogen-chlorine interactions does lead to a smaller $|C_Q(^{35}Cl)|$, as has been noted earlier in this document and in earlier chlorine studies.[27-29] However in two cases, one of the chlorine sites

in $MgCl_2 \cdot H_2O$ and the chlorine site in $MgCl_2 \cdot 2H_2O$, calculations predict a $|C_Q(^{35}Cl)|$ which is much greater than the calculated value for the anhydrous version. Interestingly, in the case of magnesium chloride monohydrate it is the site which has an interaction with two hydrogens which actually has the *larger* $|C_Q(^{35}Cl)|$! It is significant that the hexahydrate, which displays the smallest $|C_Q(^{35}Cl)|$ only interacts with hydrogens (no magnesium), as shown in Figure 5.11, which is different from all the other hydrates. Unlike the case for $|C_Q(^{35}Cl)|$, the trend that the chlorine chemical shift decreases upon hydration is observed for all hydrates experimentally (see Table 5.3) and computationally (Table 5.4). There is no trend between the *degree* of hydration and either property, however, similar to the case for other alkaline earth chlorides (e.g., strontium chloride).[6]

Examination of the known properties of the mono-, di- and tetrahyrates of magnesium chloride also point to the spectra in Figure 5.10 being that of the tetrahydrate. As expected, the tetrahydrate is the first lower hydrate to form upon heating bischofite, appearing at 369 K,[9] but can also be synthesized by passing hydrochloric acid into a solution of magnesium chloride.[30] The dihydrate and monohydrate do not appear in the dehydration of bischofite until heating temperatures of 380 and 426 K, respectively.[9] The dihydrate can also be produced in excess of hydrochloric acid while the monohydrate has been produced by blowing hydrochloride gas over the hexahydrate at 408 K.[31] Clearly high temperatures are needed to produce the monohydrate while excess reagent or high temperatures are needed to produce the dihydrate. Thus, it is not surprising that it was the tetrahydrate which formed when anhydrous beads were exposed to air. Given the stability of the hexahydrate, it is possible that bischofite would have been the eventual product had the beads been exposed to a more humid environment, or been left in air for a longer period of time.

5.3.2.3 Another Magnesium Chloride Solvate: $MgCl_2 \cdot 6NH_3$

In addition to the hexahydrate, a hexammine is also stable at room temperature and is a fluffy, white powder which smells vaguely of ammonia. Spectra of the hexammine were collected under MAS and stationary conditions at 11.7 T and 21.1 T. All displayed the same basic shape and therefore only one spectrum is shown in Figure 5.12, collected under stationary conditions at 11.7 T. No lineshape could be observed under MAS or, unlike the chloride ion receptor studied in Chapter 4, under stationary conditions at either 11.7 T or 21.1 T. The appearance of these spectra is *very* different from all of the magnesium chloride species, as it is much narrower and does not display a second-order quadrupolar lineshape. This indicates a negligible EFG at the chlorine nucleus and no extraction of chlorine SSNMR parameters was attempted. Variable temperature experiments were done at 11.7 T to determine if the shape was entirely due to motion and if lower temperature experiments would result in the emergence of a signal with a more defined lineshape. The temperature was varied from 80°C down to -72°C. Throughout all temperatures, the shape of the spectrum did not change significantly, nor did any additional sites appear. This demonstrates that the narrow nature of the spectrum is likely not solely caused by motion about the chlorine.

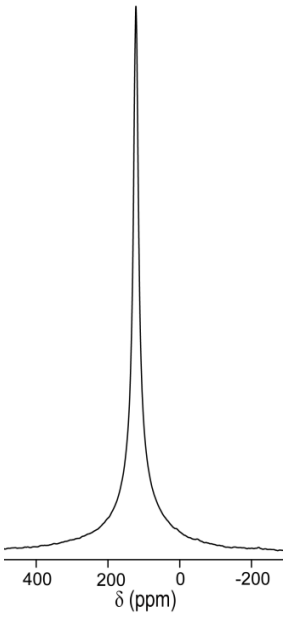

Figure 5.13. Chlorine-35 SSNMR spectrum of $MgCl_2 \cdot (6NH_3)$ collected under stationary conditions at 11.7 T.

The narrow lineshape for $MgCl_2 \cdot (6NH_3)$ can be explained easily by looking at the local environment about chlorine in the material. The material crystallizes in the very high symmetry rock-salt structure (*Fm-3m*), with chlorine sitting at a -43m site (i.e., the same as tetrahedral).[20] This is not the actual symmetry in the case of $MgCl_2 \cdot 6NH_3$ as the 96j sites are only 3/4 occupied (they would be fully occupied in the case of NH_4^+ groups). The symmetry is quite high, however, as chlorine is surrounded by 12 NH_3 groups – with all the Cl-N distances at 3.440 Å and distributed evenly about the chlorine.[12,20] This configuration explains why the chlorine SSNMR spectrum is so close to that of ammonium chloride – with a difference of between 1-2 ppm between the chemical shifts of $MgCl_2 \cdot 6NH_3$ and NH_4Cl! Spectra of ammonium chloride were collected to ensure the sample was not just the simple salt and the small chemical shift, and a slight change in shape, was noted. In addition, heating the sample did lead to a significant broadening of the spectrum (and a loss of the narrow signal at ~122 ppm) as would be expected

as ammonia is known to released from the structure at certain heating temperatures (see introduction). This behaviour would not be expected if the sample was simply ammonium chloride. Magnesium chloride hexammine would be expected to have a very narrow signal given the structure, as confirmed by B3LYP/RHF cluster calculations which predict a small, but nonzero $|C_Q(^{35}Cl)|$ of 1.1 MHz, an η_Q value near 1 (0.97). While the calculations predict some CSA (Ω of 19 ppm), no real lineshape is observed under stationary conditions, even at 21.1 T, indicating near isotropy of the CS tensor. Unfortunately, GIPAW-DFT calculations could not be done due to the ¾ occupancy of the hydrogen sites. The broadness at the base of the peaks in Figure 5.12 is potentially the result of some $MgCl_2$ which is only partially aminated, as lower amminates (such as $MgCl_2 \cdot 2NH_3$) are also known[13] and the hump is not broad enough to be anhydrous $MgCl_2$.

It is clear from the spectra presented in Figures 5.8, 5.9, 5.10 and 5.13 that the chlorine SSNMR parameters are highly sensitive in the case of hydrates and solvates. The above sections demonstrate that chlorine SSNMR can be used to easily distinguish, and in some cases identify an unknown species.

5.4 Conclusions

Chlorine-35/37 SSNMR spectroscopy was used to characterize the chlorine environments in the two polymorphs of benzidine hydrochloride and various hydrates/solvates of magnesium chloride. In both cases, it was clearly demonstrated that chlorine SSNMR had the ability to unequivocally distinguish between different polymorphs and solvates. The accuracy of both the EFG and CS tensor parameters was ensured through the collection of the spectra at a minimum of two applied magnetic fields, including the ultrahigh-field 21.1 T instrument. As has been

observed in previous chapters, the high field was essential for determination of accurate determination of the CS tensor parameters, in particular.

The two room-temperature polymorphs of benzidine hydrochloride, which were both crystallized under the *same* conditions, were found to have unique EFG tensor parameters and CS, although the full CS tensor could only be fully characterized for the more common triclinic polymorph. Notably, the less common orthorhombic form was found to have a significantly larger $|C_Q(^{35}Cl)|$ than the two sites in the triclinic form (5.8 MHz vs. 4.56 and 4.47 MHz, respectively) but also displayed significantly smaller CSA, demonstrating the independence of these two tensors. GIPAW-DFT calculations on the two polymorphs displayed the same overestimation previously observed for $|C_Q(^{35}Cl)|$ and the chlorine CS.

Chlorine-35/37 SSNMR spectra were also collected for the anhydrous form of magnesium chloride and an unknown hydrated form that resulted from exposing the anhydrous beads to air for several months. The EFG and CS tensor parameters, along with their relative orientation, were determined for both compounds and found to be distinct from one another and magnesium chloride hexahydrate, which has been previously studied. As many lower hydrates of magnesium chloride are known and have had their crystal structures determined, GIPAW-DFT calculations were carried out to determine the identity of the unknown hydrate. Using the trends observed in previous chapters and the extracted SSNMR parameters, the unknown hydrate was identified as magnesium chloride tetrahydrate. The experimental data from the anhydrous, tetrahydrate and hexahydrate forms of magnesium chloride were found to follow the previously observed trends that hydration leads to a smaller $|C_Q(^{35}Cl)|$ and a lower chlorine CS. In addition, a second solvate, magnesium chloride hexammine, was also examined and found to have a very

different chlorine SSNMR spectrum from both the anhydrous and hexahydrate forms, demonstrating the ability of chlorine SSNMR to distinguish between different *types* of solvates.

5.5 References

1 J. Bernstein, *Cryst. Growth Des.,* **2011**, *11*, 632.

2 S. Lohani and D. J. W. Grant, *Polymorphism,* **2006**, 21.

3 C. E. Housecroft and A. G. Sharpe, *Inorganic Chemistry*, Prentice Hall, Harlow, England, 2008.

4 W. C. McCrone, Polymorphism. In *Physics and Chemistry of the Organic Solid St*ate, D. Fox, M. M. Labes and A. Weissberger, Eds., Wiley Interscience, New York, 1965.

5 H. Hamaed, J. M. Pawlowski, B. F. T. Cooper, R. Fu, S. H. Eichhorn and R. W. Schurko, *J. Am. Chem. Soc.,* **2008**, *130*, 11056.

6 D. L. Bryce and E. B. Bultz, *Chem. Eur. J.,* **2007**, *13*, 4786.

7 C. H. Koo, H. S. Kim and H. S. Shin, *J. Korean Chem. Soc.,* **1972**, *16*, 18.

8 L. Dobrzycki and K. Wozniak, *CrystEngComm,* **2006**, *8*, 780.

9 K. Sugimoto, R. E. Dinnebier and J. C. Hanson, *Acta Crystallogr., Sect. B: Struct. Crystallogr. Cryst. Chem.,* **2007**, *63*, 235.

10 F. Cotton and G. Wilkinson, *Basic Inorganic Chemistry*, Wiley, New York, New York, 1976.

11 P. A. Agron and W. R. Busing, *Acta Crystallogr., Sect. C: Cryst. Struct. Commun.,* **1985**, *41*, 8.

12 C. H. Christensen, R. Z. Sørensen, T. Johannessen, U. J. Quaade, K. Honkala, T. D. Elmøe, R. Køhler and J. K. Nørskov, *J. Mater. Chem.,* **2005**, *15*, 4106.

13 H. S. Jacobsen, H. A. Hansen, J. W. Andreasen, Q. Shi, A. Andreasen, R. Feidenhans'l, M. M. Nielsen, K. Ståhl and T. Vegge, *Chem. Phys. Lett.,* **2007**, *441*, 255.

14 J. S. Hummelshøj, R. Z. Sørensen, M. Y. Kustova, T. Johannessen, J. K. Nørskov and C. H. Christensen, *J. Am. Chem. Soc.,* **2006**, *128*, 16.

15K. Bradenburg, *Diamond,* version 3.0e, Crystal Impact GbR, Bonn, Germany, 1997–2005.

16 I. D. Weisman and L. H. Bennett, *Phys. Rev.,* **1969**, *181*, 1341.

17 A. C. Kunwar, G. L. Turner and E. Oldfield, *J. Mag. Reson.,* **1986**, *69*, 124.

18 I. Solomon, *Phys. Rev.,* **1958**, *110*, 61.

19 D. E. Partin and M. O'Keeffe, *J. Solid State Chem.,* **1991**, *95*, 176.

20 I. -. Hwang, T. Drews and K. Seppelt, *J. Am. Chem. Soc.,* **2000**, *122*, 8486.

21 D. L. Bryce, C. M. Widdifield, R. P. Chapman and R. J. Attrell, Chlorine, Bromine and Iodine Solid-State NMR. In *NMR of Quadrupolar Nuclei Handbook*, R.E. Wasylishen, S. E. Ashbrook and S. Wimperis, S., Eds., John Wiley and Sons Ltd., Chichester, UK, 2011.

22 D. L. Bryce, M. Gee and R. E. Wasylishen, *J. Phys. Chem. A,* **2001**, *105*, 10413.

23 R. Custelcean, L. H. Delmau, B. A. Moyer, J. L. Sessler, W. -S. Cho, D. Gross, G. W. Bates, S. J. Brooks, M. E. Light and P. A. Gale, *Angew. Chem., Int. Ed.,* **2005,** *44*, 2537.

24 P. A. Gale, J. L. Sessler, V. Kral and V. Lynch, *J. Am. Chem. Soc.,* **1996**, *118*, 5140.

25 C. M. Widdifield and D. L. Bryce, *Can. J. Chem.,* **2011,** *89*, 754.

26 K. Sasvari and G. A. Jeffrey, *Acta. Cryst.,* **1966**, *20*, 875.

27 D. L. Bryce, G. D. Sward and S. Adiga, *J. Am. Chem. Soc.,* **2006**, *128*, 2121.

28 D. L. Bryce and G. D. Sward, *J. Phys. Chem. B.,* **2006**, *110*, 26461.

29 D. L. Bryce, G. M. Bernard, M. Gee, M. D. Lumsden, K. Eichele and R. E. Wasylishen, *Can. J. Anal. Sci. Spect.,* **2001**, *46*, 46.

30 H. Lescoeur, *Ann. Chim. Phys.,* **1894**, *2*, 78.

31 W. Moldenhauer, *Z. Anorg. Chem.,* **1906**, *51*, 369.

Chapter 6

Multinuclear Solid-State Nuclear Magnetic Resonance and GIPAW-DFT Analysis of Solid Group 13 Chlorides

6.1 Introduction and Objectives

6.1.1 Introduction

Inorganic catalyst systems play an important role in a variety of organic and inorganic chemical reactions.[1] Several group 13 chloride salts are of synthetic importance, with each of the aluminum, gallium, and indium trichlorides acting as a catalyst in a variety of organic reactions.[2-8] These include the synthesis of substituted tetrahydrofurans,[2] aromatic alkylation,[7] and the Diels-Alder reaction.[5] There are fewer synthetic applications of gallium dichloride and indium monochloride, but $GaCl_2$ has found use as a catalyst in the production of carbonyl chlorides from chlorine and carbon monoxide,[9] while InCl has found recent use in mediating radical carbon-carbon bond formation in aqueous media.[10]

As has been shown in earlier chapters, while the presence of a QI complicates the acquisition of NMR spectra, proper interpretation of the data provides additional information compared to spin-1/2 nuclei. In chapters 3 and 5, while the QI was the dominant interaction, the spectra collected were narrow enough to be collected in a single spectral window. In the case of the group 13 chlorides, the QI is expected to be much greater due to the high deviation from symmetric environments about the chlorine in these materials. Despite the expected dominance of the QI over the $^{35/37}$Cl NMR spectra, it is still hypothesized that under favourable conditions, information on both the EFG and CS tensors may be determined. As described in Chapter 1, as the effects of second-order quadrupolar broadening are inversely proportional to the applied field

(B_0), SSNMR experiments on quadrupolar nuclei in the highest possible magnetic fields are desirable. In addition to the reduction of second-order quadrupolar effects, high magnetic fields aid in the extraction of the CS tensor, as the impact of this tensor on the spectrum is proportional to B_0. The need for a large B_0 field is therefore most pronounced for materials which are expected to have very large QIs, such as the group 13 chlorides. The availability of a 21.1 T magnet at the Ultrahigh-field NMR Facility for Solids in Ottawa has been a boon to chlorine SSNMR studies on materials with large QIs. For example, Schurko and co-workers recently acquired $^{35/37}$Cl SSNMR spectra for a series of organometallic compounds, including Schwartz's reagent, in which chlorine-35 C_Q values of up to 22.1 MHz were observed.[11]

Prior chlorine SSNMR studies of the group 13 chlorides are non-existent, except for a single ^{35}Cl spectrum of $AlCl_3$ collected under stationary conditions.[12]

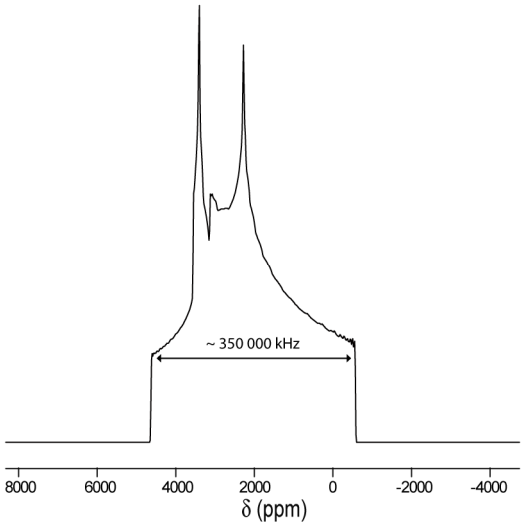

Figure 6.1. Simulated spectrum of aluminum trichloride at 14.4 T, using the parameters reported by Stebbins and co-workers in reference 12.

This spectrum, which was collected as part of a larger SSNMR study of chlorine-containing glasses, was analyzed to give a chemical shift of 2880 ppm (w.r.t. 1 M NaCl(aq)) and a quadrupolar coupling constant of 9.4 MHz. A spectral simulation using the parameters reported in the study is shown in Figure 6.1. The breadth of the simulated spectrum shown in Figure 6.1 is approximately 350 000 Hz. While the quadrupolar coupling constant value seems reasonable for ionic chloride in a non-symmetric environment, the chemical shift is anomalous, appearing to be deshielded by more than 1700 ppm with respect to any other material on the chemical shift scale shown in Chapter 1 and reproduced below in Figure 6.2.[13]

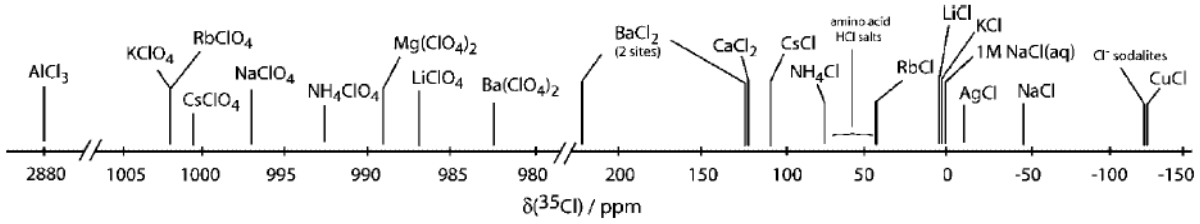

Figure 6.2. Representative solid-state chlorine isotropic chemical shifts with respect to 1 M NaCl(aq) published in 2006. Reproduced from reference 13.

The causes of this high chemical shift were not discussed and therefore the origin of the large deshielding about the chlorine nucleus is unknown.[12]

Aluminum, gallium, and indium are also candidates for study by SSNMR spectroscopy. ^{27}Al (N.A. = 100 %; I = 5/2; Q = 146.6 mb)[14] NMR is very common in the solid state due to the prevalence of aluminum in a wide variety of materials (*e.g.*, glasses, soils) and its favourable NMR properties.[15] Gallium-69 (N.A. = 60.4 %) and gallium-71 (N.A. = 39.6 %) have nuclear spin quantum numbers of 3/2 and quadrupole moments of 171 mb and 107 mb, respectively.[14] While the Larmor frequency and quadrupole moment of ^{71}Ga are similar to those of ^{27}Al, the

lower spin number results in spectra that are broader, due to the inverse relationship between *I* and broadening of the CT. Indium also has two NMR-active quadrupolar isotopes: indium-113 (N.A. = 4.28 %) and indium-115 (N.A. = 95.72 %). Both isotopes have spins of 9/2 with particularly large *Q* values of 770 and 759 mb, respectively.[14] These large *Q* values result in proportionately large nuclear quadrupolar coupling constants; however, the high spin values significantly reduce the broadening of the CT, as shown in equation 1.21 in Chapter 1.[16] Given the periodic nature of the highly ionic salts studied, GIPAW-DFT was selected as the computational method to be used.

6.1.2 Objectives

Given the anomalously high chlorine CS previously reported for aluminium trichloride (*vide supra*), a chlorine SSNMR study of several group 13 chlorides was undertaken to determine if this property would be observed for other similar systems, and potentially determine its cause. In addition, the study was an opportunity to determine if chlorine SSNMR and GIPAW-DFT could successfully characterize inorganic systems in which the quadrupolar interaction is much greater than in organic chlorides.

6.2 Experimental

6.2.1 Sample Preparation

All samples were purchased from Sigma-Aldrich Canada Ltd. and used without further purification. Due to the air and moisture sensitivity of the compounds, all NMR samples were packed in the dry argon atmosphere of a glove box. As it has been shown that a capped rotor is protected completely from the atmosphere,[17] no additional methods were done to seal samples packed in 4 mm rotors. Those samples packed in 10 mm glass tubes were hermetically sealed with epoxy prior to removal from the inert atmosphere.

6.2.2 NMR spectroscopy

6.2.2.1 Experiments Carried out at 11.7 T

Indium-115, aluminum-27, chlorine-35 and gallium-69/71 SSNMR experiments were carried out on a 500 MHz (B_0 = 11.75 T) Bruker Avance spectrometer at the University of Ottawa, at resonance frequencies of 109.57, 130.29, 49.00, 120.02, and 152.48 MHz, respectively. All experiments were carried out using a 4 mm Bruker triple resonance probe. Samples were ground into fine powders and packed into 4 mm o.d. zirconia rotors in an argon atmosphere. Experimental setup and pulse calibration for chlorine-35 was performed using powdered NaCl. In all other cases, experimental setup and pulse calibrations were performed using the recommended IUPAC standards:[18] 0.1 M indium nitrate in 0.5 M nitric acid, 0.1 M aluminum nitrate in D_2O and 1.1 *m* gallium nitrate in D_2O. All spectra were collected at room temperature and were referenced to their standard (or solid NaCl for chlorine) at 0 ppm. The solid (solution value scaled by I+1/2) $\pi/2$ pulse lengths were 1.2 µs for ^{27}Al, 3.0 µs for ^{35}Cl, 1.2 µs for ^{115}In, 3.1 µs for ^{71}Ga and 2.9 µs for ^{69}Ga. The recycle delays used were 4 s for chlorine 0.5 to 1.0 s for all other nuclei. Spectra collected under stationary conditions used echo sequence introduced in Chapter 2. MAS spectra were collected using a simple Bloch decay following a single π /2 pulse.

6.2.2.2 Experiments Carried out at 21.1 T

Chlorine-35/37, indium-113/115, aluminum-27, and gallium-69/71 NMR experiments were performed on the 900 MHz (B_0 = 21.14 T) Bruker Avance II spectrometer at the National Ultrahigh-Field NMR Facility for Solids in Ottawa. Resonance frequencies were 88.18, 73.40, 197.23, 196.79, 234.51, 216.03, and 274.46 MHz, respectively. A specially produced single-channel 10 mm static solenoid probe was used for all chlorine NMR experiments. A 4 mm

double resonance probe and a 3.2 mm Bruker DVT MAS HX probe were used for all other experiments. Experimental setup, pulse calibration, and referencing were done using the same setup samples as described above, with powdered NaCl also serving as the ^{37}Cl reference. The CT centreband of NaCl was set to 0 ppm and the 'solid' $\pi/2$ chlorine-35 and chlorine-37 pulses were found to be 4.4 μs and 4.5 μs respectively. A recycle delay of 2 s was used for all chlorine acquisitions. The solid (scaled) $\pi/2$ pulses used were 0.6 μs for ^{113}In, 0.6 μs for ^{115}In, 1.4 μs for ^{69}Ga and 1.8 μs for ^{71}Ga. $^{35/37}$Cl NMR spectra of all stationary samples, with the exception on InCl, were collected using the quadrupolar Carr-Purcell-Meiboom-Gill (QCPMG) pulse sequence and VOCS acquisition, as described in Chapter 2. The QCPMG experiment, consisting of a train of π pulses following an initial $\pi/2$ pulse, was necessary in order to achieve a sufficiently high signal-to-noise ratio in a reasonable amount of time. Between 20 and 45 experiments were performed for each material, with the transmitter frequency being stepped in increments of either 25000 or 50000 Hz. The chlorine spectra of InCl were all collected using the $\pi/2 - \tau - \pi/2 - \tau$ - ACQ solid-echo pulse sequence.[19-21]

6.2.3 Data Processing and Simulations

NMR spectra were processed using the Bruker TopSpin 1.3 program. For variable-offset experiments, individual subspectra were co-added to produce the overall spectrum, the static bandshape of which was then simulated. The WSolids software package was used to simulate all NMR spectra.[22] This software incorporates the space-tiling algorithm of Alderman *et al.*[23] All NMR plots were created with DMFit.[24]

All simulations were in the absence of dipolar coupling between $^{35/37}$Cl and nearby group 13 metals, as these interactions are negligible. For example, the shortest contact between chlorine and a neighbouring group 13 ion is 2.095 Å in $GaCl_3$ which corresponds to a dipolar coupling

constant of 308 Hz (between chlorine-35 and gallium-69), an insignificant value given the breadth of the spectrum. All other dipolar couplings were less than this value.

6.2.4 GIPAW-DFT Calculations

All quantum chemical calculations were carried out with the CASTEP program in Materials Data Studio 3.2.[25,26] Calculations of the chlorine nuclear MS and EFG tensors were done using atomic coordinates and cell parameters from the X-ray structures of Troyanov for aluminum trichloride,[27] Troyanov and co-workers for gallium trichloride,[28] Templeton and Carter for indium trichloride,[29] Garton and Powell for gallium dichloride[30] and Maaskant and co-workers for indium monochloride.[31]

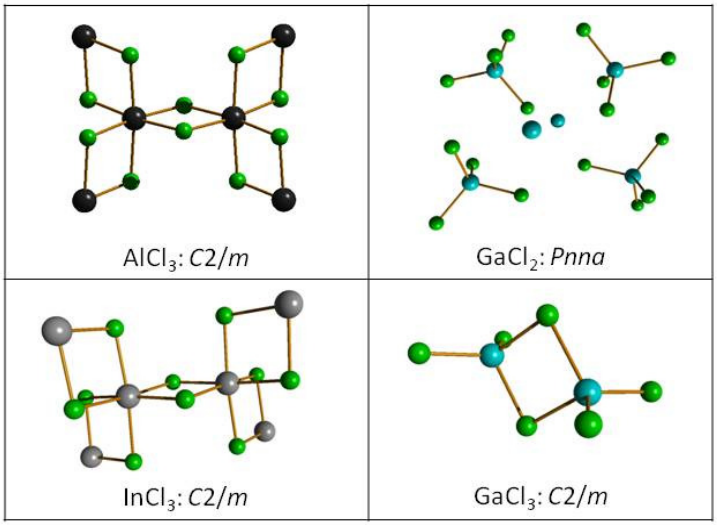

Figure 6.3. Local structures and space groups of the anhydrous group 13 trichlorides and dichloride included in this study. Chlorine atoms are shown in green, aluminum in black, indium in grey and gallium in turquoise.

The atomic coordinates, cell parameters and space groups were used in the input file. The local structures of the group 13 dichloride and trichlorides are shown in Figure 6.3, with the exception of indium trichloride hexahydrate, for which no crystal structure exists. The structure about one

of the four chlorine sites in indium monochloride is shown in Figure 6.4. However, it should be emphasized that the infinite crystal lattice is treated within the GIPAW-DFT calculations, not the isolated models shown in Figure 6.3 and 6.4.

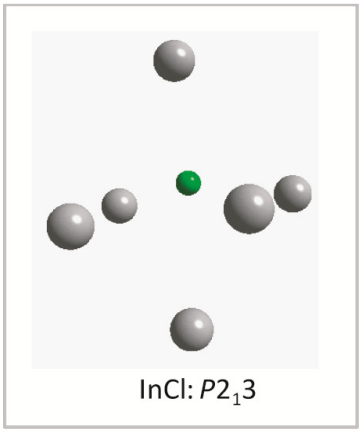

Figure 6.4. Local structure of indium chloride. Chlorine atoms are shown in green and indium in grey.

The plane wave energy cutoff and number of k-points were increased to ensure convergence for all materials. For example, a graph demonstrating the convergence of the ^{35}Cl $\delta_{iso}(^{35}Cl)$ values for $AlCl_3$ with respect to cutoff energy is shown in Figure 6.5. All calculated values reported here use a 610 eV energy cutoff and a minimum of 30 k-points for the trichlorides. The k-point grids used for all calculations are included in Appendix 5. The 'on-the-fly' pseudopotential files used for indium and gallium were obtained directly from Accelrys.

The EFG and shielding tensors contained in the CASTEP .magres files were analyzed using a modified version of the EFGShield program (version 2.2).[32]

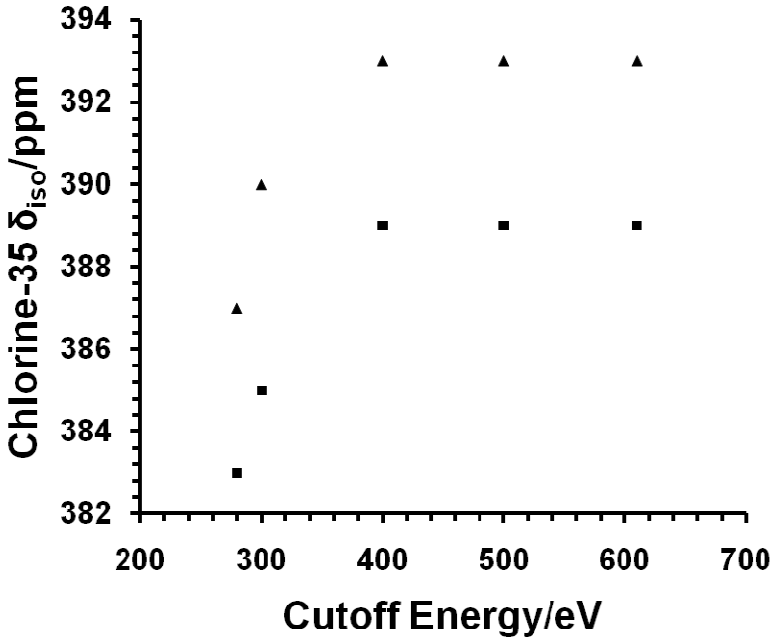

Figure 6.5. Convergence of the chlorine chemical shift with increasing plane-wave cutoff energy, for $AlCl_3$. Site one appears in squares and site two is triangles. A cutoff energy of 610 eV was used for all calculations presented in this chapter.

6.3 Results and Discussion

6.3.1 NMR Spectroscopy

The experimentally determined chlorine EFG and CS tensor data, obtained by spectral simulation of the ^{35}Cl and ^{37}Cl NMR spectra of the group 13 chloride salts, are listed in Table 6.1. For each of the salts, two spectra were simulated simultaneously: a ^{35}Cl spectrum and a ^{37}Cl spectrum both collected at 21.1 T. For all materials studied, the ^{37}Cl NMR spectrum was fit with identical parameters to the corresponding ^{35}Cl NMR spectrum, with only the quadrupolar coupling constant reduced to 78.8 % of the original value, due to the smaller value of $Q(^{37}\text{Cl})$.

Table 6.1. Experimental chlorine-35/37 EFG and CS tensor parameters for solid group 13 chlorides

		$\lvert C_Q(^{35}Cl)\rvert$ / MHz[a]	η_Q	δ_{iso} / ppm[b]	Ω / ppm	κ	α, β, γ/°
aluminum trichloride		22.5(1.0)	0.63(10)	325(100)	300(200)	-0.5(5)	90(20), 90(20), 0(20)
gallium trichloride	terminal	40.4(2.0)	0.03(5)	200(100)			[c]
	terminal	38.1(2.0)	0.09 (5)	150(100)			
	bridging	28.3(2.0)	0.48(5)	250(100)			
gallium dichloride		31.2(7)	0.15(20)	200(100)	200(200)	-0.5(5)	90(20), 90(20), 0(20)
		32.0(7)	0.20(20)	200(100)	200(200)	-0.5(5)	90(20), 90(20), 20(20)
indium trichloride		24.5(1.0)	0.52(10)	375(100)	500(200)	0.5(5)	20(20), 90(20), 30(20)
indium trichloride hexahydrate		23.4(3.0)	0.27(20)	130(100)			[c]

[a]Chlorine-37 quadrupolar coupling constants were identical to $C_Q(^{35}Cl)$ x $Q(^{37}Cl)/Q(^{35}Cl) = C_Q(^{35}Cl)$ x 0.788, within experimental error. [b]Isotropic chemical shifts are reported relative to solid NaCl at 0 ppm. [c]Not determined

The above approach was successful for the extraction of NMR parameters in all cases but indium monochloride. In the latter case, the presence of four unique chemical environment with similar, and relatively small, $C_Q(^{35}Cl)$ magnitudes made it impossible to accurately extract the NMR parameters and therefore it is not included in Table 6.1. For all other cases, the magnitude of $C_Q(^{35}Cl)$ ranges from 22.45 to 40.44 MHz. This range is significantly larger than those observed for the alkaline earth metal chlorides and their hydrates, for which $C_Q(^{35}Cl)$ ranges from 0 to 8.82 MHz.[33,34] The CS tensor spans measured are also slightly larger, ranging from 200 to 500 ppm, compared to less than 100 ppm for the alkaline earth metal chloride hydrate salts. The observed isotropic chemical shifts, which range from 150 to 375 ppm, are slightly higher than those of the alkaline earth metal chlorides but in line with those observed by Rossini *et al.* in their recent study of chlorine-containing organometallic compounds.[13] Below, specific results for each of the compounds are discussed in turn.

6.3.1.1 $AlCl_3$

The chlorine-35 C_Q value observed for $AlCl_3$ is 22.5 ± 1.0 MHz. Both chlorine-35 and chlorine-37 SSNMR spectra and simulations are shown in Figure 6.6. The small amount of intensity that is observed on either side of the CT arises from the STs. Unlike the C_Q, the CS tensor span observed was not the smallest amongst the group 13 chlorides, at 300 ± 200 ppm. The isotropic chemical shift was at the upper end of those observed, 325 ± 100 ppm.

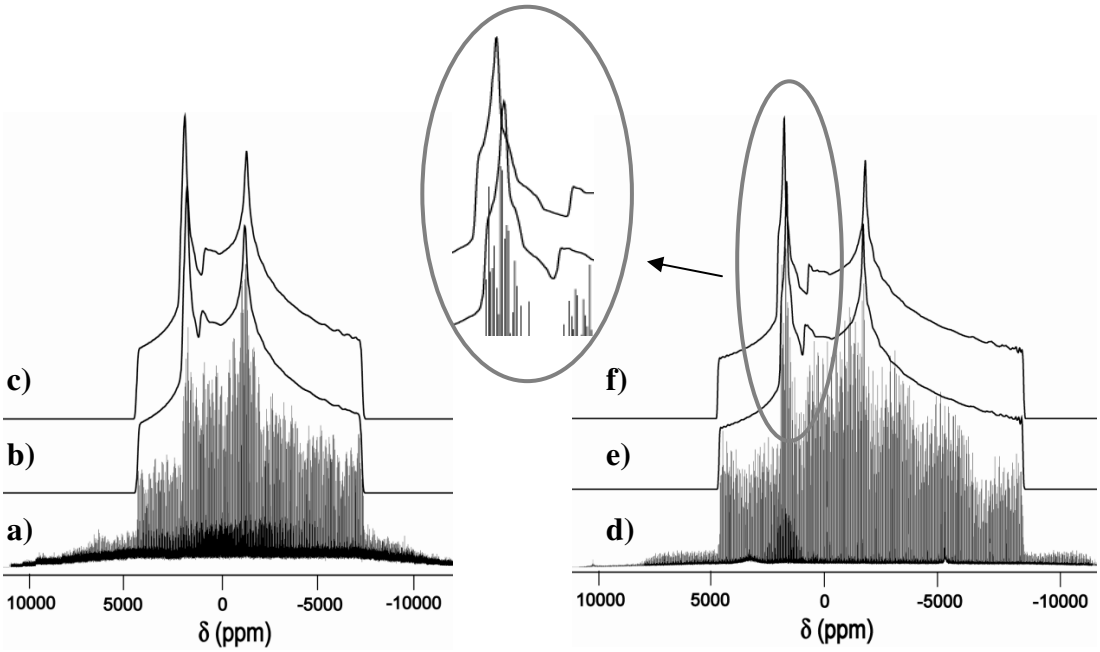

Figure 6.6. Experimental (a, d) and simulated solid-state chlorine-35 (right) and chlorine-37 (left) NMR spectra of aluminum trichloride at 21.1 T. Best-fit simulations are shown in b and e. Simulations assuming no CSA are shown are in c and f. The inset highlights the necessity of including CSA in the fit. The spikelet spacing used in all spectra was 2500 Hz.

The structure of $AlCl_3$ is known to consist of Cl^- ions in a distorted cubic close packed arrangement, with the Al^{3+} ions occupying the octahedral holes of alternating Cl^- layers (Figure 6.3).[27] Although aluminum trichloride has two magnetically distinct chlorine sites, their very similar chemical environments and the large amount of second-order quadrupolar broadening prevented their resolution, and therefore a single set of average parameters representative of both sites is reported. Both chlorides are 'bridging' and therefore the reported EFG and CS tensor parameters may be taken as representative of this type of chemical environment. Given the large value of $C_Q(^{35}Cl)$ for $AlCl_3$ and the breadth of the chlorine-35/37 SSNMR spectra (over 1 MHz at 21.1 T), it is clear that the QI dominates the CS contributions. Despite this, however, the CT line shape could not be perfectly simulated in the absence of some CSA. Included in Figure 6.6

are simulations assuming an isotropic chemical shift tensor and, while the effects are small compared to the second-order quadrupolar broadening, it is seen that CSA is required to achieve the best possible fit. Removal of CSA in the simulation shifts the position of a key spectral feature by ~150 ppm (Figure 6.6). This feature cannot be shifted in the same manner, without perturbing other spectral features, by including only quadrupolar effects in the simulation. Perhaps the most convincing evidence for the presence of CSA is its required inclusion in both the chlorine-35 and chlorine-37 NMR spectral simulations. Since the value of C_Q changes but the CSA remains constant when observing the other isotope, the simultaneous fit of the spectra of both isotopes strongly supports our conclusion. It is emphasized that large errors are assigned to the span to account for the presence of two sites; quantum chemical calculations corroborate the conclusions regarding the non-negligible CSA (*vide infra*). The above arguments regarding CSA apply also to $InCl_3$ and $GaCl_2$.

As mentioned in Section 6.1.1, a ^{35}Cl SSNMR spectrum of $AlCl_3$ was collected previously in a magnetic field of 14.1 T and values of 2880 ± 40 ppm, 9.4 ± 0.2 MHz, and 0.4 ± 0.2 for δ_{iso}, $C_Q(^{35}Cl)$, and η_Q, respectively, were obtained.[12] These values differ significantly from the presently reported results. We hypothesize that the previously reported parameters likely resulted from the collection of only one 'piece' of the total spectrum. The ^{35}Cl SSNMR spectrum acquired piece-wise in this study spans over 1 MHz, including the region observed previously. Thus, it is possible that the spectrum acquired in the earlier study was only one piece of a larger spectrum, which is plausible given that the published spectrum is largely featureless. An alternative possibility is that the spectrum collected was actually that of a hydrated form of aluminum trichloride, such as $AlCl_3 \cdot 6H_2O$.[35] Addition of water to the structure would be expected to increase the symmetry about the chlorine site, and therefore decrease the ^{35}Cl

quadrupolar coupling constant, consistent with the value observed previously. The chlorine chemical shift, however, would not be expected to increase by such an amount (more than 2500 ppm) and therefore the hypothesis that only a section of the total spectrum was collected is more plausible.

The aluminum-27 SSNMR spectrum of $AlCl_3$ was also collected at 11.75 T under stationary conditions (not shown) and was consistent with the C_Q values reported in literature from previous ^{27}Al SSNMR and NQR studies.[36,37] A small C_Q value is expected given the high symmetry pseudo-octahedral environment of the aluminum. An upper limit on C_Q of 0.7 MHz could be determined, consistent with the prior studies.[36,37]

6.3.1.2 $InCl_3$

The chlorine SSNMR spectra for $InCl_3$ were found to be quite similar to those observed for $AlCl_3$, as shown in Figure 6.7. This is consistent with the fact that the two salts crystallize in the *C*2/*m* space group and have similar structures (see Figure 6.3). Simulation of the spectra resulted in a chlorine-35 C_Q value of 24.5 ± 1.0 MHz, slightly larger than that observed for $AlCl_3$. Once again, CSA was required to achieve the best possible fit (Ω = 500 ± 200 ppm), as shown in Figure 6.7. Similarly to aluminum trichloride, the indium salt has two magnetically unique 'bridging' chlorine sites that cannot be convincingly distinguished in the ^{35}Cl SSNMR spectrum and as a result the spectra were fit with only one set of parameters.

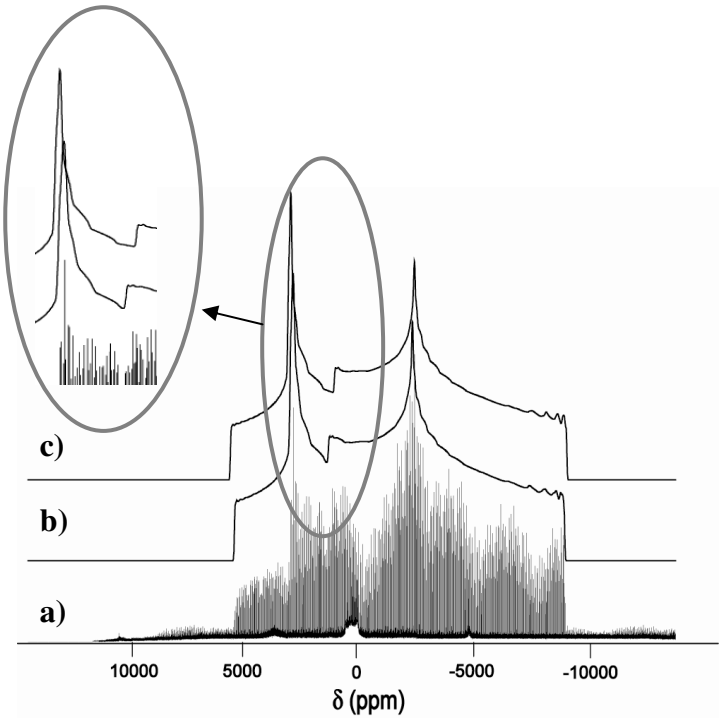

Figure 6.7. Experimental (a) and simulated solid-state chlorine-35 NMR spectra of indium trichloride at 21.1 T. The best-fit simulation is shown in b. The simulation assuming no CSA is shown in c. The inset highlights the impact of including a small amount of CSA in the fit.

Compared to aluminum trichloride, indium trichloride is a significantly weaker Lewis acid, but many of their reactive properties are similar. As shown in Figure 6.3 the structure consists of In^{3+} ions occupying the octahedral holes of alternating layers of chloride ions.[29] The primary difference between the structures of the anhydrous aluminum and indium trichlorides is the slightly longer chlorine-metal distances in indium trichloride; the average first coordination sphere Cl-M distance is 2.502 Å in $InCl_3$, while it is 2.313 Å in $AlCl_3$.[27, 29] The larger magnitude of C_Q for indium trichloride resulted in slightly wider SSNMR spectra, with the chlorine-35 spectrum spanning ~1.25 MHz. Indium trichloride displayed the largest chlorine chemical shift observed in the study at 375 ± 100 ppm, which is very close to the value observed for aluminum

trichloride. It is interesting to note that in addition to having the largest chemical shift, indium trichloride also had the longest average M-Cl distance and aluminum trichloride, with the second largest M-Cl distance, has the second largest chemical shift.

Indium-115 SSNMR spectra of $InCl_3$ were collected at 21.1 and 11.75 T under stationary conditions and are shown, along with simulations, in Figure 6.8. An indium-113 SSNMR spectrum was also collected at 21.1 T (Figure 6.8). The NMR parameters determined from simulations of these spectra are shown in Table 6.2. A single indium site was observed, consistent with the crystal structure.[29] The distorted octahedral environment about the indium site (Figure 6.3) resulted in a fairly small QI, and therefore a relatively narrow CT powder pattern, despite the large Q values for both indium isotopes. The observed indium-115 C_Q value of 28.8 ± 2.0 MHz is significantly smaller than the values of 106 to 160 MHz observed for the lower-symmetry six-coordinate indium coordination complexes included in the recent study by Wasylishen and co-workers.[38] The values obtained presently are closer to those observed for indium(III) in other highly symmetrical environments, such as tetrahedral InX_4^- or octahedral InX_6^{3-} systems.[39,40]

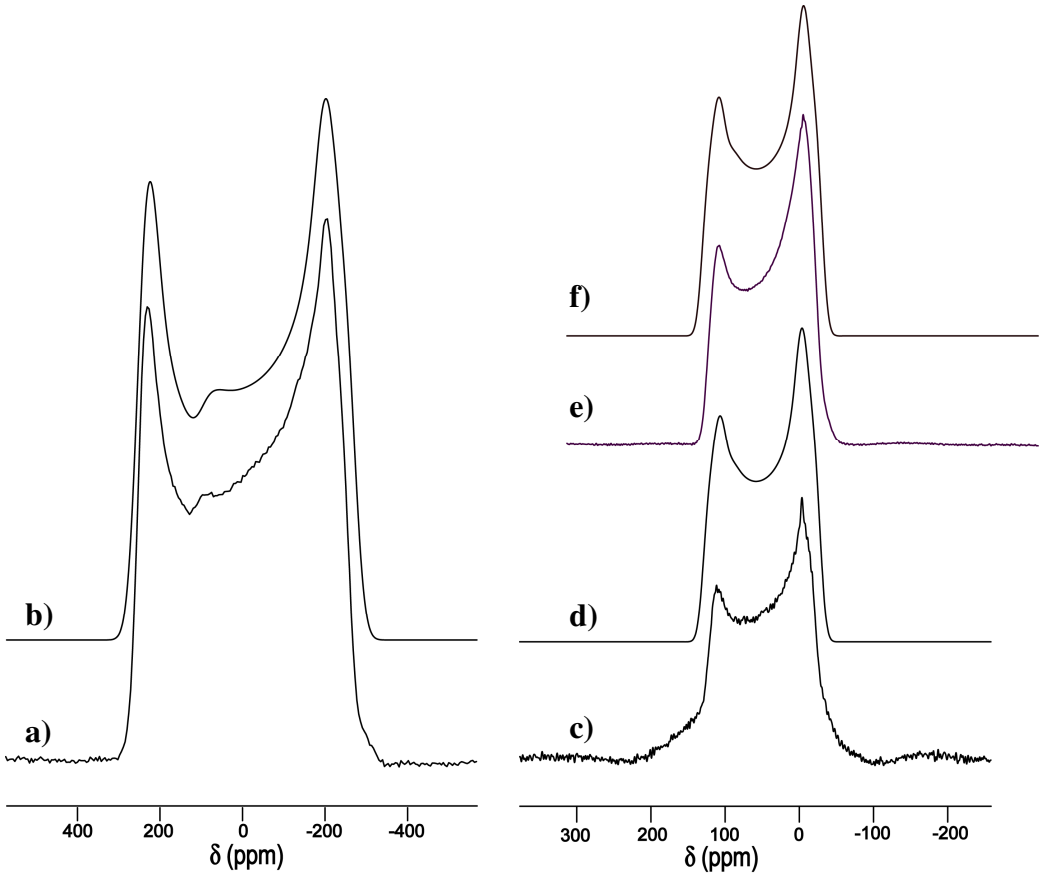

Figure 6.8. Solid-state indium NMR spectra of indium trichloride. Experimental spectra of stationary powdered samples: (a) ^{115}In at 11.75 T; (c) ^{113}In at 21.1 T; (e) ^{115}In at 21.1 T. Corresponding best-fit simulations appear in b, d and f.

Table 6.2. Experimental gallium-69/71 and indium-113/115 EFG and CS tensor parameters

	$\lvert C_Q(X)^a \rvert$ / MHz[b]	η_Q	δ_{iso} / ppm[c]	Ω / ppm	κ	α, β, γ/°
gallium dichloride	site 1 (Ga^{3+}): 6.7(1) site 2 (Ga^{+}): < 1.6	0.5(1) ~1	231(10) -610(10)	10(10) < 20	-0.5 ± 0.5 [d]	90(20), 90(20), 0(20) [d]
indium trichloride	28.80(50)	0.11(10)	74(10)	[d]	[d]	[d]

[a]X = Gallium-69 or indium-115. [b]Gallium-71 quadrupolar coupling constants were identical to $C_Q(^{69}Ga)$ x $Q(^{71}Ga)/Q(^{35}Cl) = C_Q(^{69}Ga)$ x 0.623; indium-113 quadrupolar coupling constants were identical to $C_Q(^{115}In)$ x $Q(^{113}In)/Q(^{115}In) = C_Q(^{115}In)$ x 0.986. [c]Isotropic chemical shifts are reported relative to 1.1 *m* gallium nitrate in D_2O or 0.1 M indium nitrate in 0.5 M nitric acid. [d]Not determined

6.3.1.3 $InCl_3 \cdot 4H_2O$

As described in chapter 5, chlorine SSNMR is a useful tool for study of polymorphism and solvates due to the sensitivity of SSNMR parameters to small changes in structural and electronic environment. In that chapter, this was shown for multiple materials all of which possess *relatively* small EFGs about the chlorine nucleus in contrast to many of the materials studied in this chapter. It was therefore of interest to study the effects of solvateson the chlorine SSNMR parameters of one of the chlorides included in this study, to determine if the sensitivity shown in chapter 4 is extended to materials with large QIs. Therefore, chlorine-35 and chlorine-37 VOCS spectra were collected for $InCl_3 \cdot 4H_2O$ in order to compare the resulting spectra to those of anhydrous indium trichloride.

The chlorine-35 SSNMR spectra and simulations for $InCl_3 \cdot 4H_2O$ appear in Figure 6.9. No crystal structure is available for this material and therefore the number of unique chlorine sites is not known; a single chloride site was assumed, as a single site simulation gave a reasonable fit. This hydrate of $InCl_3$ was particularly hygroscopic making data collection difficult and leading to the poor signal-to-noise ratio observed Figure 6.9. The absence of a crystal structure also eliminated the possibility for GIPAW-DFT calculations, which meant no estimation of CSA could be done. For these reasons, and the good fit obtained including only the EFG tensor parameters (along with chlorine chemical shift), none of the CSA parameters for $InCl_3 \cdot 4H_2O$ could be confidently extracted.

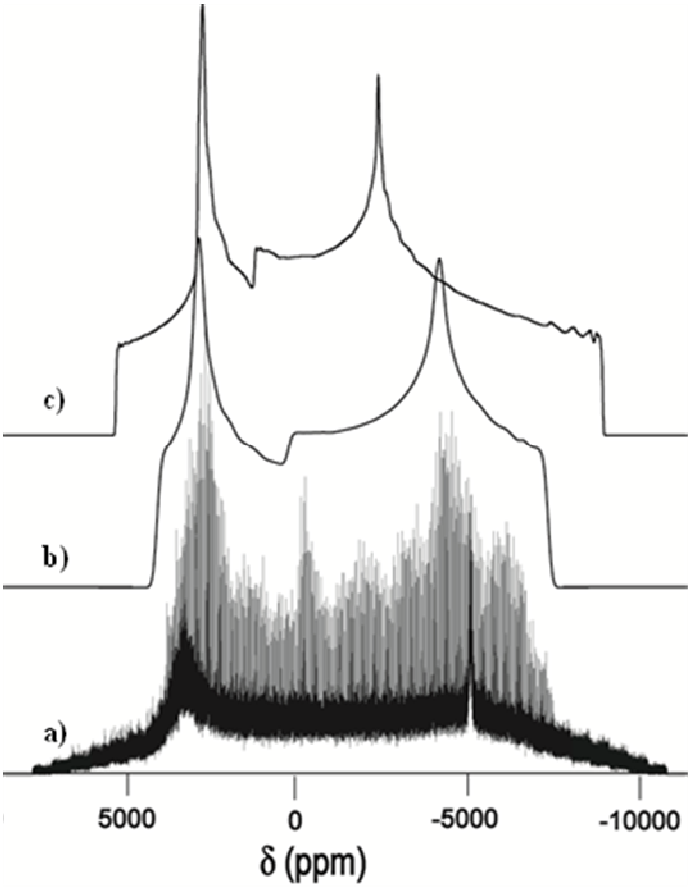

Figure 6.9. Experimental (a) and simulated solid-state chlorine-35 NMR spectra of indium trichloride hexahdyrate at 21.1 T. The best-fit simulation is shown in b. The simulation using the chlorine SSNMR parameters of anhydrous indium trichloride is shown in c.

Direct comparison of the chlorine-35 SSNMR spectra for the tetrahydrate of indium trichloride and the simulation assuming the parameters determined for anhydrous indium trihcloride, as shown in Figure 6.9, demonstrate the large difference in the chlorine-35 EFG parameters for the two materials. While the chlorine-35 C_Q does not change by a large amount, at 24.5 MHz for the anhydrous material and 23.4 MHz for the tetrahydrate, the change in the asymmetry parameter (0.52 for the anhydrous material versus 0.27 for hydrate) gives the two spectra a very different appearance. While no X-ray structure is available, the slightly lower

chlorine-35 C_Q of the hydrate versus the anhydrous salt indicates a shift to a higher symmetry environment about the chlorine nucleus. This is an expected result due to the expected formation of hydrogen-chlorine bonds in the material upon the addition of water, as was discussed in Chapter 5. These results clearly show that chlorine-NMR can distinguish solvates, even in cases of extremely large chlorine C_Q magnitudes, in addition to the cases of small EFG interactions as discussed in Chapter 4.

6.3.1.4 InCl

The chlorine environments in indium monochloride differ significantly from the other group thirteen chlorides; there are four unique chlorine environments in comparatively high symmetry environments. For this reason, the chlorine NMR spectra on InCl were much narrower than all others shown in this chapter and were collected in a single piece with the solid echo pulse sequence in lieu of QCMPG.

The chlorine-35 and chlorine-37 spectra for indium chloride collected under stationary conditions at 21.1 T appear in Figure 6.10 along with a chlorine-35 spectrum collected at 11.7 T. A simple visual comparison of these spectra with the other chlorine spectra included in this chapter demonstrates the large difference in their chlorine SSNMR parameters. The breadth of the stationary chlorine-35 spectrum at 21.1 T is roughly a mere 60 kHz, compared to the 1.25 MHz of $InCl_3$! The much smaller QI is further demonstrated by the successful collection of a spectrum at 11.7 T; attempts were made to collect the chlorine-35 spectra of the other chloride salts at 11.7 T, but their large breadths and overlap with the chlorine-37 signal, in addition to the low receptivity of chlorine, made data collection impossible. Given the reduction in the breadth of the powder pattern, collection of a chlorine-35 MAS spectrum at 21.1 T was possible, and is shown in Figure 6.11. Unfortunately the four unique, but similar, chlorine sites could not be

resolved by MAS and it was impossible to accurately fit either the MAS or static spectra. Based on the breadth of the spectra, however, it can be definitively concluded that none of the sites have a chlorine-35 quadrupolar coupling constant with a magnitude greater than 6 MHz, consistent with the GIPAW-DFT results (*vide infra*) which range of 3.64-5.34 MHz.

Examination of the crystal structure of indium monochloride helps to explain its small QI compared to the other group 13 chlorides. Indium chloride crystallizes in a distorted version of the rocksalt structure, with cubic symmetry.

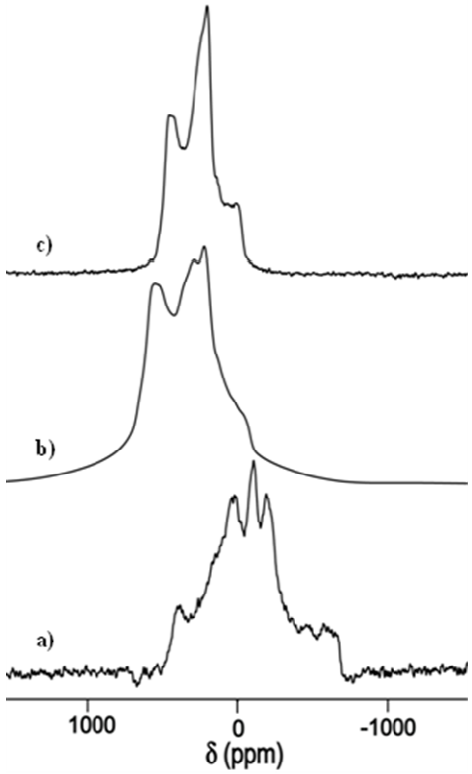

Figure 6.10. Experimental solid-state chlorine-35 NMR spectra of indium monochloride collected under stationary conditions. Chlorine-35 at 11.7 T (a), chlorine-35 at 21.1 T (b), and chlorine-37 at 21.1 T (c).

All four chlorine sites are at points of relatively high symmetry; while the In-Cl distances are long and there are no formal chlorine-indium bonds, each chlorine sits in a distorted octahedron produced by the neighbouring indium atoms, as shown in Figure 6.4. While these octahedral environments are highly distorted, they still provide a much more uniform EFG about chlorine than is observed in the indium/aluminum trichloride salts in which chlorine acts a bridge between two metal cations.

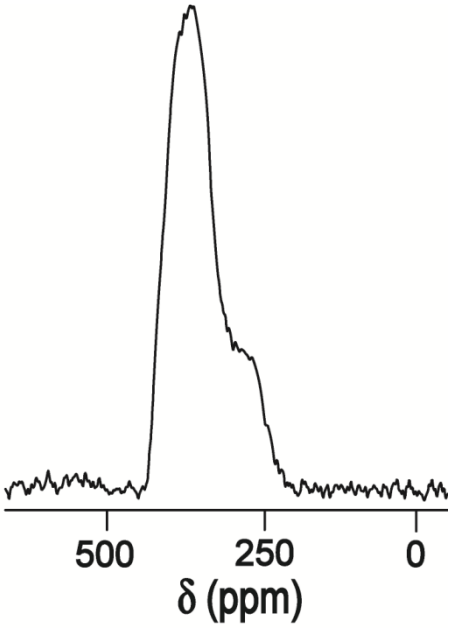

Figure 6.11. Experimental solid-state chlorine-35 MAS NMR spectrum of indium monochloride at 21.1 T.

Given the presence of multiple overlapping sites and the ability to collect a MAS spectrum, InCl was an ideal candidate to test the limits of the two-dimensional (2D) NMR pulse sequence known as multiple-quantum MAS (MQMAS) developed to collect high-resolution "isotropic" spectra of half-integer quadrupolar nuclei in which the quadrupolar effects have been removed from the MAS spectrum.[41] This 2D sequence removes the quadrupolar broadening in

one dimension through excitation of multiple quantum coherences and then a transfer of this magnetization to the CT for detection.[42] This sequence results in a 2D spectrum where the f1 dimension consists of an isotropic spectrum free of both first order and second order quadrupolar broadening. It appears there exist only two examples of MQMAS applied to chlorine. In the first, Trill *et al.* reported the collection of a ^{35}Cl MQMAS spectrum in their study of chlorine-containing sodalites, although the spectrum is not shown in their publication.[43] However, in that study the materials under investigation all had very small QI at chlorine, with largest $|C_Q(^{35}\text{Cl})|$ value being only ~0.2 MHz.[43] The second example was described by Ratcliffe *et al.* in the 2007-2008 Annual Report of the National Ultrahigh Facility for Solids in Ottawa when they described the technique being used to separate several different chlorine sites in a RbCl/KCl solid solution, but these also had very small $|C_Q(^{35}\text{Cl})|$ values (< 1 MHz). In fact, two expected sites with larger $|C_Q(^{35}\text{Cl})|$ values (> 1 MHz) were *not* observed in the MQMAS spectrum.[44]

Several attempts were made to collect a ^{35}Cl MQMAS of indium monochloride at a spin rate of 20 kHz at 21.1 T. Unfortunately, even with a large number of scans and a very long pulse delay, very little signal could be observed in 1D, and none could be observed in 2D. While disappointing, this result was not entirely unexpected due to the properties of the chlorine-35 nucleus. Generally, the MQMAS pulse sequence is applied to nuclei which possess a Q value which is much smaller than those of chlorine. The smaller Q results in the relaxation as a result of the QI being much smaller than in the case of chlorine. In the case of InCl, the fast spin-spin relaxation rate due to the moderate Q of chlorine results in a loss of magnetization before acquisition of the FID and thus no signal is observed. Thus while there may be select systems in which MQMAS can be applied to the chlorine nucleus, they will most surely be limited to cases in which the QI is significantly less than that for the four sites of InCl.

6.3.1.5 $GaCl_2$

The chlorine-35 and chlorine-37 SSNMR spectra of $GaCl_2$, along with simulations of the overall spectra and of the subspectra arising due to each of the two sites, are shown in Figure 6.12. The quadrupolar and CS tensor parameters are listed in Table 6.1. The presence of two magnetically unique sites, consistent with the crystal structure, is clearly evident by examining the shoulders that appear on both sides of the spectra, which cannot be simulated assuming a single site. The C_Q values observed for this material, 31.2 ± 0.7 and 32.0 ± 0.7 MHz, are slightly larger than those observed for the trichlorides of indium and aluminum. The CS tensor spans observed, however, were lower than those observed for the $AlCl_3$ and $InCl_3$, at 200 ± 200 ppm for each site. We note that, as was the case for $AlCl_3$ and $InCl_3$, CSA had to be included to obtain the best fits to both the ^{35}Cl and ^{37}Cl SSNMR spectra, but the errors assigned to the relevant parameters are large. Once again, the isotropic chemical shifts were also within the normal range of chloride salts at 200 ± 100 ppm for both sites.

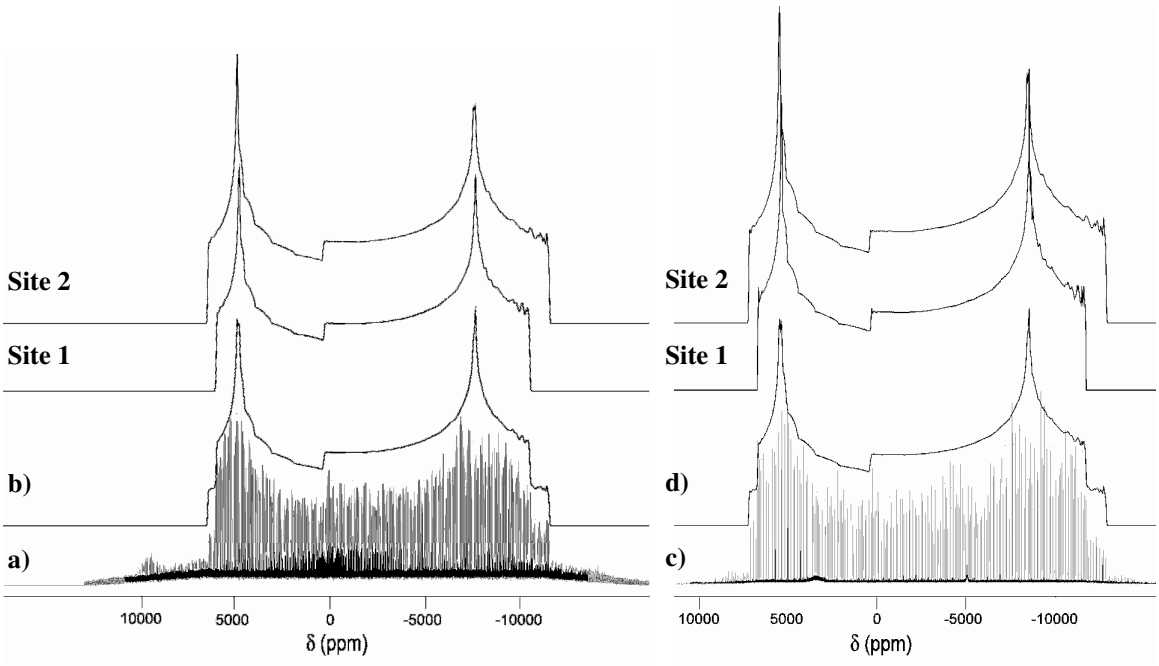

Figure 6.12. Experimental (a, c) and simulated solid-state chlorine-35 (right) and chlorine-37 (left) NMR spectra of gallium dichloride at 21.1 T. Best-fit simulations appears in b and d. Simulations of the two individual sites appear above.

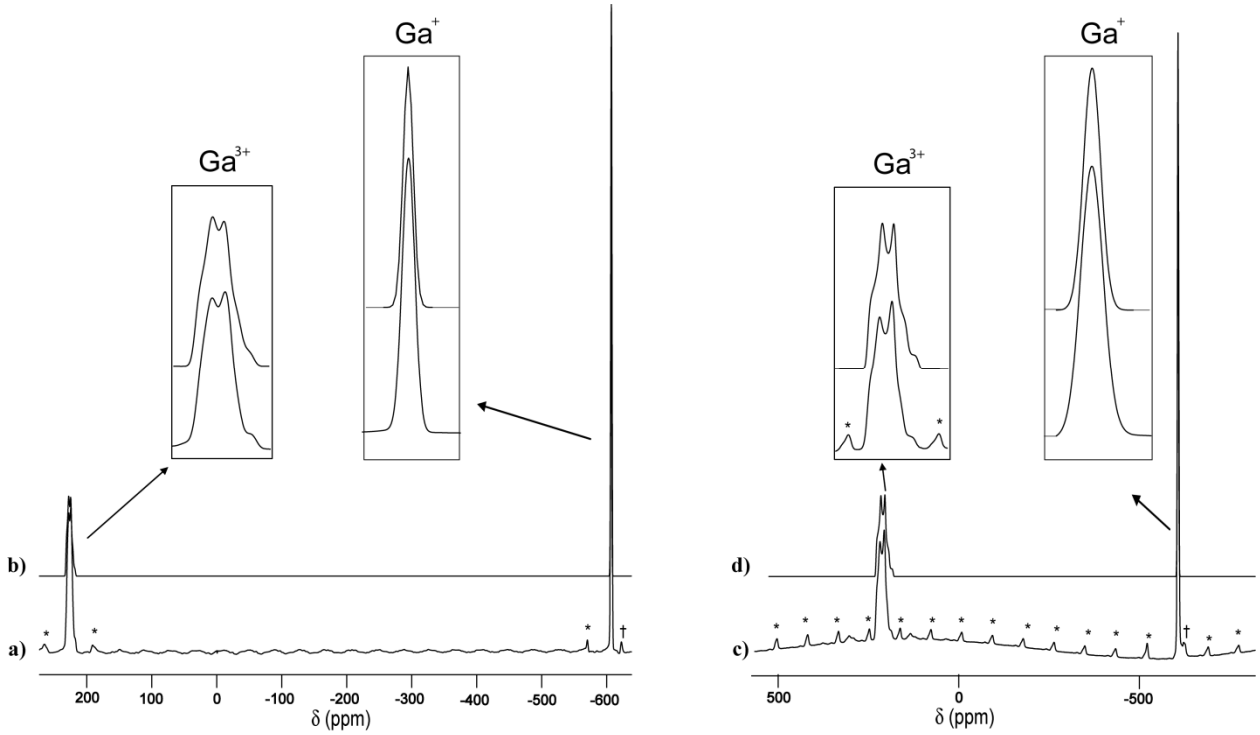

Figure 6.13. Solid-state gallium-71 MAS NMR spectra of gallium dichloride (a) at 21.1 T with ν_{rot} = 10 kHz (c) at 11.7 T with ν_{rot} = 12 kHz. (b, d) Best-fit simulations using WSolids under the assumption of an infinite MAS rate. ST spinning sidebands are indicated by asterisks. The cross denotes an unknown impurity.

The structure of the dichloride is very different from those of the trichloride salts, as shown in Figure 6.3. Gallium dichloride exhibits a mixed valent structure, which consists of slightly distorted $GaCl_4^-$ tetrahedra, in which gallium is in the +3 oxidation state, and Ga^+ ions. The tetrahedra are arranged in rows, with the Ga^+ ions lying in between rows. The Ga^+ ions are surrounded by eight Cl atoms that form an irregular dodecahedron. There are two distinct chlorine sites in the $GaCl_4^-$ ions, with slightly different Ga-Cl bond lengths, 2.186 Å and 2.193 Å, in a 1:1 ratio. The chlorine chemical shift values are consistent with the trend observed in

aluminum and indium trichloride, as the Ga-Cl bond lengths in gallium dichloride are shorter than those of the aluminum and indium trichloride, and the isotropic chlorine chemical shift is lower than that observed in both those systems.

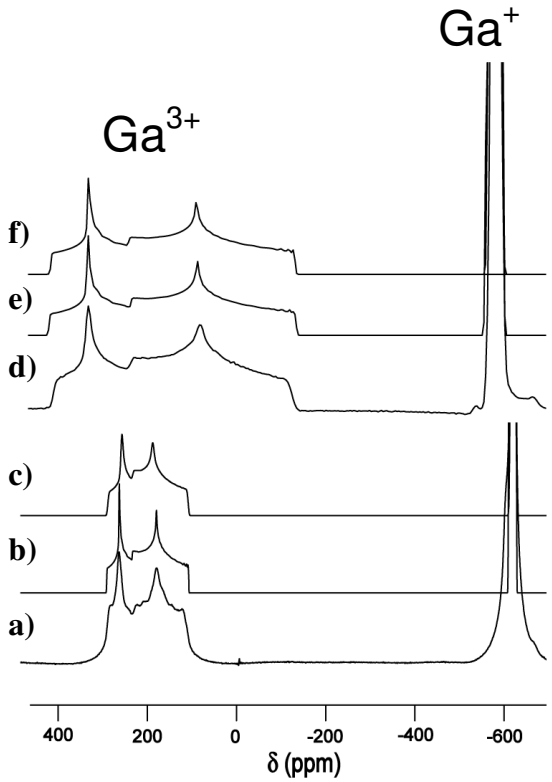

Figure 6.14. Gallium-69 SSNMR spectra of gallium dichloride collected under stationary conditions (a) at 21.1 T (d) at 11.75 T. (b, e) Best-fit simulations. Simulations assuming no CSA are shown in c and f.

Gallium-69/71 SSNMR spectra were also collected for $GaCl_2$ under stationary conditions at 11.75 and 21.1 T. In addition, ^{71}Ga MAS NMR spectra were collected at both fields. The MAS NMR spectra and simulations are shown in Figure 6.13, while the static gallium-69 spectra and simulations are presented in Figure 6.14. The gallium NMR parameters determined from

simulations of these spectra are reported in Table 6.2. Gallium dichloride has two magnetically distinct gallium sites, as mentioned above. The material has been briefly studied with gallium-69/71 SSNMR in an earlier report at 4.7 T, and gallium-69 C_Q and η_Q values of 1.7 ± 0.1 MHz and 0.44 ± 0.05 were reported for the Ga^+ site, while the Ga^{3+} site could not be observed due to quadrupolar broadening.[45] No CSA was included in the analysis.[45] Presently, both sites have been observed and their CT NMR spectra simulated. In good agreement with the prior study, the Ga^+ site was found to have a gallium-69 C_Q value of less than 1.6 MHz. This site is quite shielded with a gallium chemical shift of -610 ppm, consistent with literature values for Ga^+ ions in solution, as well as the value obtained in the previous SSNMR study.[46] We were able to determine the EFG and CS tensor parameters for the first time for the Ga^{3+} site, for which second-order quadrupolar effects were visible (Figures 6.13 and 6.14). The observed gallium-69 C_Q value is 6.7 MHz, and η_Q is 0.5.

The collection of SSNMR spectra of both ^{69}Ga and ^{71}Ga at two different fields provides additional confidence in the accuracy of the reported parameters. The gallium chemical shift of 231 ppm is consistent with the range observed for the $GaCl_4^-$ anion in solution.[46] The observed CSA for both gallium sites is very small, and even at 21.1 T it is difficult to conclusively determine the span ($\Omega < 20$ ppm). The data obtained from the characterization of the Ga^{3+} site, previously 'invisible' to ^{69}Ga SSNMR at 4.7 T, are consistent with the distorted tetrahedral environment suggested by X-ray diffraction data, *i.e.*, $C_Q(^{69}Ga)$ is smaller than is observed for many gallium compounds. For example, in the recent study by Haarmann *et al.* of the digallides of selected alkaline earth metals, $C_Q(^{69}Ga)$ ranges from 18.3 to 21.5 MHz for anionic gallium.[47]

6.3.1.6 $GaCl_3$

Gallium trichloride is the material for which the broadest NMR spectrum was observed, with the chlorine-37 spectrum (shown in Figure 6.15, along with simulations of each of the sites) spanning approximately 2.5 MHz at 21.1 T. The parameters extracted from the simulation of both the chlorine-35 and chlorine-37 NMR spectra are listed in Table 6.1.

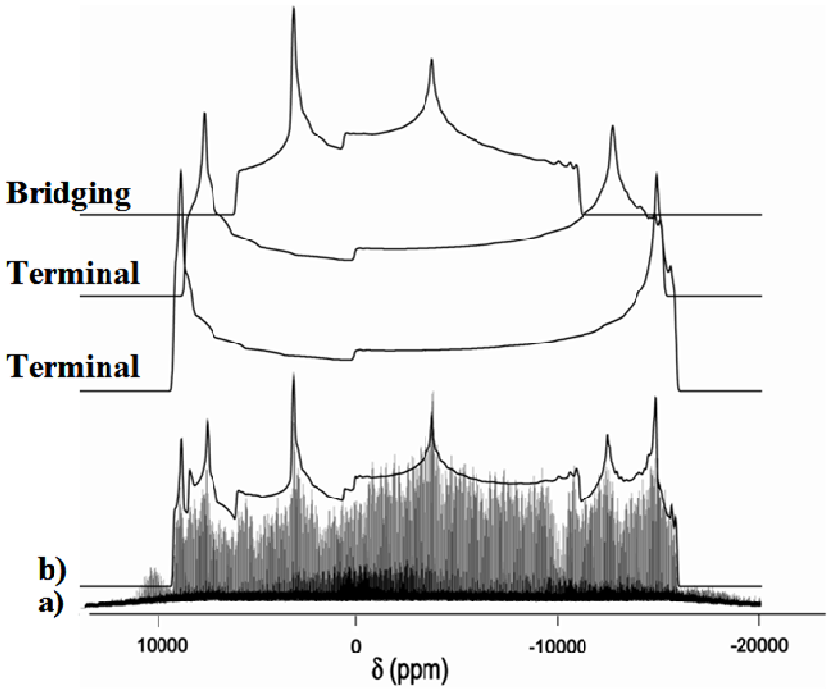

Figure 6.15. Experimental (a) and simulated solid-state chlorine-37 NMR spectra of gallium trichloride at 21.1 T. The best-fit simulation appears in b. Simulations of the three individual sites appear above.

Due to the presence of three distinct sites, and the large amount of quadrupolar broadening, it was impossible to confidently extract any CSA. Gallium trichloride was the sole material included in this study for which previous chlorine nuclear quadrupole resonance (NQR) data were available.[48] That study determined large chlorine-35 quadrupole resonance

frequencies, equal to C_Q values of 40.44, 38.12 and 28.3 MHz (no errors reported), which were consistent with the spectra acquired in this study.[†] The simulations are also consistent with the previously reported η_Q values of 0.03, 0.09, and 0.48, for the three sites, respectively.[48] Additional information was obtained from this SSNMR study in the form of the isotropic chlorine chemical shifts: 200 ± 100 ppm, 150 ± 100 ppm, and 250 ± 100 ppm for the three sites. The chlorine NMR parameters of $GaCl_3$ are consistent with its crystal structure, which differs significantly compared to the trichlorides of indium and aluminum as it consists of isolated Ga_2Cl_6 dimers, as shown in Figure 6.3. In the dimer structure, there are three distinct chlorine sites: two terminal sites and one bridging site, in a 1:1:1 ratio. Unlike the indium and aluminum cases, the three environments in gallium trichloride are quite different and thus, the spectrum could not be simulated without the inclusion of three separate chlorine sites. The relatively isolated nature of the dimers results in a very asymmetrical environment about all three chlorine sites, consistent with the large magnitudes of $C_Q(^{35}Cl)$. Based on the structural similarity between the two terminal chlorine environments, the two sites with comparable SSNMR parameters were assigned to these environments. In addition, the near-zero η_Q values associated with the two sites with larger C_Q magnitudes are also consistent with the expected axial symmetry of the terminal chlorine sites. This assignment agrees with the GIPAW-DFT calculations (*vide infra*). The chemical shifts under this assignment agree with the trend observed as a function of M-Cl distance for the other salts in the study. The terminal chlorine sites have M-Cl bond lengths of 2.111 and 2.097 Å, which are the shortest of any in this study, and these sites also have the smallest observed chemical shifts at 200 ± 100 and 150 ± 100 ppm,

[†] Values converted using the formula: $\nu_Q = \frac{3C_Q(1+\frac{\eta_Q^2}{3})^{1/2}}{2I(2I-1)}$

respectively. The bridging chlorine site has a Ga-Cl bond length of 2.297 Å and a chemical shift of 250 ppm, consistent with the trend despite the large experimental errors on δ_{iso}. That a shorter M-Cl bond length corresponds to a lower chlorine chemical shift is consistent with the typical trend observed due to isotope effects: in most cases, the minute decrease of the bond distance due to isotopic substitution tends to lower the chemical shift of atoms directly bonded to that isotope.[49] The change in bond length in the present cases is for different reasons, but the same trend is noted. The chlorine CSA present in gallium trichloride is likely of the same order of magnitude as those of the other group 13 salts (supported by calculations, *vide infra*), but it is simply too small to be quantified due to the large second-order quadrupolar broadening of the CT and due to the presence of three overlapping patterns.

That the bridging chlorine site is assigned as the site having the smallest C_Q magnitude, and that the terminal sites have larger C_Q magnitudes, is consistent with NQR results observed for some of the halogen atoms in other group 13 halides which crystallize in a dimeric structure, *i.e.*, $AlBr_3$, AlI_3, GaI_3, $InBr_3$, and InI_3.[50, 51] This relationship contrasts that observed recently by Rossini *et al.* in two group IV organometallic systems, for which they observed that bridging chlorine sites had *larger* quadrupolar coupling constants than terminal sites.[11] It therefore appears that there is no universal relationship across different types of compounds between the relative magnitude of $C_Q(^{35}Cl)$ and the presence of a bridging or terminal chlorine.

6.3.2 Quantum Chemical Calculations

6.3.2.1 GIPAW-DFT calculations

In the Bryce group's previous studies of alkaline earth chloride salts,[33] it was found that GIPAW-DFT calculations of chlorine NMR parameters, particularly C_Q, were typically in excellent agreement with experimental SSNMR results. The GIPAW-DFT method was also

used to calculate the EFG and nuclear MS tensor parameters in this study, as crystal structures were available for four salts. The results for ^{35}Cl are summarized in Table 6.3, and simulations based on the calculated parameters are included in the Appendix 5.

As mentioned, both indium and aluminum trichloride each have two very similar, but magnetically nonequivalent, chlorine sites that could not be distinguished in the chlorine SSNMR spectra for those materials. Consistent with the experimental results, the calculated NMR parameters for the two chlorine sites were very similar in both the aluminum and indium trichlorides. In both cases, the difference between the magnitudes of the two chlorine-35 C_Q values is less than the error on the experimental values. Considering the results for all four salts, excellent agreement was observed between the calculated and experimental chlorine-35 C_Q values, as is demonstrated in Figure 6.16.

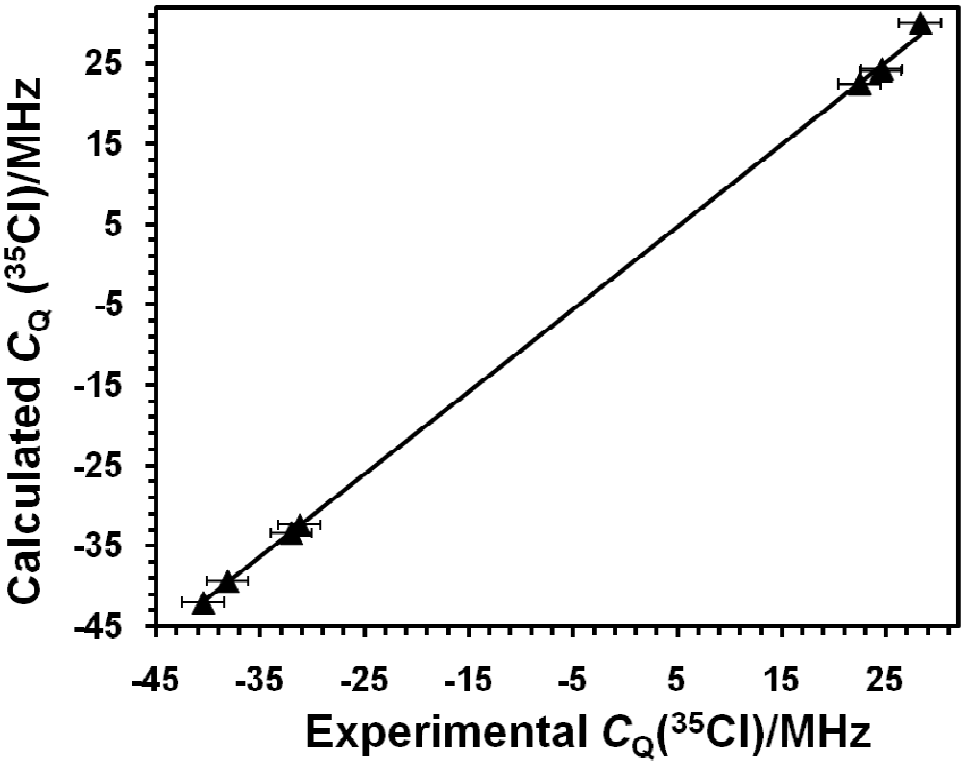

Figure 6.16. Comparison between the experimentally determined chlorine-35 quadrupolar coupling constants, on the x-axis and the calculated values (GIPAW-DFT), on the y-axis. The equation for the line of best fit is $y = 1.0265x - 0.3993$, with an R^2 value of 0.9997.

The slope of the line of best fit is nearly perfect at 1.026 and the R^2 value is 0.9997. Generally, the sign of C_Q cannot be determined experimentally and therefore additional information is provided by calculation. A distinct trend is noted in this study, with all terminal chlorine sites (both sites in $GaCl_2$ and two sites in $GaCl_3$) having negative ^{35}Cl C_Qs, while the bridging sites (those in $AlCl_3$, $InCl_3$ and one in $GaCl_3$) have positive values. This trend is consistent with prior results for bridging and terminal chlorine.[50] Visualization of the orientation of the chlorine EFG tensor reveals the largest component of the EFG, V_{33}, is close to the metal-chlorine bond in the case of the two gallium dichloride sites and the terminal sites in gallium trichloride. In all other

cases, the sites in aluminum and indium trichloride, and the bridging sites in gallium trichloride, V_{33} lies approximately perpendicular to the metal-chlorine site. These observed differences between the terminal and bridging chlorine sites, ie. the orientation of the primary component of the EFG tensor and sign of C_Q, is consistent with those observations of Rossini *et al.* in their study of several chlorine-containing zirconium organometallics.[11]

Experimentally, the chlorine SSNMR parameters for indium monochloride varied greatly from those of the other group 13 chlorides and the GIPAW-DFT results mirrored this difference. Unfortunately, as the overlapping nature of the four chlorine sites prevented the extraction of exact chlorine SSNMR parameters, it is impossible to compare experimental results to the calculated values. However, it can be noted that the magnitudes of the calculated ^{35}Cl quadrupolar coupling constants are consistent with the experimental spectra.

Good agreement between the calculated and experimental values of C_Q for ^{27}Al and ^{69}Ga was also observed, with the GIPAW-DFT calculations predicting magnitudes of 0.33 MHz for the aluminum site in $AlCl_3$, and 6.65 and 2.71 MHz for the two gallium sites in $GaCl_2$.

Table 6.3. Calculated chlorine-35 EFG and MS tensor parameters for group 13 chlorides

		$C_Q(^{35}Cl)$ / MHz	η_Q	δ_{iso} / ppm[a]	Ω / ppm	κ
aluminum trichloride		site 1: 22.42	0.64	393	259	-0.52
		site 2: 22.48	0.61	389	257	-0.49
gallium	terminal	site 1: -39.32	0.10	249	253	0.79
trichloride	terminal	site 2: -42.00	0.03	244	269	0.86
	bridging	site 3: 30.05	0.42	380	315	-0.84
gallium dichloride		site 1: -32.36	0.34	296	209	0.38
		site 2: -33.33	0.13	289	203	0.63
indium trichloride		site 1: 24.07	0.59	437	434	-0.79
		site 2: 24.32	0.55	423	355	-0.61
indium monochloride		site 1: -3.64	0.53	332	108	-0.33
		site 2: 5.34	0.36	321	40	0.30
		site 3: 3.67	0.00	327	57	1.00
		site 4: 4.58	0.00	362	49	-1.00

[a]To convert from calculated shielding constants to chemical shifts, a shift of 45.37 ppm was used (for the conversion from solid to aqueous NaCl chemical shift scales) in addition to the absolute shielding conversion found in equation 7 in Chapter 1.

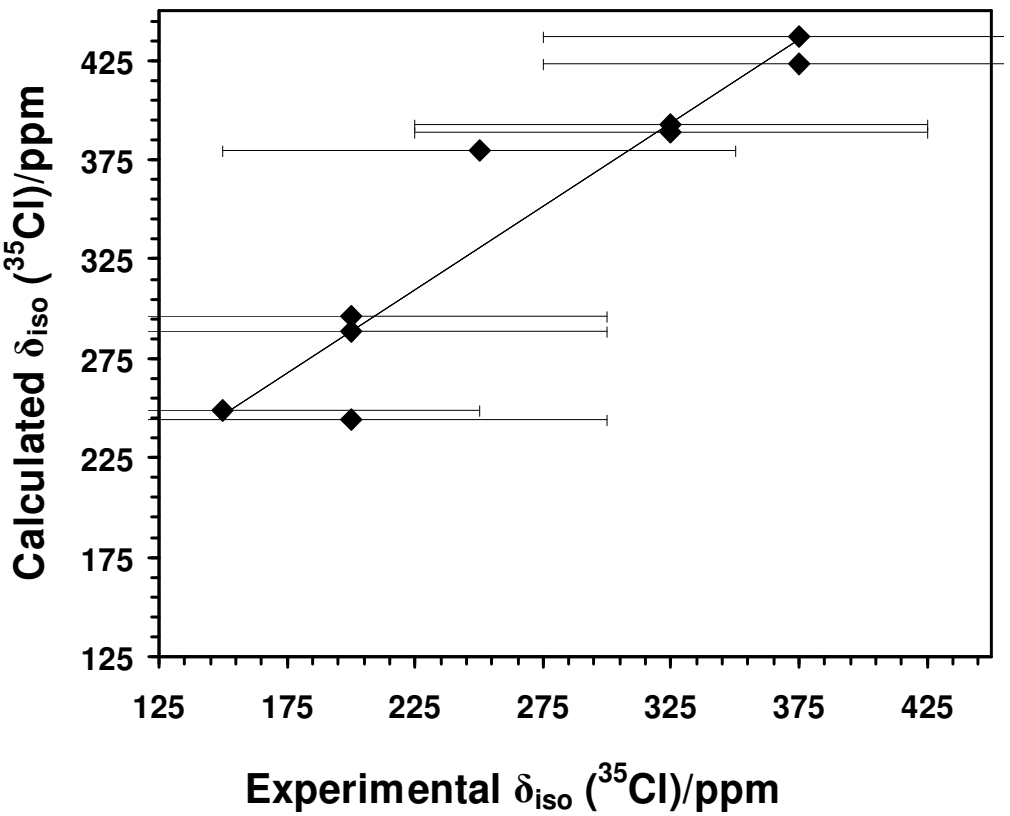

Figure 6.17. Comparison between the experimentally determined chlorine-35 chemical shifts, on the x-axis and the calculated values (GIPAW-DFT), on the y-axis for all group 13 chloride salts. The equation for the line of best fit is $y = 0.8371x + 121.22$, with an R^2 value of 0.8961.

Figures 6.17 and 6.18 present comparisons of the calculated and experimental isotropic chlorine chemical shifts and CS tensor spans, respectively. Agreement between experiment and theory was also fairly good for these parameters. In the case of the chlorine chemical shift there was a systematic overestimation in the calculated values, but the trend was generally reproduced (Figure 6.17; $R^2 = 0.8961$). The overestimation of the experimental chlorine chemical shift is consistent with the results observed for GIPAW-DFT calculations of the organic chlorides studied in Chapters 3, 4 and 5. Presently, the large experimental errors for the group 13 chlorides, resulting from their large breadths, contribute to the uncertainty in the correlation, in

contrast to the previous chapters. Figure 6.18 demonstrates the good agreement observed for the Ω values, as in all cases the calculated value is within error of experiment. As with the organic hydrochlorides, the *trend* in CS tensor span is consistent between the experimental and calculated values (ie. $GaCl_2$ has the smallest values while $InCl_3$ has the largest), however the relationship is not linear as it was in Chapter 3. Again, this is likely partially a result of the large errors associated with the experimental values. A β value of 90° for indium and aluminum trichlorides was also obtained for both chlorine sites, consistent with the experimental values. This agreement provides additional confidence that the CS tensor spans extracted are valid, despite the large errors associated with the values.

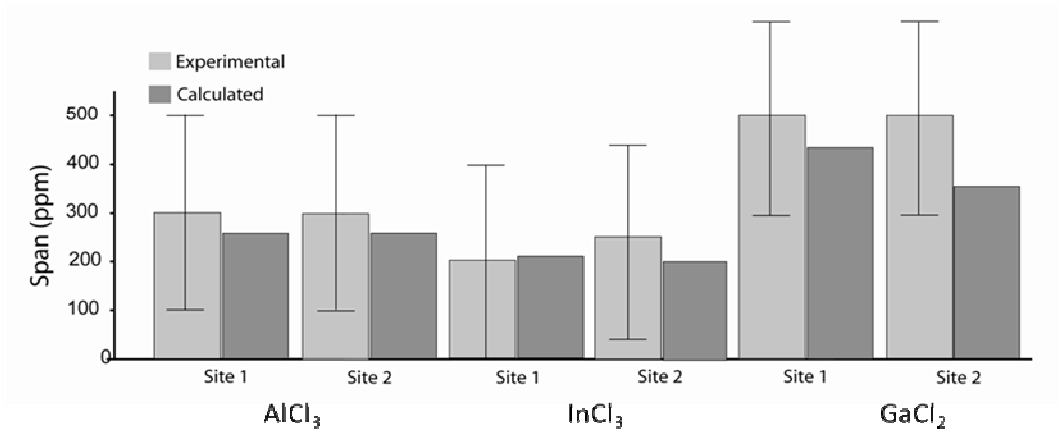

Figure 6.18. Comparison between the experimentally determined chlorine-35 CS span (light grey) and the calculated values (dark grey) for aluminum trichloride, indium trichloride and gallium dichloride.

The agreement between experiment and theory, particularly for $C_Q(^{35}Cl)$, demonstrates the ability of the GIPAW-DFT approach to accurately model EFGs in ionic solids. In addition, the agreement provides further confidence that the EFG and CS parameters determined for $AlCl_3$

in this study are correct, and that the chlorine chemical shift is within the normal range for chloride salts. In the case of indium trichloride, we note that the crystal structure used for calculations was not obtained directly, but was determined indirectly from X-ray powder data and the crystal structure of yttrium trichloride, which has the same packing structure.[29] The present results therefore suggest that the structure of $InCl_3$ determined is accurate.

6.4 Conclusions

Multinuclear solid-state NMR spectroscopy has been used to study the structures of five anhydrous group 13 chlorides: the trichlorides of aluminum, gallium, and indium, along with the dichloride of gallium and the monochloride salt of indium. In addition, the tetrahydrate of indium trichloride was also studied. With the exception of indium monochloride, the $^{35/37}$Cl EFG tensor information was determined in all cases, while CS tensor parameters were determined for three samples, despite the dominance of the QI in the spectra. The sensitivity of chlorine SSNMR to local structure was demonstrated by the range of quadrupolar coupling constants observed. In addition, the utility of chlorine SSNMR to distinguish hydrates in materials with large chlorine quadrupolar coupling constants was demonstrated for indium trichloride and indium trichloride tetrahydrate. Quantum chemical calculations of the NMR parameters, carried out using the GIPAW-DFT method, were found to be in good agreement with the experimental values, particularly in the case of the chlorine quadrupolar coupling constants (R^2 =0.9997).

In the case of gallium trichloride, analysis of the chlorine SSNMR spectra illustrated that the bridging chlorine sites had significantly lower $C_Q(^{35}Cl)$ magnitudes compared to the terminal sites. The lower values of $C_Q(^{35}Cl)$ for bridging sites (22-28 MHz vs 38-40 MHz for terminal sites) was confirmed for group 13 metal halides in particular, through additional values obtained for bridging chlorides in $InCl_3$ and $AlCl_3$, and further substantiated with quantum chemical

calculations. The isotropic chlorine chemical shifts exhibited a proportional relationship with the M-Cl distances, with larger distances corresponding to greater deshielding. Novel information on chlorine CS tensors in these materials was also obtained.

This study has demonstrated the utility of chlorine SSNMR in the investigations of ionic materials, even in cases of extremely broad spectra. The combination of variable offsets and large magnetic fields was critical, and allowed for the collection of full CT spectra from which, in some cases, different chemical sites could be distinguished and NMR parameters extracted. The results contribute to a greater understanding of the relationship between chlorine NMR interaction tensors and chemical structure.

6.5 References

1 T. M. Trnka, J. P. Morgan, M. S. Sanford, T. E. Wilhelm, M. Scholl, T. -L. Choi, S. Ding, M. W. Day and R. H. Grubbs, *J. Am. Chem. Soc.,* **2003,** *125*, 2546.

2 K. Sakata and H. Fujimoto, *J. Am. Chem. Soc.,* **2008,** *130*, 12519.

3 P. D. Pohlhaus, S. D. Sanders, A. T. Parsons, W. Li and J. S. Johnson, *J. Am. Chem. Soc.,* **2008,** *130*, 8642.

4 S. Kashimura, Y. Tane, M. Ishifune, Y. Murai, S. Hashimoto, T. Nakai, R. Hirose and H. Murase, *Tetrahedron Lett.,* **2008,** *49*, 269.

5 G. Babu and P. T. Perual, *Aldrichimica Acta,* **2000,** *33*, 16.

6 S. A. Babu, *Synlett,* **2002,** *3*, 531.

7 D. C. Barman, *Synlett,* **2003,** *15*, 2440.

8 M. Yamaguchi and Y. Nishimura, *Chem. Comm.,* **2008,** , 35.

9 G. Wegener, M. Brandt, L. Duda, J. Hofmann, B. Klesczewski, D. Koch, R. -J. Kumpf, H. Orzesek, H. -G. Pirkl, C. Six, C. Steinlein and M. Weisbeck, *Appl. Catyl. , A,* **2001,** *221*, 303.

10 M. Ueda, H. Miyabe, M. Torii, T. Kimura, O. Miyata and T. Naito, *Synlett,* **2010,** *9*, 1341.

11 A. J. Rossini, R. W. Mills, G. A. Briscoe, E. L. Norton, S. J. Geier, I. Hung, S. Zheng, J. Autschbach and R. W. Schurko, *J. Am. Chem. Soc.,* **2009,** *131*, 3317.

12 T. O. Sandland, L. S. Du, J. F. Stebbins and J. D. Webster, *Geochem Cosmochim. Acta,* **2004,** *68*, 5059.

13 D. L. Bryce and G. D. Sward, *Magn. Reson. Chem.,* **2006,** *44*, 409.

14 P. Pyykkö, *Mol. Phys.,* **2008,** *106*, 1965.

15 K. J. D. MacKenzie and M. E. Smith, *Multinuclear Solid-State NMR of Inorganic Materials*, Pergamon, Amsterdam, 2002.

16 D. L. Bryce, G. M. Bernard, M. Gee, M. D. Lumsden, K. Eichele and R. E. Wasylishen, *Can. J. Anal. Sci. Spect.,* **2001,** *46*, 46.

17 S. Hayashi, *Anal. Sci.,* **2009,** *25*, 133.

18 R. K. Harris, E. D. Becker, Cabral De Menezes, S. M., P. Granger, R. E. Hoffman and K. W. Zilm, *Pure Appl. Chem.,* **2008,** *80*, 59.

19 I. Solomon, *Phys. Rev.,* **1958,** *110*, 61.

20 I. D. Weisman and L. H. Bennett, *Phys. Rev.,* **1969,** *181*, 1341.

21 A. C. Kunwar, G. L. Turner and E. Oldfield, *J. Mag. Reson.,* **1986,** *69*, 124.

22 K. Eichele and R. E. Wasylishen, WSolids Simulation Software, 2001, version 1.17.30.

23 D. W. Alderman, M. S. Solum and D. M. Grant, *J. Chem. Phys.,* **1986,** *84*, 3717.

24 D. Massiot, F. Fayon, M. Capron, I. King, S. Le Calve, B. Alonso, J. -. Durand, B. Bujoli, Z. Gan and G. Hoatson, *Magn. Reson. Chem.,* **2002,** *40*, 70.

25 M. D. Segall, P. J. D. Lindan, M. J. Probert, C. J. Pickard, P. J. Hasnip, S. J. Clark and M. C. Payne, *J. Phys.: Condens. Matter,* **2002,** *14*, 2717.

26 S. J. Clark, M. D. Segall, C. J. Pickard, P. J. Hasnip, M. I. J. Probert, K. Refson and M. C. Payne, *Z. Kristallogr.,* **2005,** *220*, 567.

27 S. I. Troyanov, *Zh. Neorg. Khim.,* **1992,** *37*, 266.

28 S. I. Troyanov, T. Krahl and E. Kemnitz, *Z. Kristallogr.,* **2004,** *219*, 88.

29 D. H. Templeton and G. F. Carter, *J. Phys. Chem.,* **1953,** *58*, 940.

30 G. Garton and H. M. Powell, *J. Inorg. Nucl. Chem.,* **1957,** *4*, 84.

31 C. P. J. M. van der Vorst, G. C. Verschoor and W. J. A. Maaskant, *Acta Cryst.,* **1978,** *B34*, 3333.

32 S. Adiga, D. Aebi and D. L. Bryce, *Can. J. Chem.,* **2007,** *85*, 496.

33 D. L. Bryce and E. B. Bultz, *Chem. Eur. J.,* **2007,** *13*, 4786.

34 C. M. Widdifield and D. L. Bryce, *Can. J. Chem.,* **2011,** *89*, 754.

35 D. R. Buchanan and P. M. Harris, *Acta Cryst.,* **1968,** *B24*, 953.

36 P. A. Casabella and N. C. Miller, *J. Chem. Phys.,* **1964,** *40*, 1363.

37 G. D. Zissi and C. Bessada, *Z. Naturforsch,* **2001,** *56a*, 697.

38 F. Chen, G. Ma, R. G. Cavell, V. V. Terskikh and R. E. Wasylishen, *Chem. Comm.,* **2008,** , 5933.

39 K. Yamada, K. Kumano and T. Okuda, *Solid State Ionics,* **2005,** *176*, 823.

40 A. Breuer and D. Siebert, *Ber. Bunsen-Ges. Phys. Chem.,* **1996,** *100*, 1736.

41 M. Grasselli, L. Diaz and A. C. Olivieri, *Spectrosc. Lett.,* **1991,** *24*, 895.

42 M. J. Duer, *Solid-State NMR Spectroscopy*, Blackwell Publishing, Oxford, 2004.

43 R. B. Creel, E. von Meerwall, C. F. Griffin and R. G. Barnes, *J. Chem. Phys.,* **1973,** *58*, 4930.

44 C. I. Ratcliffe, J. A. Ripmeester and V. V. Terskikh, Solid-state NMR studies of chemical shifts and quadrupolar interactions in alkali halide solid solutions. In *2007-2008 Annual Report of the National Ultrahigh-Field NMR Facility*, 2008.

45 H. Schmidbaur, *Angew. Chem., Int. Ed. Engl.,* **1985,** *24*, 893.

46 J. Mason, *Multinuclear NMR*, Plenum Press, New York, 1987.

47 F. Haarmann, K. Koch, D. Grüner, W. Schnelle, O. Pecher, R. Cardoso-Gil, H. Borrmann, H. Rosner and Y. Grin, *Chem. Eur. J.,* **2009,** *15*, 1673.

48 G. E. Peterson and P. M. Bridenbaugh, *J. Chem. Phys.,* **1969,** *51*, 238.

49 C. J. Jameson. In *Encyclopaedia of Nuclear Magnetic Resonance,* D. M. Grant and R. R. Harris, Eds., Wiley, West Sussex, England, 1996.

50 E. A. C. Lucken, *Nuclear Quadrupole Coupling Constants*, Academic Press, London, 1969.

51 R. G. Barnes and S. L. Segel, *J. Phys. Chem.,* **1956,** *25*, 180.

Chapter 7

Computational Analysis of the Differences in the Magnitude of ^{35}Cl Quadrupolar Coupling Constant of Bridging and Terminal Chlorines in Dimer Compounds

7.1 Introduction and Objectives

7.1.1 Introduction

Many of the trihalides of the group 13 elements possess a common dimeric structure in which two metal trihalides are linked by two halide bridges. The metal environment in these structures is distorted tetrahedral and the dimeric units are relatively isolated from one another in the packing structure. In this structure there is a single crystallographically unique bridging halogen site and two unique terminal halogen sites. A simple schematic of the structure is shown below where black circles represent terminal halogens, white circles represent bridging halogens and grey circles represent a metal ion:

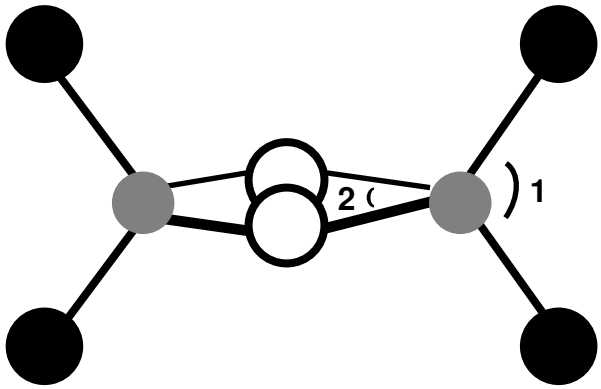

Figure 7.1. MX_3 Dimeric Structure

Several of these compounds have been studied by nuclear quadrupole resonance (NQR) spectroscopy and their halogen quadrupole resonances determined.[1] These compounds include $AlBr_3$, $GaCl_3$, $GaBr_3$, GaI_3, $InBr_3$, and InI_3. In all of these cases, it was found that there were three halide resonances – two closely spaced resonances and a third resonance at a significantly lower frequency. Based on the crystal structure, the two high resonance frequencies were assigned to the terminal bridging sites while the lower frequency was assigned to the bridging halogen. These results are converted into quadrupolar coupling constants[‡] and are summarized below in Table 7.1:

Table 7.1. Halogen NQR results for dimeric M_2X_6 systems.[‡]

Material	Halogen $\lvert C_Q(X)\rvert$[a]/ MHz (assuming $\eta = 1$)	Halogen $\lvert C_Q(X)\rvert$[a] /MHz (assuming $\eta = 0$)
$GaCl_3$	35.07, 33.09, 25.43	40.45, 38.168, 29.334
$AlBr_3$	169.07, 197.32, 200.20	194.99, 227.58, 230.9
$GaBr_3$	209.13, 292.02, 292.20	241.20, 336.80, 337.00
$InBr_3$	180.54, 222.16, 223.02	208.22, 256.22, 257.22
GaI_3	784.50, 1020.21, 1025.65	904.79, 1176.64, 1182.92
InI_3	709.41, 1001.02, 1003.66	818.19, 1154.5, 1157.55

[a] X = ^{35}Cl, ^{81}Br or ^{127}I

The $^{35/37}$Cl SSNMR analysis of the $GaCl_3$ dimer (Chapter 6) is consistent with the results observed in the NQR study of that material,[2] with ^{35}Cl C_Q magnitudes of 40.4 and 38.1 MHz for the terminal sites and 28.3 MHz for the bridging site, respectively. These C_Q magnitudes are consistent with the η_Q values, which were also reported in the NQR study of Peterson and Bridenbaugh.[2]

The halides of the group 13 metals are not the only halides which form the type of structure shown in Figure 7.1. Another example of a material with this core structure is bis(pentamethylcyclopentadienyl)zirconium trichloride ($ZrCp^*Cl_3$), which has a Cp^* group attached to each Zr^{4+} ion in addition to the four chlorines. This material was included in a

chlorine NMR study by Rossini *et al.*, published in 2009.[3] The results, shown in Figure 7.7, were found to differ from the trend observed by NQR for the group 13 halides in that the bridging chloride sites (they used 2 for their simulations) had $|C_Q(^{35}Cl)|$s values that were *larger* than those of the terminal chloride sites.

7.1.2 Objectives

Given the discrepancy between the NMR results of $GaCl_3$ and $ZrCp^*Cl_3$, a computational study was undertaken to determine if there were distinct structural properties which would lead to the bridging chlorine site of gallium trichloride having a larger $|C_Q(^{35}Cl)|$ than its terminal counterpart or if the $ZrCl_3$ fragment is an anomaly in having this relationship.

7.2 Experimental

7.2.1 Quantum Chemical Calculations

All calculations on gallium trichloride and zirconium trichloride described in this chapter were carried out using the Gaussian 03 software package[4] using the Restricted Hartree-Fock (RHF) level of theory. The crystal structure of Troyanov and co-workers was used as the starting point for all calculations performed on gallium trichloride.[5] The same structure was used for the zirconium chloride calculations, with the gallium ion replaced by zirconium. A single dimer unit was created in the Diamond program[6], using the atomic coordinates, cell parameters and space group of the crystal structure of the trichlorides. All modifications in structure (systematic changes in bond length or angle, *vide infra*) were done using the GaussView program, and there was no optimization of the resulting structures.

The optimal method for determining chlorine EFG tensors, RHF level of theory with the Dunning type cc-pVTZ basis set for the central chloride ion and the cc-pVDZ basis set for the gallium, was used for the calculations on gallium trichloride (see Chapter 2). Calculations on

$ZrCl_3$ utilized the same level of theory and basis set on chlorine, however the Zr-5F3 basis set of Huzinaga[7] was used for zirconium, as this was the basis set shown to be effective in the study by Rossini *et al*.[3] The chlorine EFG tensors contained in the Gaussian output files were analyzed using the EFGShield program (version 2.2).[8]

7.3 Results and Discussion

7.3.1 Gallium Trichloride

As discussed in Chapter 6, the GIPAW-DFT calculations based on the crystal structure of gallium trichloride yielded excellent agreement with experiment for the chlorine quadrupolar coupling constant (to better than 6.5% for all three sites) and also confirmed the terminal and bridging assignment.

NMR calculations were also performed on gallium trichloride using the RHF level of theory using the Gaussian03 program, and excellent agreement with the experimental results was also achieved, as shown in Table 7.2. The RHF results also confirmed the terminal-bridging halogen assignments, and while the calculated $|C_Q(^{35}Cl)|$ values were underestimated compared to the experimental values, for each site, the magnitudes were reproduced to within 12 % for all three sites. This underestimation is not unexpected given the results observed in Chapter 3 and in earlier studies of organic chlorides when the RHF level of theory is used.[9]

Table 7.2. Comparison of Experimental and RHF Calculated EFG Parameters for Gallium Trichloride

$GaCl_3$	Experimental		Calculated[a]	
	$\lvert C_Q\ (^{35}Cl)\rvert$/ MHz	η_Q	$\lvert C_Q\ (^{35}Cl)\rvert$/ MHz	η_Q
terminal	40.4(2.0)	0.03(5)	35.5	0.08
terminal	38.1(2.0)	0.09 (5)	35.3	0.08
bridging	28.3(2.0)	0.48(5)	26.0	0.48

[a]Calculated using RHF level of theory with a cc-pVTZ basis set on all atoms.

As good agreement between experiment and the RHF theory was shown for $GaCl_3$, calculations were performed using the Gaussian03 to program determine if there were structural distortions which could result in the bridging $|C_Q(^{35}Cl)|$ being larger than the $|C_Q(^{35}Cl)|$ of the terminal sites in the case of this dimer, as was observed for $ZrCp^*Cl_3$.[3] The actual structure of $GaCl_3$ was used as a starting point and various structural features were systematically altered in order to determine their effect on the quadrupolar coupling constant. In the actual gallium trichloride structure, angle 1 is 122º and angle 2 is 90º, the dihedral angle between the two trans terminal chlorines and the metal centers is 180º (dihedral angle 1), and the two terminal Cl-Ga bond distances are 2.09 and 2.11 Å, respectively (see Figure 7.1).[5]

The first series of calculations examined the effect of changing a variety of angles in the dimer structure, as described in Table 7.3.

Table 7.3. Variables Used in Calculations – Angles[a]

Angle Varied	Bond Angle 1/º	Bond Angle 2/º	Terminal Ga-Cl Distance/Å	Dihedral Angle 1/º
bond angle 1	Varied	90	2.110, 2.095	180
bond angle 2	122.2	Varied	2.110, 2.095	180
dihedral angle 1	*	90	2.10, 2.00	Varied

*varied as a result of the varying dihedral angle
[a]see Figure 7.1 for angle descriptions

The results of varying angles 1 and 2 while keeping all bond lengths and bond angles constant are shown in Figures 7.2 and 7.3. Angle 1 was varied from 70 to 130° while angle 2 ranged from 75.2 to 108º. As mentioned, the actual values for angle 1 and angle 2 according to the crystal structure are 122º and 90º, respectively.

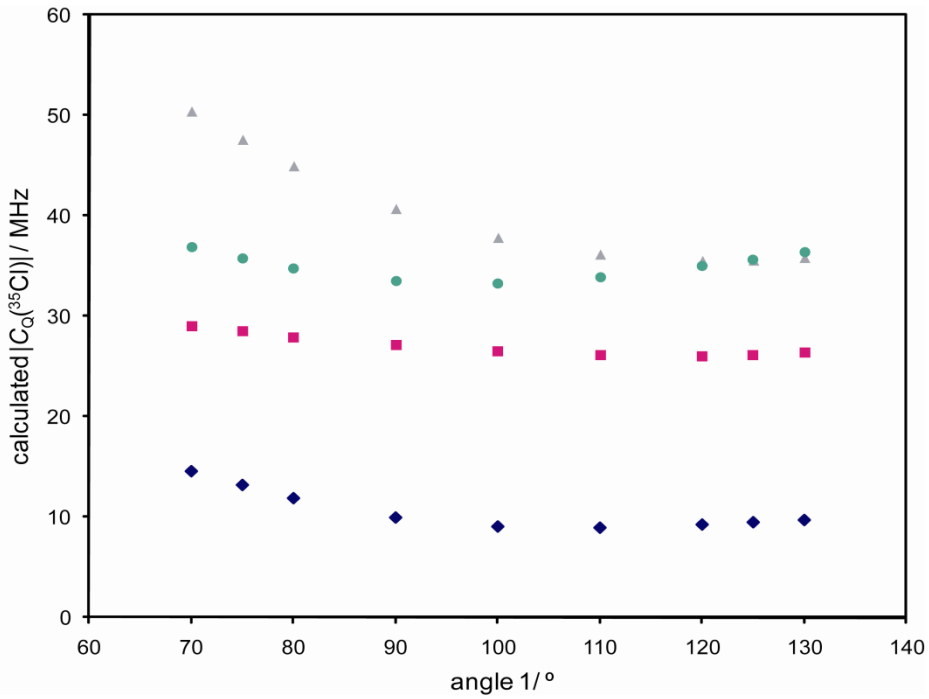

Figure 7.2. Chlorine-35 quadrupolar coupling constant as a function of angle 1 for gallium trichloride. The bridging chlorine is represented by pink squares, terminal chlorine 1 is represented by grey triangles, terminal chlorine 2 is represented by green circles, and the difference between the average terminal coupling constant magnitude and the bridging coupling constant magnitude is represented by blue diamonds.

On these figures, as with all subsequent graphs of results, there are four data sets: the $|C_Q(^{35}Cl)|$ of the bridging chlorine site, terminal chlorine site 1 and terminal chlorine site 2, as well as the difference between the average terminal chlorine site $|C_Q(^{35}Cl)|$ and the bridging site value. If the difference point is above zero, it demonstrates that the terminal $|C_Q(^{35}Cl)|$ values are larger than those of the bridging site, while a point below zero indicates the opposite. These graphs demonstrate that these bond angles have no strong relationship on the difference between the average terminal $|C_Q(^{35}Cl)|$ or the bridging $|C_Q(^{35}Cl)|$ values. In the case of angle 1, the $|C_Q(^{35}Cl)|$

for the bridging site remains relatively constant, while the average $|C_Q(^{35}Cl)|$ for the terminal site decreases only slightly as the angle increases. Changing angle 2 had a greater effect on the magnitudes of both the terminal and bridging $|C_Q(^{35}Cl)|$ values, but there is no consistent change in the difference between the average terminal and bridging magnitudes. Specifically, as angle 2 is increased, the average $|C_Q(^{35}Cl)|$ for the terminal site also increases while the $|C_Q(^{35}Cl)|$ for the bridging site decreases until 85º at which point it begins to steadily increase. The difference between the average terminal and bridging $|C_Q(^{35}Cl)|$ follows the reverse trend as observed for the bridging chlorine site – decreasing until an angle of 85º at which point it begins to increase. At the lower region (between ~60-70 º), all three sites have almost identical $|C_Q(^{35}Cl)|$ values – potentially if angle 2 could be made smaller this would lead to a region where the bridging site did have a larger $|C_Q(^{35}Cl)|$, but this is not structurally possible.

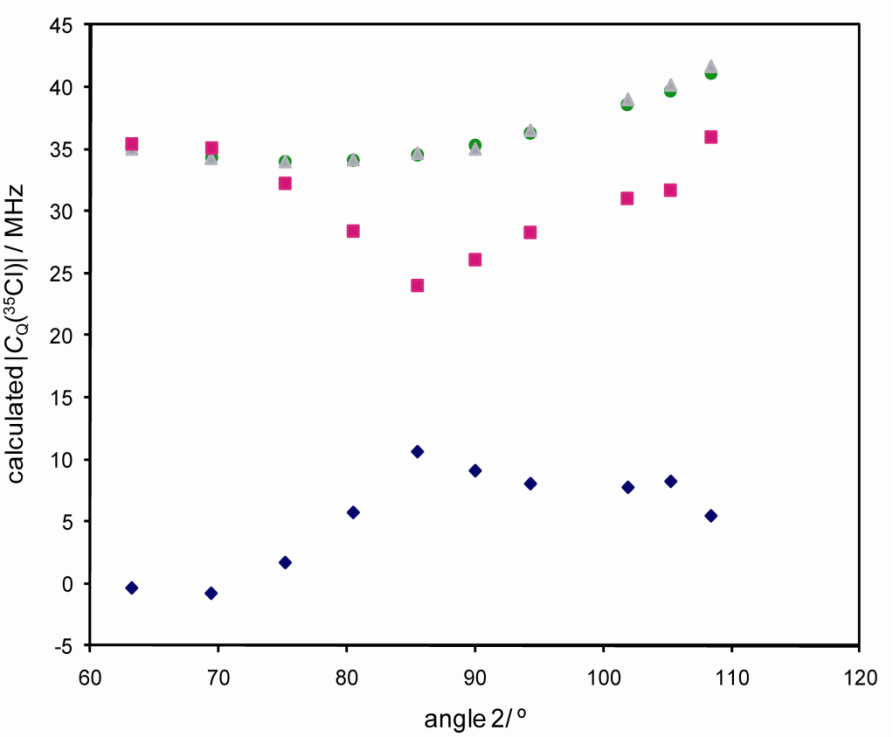

Figure 7.3. Chlorine-35 quadrupolar coupling constant as a function of angle 2 for gallium trichloride. The bridging chlorine is represented by pink squares, terminal chlorine 1 is represented by grey triangles, terminal chlorine 2 is represented by green circles, and the difference between the average terminal coupling constant magnitude and the bridging coupling constant magnitude is represented by blue diamonds.

Calculations were also done changing dihedral angle 1, as shown in Table 7.2. As mentioned, this dihedral angle is 180º in the actual $GaCl_3$ structure. The results from these calculations are shown in Figure 7.4. Changing this angle had little effect on the $|C_Q(^{35}Cl)$ value of any of the sites, and subsequently the difference in the $|C_Q(^{35}Cl)|$ values remained relatively constant. Figures 7.2 to 7.4 clearly demonstrate that there are no realistic angle changes which would

result in the bridging sites of gallium trichloride being larger in the $|C_Q(^{35}Cl)|$ value than the terminal sites.

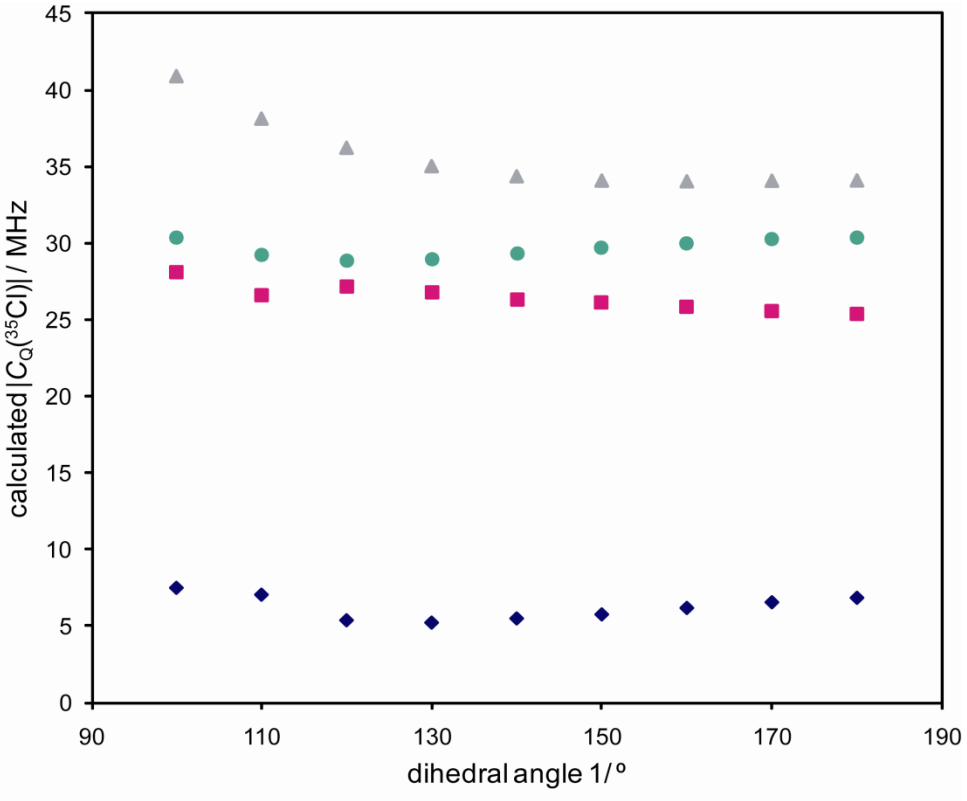

Figure 7.4. Chlorine-35 quadrupolar coupling constant as a function of dihedral angle 1 for gallium trichloride. The bridging chlorine is represented by pink squares, terminal chlorine 1 is represented by grey triangles, terminal chlorine 2 is represented by green circles, and the difference between the average terminal coupling constant magnitude and the bridging coupling constant magnitude is represented by blue diamonds.

Next, several calculations in which only the terminal gallium-chloride bond distances were varied while all bond angles were kept constant, as described in Table 7.4.

Table 7.4. Variables Used in Calculations - Distance

Bond Angle 1/º	Bond Angle 2/º	Terminal Ga-Cl Distance/Å	Dihedral Angle 1/º
122.24	90	Varied	180

In the experimental gallium trichloride structure,[5] the Ga-Cl terminal bond lengths are 2.09 and 2.11 Å, leading to an average value of 2.1 Å. For simplicity, in the calculations the two terminal Ga-Cl bond lengths were varied so that they consistently differed by 0.1 Å (i.e. the two terminal bond lengths would be 2.10 and 2.00 Å, leading to an average value of 2.05 Å). Figure 7.5 presents the results of these calculations, with the difference in the $|C_Q(^{35}Cl)|$ values plotted as a function of average terminal bond distance. As expected, the change in terminal bond length had minimal effect on the value of $|C_Q(^{35}Cl)|$ for the bridging site, but did have a significant effect on the terminal $|C_Q(^{35}Cl)|$s and thus an effect on the difference between the magnitudes of the terminal and bridging coupling constants.

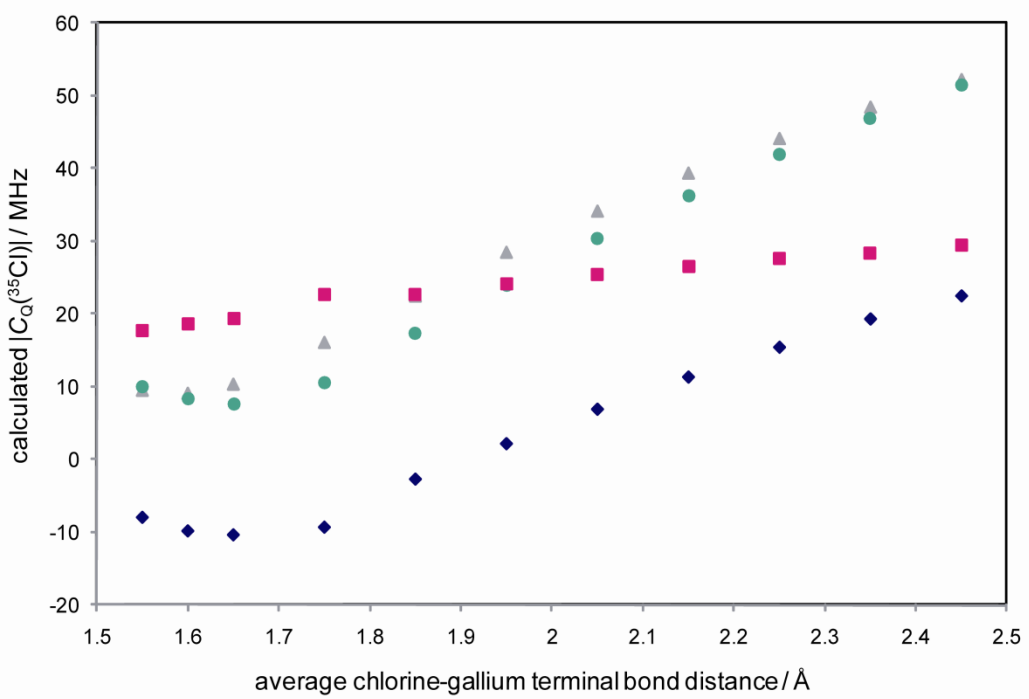

Figure 7.5. Chlorine-35 quadrupolar coupling constant as a function of gallium-chlorine bond length for gallium trichloride. The bridging chlorine is represented by pink squares, terminal chlorine 1 is represented by grey triangles, terminal chlorine 2 is represented by green circles, and the difference between the average terminal coupling constant magnitude and the bridging coupling constant magnitude is represented by blue diamonds.

The relationship between terminal Ga-Cl bond length and the difference between the average terminal $|C_Q(^{35}Cl)|$ and that of the bridging site is almost perfectly linear above bond lengths of 1.75 Å. As the ionic radius of Cl^- is 1.81 Å and that of Ga^{3+} in a 4-coordinate structure is 0.61 Å,[10] bond lengths below 1.75 Å are not that realistic and therefore it is not surprising that these values do not follow the trend observed above that value. These results demonstrate that while there is a region in which the bridging chlorine site $|C_Q(^{35}Cl)|$ is larger than those of the terminal chlorine sites (below a terminal Ga-Cl bond length of 1.9 Å), in most cases the opposite is true.

One method to quantify the degree of distortion from an ideal tetrahedral environment is through Ghose and Tsang's formulae[11] for shear strain (ψ, based on deviations from ideal tetrahedral bond angle) and longitudinal strain (α, based on the deviation from ideal tetrahedral bond length), the formulas for which are shown below.

$$\psi = \sum_{i=1}^{6} \left| \tan(\theta_i - \theta_0 \right|, \quad \alpha = \sum_{i=1}^{4} \left| \ln(l_i / l_0) \right|$$

Where Θ_i and Θ_0 refer to the observed and ideal X-M-X bond angle respectively and l_i and l_0 refer to the observed and ideal M-X bond length. In the actual structure of gallium trichloride, discussed in the previous chapter, both strains are relatively low at 0.647 and 1.915 for the longitudinal and shear strains, respectively.[5]

Given the above relationships, the calculations of varying angle and bond distance were analyzed as a function of their longitudinal and shear strains. While no clear relationship between the difference in the magnitudes of the terminal and bridging chlorine sites and the longitudinal strain, such a relationship was found to exist between the difference in magnitude and the shear strain. These results are shown in Figure 7.6. While the relationship is far from linear, it is clear that as the shear strain increases, the $|C_Q(^{35}Cl)|$ values for the terminal sites increase much more significantly then that of the bridging chlorine sites, resulting in a greater gap between the C_Q magnitudes.

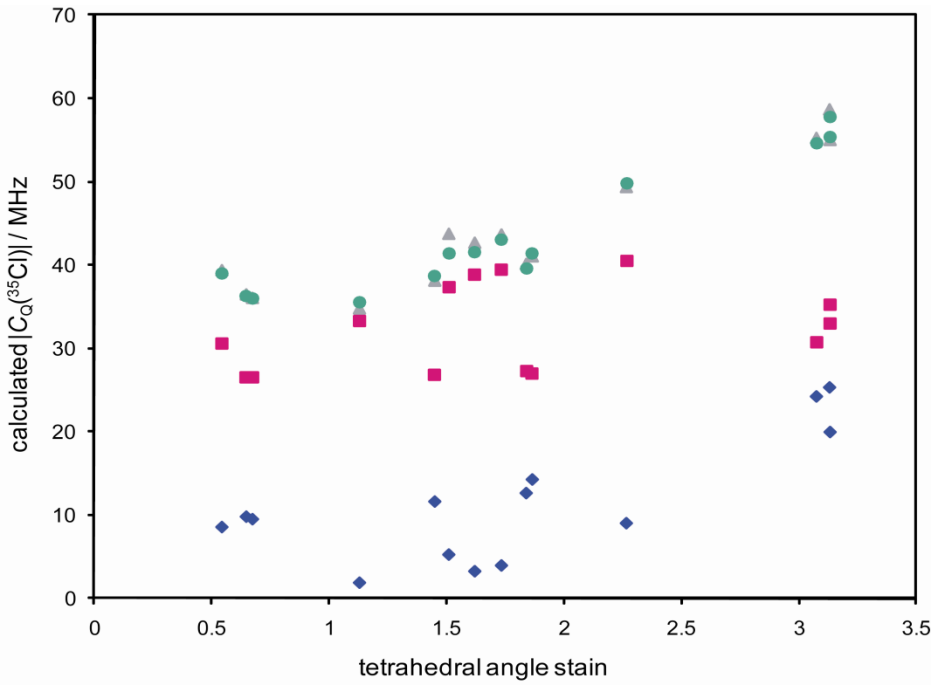

Figure 7.6. Chlorine-35 quadrupolar coupling constant as a function of tetrahedral angle strain for gallium trichloride. The bridging chlorine is represented by pink squares, terminal chlorine 1 is represented by grey triangles, terminal chlorine 2 is represented by green circles, and the difference between the average terminal coupling constant magnitude and the bridging coupling constant magnitude is represented by blue diamonds.

The large series of calculations on the gallium trichloride dimer structure demonstrate that for this particular compound, there are almost no realistic structural configurations which would lead to the bridging chlorine site $|C_Q(^{35}Cl)|$ being larger than those of the terminal sites. Specifically, as distortion from the ideal tetrahedral chlorine environment increases, the $|C_Q(^{35}Cl)|$ of the terminal sites increase at a rate much quicker than those of the bridging site. These observations suggest that this relationship may be a property of all group 13 halides, as has been so far observed experimentally.

7.3.2 Zirconium Trichloride

As mentioned in the introduction, the EFG tensor parameters of zirconium trichloride (as part of $ZrCp^*Cl_3$) studied by Rossini *et al.* differ from those of the group thirteen trichlorides in that the $|C_Q(^{35}Cl)|$ of the bridging chlorine site is actually larger than that of the terminal site.[3] The structure of $ZrCp^*Cl_3$ consists of a zirconium trichloride dimer with additional Cp* ring bonded to each zirconium. Thus, in $ZrCp^*Cl_3$ the central Zr^{4+} is actually octrahedrally coordinated, but the chlorine environments remain very similar to a '$ZrCl_3$' dimer. The exact structure of the compound is known as the crystal structure is available, having been published by Martin *et al.*[12] Simulations of the chlorine-35 spectra for the terminal and bridging chlorine sites in $ZrCp^*Cl_3$, using the parameters determined in the Rossini report, are shown below in Figure 7.7. The determined parameters were:[3] $|C_Q(^{35}Cl)|$ values of 14.0 and 14.6 MHz for the bridging sites, and 12.8 and 13.3 MHz for their terminal counterparts. Despite the presence of only three magnetically unique chlorines, the authors determined that the spectrum could only be adequately fit with a four site simulation.

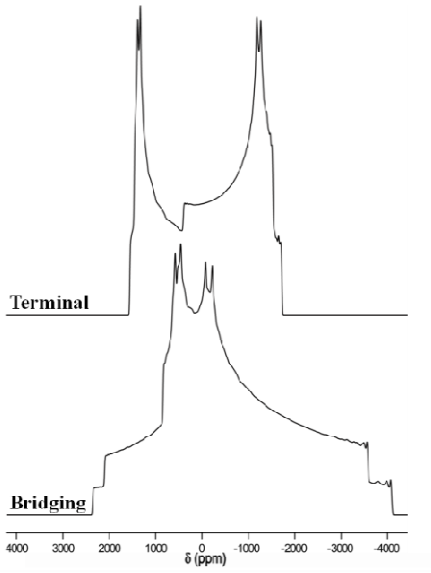

Figure 7.7. Analytical simulations of the ^{35}Cl spectra for the bridging and terminal sites in $ZrCp^*Cl_3$ using the parameters listed in reference 3. Simulations assume a field of 21.1 T.

In order to study if it was the zirconium cation itself which accounted for the differences in the relationship between the bridging and terminal $|C_Q(^{35}Cl)|$ values, all of the calculations performed on the various $GaCl_3$ models were repeated, with the gallium +3 ion replaced with a zirconium +4 ion. As the Zr ions in this structure have a +4 charge, this dimer unit had an overall change of +2. This model unit does differ slightly from the actual the skeleton "$ZrCl_3$" within the $ZrCp^*Cl_3$ structure, produced by removing the Cp^* functional groups. According to the published crystal structure of $ZrCp^*Cl_3$, angle 1 is 74.6º, angle 2 is 82.2º, dihedral angle 1 is again 180º and the two terminal Zr-Cl bond lengths are 2.385 and 2.402 Å (see Figure 1).[11] This results in a dimer with high tetrahedral shear strain and longitudinal strain values of 3.047 and 3.13, respectively.

The effects of changing bond angles on the calculated $|C_Q(^{35}Cl)|$, as described in Table 7.2, are shown in Figures 7.8, 7.9, and 7.10. The results for changing bond angle 1 and 2 in

zirconium trichloride (Figure 7.8 and Figure 7.9) differ from those of the gallium analog in that there is a much more noticeable correlation between these angles and the magnitudes of the terminal and bridging chlorine quadrupolar coupling constants, as well as the difference between them. As shown in Figure 7.8, when angle 1 increases from 75º to 120º, the difference between the average value of $|C_Q(^{35}Cl)|$ for the terminal sites and the bridging site $|C_Q(^{35}Cl)|$ decreases in a fairly linear fashion. After this point, the difference remains relatively constant. Unlike the $GaCl_3$ case, there is a large region (from just under 100º to 130º) in which the bridging chlorine site has a C_Q that is larger in magnitude than the average value of the two terminal sites. It is only in the region below 90º in which the average terminal $|C_Q(^{35}Cl)|$ is noticeably greater than that of the bridging chlorine site.

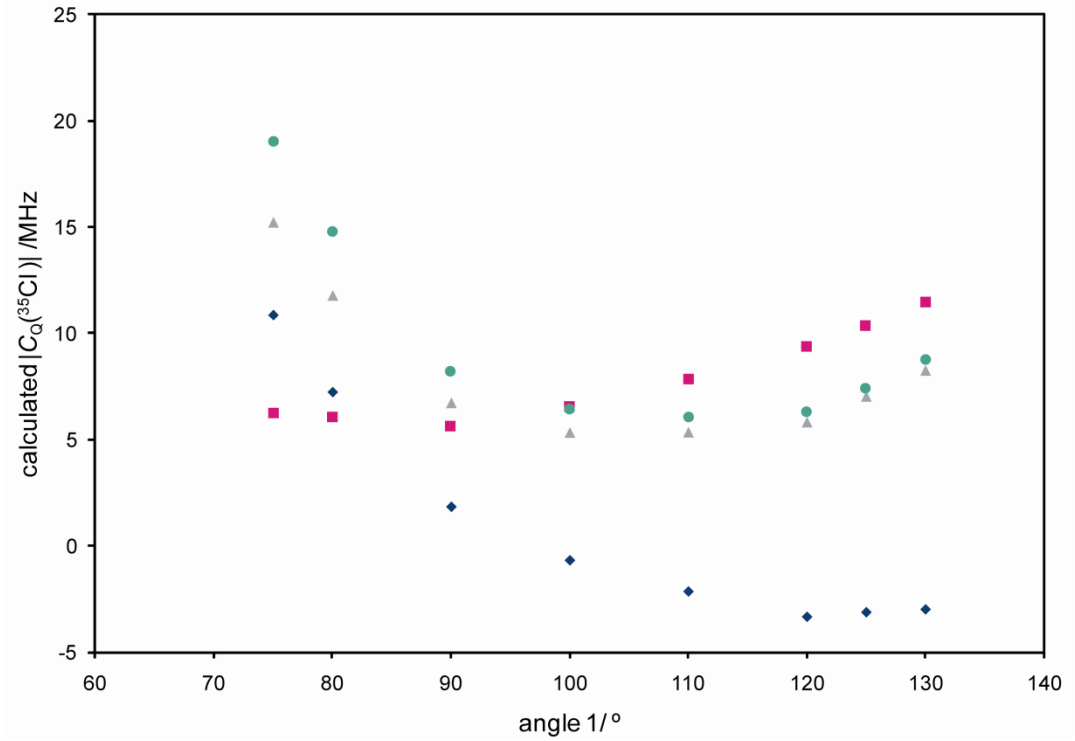

Figure 7.8. Chlorine-35 quadrupolar coupling constant as a function of angle 1 for zirconium trichloride. The bridging chlorine is represented by pink squares, terminal chlorine 1 is represented by grey triangles, terminal chlorine 2 is represented by green circles, and the difference between the average terminal coupling constant magnitude and the bridging coupling constant magnitude is represented by blue diamonds.

Upon varying angle 2 in $ZrCl_3$, there is also a clear trend in the difference between the average terminal $|C_Q(^{35}Cl)|$ and the bridging value. Increasing this angle causes a steady increase in the magnitude of the bridging chlorine C_Q above 85º, while the $|C_Q(^{35}Cl)|$ of the average terminal chlorine remains relatively constant. Therefore, above an angle 2 of 85º, there is a relatively linear decrease in the difference between the average terminal $|C_Q(^{35}Cl)|$ and the bridging value, with the latter value becoming larger in a linear fashion while the former values stay relatively constant. There is actually only a small region where the bridging chlorine site

has a smaller $|C_Q(^{35}Cl)|$ compared to the average terminal site, between just above 70º to 85º, and this difference is very small as the three values are almost identical. In the actual $ZrCl_3$ structure angle 1 and angle 2 are ~75º and 82.2º, respectively.[12] This is curious as on both graphs these are some of the only regions where a smaller bridging $|C_Q(^{35}Cl)|$ value is predicted. In the experimental case, however, the difference is quite small as all $|C_Q(^{35}Cl)|$ values are relatively similar (within 1.8 MHz).[3]

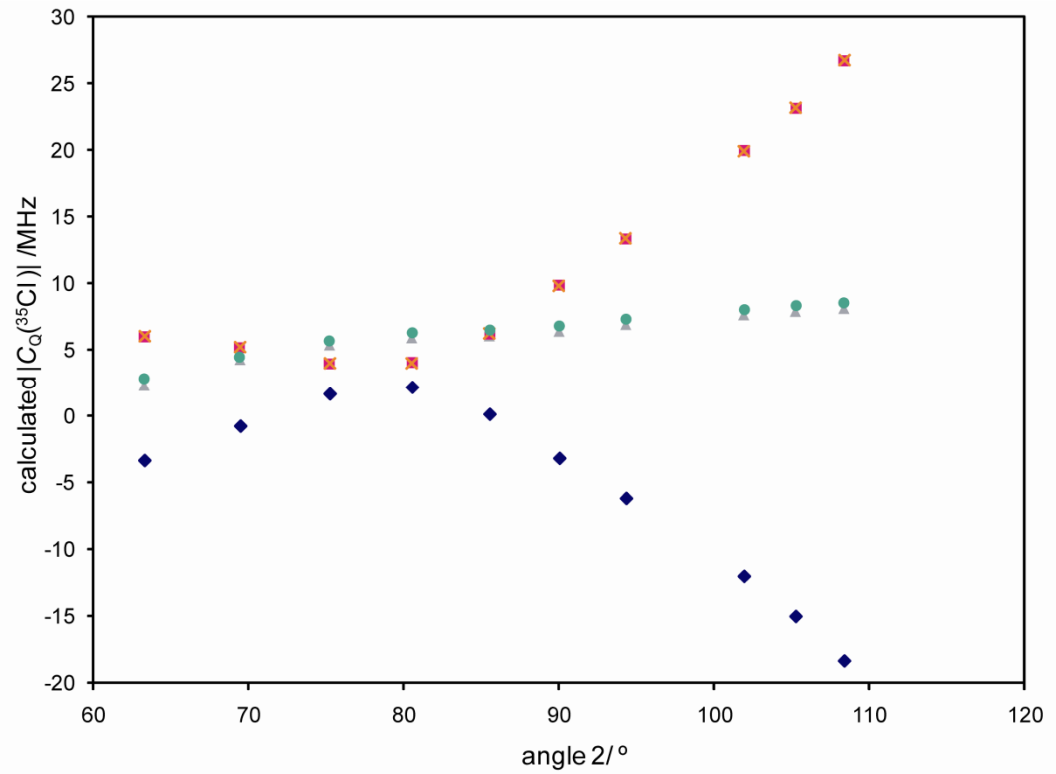

Figure 7.9. Chlorine-35 quadrupolar coupling constant as a function of angle 2 for zirconium trichloride. The bridging chlorine is represented by pink squares, terminal chlorine 1 is represented by grey triangles, terminal chlorine 2 is represented by green circles, and the difference between the average terminal coupling constant magnitude and the bridging coupling constant magnitude is represented by blue diamonds.

In the case of dihedral angle 1, as with gallium trichloride, changing this angle had minimal effect on both the terminal and bridging site $|C_Q(^{35}Cl)|$ values, and the difference between them, as shown in Figure 7.10. In *none* of these calculations were the bridging $|C_Q(^{35}Cl)|$ smaller than the average value of the terminal sites. Thus the angle calculations indicate that it is in fact the presence of the zirconium metal center which results in the bridging chlorine site having a larger $|C_Q(^{35}Cl)|$ than the terminal sites. To verify, all of the calculations which appear in Figures 7.8, 7.9, and 7.10 were redone using the actual Zr-Cl bond distances of 2.404 Å and 2.385 Å for the terminal sites and 2.588 Å for the bridging site.[12] The trends observed differed only slightly from those observed using the Ga-Cl bond lengths, with the region corresponding to the bridging site $|C_Q(^{35}Cl)|$ being larger than the average terminal site occurring above 100º for both angle 1 and angle 2. In the case of changing the dihedral angle, the results were identical to the above in that there was no region where the bridging site $|C_Q(^{35}Cl)|$ was not larger than the average terminal value.

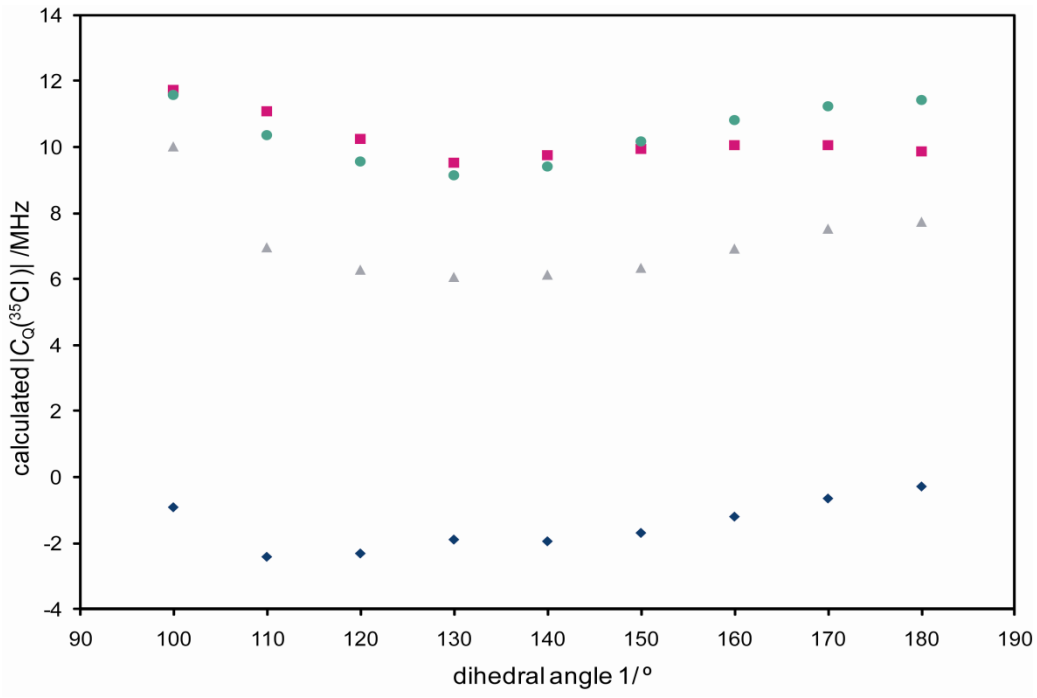

Figure 7.10. Chlorine-35 quadrupolar coupling constant as a function of dihedral angle 1 for zirconium trichloride. The bridging chlorine is represented by pink squares, terminal chlorine 1 is represented by grey triangles, terminal chlorine 2 is represented by green circles, and the difference between the average terminal coupling constant magnitude and the bridging coupling constant magnitude is represented by blue diamonds.

As in the case of bond angles, the relationship between the terminal M-Cl bond distance and the difference between the $|C_Q(^{35}Cl)|$ values of the terminal and bridging sites is quite different for $ZrCl_3$ compared to $GaCl_3$, as is shown in Figure 7.11. Once again, increasing this bond length only slightly changes the bridging $|C_Q(^{35}Cl)|$ value, with all values outside the extremes (1.55 Å and 2.45 Å) being almost identical. There is a linear region, between ~1.75 Å and ~ 2.15 Å in which, unlike the $GaCl_3$ case, longer terminal bond lengths results in a smaller $|C_Q(^{35}Cl)|$ values for the terminal chloride sites. Above terminal bond lengths of ~2.0 Å, the

bridging chlorine site has a larger $|C_Q(^{35}Cl)|$ than the average terminal value, while the opposite is true below that distance. Once again, the very short bond lengths are not very realistic given that Zr^{4+} has an ionic radius of 0.73 Å, even greater than that of Ga^{3+}.[10]

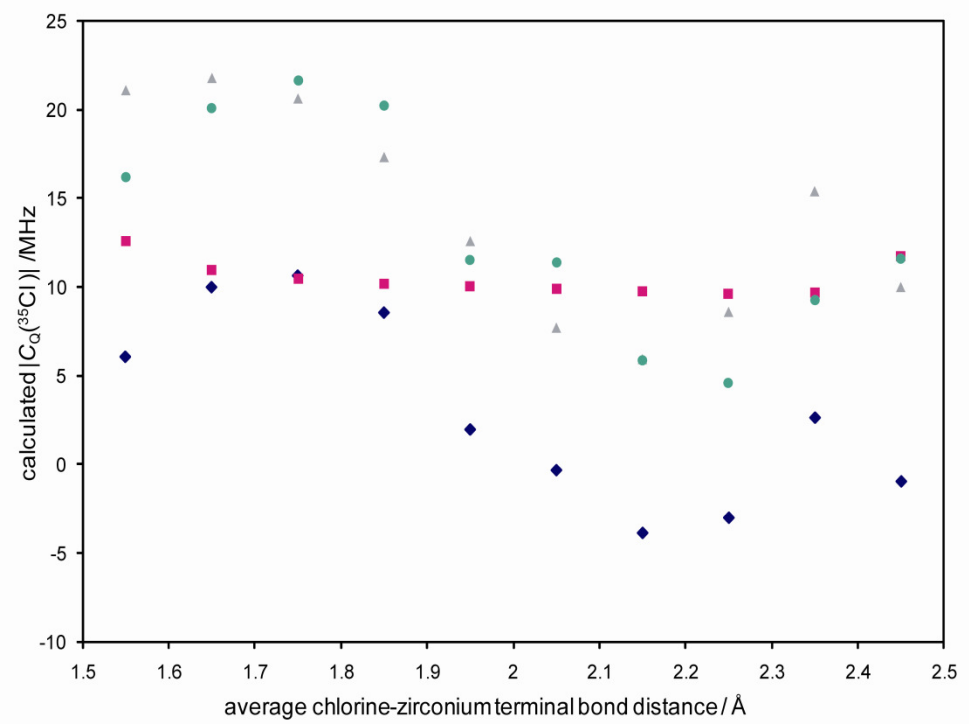

Figure 7.11. Chlorine-35 quadrupolar coupling constant as a function of average chlorine-zirconium terminal bond length for zirconium trichloride. The bridging chlorine is represented by pink squares, terminal chlorine 1 is represented by grey triangles, terminal chlorine 2 is represented by green circles, and the difference between the average terminal coupling constant magnitude and the bridging coupling constant magnitude is represented by blue diamonds.

Lastly, as with the gallium trichloride, the calculations were then analyzed to see if any relationship existed being the $|C_Q(^{35}Cl)|$ values and the tetrahedral shear or longitudinal strain. Unlike gallium trichloride case, however, there appeared to be no real correlation between either strain and the $|C_Q(^{35}Cl)|$ of the bridging or the terminal sites, or the difference between them.

7.4 Conclusions

A large series of RHF calculations were carried out on the gallium trichloride and zirconium trichloride dimers in order to determine what properties would lead to the anomalous case of the bridging chlorine sites having larger chlorine-35 quadrupolar coupling constants than the terminal chlorine sites, as was observed experimentally for $ZrCp^{*}Cl_3$. These calculations, in which several bond angles and the terminal bond lengths were varied, demonstrated that it was the metal center itself which was the most important factor in determining whether it was the bridging or terminal chlorine site(s) which have a larger value of $|C_Q(^{35}Cl)|$. Specifically, the calculations demonstrated that there were almost no structural configurations which would lead to the gallium trichloride bridging chlorine having a larger $|C_Q(^{35}Cl)|$ than those of the terminal chlorine sites, while there were many cases where this was the case for zirconium trichloride. Therefore, only for the group thirteen halides can it be taken for granted that the terminal sites have the larger $|C_Q(^{35}Cl)|$; for all other cases this assumption cannot be made.

7.5 References

1 E. A. C. Lucken, *Nuclear Quadrupole Coupling Constants*, Academic Press, London, 1969.

2 G. E. Peterson and P. M. Bridenbaugh, *J. Chem. Phys.,* **1969**, *51*, 238.

3 A. J. Rossini, R. W. Mills, G. A. Briscoe, E. L. Norton, S. J. Geier, I. Hung, S. Zheng, J. Autschbach and R. W. Schurko, *J. Am. Chem. Soc.,* **2009**, *131*, 3317.

4 M. J. Frisch, G. Trucks, H. B. Schlegel, G. E. Scuseria, M. A. Robb, J. R. Cheeseman, J. Montgomery J.A., T. Vreven, K. N. Kudin, J. C. Burant, J. M. Millam, S. S. Iyengar, J. Tomasi,

V. Barone, B. Mennucci, M. Cossi, G. Scalmani, N. Rega, G. A. Petersson, H. Nakatsuji, M. Hada, M. Ehara, K. Toyota, R. Fukuda, J. Hasegawa, M. Ishida, T. Nakajima, Y. Honda, O. Kitao, H. Nakai, M. Klene, X. Li, J. E. Knox, H. P. Hratchian, J. B. Cross, V. Bakken, C. Adamno, J. Jaramillo, R. Gomperts, R. E. Stratmann, O. Yazyev, A. J. Austin, R. Cammi, C. Pomelli, J. W. Ochterski, P. Y. Ayala, K. Morokuma, G. A. Voth, P. Salvador, J. J. Dannenberg, V. G. Zakrzewski, S. Dapprich, A. D. Daniels, M. C. Strain, O. Farkas, D. K. Malick, A. D. Rabuck, K. Raghavachari, J. B. Foresman, J. V. Ortiz, Q. Cui, A. G. Baboul, S. Clifford, j. Cioslowski, B. B. Stefanov, G. Liu, A. Liashenko, P. Piskorz, I. Komaromi, R. L. Martin, D. J. Fox, T. Keith, M. A. Al-Laham, C. Y. Peng, A. Nanayakkara, M. Challacombe, P. M. W. Gill, B. Johnson, W. Chen, M. W. Wong, C. Gonzalez and J. A. Pople, *Revision C.02 Gaussian, Inc.*, Gaussian Inc.,Wallingford, CT, 2004.

5 S. I. Troyanov, T. Krahl and E. Kemnitz, *Z. Kristallogr.,* **2004,** *219*, 88-92.

6 K. Bradenburg, *Diamond,* version 3.0e, Crystal Impact GbR, Bonn, Germany, 1997–2005.

7 S. Huzinaga, *Gaussian Basis Sets for Molecular Calculations*, Elsevier, New York, 1984.

8 S. Adiga, D. Aebi and D. L. Bryce, *Can. J. Chem.,* **2007**, *85*, 496.

9 D. L. Bryce, G. D. Sward and S. Adiga, *J. Am. Chem. Soc.,* **2006**, *128*, 2121.

10 R. D. Shannon, *Acta Crystallogr., Sect. A: Cryst. Phys., Diffr., Theor. Gen. Crystallogr.,* **1976**, *32*, 751-767.

11 S. Ghose and T. Tsang, *Am. Mineral.,* **1973**, *58*, 748.

12 A. Martin, M. Mena and F. Palacios, *J. Organomet. Chem.,* **1994**, *480*, C10-C11.

Chapter 8

Future Directions and Conclusions

8.1 Future Directions

In addition to the work presented in the preceding chapters, there have been a handful of other chlorine SSNMR studies published in the literature since 2006. These include studies on ionic liquids (in their solid form), alkaline earth chlorides, pharmaceuticals and some zirconium organometallics.[1-6] While the range of materials which have been shown to be amenable to chlorine SSNMR has grown significantly in the last five years, some limitations remain. Despite the large spectral breadths observed for the group thirteen chlorides in Chapter 6, systems in which chlorine is in a purely covalent environment will have a QI that is much greater, with $C_Q(^{35}Cl)$ magnitudes of 73 MHz having been indirectly determined for two chloroketosulfones.[7] Spectra with C_Q magnitudes on the order of several hundred MHz have been collected for the other quadrupolar halides which have larger Q values (bromine and iodine),[8,9] but these nuclei benefit from higher resonance frequencies. However, with continued advancements, such as the wideband uniform-rate smooth truncation-QCPMG (WURST-QCMPG) method[10,11] - which allows for the efficient acquisition of broad spectra - there is the potential to overcome sensitivity issues and successfully collect a chlorine-35/37 spectrum that has a width on the order of tens of MHz broad. The collection of the chlorine SSNMR spectrum of covalent chlorine will surely require the use of an ultrahigh field, such as the 21.1 T instrument used often in this work.

In addition to the types of material that can be analyzed using chlorine SSNMR, there is the potential for *additional information* from these studies to be extracted as well. As discussed in Chapter 6, the MQMAS pulse sequence has been successfully applied to two systems: a

sodalite sample and a mixture of ionic chloride salts,[12,13] although neither of these spectra have been published in an academic journal. The MQMAS method should prove useful for other interesting chlorine containing systems, despite the difficulties discussed in this thesis. Unfortunately, as quadrupolar relaxation was the cause of the difficulties faced in Chapter 6, it is likely that the MQMAS technique would only be successful on a sample with a very small QI for all sites (likely $|C_Q| < 2$ MHz). Despite this limitation, there are still many systems for which useful chlorine SSNMR information could be extracted using the MQMAS sequence.

Dipolar coupling is one of the most useful NMR interactions, as the dipolar coupling constant varies with r^3, where r is the distance between the two coupled spins. Thus, if the dipolar coupling constant between a chlorine atom and a hydrogen atom could be accurately determined, the exact distance between them could be calculated. This would be particularly useful given that hydrogen atoms are too small to be detected by single crystal X-ray crystallography. Dipolar coupling is removed by MAS, but there are several pulse programs available which reintroduce the coupling in order to determine the dipolar coupling constant. The simplest of these, the rotational echo double resonance (REDOR) sequence,[14,15] was attempted several times during the course of the research presented in this document. Unfortunately, the 'REDOR' effect was found to be too small to detect for the sample chosen, tyrosine hydrochloride monohydrate. In all of these attempts, chlorine-35 was the observe channel with pulses on the hydrogen-1 channel used to reintroduce the dipolar coupling between those two nuclei. The difficulties associated with the applications of the REDOR pulse sequence to chlorine are similar to those of the MQMAS sequence, stemming from the fast relaxation of chlorine due to its moderately large Q. Thus the technique will likely only be successful in cases where the QI for chlorine is small and the dipolar coupling between chlorine and hydrogen is

large (i.e., short Cl-H bond distances). More development is necessary in the pursuit of achieving quantitative results from these experiments, but presently qualitative results should be attainable using current methods and could aid in structural studies. In addition to the chlorine-35 REDOR experiments, preliminary experiments on tyrosine hydrochloride monohydrate have been done using the symmetry based rotary resonance echo saturation pulse double resonance (RESPDOR) pulse sequence.[16] In these experiments, hydrogen-1 is the nucleus of the observe channel with pulses on the chlorine-35 channel used to reintroduce coupling. While the data resulting from these experiments have not been fully analyzed, initial results seem promising for *qualitative* structural studies.

While benchmark chlorine SSNMR parameters have now been established for organic chlorides, there is still need for the collection of parameters for non-cubic inorganic systems. Currently, there are only limited examples for inorganic systems in the literature and thus few benchmark parameters exist. In addition, the determination of chlorine SSNMR parameters for other ion receptors would be useful to determine if the observations in Chapter 4 are consistent with similar systems. Attempts to use chlorine SSNMR to analyze a second ion receptor during the course of this research were unsuccessful, as the sample suffered from a CsCl impurity which made analysis impossible. Thus, future work on these systems must wait until non-contaminated samples can be produced.

Lastly, the presence of large volume of benchmark organic chloride experimental and computational data also opens the door for more sophisticated structure refinement. For example, the experimental versus computational curves for the $|C_Q(^{35}Cl)|$ and Ω shown in Chapter 3 could be used for the optimization of calculated hydrogen positions in similar systems.

8.2 Conclusions

The research presented in this thesis clearly achieves the objectives laid out in Chapter 1. Throughout, chlorine SSNMR has been shown to be an effective means to characterize a wide variety of systems, both organic and inorganic. There now exists a large volume of benchmark data for organic chloride systems ranging from biologically relevant systems (amino acid hydrochlorides) to an anion receptor. In the case of benzidine hydrochloride, it was shown unequivocally that chlorine SSNMR could be used to distinguish between different room temperature polymorphs of the same compound, despite the similarities in the chlorine environments. Additionally, benchmark values for anhydrous and hydrated inorganic systems were determined. For both the chlorine EFG and CS tensor parameters, the values for inorganic chlorides were found to span a much greater range than organic chloride systems. Importantly, chlorine SSNMR was also shown to be sensitive to the local environment about chlorine in inorganic chloride systems in which the QI is large, even though the resulting spectra are several MHz broad. Due to the breadth of the CT, the QCPMG pulse sequence and VOCS acquisition were essential and allowed for the extraction of EFG tensor parameters and CS tensor parameters, in most cases. In addition, multiple sites could be resolved in the case of gallium dichloride and gallium trichloride.

Quantum chemical calculations were used throughout the research presented in this document to both aid in simulation and to find additional information. The B3LYP and RHF methods were shown to be relatively accurate for calculations of some chlorine SSNMR parameters, but also had some limitations such as not reproducing the *trends* of the chlorine CS/MS tensor span. The GIPAW-DFT method was also tested for its accuracy in calculating the chlorine SSNMR parameters for both organic and inorganic systems. For the former, the amino

acid hydrochlorides provided a large data series to test the accuracy of the calculations, which were found to be improved by hydrogen position optimization. Importantly, GIPAW-DFT was found to *systematically* overestimate the magnitude of both the $|C_Q(^{35}Cl)|$ and the Ω in cases where a neutron structure was known or hydrogen position optimization was carried out prior to the NMR calculation. The chlorine CS was also found to be consistently overestimated. These relationships aided in the determination of the exact solvate studied in Chapter 4 and the identity of the unknown magnesium chloride hydrate in Chapter 5. GIPAW-DFT was also effective at calculating the chlorine SSNMR parameters of inorganic chlorides with very large QI, although the trends in Ω were not reproduced. Overall, GIPAW-DFT calculations were found to have better agreement than B3LYP/RHF calculations in cases where the hydrogen positions were known or could be optimized.

With the research presented in this thesis, along with other work carried out during the completion of this research, the chlorine chemical shift scale now looks very different from that shown in Chapter 1. The updated shift scale, in which all values are referenced to the IUPAC standard, is shown in Figure 8.1, below.

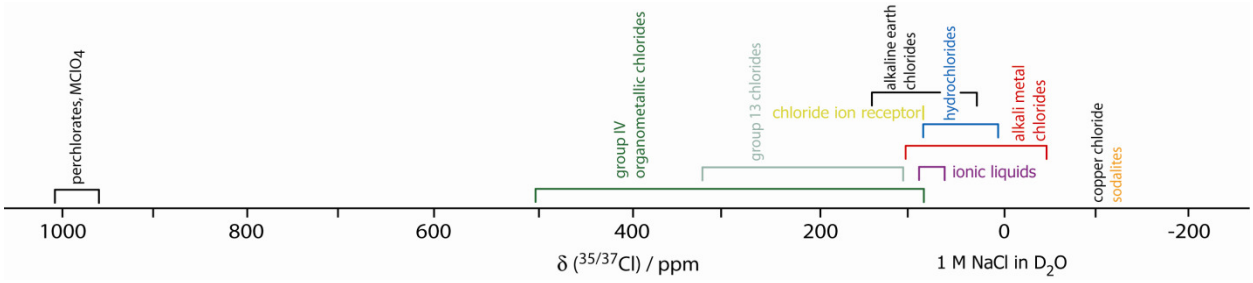

Figure 8.1. Representative solid-state chlorine isotropic chemical shifts with respect to 0.1 M NaCl in D_2O published up to this point.

The advancements made in chlorine SSNMR over the course of this research have been significant, and demonstrate the utility of the technique to study a wide variety of materials. Despite this, there still remains room for significant further progress and the field has potential to grow into a widely used spectroscopic tool for the study of chlorine-containing systems.

8.3. References

1 C. M. Widdifield and D. L. Bryce, *Can. J. Chem.,* **2011,** *89*, 754.

2 D. L. Bryce and E. B. Bultz, *Chem. Eur. J.,* **2007,** *13*, 4786.

3 H. Hamaed, J. M. Pawlowski, B. F. T. Cooper, R. Fu, S. H. Eichhorn and R. W. Schurko, *J. Am. Chem. Soc.,* **2008,** *130*, 11056.

4 P. G. Gordon, D. H. Brouwer and J. A. Ripmeester, *J. Phys. Chem. A,* **2008,** *112*, 12527.

5 P. G. Gordon, D. H. Brouwer and J. A. Ripmeester, *ChemPhysChem,* **2010,** *11*, 260.

6 A. J. Rossini, R. W. Mills, G. A. Briscoe, E. L. Norton, S. J. Geier, I. Hung, S. Zheng, J. Autschbach and R. W. Schurko, *J. Am. Chem. Soc.,* **2009,** *131*, 3317.

7 K. Eichele, R. E. Wasylishen, J. S. Grossert and A. C. Olivieri, *J. Phys. Chem.,* **1995,** *99*, 10110.

8 R. P. Chapman, C. M. Widdifield and D. L. Bryce, *Prog. Nucl. Magn. Reson. Spectrosc.,* **2009,** *55*, 215.

9 C. M. Widdifield, R. P. Chapman and D. L. Bryce, *Annu. Rep. Nucl. Magn. Reson. Spectrosc.,* **2009**, *66*, 195.

10 L. A. O'Dell, A. J. Rossini and R. W. Schurko, *Chem. Phys. Lett.,* **2009,** *468*, 330.

11 10 L. A. O'Dell and R. W. Schurko, *Chem. Phys. Lett.,* **2008,** *464*, 97.

12 H. Trill, H. Eckert and V. I. Srdanov, *J. Phys. Chem. B,* **2003,** *107*, 8779.

13 C. I. Ratcliffe, J. A. Ripmeester and V. V. Terskikh, Solid-state NMR studies of chemical shifts and quadrupolar interactions in alkali halide solid solutions. In *2007-2008 Annual Report of the National Ultrahigh-Field NMR Facility*, 2008.

14 T. Gullion and J. Schaefer, *J. Magn. Reson.,* **1989,** *81*, 196.

15 T. Gullion and J. Schaefer, *Adv. Magn. Reson.,* **1989,** *13*, 57.

16 L. Chen, Q. Wang, H. Bingwen, O. Lafon, J. Trébosc, F. Deng and J. -P. Amoureux, *Phys. Chem. Chem. Phys.,* **2010,** *12*, 9395.

Appendix 1

Information about the chlorine on-the-fly pseudopotential

Information on the chlorine on-the-fly pseudopotential: (i) core states include $1s^2$, $2s^2$, $2p^6$; valence states include $3s^2$, $3p^5$ (ii) the local channel is chosen to be d; (iii) the pseudisation radius for local and non-local channels is 1.705 a.u.; (iii) the pseudisation radius for augmentation functions is 1.191 a.u.; (iv) augmentation charge and partial core correction are 1.191 a.u.; (v) the string used for the generation of the pseudopotential, in the format used by Materials Studio is "2|1.7|5.88|7.35|9.187|30UU:31UU:32LGG[]" (see http://www.tcm.phy.cam.ac.uk/castep/usp-string-notes.txt and http://www.tcm.phy.cam.ac.uk/castep/otfg.pdf for further explanation).

Appendix 2

L-Aspartic Acid Hydrochloride .cif File

```
data_AsparticAcidHydrochloride

_audit_creation_method            SHELXL-97
_chemical_name_systematic
;
 ?
;
_chemical_name_common             L-aspartic_acid_hydrochloride
_chemical_absolute_configuration  L
_chemical_melting_point           178-182C
_chemical_formula_moiety          ?
_chemical_formula_sum
 'C4 H8 Cl N O4'
_chemical_formula_weight          169.56

loop_
 _atom_type_symbol
 _atom_type_description
 _atom_type_scat_dispersion_real
 _atom_type_scat_dispersion_imag
 _atom_type_scat_source
 'C'  'C'   0.0033   0.0016
 'International Tables Vol C Tables 4.2.6.8 and 6.1.1.4'
 'H'  'H'   0.0000   0.0000
 'International Tables Vol C Tables 4.2.6.8 and 6.1.1.4'
 'N'  'N'   0.0061   0.0033
 'International Tables Vol C Tables 4.2.6.8 and 6.1.1.4'
 'O'  'O'   0.0106   0.0060
 'International Tables Vol C Tables 4.2.6.8 and 6.1.1.4'
 'Cl'  'Cl'   0.1484   0.1585
 'International Tables Vol C Tables 4.2.6.8 and 6.1.1.4'

_symmetry_cell_setting            Triclinic
_symmetry_space_group_name_H-M    P1

loop_
 _symmetry_equiv_pos_as_xyz
 'x, y, z'

_cell_length_a                    5.612(2)
_cell_length_b                    5.647(2)
_cell_length_c                    6.169(2)
_cell_angle_alpha                 114.218(3)
_cell_angle_beta                  97.874(4)
_cell_angle_gamma                 95.710(4)
_cell_volume                      173.96(11)
_cell_formula_units_Z             1
```

```
_cell_measurement_temperature     200(2)
_cell_measurement_reflns_used     732
_cell_measurement_theta_min       3.69
_cell_measurement_theta_max       24.65

_exptl_crystal_description        block
_exptl_crystal_colour             colorless
_exptl_crystal_size_max           0.15
_exptl_crystal_size_mid           0.15
_exptl_crystal_size_min           0.15
_exptl_crystal_density_meas       n/a
_exptl_crystal_density_diffrn     1.619
_exptl_crystal_density_method     'not measured'
_exptl_crystal_F_000              88
_exptl_absorpt_coefficient_mu     0.505
_exptl_absorpt_correction_type    multi-scan
_exptl_absorpt_correction_T_min   0.9281
_exptl_absorpt_correction_T_max   0.9281
_exptl_absorpt_process_details    'SADABS, Bruker (2000)'

_exptl_special_details
;
 Data collection is performed with four batch runs at phi = 0.00 deg
 (650 frames), at phi = 90.00 deg (650 frames), at phi = 180.00 deg
 (650 frames), and at phi = 270.00 deg (650 frames).
 A fifth batch run is collected at phi = 0.00 deg (50 frames) to monitor
 crystal and diffractometer stability. Frame width = 0.30 deg in omega.
 Data is merged, corrected for decay (if any), and treated with multi-scan
 absorption corrections (if required). All symmetry-equivalent reflections
 are merged for centrosymmetric data.
 Friedel pairs are not merged for noncentrosymmetric data.
;

_diffrn_ambient_temperature       200(2)
_diffrn_radiation_wavelength      0.71073
_diffrn_radiation_type            MoK\a
_diffrn_radiation_source          'fine-focus sealed tube'
_diffrn_radiation_monochromator   graphite
_diffrn_measurement_device_type   'CCD area detector'
_diffrn_measurement_method        'phi and omega scans'
_diffrn_detector_area_resol_mean  ?
_diffrn_standards_number          ?
_diffrn_standards_interval_count  ?
_diffrn_standards_interval_time   ?
_diffrn_standards_decay_%         <1
_diffrn_reflns_number             1683
_diffrn_reflns_av_R_equivalents   0.0154
_diffrn_reflns_av_sigmaI/netI     0.0302
_diffrn_reflns_limit_h_min        -6
_diffrn_reflns_limit_h_max        6
_diffrn_reflns_limit_k_min        -6
_diffrn_reflns_limit_k_max        6
_diffrn_reflns_limit_l_min        -7
_diffrn_reflns_limit_l_max        7
```

```
_diffrn_reflns_theta_min          3.69
_diffrn_reflns_theta_max          24.65
_reflns_number_total              1122
_reflns_number_gt                 1117
_reflns_threshold_expression      >2sigma(I)

_computing_data_collection        'SMART, Bruker (2000)'
_computing_cell_refinement        'SMART, Bruker (2000)'
_computing_data_reduction         'XPREP, Bruker (2000)'
_computing_structure_solution     'SHELXS-97 (Sheldrick, 1990)'
_computing_structure_refinement   'SHELXL-97 (Sheldrick, 1997)'
_computing_molecular_graphics     'SHELXTL, Bruker (2000)'
_computing_publication_material   'SHELXTL, Bruker (2000)'

_refine_special_details
;
 Refinement of F^2^ against ALL reflections.  The weighted R-factor wR and
 goodness of fit S are based on F^2^, conventional R-factors R are based
 on F, with F set to zero for negative F^2^. The threshold expression of
 F^2^ > 2sigma(F^2^) is used only for calculating R-factors(gt) etc. and
is
 not relevant to the choice of reflections for refinement.  R-factors
based
 on F^2^ are statistically about twice as large as those based on F, and
R-
 factors based on ALL data will be even larger.
;

_refine_ls_structure_factor_coef  Fsqd
_refine_ls_matrix_type            full
_refine_ls_weighting_scheme       calc
_refine_ls_weighting_details
 'calc w=1/[\s^2^(Fo^2^)+(0.0433P)^2^+0.0071P] where P=(Fo^2^+2Fc^2^)/3'
_atom_sites_solution_primary      direct
_atom_sites_solution_secondary    difmap
_atom_sites_solution_hydrogens    geom
_refine_ls_hydrogen_treatment     constr
_refine_ls_extinction_method      none
_refine_ls_extinction_coef        ?
_refine_ls_abs_structure_details
 'Flack H D (1983), Acta Crystallogr. A39, 876-881'
_refine_ls_abs_structure_Flack    0.00(5)
_refine_ls_number_reflns          1122
_refine_ls_number_parameters      91
_refine_ls_number_restraints      3
_refine_ls_R_factor_all           0.0222
_refine_ls_R_factor_gt            0.0220
_refine_ls_wR_factor_ref          0.0568
_refine_ls_wR_factor_gt           0.0566
_refine_ls_goodness_of_fit_ref    1.012
_refine_ls_restrained_S_all       1.011
_refine_ls_shift/su_max           0.001
_refine_ls_shift/su_mean          0.001
```

```
loop_
 _atom_site_label
 _atom_site_type_symbol
 _atom_site_fract_x
 _atom_site_fract_y
 _atom_site_fract_z
 _atom_site_U_iso_or_equiv
 _atom_site_adp_type
 _atom_site_occupancy
 _atom_site_symmetry_multiplicity
 _atom_site_calc_flag
 _atom_site_refinement_flags
 _atom_site_disorder_assembly
 _atom_site_disorder_group
Cl1 Cl 0.34495(4) 0.50102(5) 0.49552(4) 0.02199(14) Uani 1 1 d . . .
N1 N 0.9307(3) 0.7768(3) 0.7594(2) 0.0177(3) Uani 1 1 d . . .
H1A H 0.8838 0.8486 0.6464 0.027 Uiso 1 1 d R . .
H1B H 1.0919 0.7355 0.7500 0.027 Uiso 1 1 d R . .
H1C H 0.8175 0.6194 0.7205 0.027 Uiso 1 1 d R . .
O1 O 0.7824(2) 1.3118(3) 0.8118(3) 0.0316(4) Uani 1 1 d . . .
O2 O 0.3902(3) 1.2089(3) 0.8243(3) 0.0297(4) Uani 1 1 d . . .
H2 H 0.3672 1.2910 0.7386 0.045 Uiso 1 1 calc R . .
O3 O 0.8902(3) 0.8689(4) 1.3424(3) 0.0377(4) Uani 1 1 d . . .
O4 O 1.2061(3) 0.7607(3) 1.1570(3) 0.0247(3) Uani 1 1 d . . .
H4 H 1.2423 0.7002 1.2587 0.037 Uiso 1 1 calc R . .
C1 C 0.6270(4) 1.2071(4) 0.8770(3) 0.0186(4) Uani 1 1 d . . .
C2 C 0.6842(4) 1.0609(4) 1.0304(4) 0.0208(4) Uani 1 1 d . . .
H2A H 0.5561 0.9039 0.9770 0.025 Uiso 1 1 calc R . .
H2B H 0.6841 1.1768 1.2020 0.025 Uiso 1 1 calc R . .
C3 C 0.9305(3) 0.9755(3) 1.0098(3) 0.0159(4) Uani 1 1 d . . .
H3A H 1.0549 1.1339 1.0482 0.019 Uiso 1 1 calc R . .
C4 C 1.0051(4) 0.8607(4) 1.1903(4) 0.0189(4) Uani 1 1 d . . .

loop_
 _atom_site_aniso_label
 _atom_site_aniso_U_11
 _atom_site_aniso_U_22
 _atom_site_aniso_U_33
 _atom_site_aniso_U_23
 _atom_site_aniso_U_13
 _atom_site_aniso_U_12
Cl1 0.0238(2) 0.0258(2) 0.0205(2) 0.01319(16) 0.00337(15) 0.00918(15)
N1 0.0218(8) 0.0212(7) 0.0140(8) 0.0101(6) 0.0057(6) 0.0059(6)
O1 0.0237(7) 0.0394(8) 0.0474(9) 0.0337(7) 0.0071(7) 0.0067(6)
O2 0.0209(8) 0.0398(8) 0.0442(9) 0.0317(7) 0.0080(6) 0.0114(6)
O3 0.0403(9) 0.0656(11) 0.0308(8) 0.0368(8) 0.0171(7) 0.0259(8)
O4 0.0227(8) 0.0367(8) 0.0260(7) 0.0233(6) 0.0050(6) 0.0106(7)
C1 0.0206(9) 0.0174(10) 0.0195(11) 0.0084(8) 0.0053(8) 0.0072(8)
C2 0.0208(10) 0.0268(10) 0.0240(10) 0.0172(8) 0.0087(8) 0.0095(8)
C3 0.0188(9) 0.0172(9) 0.0135(9) 0.0084(7) 0.0030(7) 0.0029(8)
C4 0.0201(10) 0.0240(9) 0.0160(9) 0.0120(7) 0.0023(7) 0.0050(7)

_geom_special_details
;
```

```
 All esds (except the esd in the dihedral angle between two l.s. planes)
 are estimated using the full covariance matrix.  The cell esds are taken
 into account individually in the estimation of esds in distances, angles
 and torsion angles; correlations between esds in cell parameters are only
 used when they are defined by crystal symmetry.  An approximate
(isotropic)
 treatment of cell esds is used for estimating esds involving l.s. planes.
;

loop_
 _geom_bond_atom_site_label_1
 _geom_bond_atom_site_label_2
 _geom_bond_distance
 _geom_bond_site_symmetry_2
 _geom_bond_publ_flag
N1 C3 1.491(2) . ?
O1 C1 1.209(3) . ?
O2 C1 1.326(3) . ?
O3 C4 1.198(3) . ?
O4 C4 1.315(3) . ?
C1 C2 1.513(3) . ?
C2 C3 1.513(3) . ?
C3 C4 1.535(3) . ?

loop_
 _geom_angle_atom_site_label_1
 _geom_angle_atom_site_label_2
 _geom_angle_atom_site_label_3
 _geom_angle
 _geom_angle_site_symmetry_1
 _geom_angle_site_symmetry_3
 _geom_angle_publ_flag
O1 C1 O2 124.09(18) . . ?
O1 C1 C2 123.06(18) . . ?
O2 C1 C2 112.85(16) . . ?
C1 C2 C3 111.00(15) . . ?
N1 C3 C2 111.36(14) . . ?
N1 C3 C4 109.28(15) . . ?
C2 C3 C4 111.26(16) . . ?
O3 C4 O4 126.2(2) . . ?
O3 C4 C3 122.02(19) . . ?
O4 C4 C3 111.80(17) . . ?

loop_
 _geom_torsion_atom_site_label_1
 _geom_torsion_atom_site_label_2
 _geom_torsion_atom_site_label_3
 _geom_torsion_atom_site_label_4
 _geom_torsion
 _geom_torsion_site_symmetry_1
 _geom_torsion_site_symmetry_2
 _geom_torsion_site_symmetry_3
 _geom_torsion_site_symmetry_4
 _geom_torsion_publ_flag
```

```
O1 C1 C2 C3 -21.5(3) . . . . ?
O2 C1 C2 C3 158.99(16) . . . . ?
C1 C2 C3 N1 -65.5(2) . . . . ?
C1 C2 C3 C4 172.34(16) . . . . ?
N1 C3 C4 O3 -130.9(2) . . . . ?
C2 C3 C4 O3 -7.6(3) . . . . ?
N1 C3 C4 O4 50.0(2) . . . . ?
C2 C3 C4 O4 173.37(16) . . . . ?

_diffrn_measured_fraction_theta_max    0.968
_diffrn_reflns_theta_full              24.65
_diffrn_measured_fraction_theta_full   0.968
_refine_diff_density_max    0.168
_refine_diff_density_min   -0.197
_refine_diff_density_rms    0.045
```

L-Cysteine Hydrochloride Monohydrate .cif File

```
data_CysteineHydrochlorideMonohydrate

_audit_creation_method            SHELXL-97_chemical_name_systematic
;
?
;
_chemical_name_common             L-cysteine_hydrochloride_monohydrate
_chemical_absolute_configuration  L
_chemical_melting_point           90-93C
_chemical_formula_moiety          ?
_chemical_formula_sum
'C3 H10 Cl N O3 S'
_chemical_formula_weight          175.63

loop_ _atom_type_symbol
_atom_type_description
_atom_type_scat_dispersion_real
_atom_type_scat_dispersion_imag
_atom_type_scat_source
'C'  'C'   0.0033   0.0016
'International Tables Vol C Tables 4.2.6.8 and 6.1.1.4'
'H'  'H'   0.0000   0.0000
'International Tables Vol C Tables 4.2.6.8 and 6.1.1.4'
'N'  'N'   0.0061   0.0033
'International Tables Vol C Tables 4.2.6.8 and 6.1.1.4'
'O'  'O'   0.0106   0.0060
'International Tables Vol C Tables 4.2.6.8 and 6.1.1.4'
'S'  'S'   0.1246   0.1234
'International Tables Vol C Tables 4.2.6.8 and 6.1.1.4'
'Cl'  'Cl'   0.1484   0.1585
'International Tables Vol C Tables 4.2.6.8 and 6.1.1.4'

_symmetry_cell_setting
Orthorhombic_symmetry_space_group_name_H-M    P2(1)2(1)2(1)

loop_
_symmetry_equiv_pos_as_xyz
'x, y, z'
'-x+1/2, -y, z+1/2'
'-x, y+1/2, -z+1/2'
'x+1/2, -y+1/2, -z'

_cell_length_a                    5.4588(9)
_cell_length_b                    7.1570(11)
_cell_length_c                    19.389(3)
_cell_angle_alpha                 90.00
_cell_angle_beta                  90.00
_cell_angle_gamma                 90.00
_cell_volume                      757.5(2)
_cell_formula_units_Z             4
_cell_measurement_temperature     203(2)
```

```
_cell_measurement_reflns_used     507
_cell_measurement_theta_min       2.10
_cell_measurement_theta_max       24.71

_exptl_crystal_description        block
_exptl_crystal_colour             colorless
_exptl_crystal_size_max           0.40
_exptl_crystal_size_mid           0.20
_exptl_crystal_size_min           0.20
_exptl_crystal_density_meas       n/a
_exptl_crystal_density_diffrn     1.540
_exptl_crystal_density_method     'not measured'
_exptl_crystal_F_000              368
_exptl_absorpt_coefficient_mu     0.722
_exptl_absorpt_correction_type    multi-scan
_exptl_absorpt_correction_T_min   0.7610
_exptl_absorpt_correction_T_max   0.8690
_exptl_absorpt_process_details    'SADABS, Bruker (2000)'

_exptl_special_details
;
Data collection is performed with three batch runs at phi = 0.00 deg (650
frames), at phi = 120.00 deg (650 frames), and at phi = 240.00 deg (650
frames).
A fourth batch run is collected at phi = 0.00 deg (50 frames) to monitor
crystal and diffractometer stability. Frame width = 0.30 deg in omega.
Data is merged, corrected for decay (if any), and treated with multi-scan
absorption corrections (if required). All symmetry-equivalent reflections
are merged for centrosymmetric data.
Friedel pairs are not merged for noncentrosymmetric data.
;
_diffrn_ambient_temperature       203(2)
_diffrn_radiation_wavelength      0.71073
_diffrn_radiation_type            MoK\a
_diffrn_radiation_source          'fine-focus sealed tube'
_diffrn_radiation_monochromator   graphite
_diffrn_measurement_device_type   'CCD area detector'
_diffrn_measurement_method        'phi and omega scans'
_diffrn_detector_area_resol_mean  ?
_diffrn_standards_number          ?
_diffrn_standards_interval_count  ?
_diffrn_standards_interval_time   ?
_diffrn_standards_decay_%         <1
_diffrn_reflns_number             5437
_diffrn_reflns_av_R_equivalents   0.0197
_diffrn_reflns_av_sigmaI/netI     0.0155
_diffrn_reflns_limit_h_min        -6
_diffrn_reflns_limit_h_max        6
_diffrn_reflns_limit_k_min        -8
_diffrn_reflns_limit_k_max        8
_diffrn_reflns_limit_l_min        -22
_diffrn_reflns_limit_l_max        22
_diffrn_reflns_theta_min          3.03
_diffrn_reflns_theta_max          24.71
```

```
_reflns_number_total              1242
_reflns_number_gt                 1203
_reflns_threshold_expression      >2sigma(I)

_computing_data_collection        'SMART, Bruker (2000)'
_computing_cell_refinement        'SMART, Bruker (2000)'
_computing_data_reduction         'XPREP, Bruker (2000)'
_computing_structure_solution     'SHELXS-97 (Sheldrick, 1990)'
_computing_structure_refinement   'SHELXL-97 (Sheldrick, 1997)'
_computing_molecular_graphics     'SHELXTL, Bruker (2000)'
_computing_publication_material   'SHELXTL, Bruker (2000)'

_refine_special_details
;
Refinement of F^2^ against ALL reflections.  The weighted R-factor wR and
goodness of fit S are based on F^2^, conventional R-factors R are based on
F, with F set to zero for negative F^2^. The threshold expression of F^2^
> 2sigma(F^2^) is used only for calculating R-factors(gt) etc. and
is
not relevant to the choice of reflections for refinement.  R-factors
based
on F^2^ are statistically about twice as large as those based on F, and
R-
factors based on ALL data will be even larger.
;
_refine_ls_structure_factor_coef  Fsqd
_refine_ls_matrix_type            full
_refine_ls_weighting_scheme       calc
_refine_ls_weighting_details
'calc w=1/[\s^2^(Fo^2^)+(0.0379P)^2^+0.0805P] where P=(Fo^2^+2Fc^2^)/3'
_atom_sites_solution_primary      direct
_atom_sites_solution_secondary    difmap
_atom_sites_solution_hydrogens    geom
_refine_ls_hydrogen_treatment     mixed
_refine_ls_extinction_method      none
_refine_ls_extinction_coef        ?
_refine_ls_abs_structure_details
'Flack H D (1983), Acta Crystallogr. A39, 876-881'
_refine_ls_abs_structure_Flack    0.06(7)
_refine_ls_number_reflns          1242
_refine_ls_number_parameters      88
_refine_ls_number_restraints      0
_refine_ls_R_factor_all           0.0206
_refine_ls_R_factor_gt            0.0197
_refine_ls_wR_factor_ref          0.0524
_refine_ls_wR_factor_gt           0.0519
_refine_ls_goodness_of_fit_ref    1.028
_refine_ls_restrained_S_all       1.028
_refine_ls_shift/su_max           0.001
_refine_ls_shift/su_mean          0.001
loop_
_atom_site_label
_atom_site_type_symbol
_atom_site_fract_x
```

```
_atom_site_fract_y
_atom_site_fract_z
_atom_site_U_iso_or_equiv
_atom_site_adp_type
_atom_site_occupancy
_atom_site_symmetry_multiplicity
_atom_site_calc_flag
_atom_site_refinement_flags
_atom_site_disorder_assembly
_atom_site_disorder_group
Cl1 Cl 0.76675(8) 0.69920(5) 0.10932(2) 0.02648(13) Uani 1 1 d . . .
S1 S 0.81579(9) 0.92891(7) 0.29938(3) 0.03276(15) Uani 1 1 d . . .
H1D H 0.7905 1.0405 0.3450 0.049 Uiso 1 1 calc R . .
N1 N 0.4453(3) 0.7880(2) 0.42225(8) 0.0240(3) Uani 1 1 d . . .
H1A H 0.3112 0.8541 0.4107 0.036 Uiso 1 1 calc R . .
H1B H 0.5694 0.8668 0.4316 0.036 Uiso 1 1 calc R . .
H1C H 0.4129 0.7180 0.4597 0.036 Uiso 1 1 calc R . .
O1 O 0.8049(2) 0.43124(18) 0.33988(6) 0.0294(3) Uani 1 1 d . . .H1E H
0.9287 0.3746 0.3533 0.044 Uiso 1 1 calc R . .
O2 O 0.8555(3) 0.5919(2) 0.43778(7) 0.0401(4) Uani 1 1 d . . .
C1 C 0.7441(3) 0.5589(2) 0.38558(8) 0.0228(4) Uani 1 1 d . . .
C2 C 0.5156(3) 0.6641(3) 0.36389(10) 0.0218(4) Uani 1 1 d . . .
H2A H 0.3823 0.5725 0.3564 0.026 Uiso 1 1 calc R . .
C3 C 0.5531(4) 0.7740(3) 0.29718(10) 0.0254(4) Uani 1 1 d . . .
H3A H 0.4057 0.8481 0.2880 0.030 Uiso 1 1 calc R . .
H3B H 0.5734 0.6857 0.2590 0.030 Uiso 1 1 calc R . .
O3 O 0.8175(3) 0.01111(19) 0.48534(8) 0.0294(3) Uani 1 1 d . . .
H3C H 0.775(5) 0.091(4) 0.5139(14) 0.044 Uiso 1 1 d . . .
H3D H 0.938(6) 0.058(4) 0.4657(14) 0.044 Uiso 1 1 d . . .
loop_
_atom_site_aniso_label
_atom_site_aniso_U_11
_atom_site_aniso_U_22
_atom_site_aniso_U_33
_atom_site_aniso_U_23
_atom_site_aniso_U_13
_atom_site_aniso_U_12
Cl1 0.0266(2) 0.0200(2) 0.0328(2) -0.00044(16) 0.0006(2) -0.00239(17)
S1 0.0347(3) 0.0311(2) 0.0325(2) 0.0036(2) 0.0040(2) -0.0069(2)
N1 0.0259(8) 0.0239(7) 0.0221(7) 0.0026(6) 0.0031(6) 0.0061(7)
O1 0.0306(7) 0.0270(6) 0.0306(7) -0.0075(5) -0.0040(6) 0.0089(6)
O2 0.0462(9) 0.0427(8) 0.0314(8) -0.0137(7) -0.0161(6) 0.0211(8)
C1 0.0271(9) 0.0203(8) 0.0209(9) -0.0006(7) 0.0027(8) 0.0009(7)
C2 0.0230(9) 0.0201(9) 0.0224(9) -0.0003(7) -0.0001(7) 0.0000(7)
C3 0.0303(9) 0.0248(9) 0.0211(9) 0.0006(8) -0.0039(8) -0.0007(8)
O3 0.0353(8) 0.0256(7) 0.0274(7) -0.0021(6) 0.0078(6) -0.0006(6)

_geom_special_details
;
All esds (except the esd in the dihedral angle between two l.s. planes)
are estimated using the full covariance matrix.  The cell esds are taken
into account individually in the estimation of esds in distances, angles
and torsion angles; correlations between esds in cell parameters are only
```

```
used when they are defined by crystal symmetry.  An approximate
(isotropic)
treatment of cell esds is used for estimating esds involving l.s. planes.
;

loop_
_geom_bond_atom_site_label_1
_geom_bond_atom_site_label_2
_geom_bond_distance
_geom_bond_site_symmetry_2
_geom_bond_publ_flag
S1 C3 1.813(2) . ?
N1 C2 1.488(2) . ?
O1 C1 1.315(2) . ?
O2 C1 1.204(2) . ?
C1 C2 1.517(2) . ?
C2 C3 1.528(3) . ?

loop_
_geom_angle_atom_site_label_1
_geom_angle_atom_site_label_2
_geom_angle_atom_site_label_3
_geom_angle
_geom_angle_site_symmetry_1
_geom_angle_site_symmetry_3
_geom_angle_publ_flag
O2 C1 O1 125.11(16) . . ?
O2 C1 C2 123.44(15) . . ?
O1 C1 C2 111.44(14) . . ?
N1 C2 C1 107.28(14) . . ?
N1 C2 C3 111.82(15) . . ?
C1 C2 C3 112.33(15) . . ?
C2 C3 S1 113.65(13) . . ?

loop_
_geom_torsion_atom_site_label_1
_geom_torsion_atom_site_label_2
_geom_torsion_atom_site_label_3
_geom_torsion_atom_site_label_4
_geom_torsion _geom_torsion_site_symmetry_1
_geom_torsion_site_symmetry_2
_geom_torsion_site_symmetry_3
_geom_torsion_site_symmetry_4
_geom_torsion_publ_flag
O2 C1 C2 N1 -7.7(2) . . . . ?
O1 C1 C2 N1 173.32(14) . . . . ?
O2 C1 C2 C3 115.6(2) . . . . ?
O1 C1 C2 C3 -63.40(19) . . . . ?
N1 C2 C3 S1 67.36(18) . . . . ?
C1 C2 C3 S1 -53.33(18) . . . . ?

_diffrn_measured_fraction_theta_max    0.943
_diffrn_reflns_theta_full              24.71
_diffrn_measured_fraction_theta_full   0.943
```

```
_refine_diff_density_max    0.150
_refine_diff_density_min   -0.202
_refine_diff_density_rms    0.041
```

L-Threonine Hydrochloride .cif File

```
data_db02

_audit_creation_method            SHELXL-97
_chemical_name_systematic
;
 ?
;
_chemical_name_common             L-threonine_hydrochloride
_chemical_melting_point           147-150C
_chemical_absolute_configuration  L
_chemical_formula_moiety          ?
_chemical_formula_sum
 'C4 H10 Cl N O3'
_chemical_formula_weight          155.58

loop_
 _atom_type_symbol
 _atom_type_description
 _atom_type_scat_dispersion_real
 _atom_type_scat_dispersion_imag
 _atom_type_scat_source
 'C'  'C'   0.0033   0.0016
 'International Tables Vol C Tables 4.2.6.8 and 6.1.1.4'
 'H'  'H'   0.0000   0.0000
 'International Tables Vol C Tables 4.2.6.8 and 6.1.1.4'
 'N'  'N'   0.0061   0.0033
 'International Tables Vol C Tables 4.2.6.8 and 6.1.1.4'
 'O'  'O'   0.0106   0.0060
 'International Tables Vol C Tables 4.2.6.8 and 6.1.1.4'
 'Cl'  'Cl'   0.1484   0.1585
 'International Tables Vol C Tables 4.2.6.8 and 6.1.1.4'

_symmetry_cell_setting            Monoclinic
_symmetry_space_group_name_H-M    P2(1)

loop_
 _symmetry_equiv_pos_as_xyz
 'x, y, z'
 '-x, y+1/2, -z'

_cell_length_a                    7.275(4)
_cell_length_b                    5.263(3)
_cell_length_c                    9.556(5)
_cell_angle_alpha                 90.00
_cell_angle_beta                  92.545(5)
_cell_angle_gamma                 90.00
_cell_volume                      365.5(3)
_cell_formula_units_Z             2
_cell_measurement_temperature     217(2)
_cell_measurement_reflns_used     485
_cell_measurement_theta_min       2.80
_cell_measurement_theta_max       24.71
```

```
_exptl_crystal_description        block
_exptl_crystal_colour             colorless
_exptl_crystal_size_max           0.25
_exptl_crystal_size_mid           0.20
_exptl_crystal_size_min           0.20
_exptl_crystal_density_meas       n/a
_exptl_crystal_density_diffrn     1.413
_exptl_crystal_density_method     'not measured'
_exptl_crystal_F_000              164
_exptl_absorpt_coefficient_mu     0.464
_exptl_absorpt_correction_type    multi-scan
_exptl_absorpt_correction_T_min   0.8929
_exptl_absorpt_correction_T_max   0.9130
_exptl_absorpt_process_details    'SADABS, Bruker (2000)'

_exptl_special_details
;
 ?
;

_diffrn_ambient_temperature       217(2)
_diffrn_radiation_wavelength      0.71073
_diffrn_radiation_type            MoK\a
_diffrn_radiation_source          'fine-focus sealed tube'
_diffrn_radiation_monochromator   graphite
_diffrn_measurement_device_type   'CCD area detector'
_diffrn_measurement_method        'phi and omega scans'
_diffrn_detector_area_resol_mean  ?
_diffrn_standards_number          ?
_diffrn_standards_interval_count  ?
_diffrn_standards_interval_time   ?
_diffrn_standards_decay_%         <1
_diffrn_reflns_number             2636
_diffrn_reflns_av_R_equivalents   0.0160
_diffrn_reflns_av_sigmaI/netI     0.0217
_diffrn_reflns_limit_h_min        -8
_diffrn_reflns_limit_h_max        8
_diffrn_reflns_limit_k_min        -6
_diffrn_reflns_limit_k_max        6
_diffrn_reflns_limit_l_min        -11
_diffrn_reflns_limit_l_max        11
_diffrn_reflns_theta_min          3.45
_diffrn_reflns_theta_max          24.72
_reflns_number_total              1175
_reflns_number_gt                 1139
_reflns_threshold_expression      >2sigma(I)

_computing_data_collection        'SMART, Bruker (2000)'
_computing_cell_refinement        'SMART, Bruker (2000)'
_computing_data_reduction         'XPREP, Bruker (2000)'
_computing_structure_solution     'SHELXS-97 (Sheldrick, 1990)'
_computing_structure_refinement   'SHELXL-97 (Sheldrick, 1997)'
_computing_molecular_graphics     'SHELXTL, Bruker (2000)'
```

```
_computing_publication_material   'SHELXTL, Bruker (2000)'

_refine_special_details
;
 Refinement of F^2^ against ALL reflections.  The weighted R-factor wR and
 goodness of fit S are based on F^2^, conventional R-factors R are based
 on F, with F set to zero for negative F^2^. The threshold expression of
 F^2^ > 2sigma(F^2^) is used only for calculating R-factors(gt) etc. and
is
 not relevant to the choice of reflections for refinement.  R-factors
based
 on F^2^ are statistically about twice as large as those based on F, and
R-
 factors based on ALL data will be even larger.
;

_refine_ls_structure_factor_coef  Fsqd
_refine_ls_matrix_type            full
_refine_ls_weighting_scheme       calc
_refine_ls_weighting_details
 'calc w=1/[\s^2^(Fo^2^)+(0.0390P)^2^+0.0540P] where P=(Fo^2^+2Fc^2^)/3'
_atom_sites_solution_primary      direct
_atom_sites_solution_secondary    difmap
_atom_sites_solution_hydrogens    geom
_refine_ls_hydrogen_treatment     constr
_refine_ls_extinction_method      none
_refine_ls_extinction_coef        ?
_refine_ls_abs_structure_details
 'Flack H D (1983), Acta Crystallogr. A39, 876-881'
_refine_ls_abs_structure_Flack    0.07(6)
_refine_ls_number_reflns          1175
_refine_ls_number_parameters      85
_refine_ls_number_restraints      1
_refine_ls_R_factor_all           0.0228
_refine_ls_R_factor_gt            0.0216
_refine_ls_wR_factor_ref          0.0582
_refine_ls_wR_factor_gt           0.0575
_refine_ls_goodness_of_fit_ref    0.999
_refine_ls_restrained_S_all       0.998
_refine_ls_shift/su_max           0.000
_refine_ls_shift/su_mean          0.000

loop_
 _atom_site_label
 _atom_site_type_symbol
 _atom_site_fract_x
 _atom_site_fract_y
 _atom_site_fract_z
 _atom_site_U_iso_or_equiv
 _atom_site_adp_type
 _atom_site_occupancy
 _atom_site_symmetry_multiplicity
 _atom_site_calc_flag
 _atom_site_refinement_flags
```

```
 _atom_site_disorder_assembly
 _atom_site_disorder_group
Cl1 Cl 1.00281(5) -0.36681(9) 0.83680(4) 0.02996(14) Uani 1 1 d . . .
N1 N 0.75250(18) 0.1395(4) 0.86738(13) 0.0241(3) Uani 1 1 d . . .
H1A H 0.8280 0.2709 0.8515 0.023(5) Uiso 1 1 calc R . .
H1B H 0.8153 -0.0072 0.8616 0.038(7) Uiso 1 1 calc R . .
H1C H 0.7082 0.1543 0.9535 0.052(7) Uiso 1 1 calc R . .
O1 O 0.46322(19) -0.1421(3) 0.92398(14) 0.0349(3) Uani 1 1 d . . .
O2 O 0.2910(2) 0.0005(3) 0.74008(16) 0.0402(4) Uani 1 1 d . . .
H2B H 0.2096 -0.0868 0.7747 0.060 Uiso 1 1 calc R . .
O3 O 0.6643(2) -0.2423(3) 0.63260(14) 0.0308(3) Uani 1 1 d . . .
H3B H 0.7532 -0.2768 0.6867 0.046 Uiso 1 1 calc R . .
C1 C 0.4427(3) -0.0147(4) 0.8192(2) 0.0259(4) Uani 1 1 d . . .
C2 C 0.5969(2) 0.1406(4) 0.76075(16) 0.0229(3) Uani 1 1 d . . .
H2A H 0.5541 0.3175 0.7460 0.027 Uiso 1 1 calc R . .
C3 C 0.6478(2) 0.0271(4) 0.61907(18) 0.0251(4) Uani 1 1 d . . .
H3A H 0.5436 0.0610 0.5515 0.030 Uiso 1 1 calc R . .
C4 C 0.8180(3) 0.1435(5) 0.55951(18) 0.0320(4) Uani 1 1 d . . .
H4A H 0.8423 0.0626 0.4710 0.048 Uiso 1 1 calc R . .
H4B H 0.9224 0.1186 0.6248 0.048 Uiso 1 1 calc R . .
H4C H 0.7983 0.3240 0.5446 0.048 Uiso 1 1 calc R . .

loop_
 _atom_site_aniso_label
 _atom_site_aniso_U_11
 _atom_site_aniso_U_22
 _atom_site_aniso_U_33
 _atom_site_aniso_U_23
 _atom_site_aniso_U_13
 _atom_site_aniso_U_12
Cl1 0.0262(2) 0.0276(2) 0.0356(2) 0.0033(2) -0.00376(15) -0.0049(2)
N1 0.0267(7) 0.0241(7) 0.0218(6) -0.0032(8) 0.0034(5) -0.0026(10)
O1 0.0314(7) 0.0409(8) 0.0321(7) 0.0109(7) -0.0012(5) -0.0101(6)
O2 0.0237(7) 0.0499(9) 0.0465(9) 0.0169(7) -0.0049(6) -0.0111(7)
O3 0.0369(8) 0.0214(6) 0.0336(7) -0.0045(5) -0.0061(6) -0.0004(6)
C1 0.0233(9) 0.0257(10) 0.0287(10) -0.0015(8) 0.0022(7) -0.0012(7)
C2 0.0224(8) 0.0205(7) 0.0255(8) 0.0013(9) -0.0011(6) -0.0006(10)
C3 0.0279(10) 0.0234(8) 0.0235(9) 0.0012(7) -0.0027(7) 0.0012(8)
C4 0.0366(9) 0.0323(9) 0.0275(8) 0.0018(10) 0.0077(7) 0.0016(11)

_geom_special_details
;
 All esds (except the esd in the dihedral angle between two l.s. planes)
 are estimated using the full covariance matrix.  The cell esds are taken
 into account individually in the estimation of esds in distances, angles
 and torsion angles; correlations between esds in cell parameters are only
 used when they are defined by crystal symmetry.  An approximate
(isotropic)
 treatment of cell esds is used for estimating esds involving l.s. planes.
;

loop_
 _geom_bond_atom_site_label_1
 _geom_bond_atom_site_label_2
```

```
 _geom_bond_distance
 _geom_bond_site_symmetry_2
 _geom_bond_publ_flag
N1 C2 1.489(2) . ?
O1 C1 1.209(2) . ?
O2 C1 1.312(2) . ?
O3 C3 1.428(2) . ?
C1 C2 1.514(3) . ?
C2 C3 1.540(3) . ?
C3 C4 1.515(3) . ?

loop_
 _geom_angle_atom_site_label_1
 _geom_angle_atom_site_label_2
 _geom_angle_atom_site_label_3
 _geom_angle
 _geom_angle_site_symmetry_1
 _geom_angle_site_symmetry_3
 _geom_angle_publ_flag
O1 C1 O2 125.48(18) . . ?
O1 C1 C2 122.59(17) . . ?
O2 C1 C2 111.89(16) . . ?
N1 C2 C1 107.39(15) . . ?
N1 C2 C3 113.28(14) . . ?
C1 C2 C3 109.00(17) . . ?
O3 C3 C4 111.65(17) . . ?
O3 C3 C2 109.14(16) . . ?
C4 C3 C2 113.93(17) . . ?

loop_
 _geom_torsion_atom_site_label_1
 _geom_torsion_atom_site_label_2
 _geom_torsion_atom_site_label_3
 _geom_torsion_atom_site_label_4
 _geom_torsion
 _geom_torsion_site_symmetry_1
 _geom_torsion_site_symmetry_2
 _geom_torsion_site_symmetry_3
 _geom_torsion_site_symmetry_4
 _geom_torsion_publ_flag
O1 C1 C2 N1 -10.0(3) . . . . ?
O2 C1 C2 N1 172.23(17) . . . . ?
O1 C1 C2 C3 113.1(2) . . . . ?
O2 C1 C2 C3 -64.7(2) . . . . ?
N1 C2 C3 O3 73.0(2) . . . . ?
C1 C2 C3 O3 -46.46(19) . . . . ?
N1 C2 C3 C4 -52.5(2) . . . . ?
C1 C2 C3 C4 -172.00(16) . . . . ?

loop_
 _geom_hbond_atom_site_label_D
 _geom_hbond_atom_site_label_H
 _geom_hbond_atom_site_label_A
 _geom_hbond_distance_DH
```

```
 _geom_hbond_distance_HA
 _geom_hbond_distance_DA
 _geom_hbond_angle_DHA
 _geom_hbond_site_symmetry_A
O3 H3B Cl1  0.83 2.31 3.1427(18) 179.1 .

_diffrn_measured_fraction_theta_max    0.946
_diffrn_reflns_theta_full              24.72
_diffrn_measured_fraction_theta_full   0.946
_refine_diff_density_max    0.167
_refine_diff_density_min   -0.142
_refine_diff_density_rms    0.034
```

Table 3S.1. Planewave energy cutoff and k-points used for proton optimization (where applicable) and calculations of the chlorine EFG and magnetic shielding tensors for amino acid hydrochlorides.

amino acid hydrochloride[a]	custom plane wave cutoff / eV	k-point grid	k-point setting
alanine	450	3 x 1 x 5	fine
arginine[b]	450	1 x 2 x 1	coarse[c]
aspartic acid	450	3 x 3 x 3	fine
cysteine	450	3 x 2 x 1	coarse[c]
glutamic acid	610	5 x 2 x 2	fine
glycine	610	4 x 5 x 2	fine
histidine	450	2 x 3 x 4	fine
lysine	450	3 x 2 x 4	fine
methionine	450	4 x 1 x 5	fine
phenylalanine	610	1 x 4 x 5	fine
proline	450	2 x 4 x 3	fine
threonine	450	3 x 5 x 3	fine
tryptophan	450	3 x 5 x 2	fine
tyrosine	610	2 x 3 x 5	fine
valine	610	2 x 4 x 5	fine

[a]Arginine, cysteine and histidine salts are monohydrates. The lysine salt is a dihydrate.
[b]Hydrogen position optimization not performed prior to NMR calculation. [c]Lower setting required in order for calculation to complete.

Table 2S.2. GIPAW-DFT calculated chlorine-35 EFG and MS tensor parameters for amino acid hydrochloride salts for which X-ray structures are available. Calculations carried out with no hydrogen positions optimization.

Amino Acid Hydrochloride[a,b]	$\lvert C_Q(^{35}Cl)\rvert$ / MHz	η_Q	δ_{iso} / ppm[c,d]	Ω / ppm	κ	α, β, γ /°
Alanine	8.04	0.577	123	89	0.3	175, 5, 112
Arganine	2.45	0.197	51	44	-0.2	65, 71, 54
Aspartic Acid	3.38	0.396	96	61	-0.2	154, 84, 69
Cysteine	1.84	0.538	87	60	-0.6	185, 32, 126
Histidine	2.38	0.721	105	99	-0.3	149, 73, 173
Methionine	4.59	0.699	81	107	0.3	55, 29, 17
Proline	4.89	0.594	107	52	0.6	149, 87, 15
Threonine	6.65	0.944	89	82	-0.2	89, 81, 43
Tryptophan	11.4	0.813	166	134	0.1	92, 88, 1

[a]Arginine, cysteine and histidine hydrochloride salts are monohydrates. [b]All amino acids are of the L-variety. [c]To convert from calculated shielding constants to chemical shifts, a shift of 45.37 ppm was used (for the conversion from solid to aqueous NaCl chemical shift scales) in addition to the absolute shielding conversion found Chapter 1. [d]Experimental values are all w.r.t. solid NaCl.

Appendix 3

Table 3S.1 Planewave energy cutoff and k-points used for hydrogen position optimization (c-e) and NMR calculations (a-e) of models based on **1**.

model	custom plane wave cutoff / eV	k-point grid	k-point setting
a	500	2 x 2 x 1	fine
b	500	2 x 2 x 1	fine
c	280[a]	1 x 1 x 1	coarse
d	280[a]	1 x 1 x 1	coarse
e	550	2 x 2 x 1	fine

[a]Lower setting required in order for calculation to complete. In select cases where the fine setting was used, coarse setting calculations were also done for comparison. Both the CS and EFG tensor parameters changed only slightly (eg. Ω changed by < 1ppm and C_Q changed by ~0.1 MHz).

Appendix 4

Table 4S.4. Planewave energy cutoff and k-points used for NMR calculations of the polymorphs of benzidine hydrochloride and the hydrates of magnesium chloride.

compound	custom plane wave cutoff / eV	k-point grid
benzidine hydrochloride polymorph A	440	4 x 3 x 2
benzidine hydrochloride polymorph B	200	1 x 2 x 2
magnesium chloride	380	8 x 8 x 2
magnesium chloride hexahydrate	500	2 x 2 x 3
magnesium chloride tetrahydrate	500	4 x 3 x 3
magnesium chloride dihydrate	500	3 x 2 x 6
magnesium chloride monohydrate	500	2 x 6 x 2

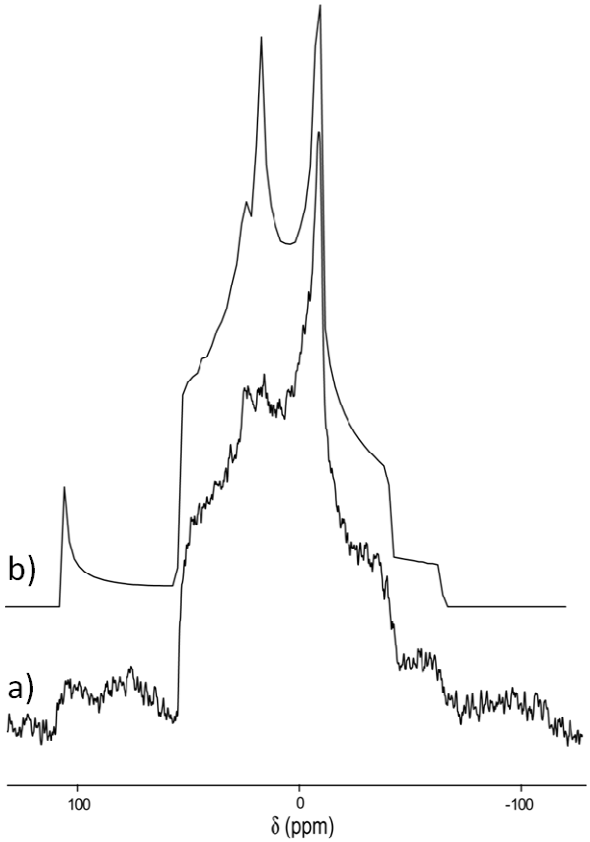

Figure S4.1. Solid-state chlorine-35 MAS NMR spectroscopy (a) of the unidentified magnesium chloride hydrate at 21.1 T with ν_{rot} = 15 kHz. Best-fit spectra simulated with WSolids appear in (b). Included in the simulation is a small amount of anhydrous magnesium chloride impurity.

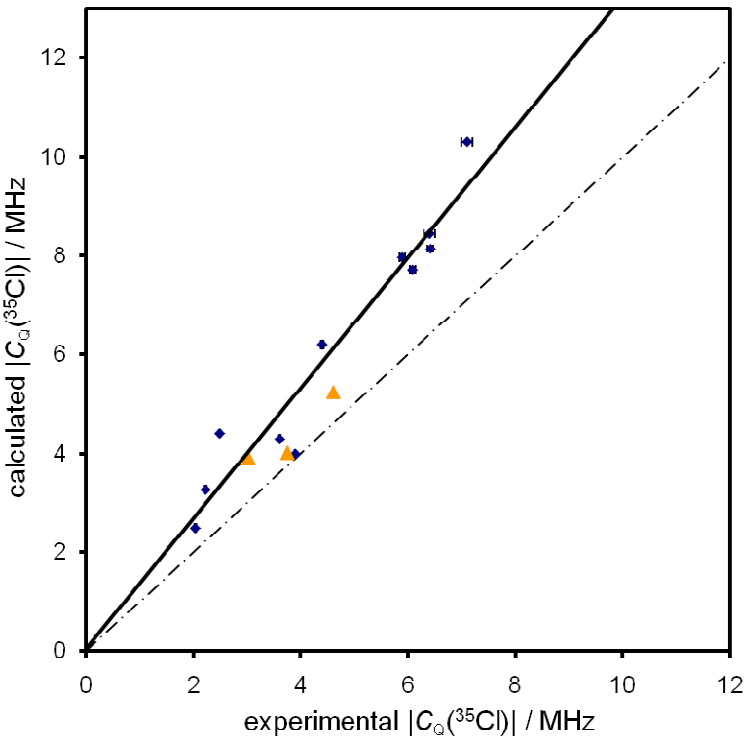

Figure 4S.2. Comparison between the experimentally determined chlorine-35 quadrupolar coupling constant, on the *x*-axis and the GIPAW-DFT calculated values, on the *y*-axis, for the amino acid hydrochlorides, with the exception of four outliers (blue diamonds), as shown in Chapter 3. Included on the curve are the data points for the anhydrous, tetrahydrate and hexahydrate forms of magnesium chloride (orange triangles triangles). See Figure 3.14 in Chapter 3 for additional details and references.

Appendix 5

Table 5S.1 Planewave energy cutoff and k-points used for NMR calculations of the group thirteen chlorides

compound	custom plane wave cutoff / eV	k-point grid
aluminum trichloride	610	5 x 5 x 4
indium monochloride	610	2 x 2 x 2
indium trichloride	610	5 x 5 x 4
gallium dichloride	610	3 x 3 x 3
gallium trichloride	610	4 x 5 x 4

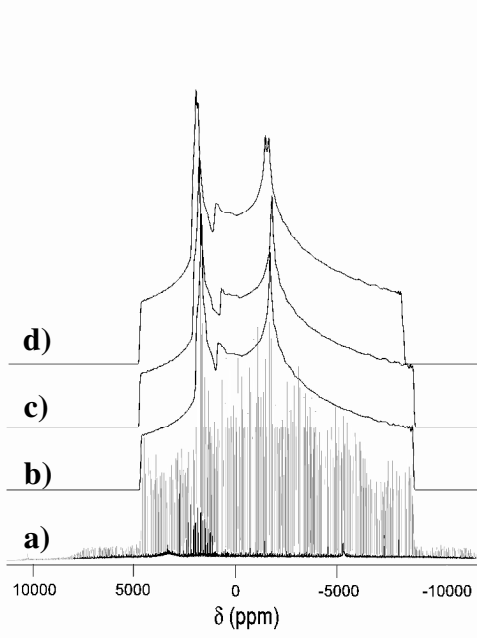

Figure 5S.1. Experimental and simulated solid-state chlorine-35 NMR spectra of aluminum trichloride at 21.1 T. Best-fit simulation is shown in b, simulation assuming no CSA is shown in c and a simulation based on the calculated parameters is shown in d.

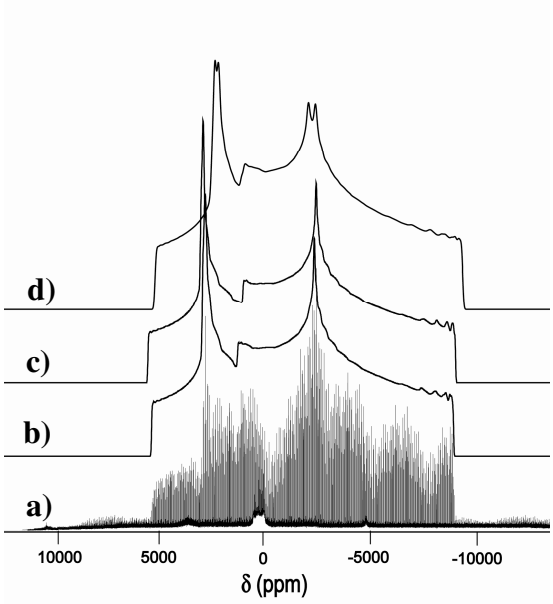

Figure 5S.2. Experimental and simulated solid-state chlorine-35 NMR spectra of indium trichloride at 21.1 T. Best-fit simulation is shown in b, simulation assuming no CSA is shown are in c and a simulation based on the calculated parameters is shown in d.

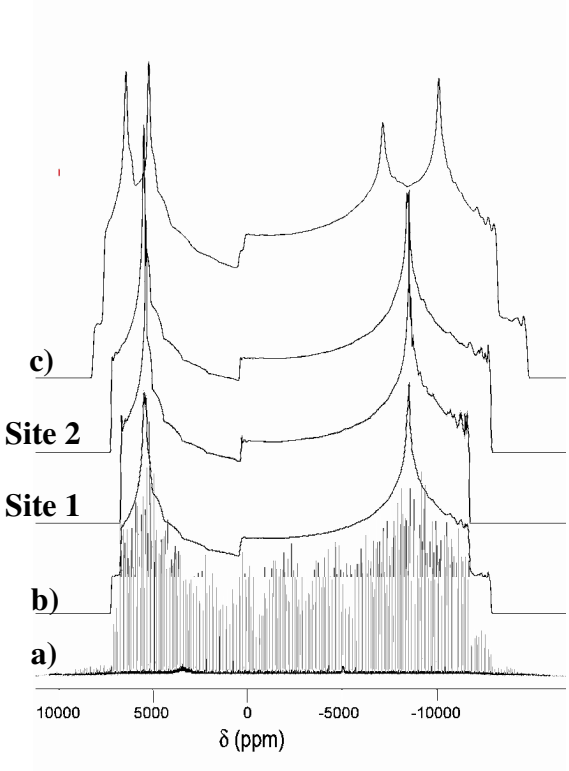

Figure 5S.3. Experimental and simulated solid-state chlorine-35 NMR spectra of gallium dichloride at 21.1 T. Best-fit simulation is shown in b, with individual simulations of the two sites shown above. Simulation based on calculated parameters is shown in c.

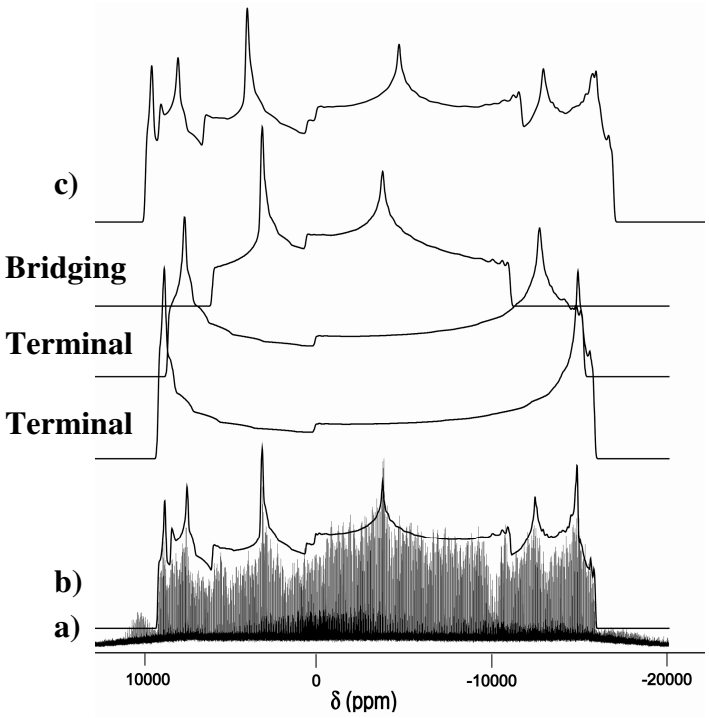

Figure 5S.4. Experimental and simulated solid-state chlorine-35 NMR spectra of gallium trichloride at 21.1 T. Best-fit simulations are shown in b, with individaul simulations of the three sites shown above. Simulation based on calculated parameters is shown in c.